Charge transfer of Rydberg hydrogen molecules and atoms at doped silicon surfaces

Ganeshalingam Sashikesh

Magdalen College, University of Oxford

A thesis submitted for the degree of Doctor of Philosophy

Hilary Term, 2012

Charge transfer of Rydberg hydrogen molecules and atoms at doped silicon surfaces

Ganeshalingam Sashikesh, Magdalen College

A thesis submitted in partial fulfilment of the requirements
for the degree of Doctor of Philosophy of the University of Oxford
Hilary Term, 2012

Abstract

The work of this thesis focuses on the interaction of high Rydberg states of hydrogen molecules and atoms with various doped Si semiconductor surfaces with the results compared with those obtained with an atomically flat gold surface. The major part of the thesis was carried out using para-H_2 molecular Rydberg states with principal quantum number $n = 17 - 21$ and core rotational quantum number $N^+ = 2$. Subsequently, this study was continued using H atomic Rydberg states with principal quantum number $n = 29 - 34$. The high Rydberg states have been produced using two-step laser excitation. For close Rydberg surface separation ($< 6\ n^2$ a.u.), the Rydberg states may be ionized due to an attractive surface potential experienced by the Rydberg electron, and the remaining ion core may be detected by applying an external electric field.

An efficient ion detectability method is introduced to compare the many surface ionization profiles quantitatively. The p-type doped Si surfaces enhance the detected ion-signal more than the n-type doped Si surfaces due to the presence of widely distributed positive dopant charge fields in the p-type doped Si surfaces. As the dopant density increases, the area sampled by the resultant ions becomes effectively '*more neutral*', and the decay rate of the potential from the surface dopant charge with distance from the surface becomes more rapid. Therefore, the minimum ionization distance is also reduced with increasing dopant density. It is found that the detected ion-signal decreases with increasing dopant density of both p- and n- type doped Si surfaces. The higher-n Rydberg states have shown higher ion detectability than that of lower-n Rydberg states and this variation also becomes smaller when increasing the dopant density.

Experiments involving H_2 Rydberg molecules incident on various doped Si surfaces in the presence of a Stark field at the point of excitation are also presented here. The surface ionization profiles produced via both electron and ion detection schemes are measured by changing the Stark polarization. Positive surface dopant charges oppose production of '*backscattered*' electrons and negative surface dopant charges enhance the electron-signal. For the electron detection scheme, lightly doped n-type Si surfaces show higher detectability but in the case of p-type Si surfaces the more heavily doped Si surfaces give a higher detected signal. This different behaviour of the detected ion or electron signal implies a different production mechanism.

Theoretical trajectory simulations were also carried out based on a new *2D* surface potential model. The results qualitatively agree with the experimental results and explain the changes of the surface ionization profiles between the various dopant types and dopant densities of the Si surfaces.

Acknowledgements

I would never have been able to finish my thesis without the guidance of my group members, help from friends, and support from my family members. First, I am sincerely and heartily grateful to my supervisor Professor Timothy P Softley for his patience, guidance, and encouragement throughout my D.Phil. studies in Oxford. I am particularly grateful to Tim for reading my thesis and his patience in polishing my grammar. I would also like to thank him for giving me an opportunity to learn higher level physics. Without his sincere efforts and willingness to help me whenever I showed up to see him, I doubt I would have this opportunity to thank him now.

I am obliged to many of my colleagues in the Softley group for their friendship during my stay in Oxford, particularly, Eric, Elin, Mark F, William, James, Mark D, Chris and Xiaolin. Thanks should also go to Tertia Softley for her hospitality and many incredible group dinners for the last four years, especially for making vegetarian foods.

It is a great pleasure to thank everyone who helped me to complete my thesis successfully; I am especially indebted to Eric So, for all his ideas, help and advice in the theoretical and experimental work. I did not have enough experimental skills in this area, when I first arrived in Oxford. Mark Ford encouraged me to learn the experimental skills needed to complete this work and initiate my experimental work on hydrogen molecular Rydberg states. I want to say thanks to Chris Rennick who read my whole thesis and suggested some valuable modifications.

I would like to thank all of my wonderful friends during my tough years in Oxford. Their support and care helped me to reduce stress and concentrate on my graduate studies. I greatly value their friendship, and deeply appreciate their belief in me. I am also grateful to some Sri Lankan families in the UK for their kindness and help shown to me since my first visit to the UK so that I never feel alone and homesick for the last four years.

I must also thank Kuganathan for his mental support and guidance to produce an effective thesis and complete my degree.

I would like to thank the Clarendon fund and Magdalen College Perkin Research studentship for their financial support to complete my research work and gain a D.Phil. from the University of Oxford.

Finally, I would like to thank my whole family for their continuous love and encouragement. I would like to dedicate this thesis to my mum and dad.

Contents

Chapter 1

Introduction

The charge transfer process between gas-phase atoms or molecules with solid surfaces is of substantial interest both experimentally and theoretically. Resonant charge transfer can occur through resonant tunneling of the excited electron into an unoccupied energy level in the surface. In fact, charge transfer is one example of a broader range of collisional processes enhanced by resonances. The first exploration of the unique collisional properties of Rydberg states began with the investigation of the pressure shifts and broadening of Na and K Rydberg levels by using rare gases [1].

The dominant motivation for the study of Rydberg states today is to take advantage of the unique opportunities afforded by their large physical size and weak binding. The intention of this thesis is to study the interaction between electronically excited hydrogen atoms or molecules and semiconductor surfaces. This is the first time that the tunneling ionization of atomic or molecular hydrogen Rydberg states at semiconductor surfaces has been analyzed, and the results are illustrated in chapters 3, 4 and 5. It is also the first time that the effect of dopant density and dopant type has been systematically investigated.

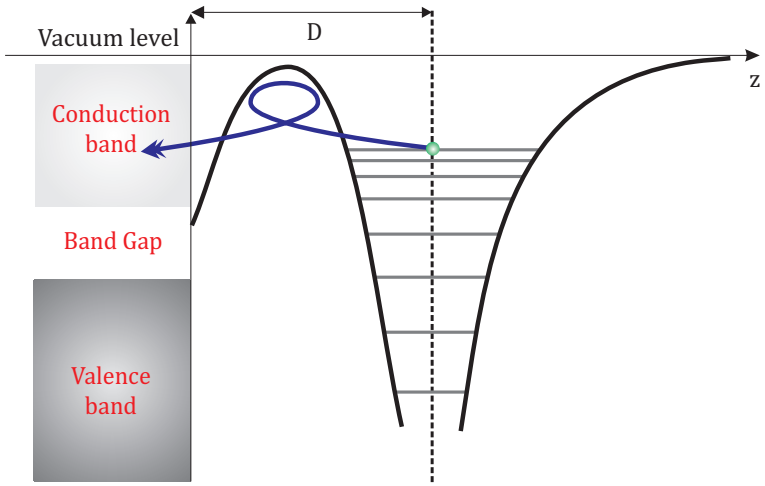

Figure 1.1: Tunneling ionization of the Rydberg electron into a conduction band of the semiconductor surface, where D is the perpendicular distance from the surface.

1.1 Tunneling ionization at surfaces

At a critical distance, charge transfer between an atom or molecule and a surface will take place through the resonant tunneling ionization of the excited electron into a vacant level (conduction band) in the surface as illustrated in Fig. 1.1. Tunneling ionization is a process in which electrons in an atom or molecule pass through a potential barrier and the ions produced move towards the surface due to the electric field associated with their image-charges (see section 1.5). Fundamental tunneling ionization techniques are used in scanning tunneling microscopy (STM) to study the geometrical structure of surfaces.

The electron transfer into the empty conduction band of the surface becomes more facile, and is many orders of magnitude greater, for states with an electron distribution oriented towards the surface. Electron transfer during the interaction of an atomic or molecular particle and a solid surface is often invoked as a key process in a variety of phenomena occurring in plasma-surface interactions, ion sputtering processes, the understanding of electronically excited states of surfaces, and the control of the novel

chemical processes. Indeed, charge transfer determines the charge state of particles, either scattered or sputtered from the surface. In addition, charge transfer is often an important step in surface reaction mechanisms, the transfer of an electron triggering an evolution in the arrangement of atoms or molecules on the surface.

The tunneling ionization from the atom or molecule to the surface and vice versa can be influenced by a variety of parameters, including the electronic state of the atom, the direction and velocity of the Rydberg core motion or the presence of external electric and magnetic fields. The behaviour of Rydberg atoms or molecules near metal surfaces in the presence of an external electric field has been examined theoretically to evaluate their potential use as an experimental probe of electron tunneling processes at surfaces. In recent years, much attention has been focused on the dynamics of Rydberg states in external fields. At the same time, Rydberg states near a metal surface play an important role as a model system for theoretical study of charge transfer and produce a measurable experimental response.

The probability of tunnelling ionization depends on the degree of overlap between the electronic wave function of the atom or molecule and the wavefunction associated with the vacant energy level of the surface and it is given for a parabolic barrier by the following equation [2],

$$p \approx \exp\left[-2d\sqrt{\frac{2m(V-E)}{\hbar^2}}\right] \tag{1.1}$$

where E is the total energy, V is the potential energy, d is the width of the tunneling barrier and m is the mass of the tunneling particle. The probability of the tunneling ionization increases with decreasing ionic core-surface separation.

1.2 Hydrogen Rydberg states

An atom or molecule in which one (or more) valence electrons has been excited into a hydrogenic orbital of high principal quantum number, n, is called a Rydberg atom/molecule. The meaning of 'high' in this context is that the electron distribution lies almost entirely orbital the core electron distribution; the n value where this occurs may vary from one atom or molecule to another. Classically, such a state corresponds to putting one electron into an orbit, in which the average separation between the ionic core and the excited electron is very high. Therefore, Rydberg states can be observed in molecules or atoms provided that the electron can be promoted to a region in which it can become dynamically autonomous of the remaining electrons and that the ion core remains stable as an observer of the excitation.

The four visible lines (410 nm, 434 nm, 486 nm and 656 nm) in the spectrum of the hydrogen atom were fitted to a formula by Johann Jakob Balmer in 1885 [3], introducing the Balmer equation which is given by:

$$\lambda = B\left(\frac{m^2}{m^2 - n^2}\right) \tag{1.2}$$

where λ is the wavelength, B is the Balmer constant, n is equal to 2 and m is an integer such that $m > n$. The Rydberg formula was introduced by Johannes Robert Rydberg and it gives the wave number of the spectral lines for the hydrogen atom [4]. For the hydrogen atom, the Rydberg formula is given by:

$$\frac{1}{\lambda} = \Re_{\mathrm{H}}\left(\frac{1}{n_1^2} - \frac{1}{n_2^2}\right) \tag{1.3}$$

where $\frac{1}{\lambda}$ is the wave number, n_1 and n_2 are integer values and $\Re_{\mathrm{H}}$ is the Rydberg constant. The above Eq. 1.3 is most accurate at high-n values, and therefore higher-n states are called Rydberg states (because effects of electron spin-orbit coupling and

the Lamb shift become negligible). The basis for the classical treatment has also been evaluated experimentally by elaborate laser excitation studies of Rydberg wave packets in atoms using both radial (low-l values) and angular (high-l values) Rydberg wave packets [5].

The energy levels of sequential n states come increasingly closer to each other, and the energy difference between two adjacent n states, ΔE, scales like n^{-3}. The larger separation between the Rydberg electron and the ionic core makes the atom more sensitive to small external electric fields giving rise to the lifting of the $2l+1$ degeneracy of a Rydberg state.

Herzberg et al. [6] measured the high resolution discrete absorption spectrum for the Rydberg series of ortho and para hydrogen molecules, and modern theoretical analysis starts with the demonstrations by Herzberg [6] and Jungen [7] that multichannel quantum defect theory could be applied to the treatment of electron motion in molecular Rydberg states. The first continuum spectrum of the para-H_2 molecule from 124223.60 cm^{-1} to 139860.13 cm^{-1} was measured by Dehmer et al. [8].

There are several methods to produce the Rydberg states, such as charge exchange between an ion and a neutral species [9], electron impact of neutral species [10], electron-ion recombination [11] and laser induced optical excitation [12]. The flexibility, efficiency and selectivity of optical excitation were enormously advanced by the introduction of narrow band laser sources extending far into the UV through the use of tunable laser systems [11, 13, 14]. More recently, the discovery of pulsed field zero kinetic energy photoelectron spectroscopy (ZEKE-PES) [15, 16], and of the interrelated technique mass analysed threshold ionization spectroscopy (MATI) [17] helped to study the higher-n Rydberg states and to understand their properties.

1.2.1 Rydberg series in non-hydrogenic species

The motion of the Rydberg electron is independent of the ionic core and it spends the majority of its lifetime far from the core. This autonomous mobility can be characterized by hydrogenic quantum numbers n and l. At the same time, in a molecule the ionic core is also considered to vibrate and rotate freely from the motion of the Rydberg electron, and this ionic core movement can be characterized by the rotational quantum number, N^+, and vibrational quantum number, v^+. The energy of Rydberg states with principal quantum number, n, relative to the neutral ground states are given by the well recognized Rydberg formula:

$$E = IP - \frac{\Re_M}{(n-\delta_1)^2} \tag{1.4}$$

where IP is the ionization threshold energy, δ_1 is the quantum defect and $\Re_{\mathrm{M}}$ is the mass specific Rydberg constant which depends on the mass of the ionic core, and is given by the following equation:

$$\Re_M = \Re_\infty \left(\frac{M}{m_e + M} \right) \tag{1.5}$$

where m_e is the rest mass of the Rydberg electron and $\Re_\infty$ is the universal Rydberg constant (109737.32 cm^{-1}). The Rydberg constant is given by the following equation:

$$\Re_\infty = \left(\frac{m_e e^4}{8\epsilon_o^2 h^3 c} \right) \tag{1.6}$$

where h is the Planck's constant, e is the elementary charge, ϵ_o is the permittivity of free space and c is the speed of light in a vacuum. The Rydberg constant for the H atom and H_2 molecule are $\Re_{\mathrm{H}} = 109667.31\ \mathrm{cm}^{-1}$ [18] and $\Re_{\mathrm{H_2}} = 109707.42\ \mathrm{cm}^{-1}$ respectively [6].

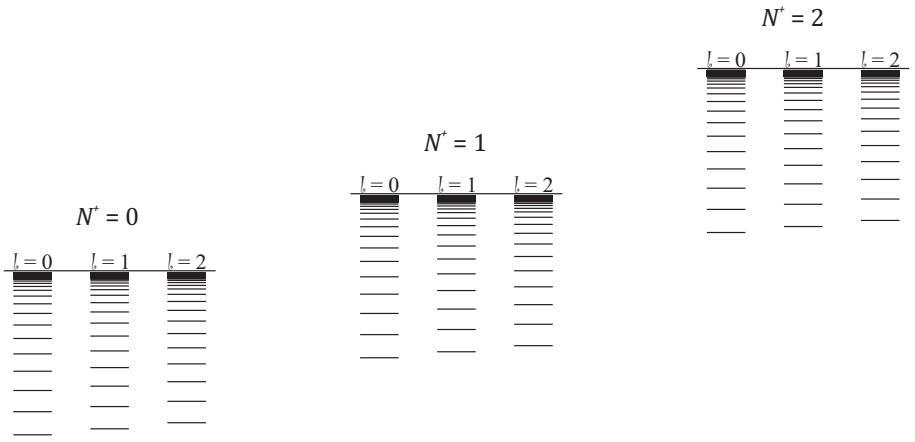

Figure 1.2: Rydberg series corresponding to different l values converge upon $N^+ = 0, 1, 2$ rotational ionization thresholds, where N^+ is a core rotational quantum number.

The different rovibrational quantum numbers of the ionic core produce several Rydberg series, and the energy levels of each of these Rydberg series converge to different ionization thresholds. Additionally, each Rydberg series contains an infinite number of states relating to the different principal quantum number of the Rydberg electron but sharing a particular ionic core configuration and electron angular momentum quantum number. Examples of Rydberg series are shown in Fig. 1.2.

In the language of quantum defect theory, the Rydberg series and their energetic continua, which are above the series, are described as channels. The different channels might be associated with different rotational and vibrational states of a molecular ion core or different spin-orbit states of the ion core in an atom. These different channels are coupled through the interaction of the Rydberg electron and the ionic core. The effect of channel interactions (see section 1.3.2) has been studied not only experimentally but also theoretically, frequently employing multichannel quantum defect theory (MQDT), first put forward by Seaton [19, 20] and further developed for molecular systems by Fano [21]. This theory provides a unified treatment of the continuum and bound parts of the channels, and it was first applied in detail to the H_2 spectrum by

Herzberg [6]. However, the H atom has different quantum numbers, arising from the interaction of the electron spin, orbital angular momentum and nuclear spin, producing several Rydberg series but those are energetically not well resolved so that different channels are not clearly observed.

1.2.2 Rydberg state wave functions

An electron moving in an elliptic orbit about the ion core can be used to illustrate the classical model of Rydberg states, where the orbital radius has a sufficiently sizeable mean radius from the ionic core, as viewed in Fig. 1.3. Sommerfeld [22] suggested that the path of this hydrogenic orbit is elliptical, and it can be characterized by both the principal quantum number, n, and the orbital angular momentum, l, of the Rydberg electron. The electron orbital aphelion ($r_{\max}$ (r_a)) increases with n^2 and the perihelion ($r_{\min}$ (r_p)) also increases with $(l + \frac{1}{2})^2$ so that the Rydberg orbital is very large; the resulting difference between low-l and high-l orbits is illustrated in Fig. 1.3. The large orbital radius of Rydberg states makes them especially susceptible to external influences such as field (both electric and magnetic) and collisions.

At low-l values for a given n, the Rydberg electron can penetrate the ionic core, thereby experiencing the non-Coulombic potential due to repulsion with core electrons and for molecules, the non-spherical potential due to nuclei, and yielding a large quantum defect. At high-l (for specified n), the effective ionic core charge experienced by the electron will decrease for multi electron atoms. The penetration will reduce when the centrifugal barrier increases as $\frac{l(l+1)}{2r^2}$. For that reason, high-l Rydberg states behave in a predominantly hydrogenic manner. The quantum defect scales approximately as l^{-5}. In practice, for $l \geq 4$ penetration is sufficiently small because of the small quantum defect ($\delta_l = 0$).

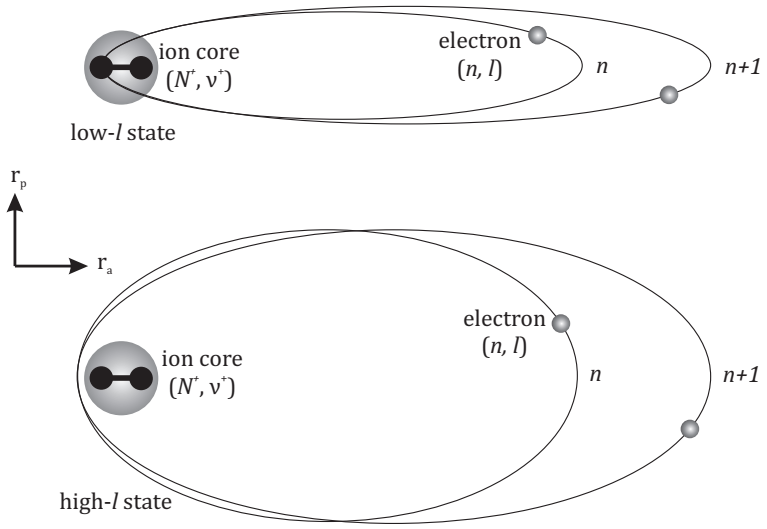

Figure 1.3: The classical representation of the elliptical Rydberg orbital for varying n and l.

The solutions of the hydrogenic Schrödinger equation [11] may be formulated as:

$$\psi_{n,l,m_l}(\theta,\phi,r) = \frac{Y_{l,m_l}(\theta,\phi)f(E_n,l,r)}{r} \tag{1.7}$$

where the angular part of the solution, $Y_{l,m_l}(\theta,\phi)$ is a spherical harmonic [23] and the radial part of the solution is dependent upon the regular Coulomb function $f(E_n,l,r)$ [24]. Using the specific boundary condition that $\psi \to 0$ as $r \to \infty$, the corresponding energy of the Rydberg states is given by Eq. 1.4 with $\delta_l = 0$.

However, in a non-hydrogenic system, the Rydberg electron can penetrate the ion core and consequently experience a non-Coulombic potential. This result is an altered effective potential at close range, and imposes a new inner boundary condition which leads to a phase shift, $\pi\delta_l$, of the radial wave function outside of the ionic core region. However, in the case of a spherically symmetric core, the angular solution remains the same as for the hydrogenic system. The phase shift scales the regular and irregular

Coulomb functions in order to delineate the radial part of the solution,

$$\psi_{n,l,m_l}(\theta,\phi,r) = \frac{Y_{l,m_l}(\theta,\phi)\,[f(E_n,l,r)\cos\pi\delta_l - g(E_n,l,r)\sin\pi\delta_l]}{r}. \qquad (1.8)$$

The above Eq. 1.8 reduces back to the hydrogenic form (as Eq. 1.7) when $\delta_l = 0$ ($\cos\pi\delta_l = 1$ and $\sin\pi\delta_l = 0$). In addition, the value of the quantum defect for diatomic molecules may be altered by the coupling of the Rydberg electron with the vibrational and rotational motion of the ionic core. However, the phase shift and quantum defect will change only moderately with principal quantum number. The interaction time with the ionic core is effectively independent of n because the kinetic energy of the Rydberg electron is extremely large close to the core due to the enormous maximum distance between the ionic core and the Rydberg electron. The kinetic energy, T, is equal to $E_n - V$ sand when $|V|$ is very large near the ionic core region the T hardly depends at all the principal quantum numbers.

1.2.3 Properties of Rydberg states

Some of the highly exaggerated properties of Rydberg states can easily be deduced from the classical Bohr model of the hydrogen atom [25]. The particular interest in this thesis is to investigate the properties of the Rydberg states in the presence of an externally applied electric field. Some interesting properties of high Rydberg states with respect to n are given in table 1.1.

Rydberg states have some intrinsically unusual properties (see table 1.1), and for that reason the studies of Rydberg states have stimulated much consideration in recent years. There are also practical applications in specific areas such as astrophysics [26], including planetary nebulae [27], plasma physics [28], laser physics and chemical physics. More recently, the properties of high Rydberg states in applied fields have

Properties of the Rydberg states	n**- dependence scaling factor**
Binding energy	n^{-2}
Level spacing between adjacent levels	n^{-3}
Degeneracy	n^2
Radiative lifetime	n^3
Rydberg orbital period	n^3
Radius of Rydberg orbit	n^2
Geometric cross-section	n^4
Polarizability	n^7
Dipole moment	n^2
Excitation cross-section	n^{-3}

Table 1.1: Properties of Rydberg states which scale with the principal quantum number, n, (adapted from [11]).

been intensely studied in different areas of chemical physics such as in the preparation of state selected ions [29, 30], studies of ion molecule interactions [30, 31], translational control of atoms or molecules [32, 33] and the investigation of Van der Waals (VDW) clusters [34, 35]. Further important applications in chemical physics are in the preparation and study of cold Rydberg molecules [36, 37].

1.3 Rydberg state decay processes

High-n Rydberg states are energetically unstable with respect to the electronic ground state, but are often kinetically stable during the lifetime of the experiments. An expression for the lifetime of a Rydberg state in a quasi-hydrogenic Rydberg atom with n and l is given by the following equation [38]:

$$\tau_{(\mathrm{ps})} = 93n^3(l + \frac{1}{2})^2. \tag{1.9}$$

There are four main mechanisms of decay processes, which are divided mainly into two groups namely radiative and non-radiative decay processes.

1.3.1 Radiative decay processes

Radiative decay processes are the principal decay mechanisms for Rydberg atoms, namely spontaneous emission and black-body radiation (BBR) stimulated transitions.

Spontaneous emission

The excited Rydberg electron undergoes a spontaneous decay to states with a lower energy by the spontaneous emission of a photon, and it is independent approximately of the presence of external fields. Classically, this decay process is only possible when a charged particle is accelerated, and it is most likely to occur when the Rydberg electron passes through the ion core region.

The overall decay rate (Γ) for the spontaneous emission of a Rydberg state $\left|n^{'}l^{'}\right\rangle$ decaying to other lower energy states $|nl\rangle$ is given by the following equation [11]

$$\Gamma_{nl} = \frac{1}{\tau_{nl}} = \sum_{n^{'}l^{'}} A_{n^{'}l^{'},nl} \tag{1.10}$$

where $A_{n^{'}l^{'},nl}$ is the Einstein coefficient for the transition from the Rydberg state nl to the lower Rydberg state $n^{'}l^{'}$. In this hydrogenic model, the lower state is always another Rydberg state but in non-hydrogenic atoms or molecules emission could also occur to the electronic ground state or an excited valence state. $A_{n^{'}l^{'},nl}$ is given by [11],

$$A_{n^{'}l^{'},nl} = \frac{-2e^2\omega^2_{n^{'}l^{'},nl}}{c^3\hbar}\overline{f}_{n^{'}l^{'},nl} \tag{1.11}$$

where $\omega_{n^{'}l^{'},nl} = \frac{(E_{n^{'}l^{'}} - E_{nl})}{\hbar}$ is the angular frequency and $\overline{f}_{n^{'}l^{'},nl}$ is the m_l-independent

average oscillator strength, given by

$$\overline{f}_{n'l',nl} = \frac{2\omega_{n'l',nl}}{3} \frac{l_{\max}}{2l+1} \left| \left\langle n'l' \left| r \right| nl \right\rangle \right|^2 . \tag{1.12}$$

The above equations (Eq. 1.11 and Eq. 1.12) show that the highest angular frequency transition typically dominates the spontaneous decay rate. The frequency of this dominant transition decreases with increasing l (because of the $\Delta l = \pm 1$ selection rule) and hence the stability of the Rydberg states with respect to spontaneous emission typically increases with increasing l. The highest frequency transition becomes approximately constant and the transition probability depends only on the squared radial matrix element, $\left| \left\langle n'l' \left| r \right| nl \right\rangle \right|^2$ for high-n and low-l ($n >> l$) Rydberg states. $\left| \left\langle n'l' \left| r \right| nl \right\rangle \right|^2$ exhibits n^{-3} scaling due to the normalization of the Rydberg state wave function, hence the lifetime scale as n^3. This is in good agreement with the classical picture (see section 1.2.2). Typical lifetimes for $n = 20$ low-l states are around 10 μs [11].

Black-Body Radiation

Rydberg states may also undergo radiative decay due to stimulated emission or absorption caused by BBR emitted by the surrounding vacuum chamber. The studies of interaction of BBR with Rydberg atoms were initiated by Gallagher and Cooke [39]. Radiative transitions between Rydberg states and continuum states (induced by ambient BBR) are a topic of current interest [40–42]. BBR-induced ionization is the main mechanism for atomic ion production [43].

The transitions between Rydberg energy levels are characterized by large dipole matrix elements resulting in excellent coupling between the Rydberg states and the thermal radiation. Therefore, Rydberg molecules and atoms are strongly affected by BBR, even

at room temperature, and transition rates can be an order of larger magnitude larger than spontaneous emission rates [11]. Both the rapid redistribution of the population and the radiative decay rates were enhanced by the BBR, and it is observed in the previous experimental analysis with Rydberg states [39]. To estimate the rate of a BBR induced transition, it is more convenient to express the radiation field in terms of photon occupation number per mode ($\overline{n}$) of the radiation field. In the presence of thermal radiation the stimulated emission rate $K_{n'l',nl}$ is $\overline{n}$ times larger than the spontaneous rate. Explicitly,

$$\begin{aligned} K_{n'l',nl} &= \overline{n} A_{n'l',nl} \\ &= \frac{-2\overline{n} e^2 \omega^2_{n'l',nl}}{c^3 \hbar} \overline{f}_{n'l',nl}. \end{aligned} \tag{1.13}$$

The frequency dependence of $K_{n'l',nl}$ is quite different from that of $A_{n'l',nl}$ and these two processes favour different final states, which is clearly shown in the previous study [44]. The black-body photons can also be absorbed by the nl Rydberg states and the favourable low frequency transition is to energetically nearby (higher or lower lying) Rydberg states ($n'l'$), whereas spontaneous emission favours high frequency transitions to the lowest lying Rydberg states. The total BBR-induced decay rate can be calculated by summing the stimulated emission and absorption rates for particular states and is given by (where $l' = l \pm 1$)

$$\Gamma_{nl} = \frac{1}{\tau^{\rm BBR}_{nl}} = \sum_{n'l'} \frac{-2\overline{n} e^2 \omega^2_{n'l',nl}}{c^3 \hbar} \overline{f}_{n'l',nl}. \tag{1.14}$$

The photon occupation number is derived from Planck's radiation law for energy

density and it is given by [11]

$$\overline{n} = \frac{1}{\exp\left[\hbar\omega/kT\right] - 1}. \tag{1.15}$$

For low frequency transitions ($\hbar\omega << \mathrm{kT}$) the limiting photon occupation number is given by

$$\overline{n} \cong \frac{kT}{\hbar\omega}. \tag{1.16}$$

In this low frequency limit, the total BBR-induced decay rate can be written as

$$\Gamma_{nl} = \frac{1}{\tau_{nl}^{\mathrm{BBR}}} = \sum_{n'l'} \frac{-2kTe^2\omega_{n'l',nl}}{c^3\hbar^2}\overline{f}_{n'l',nl}. \tag{1.17}$$

Summation over $n^{'}$ implicitly includes the continuum of states and for the one-electron atom; this formula can be evaluated by using the sum rule [24]:

$$\begin{aligned} \sum \omega_{n'l',nl}\overline{f}_{n'l',nl} &= \frac{2}{3n^2} \\ \Gamma_{nl} = \frac{1}{\tau_{nl}^{\mathrm{BBR}}} &= \frac{-4kTe^2}{3c^3n^2\hbar^2}. \end{aligned} \tag{1.18}$$

The decay rate due to the BBR depends only on n and the spontaneous emission decay rate decreases with increasing l. For high-l Rydberg states the BBR process has the greater impact on the overall lifetime. To summarize, the lifetime due to BBR induced transitions scales as n^2, while the lifetime of the spontaneous emission scales as n^3. It is clear that BBR decay processes dominate for sufficiently high-n Rydberg states, even at low-l states.

1.3.2 Non-radiative decay processes

Molecular Rydberg systems can also exhibit decay processes, which precede via a non-radiative pathway. Such mechanisms include predissociation and autoionization. These alternative pathways arise due to interaction of different Rydberg channels. A Rydberg channel is specified by a unique set of core quantum numbers and the electron orbital angular momentum. Energy exchange with the ion core via inelastic collisions can occur, and the outgoing electron will have an orbit characteristic of a different Rydberg channel. The interseries coupling arises when the electron experiences a non-centro-symmetric core potential. Such channel interactions can be attributed to configuration interaction or the presence of various multi-pole moments of the ion core.

Autoionization

Autoionization is the emission of an electron that happens when a Rydberg state has higher energy than that of the lowest ionization threshold. Energy is transferred from an internal degree of freedom of the excited ion core to the electron as kinetic energy.

$$\begin{aligned} AB^*_{(E^*)} & & AB^+_{(E^+)} + e^-_{(E^*-E^+)} \\ \left|v^+=0, N^+=2\right\rangle & \xrightarrow{\text{rotational autoionization}} & \left|v^+=0, N^+=0\right\rangle \\ \left|v^+=1, N^+=0\right\rangle & \xrightarrow{\text{vibrational autoionization}} & \left|v^+=0, N^+=0\right\rangle \\ \left|^1\Pi, v^+=0, N^+=0\right\rangle & \xrightarrow{\text{electronic autoionization}} & \left|^1\Sigma^+, v^+=0, N^+=0\right\rangle \end{aligned} \tag{1.19}$$

The ejected electron can gain energy from the excited Rydberg state (AB^*) by conversion of core rotational energy, vibrational energy, spin-orbit energy or electronic energy of the core. The channel interactions for autoionization are shown in Fig. 1.4. Rotational autoionization is more likely in higher-n states as the energy required to ionize the electron is comparable to the energy spacing of the rotational levels of the lowest

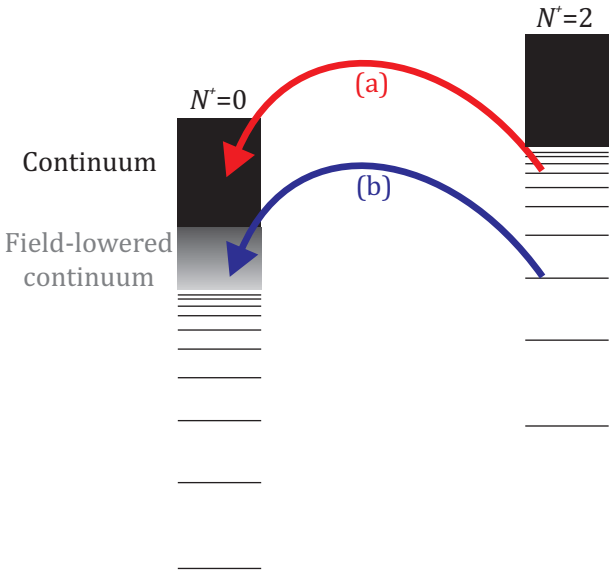

Figure 1.4: Illustration showing two non-radiative decay mechanisms facilitated by rotational channel interactions: autoionization from a bound state into continuum states (red arrow) and Field-lowered continuum states (blue arrow).

ionization threshold. On the other hand, vibrational or electronic autoionization is more favourable for the lower-n states.

Penetrating low-l states are expected to undergo autoionization most readily although high-l states may also autoionize but with a lower decay rate. Similarly the lifetimes are expected to scale as n^3 as the time the electron spends in the core region is inversely proportional to the orbital period.

A Rydberg state can also be coupled with a field-lowered threshold in the presence of an external applied field and it is called field-lowered autoionization, as shown in Fig. 1.4. In the presence of an electric field it is feasible for this field-lowered continuum to become part of a real continuum at which point the coupled Rydberg state may undergo autoionization.

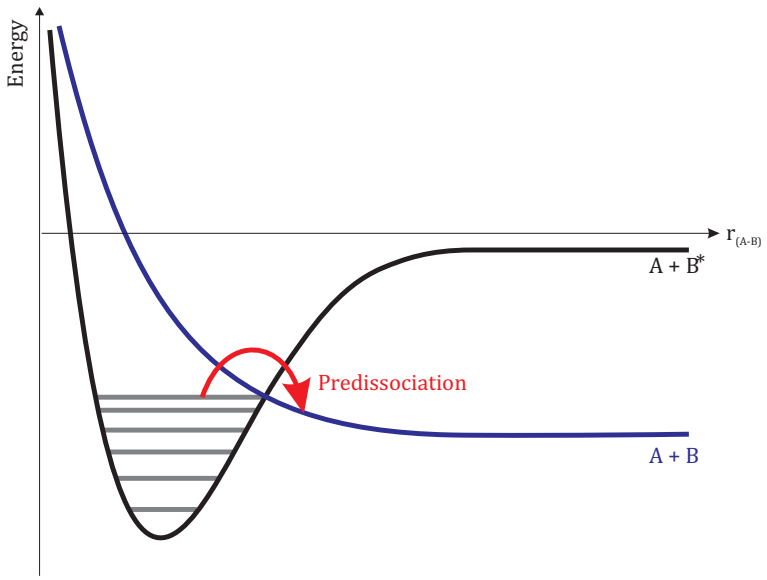

Figure 1.5: Schematic diagram illustrates the predissociation process.

Predissociation

In molecules, the channel interactions are also possible where there is some transfer of energy from the Rydberg electron to the core vibration. This intra molecular redistribution process may result in predissociation of the neutral molecule into an electronically excited or ground state neutral fragments. The dissociation energy may be divided into electronic and kinetic energy of the fragments

$$AB^*_{(E^*)} \longrightarrow A_{(E^\diamond)} + B_{(E^*-E^\diamond)}. \tag{1.20}$$

This occurs when the Rydberg potential energy curve is crossed by a dissociative, often doubly excited, valence state as in Fig. 1.5.

Such autoionization and predissociation processes can result in significant reduction of the lifetimes of excited Rydberg states with associated broadening of the energy levels. The most important mechanism in the experimental work presented later in chapter 3 and 4 is autoionization although predissociation is important in terms of molecular

lifetimes. However, for the experimental work with atomic hydrogen Rydberg states, BBR decay is an important process. These alternative pathways arise due to the ability of individual Rydberg channels to interact.

1.4 Rydberg states in an external electric field

In the presence of an applied electric field, the Rydberg states are strongly perturbed and their energy levels are split and shifted. It is therefore, appropriate to examine the interaction of Rydberg states in the presence of an applied electric field in some detail.

1.4.1 Hydrogenic system

In the field-free situation, the time-independent Schrödinger equation in three dimensions is given in atomic units by [45]:

$$\left(-\frac{1}{2}\nabla^2 - \frac{1}{r}\right)\psi_{(r)} = E\psi_{(r)} \tag{1.21}$$

where the wave functions, ψ, have corresponding energies, E, and the $1/r$ term arises from the pure Columbic potential of the ionic core. The solutions of this equation are specified using the quantum number n, l, and m_l. The l quantum number describes the sub-shell and l can have values from 0 to n-1. The m_l quantum number describes the specific orbital within that sub-shell and it takes the values from -l to +l.

In the presence of a homogeneous electric field, F, the electronic degeneracy of each l in a Rydberg state is lifted, the splitting scaling as n^2 (this effect is known as the Stark effect), and the symmetry of the system reduces from spherical to cylindrical around the applied field axis (z). As a consequence of the symmetry reduction, the

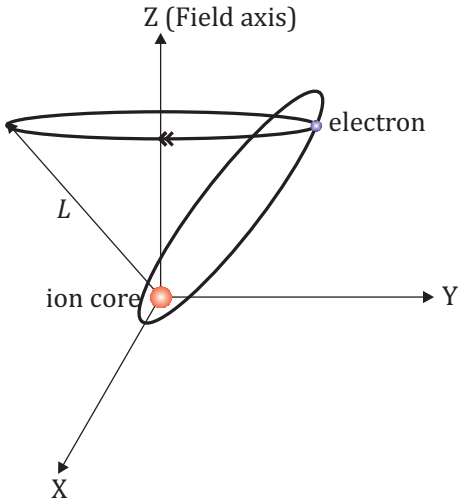

Figure 1.6: Classical representation of the Rydberg electron orbital in the presence of an external electric field.

angular momentum, L, is the no longer conserved and it processes around the field vector in an elliptic orbit, as illustrated in Fig. 1.6.

The potential experienced by the Rydberg electron is given by the sum of the Coulomb and applied field terms in the presence of the electric field along the z direction,

$$V_{(r)} = -\frac{1}{r} + Fz \tag{1.22}$$

and the resulting Schrödinger equation is given by:

$$\left(-\frac{1}{2}\nabla^2 - \frac{1}{r} + Fz\right)\psi_{(r)} = E\psi_{(r)}. \tag{1.23}$$

In the case of the hydrogenic system, the following parabolic coordinates help to solve

the Schrödinger equation;

$$\begin{aligned} \xi &= r + z \\ \phi &= \tan^{-1}\left(\frac{y}{x}\right) \\ \eta &= r - z. \end{aligned} \tag{1.24}$$

Using the above coordinate system in the Schrödinger equation for the H atom, the wave functions can be written as a product of regular and irregular Stark functions [11]

$$\psi_{(\xi,\eta,\phi)} = \frac{1}{\sqrt{2\pi\xi\eta}} f_{n_1,m_l}(\xi) g_{n_2,m_l}(\eta) \exp\left(-i m_l \phi\right) \tag{1.25}$$

where f_{n,m_l} and g_{n,m_l} are the regular and irregular Stark functions respectively. The two new parabolic quantum numbers n_1 and n_2 are introduced here and they represent the number of nodes in the separate parts of the wave functions

$$n = n_1 + n_2 + |m_l| + 1. \tag{1.26}$$

A new effective parabolic quantum number (k) can be defined as

$$k = n_1 - n_2. \tag{1.27}$$

For a given n and m_l the following values of k are possible

$$k = -\left(n - |m_l| - 1\right), -\left(n - |m_l| - 3\right), ..., \left(n - |m_l| - 1\right). \tag{1.28}$$

In this parabolic basis, $|n, n_1, n_2, m_l\rangle$, the Hamiltonian matrix is diagonal in the applied field, and using first order perturbation theory the energy levels are given in atomic

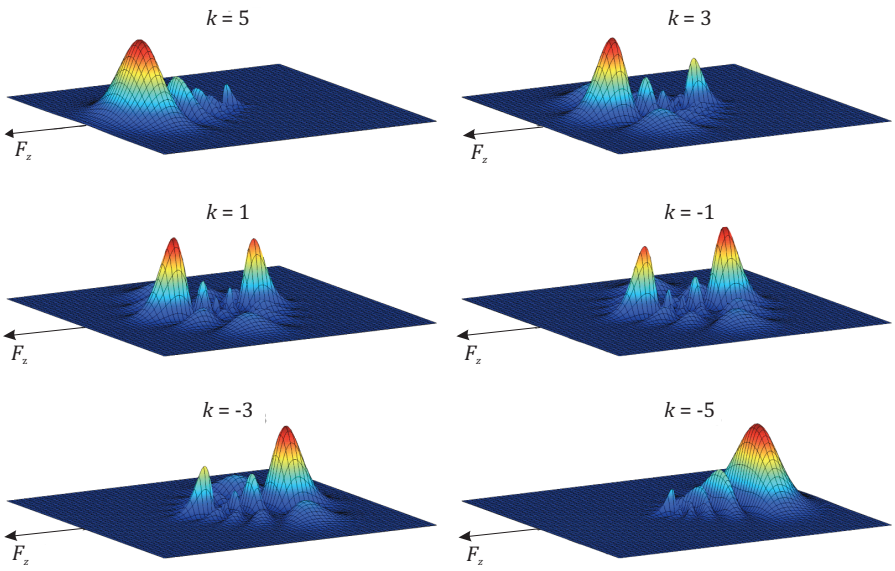

Figure 1.7: The electron probability distribution for the $n = 6$, $m_l = 0$ parabolic states of the hydrogen atom, adapted from reference [46].

units by [18]

$$E_{n,n_1,n_2,m_l} = -\frac{1}{2n^2} + \frac{3}{2}Fkn. \tag{1.29}$$

The different k states possess varying permanent dipole moments, indicating the different distribution of electron density along the direction of the electric field, given by [11]:

$$|\psi_{n,k,m_l}|^2 = r^{2n-2}\left(1-\cos\theta\right)^{2n_1+|m_l|}\left(-\cos\theta\right)^{2n_2+|m_l|}\exp\left[2r/n\right]. \tag{1.30}$$

This equation shows that the more extreme positive and negative k states are highly localized in the +z and -z directions respectively while the intermediate k states are localized more closely to the $z = 0$ plane. This dramatic variation in the distribution of electron density is highlighted in Fig. 1.7.

For the hydrogen atom, Eq. 1.23 can be solved by numerical integration but a more collective approximation is to treat the external field as a high order perturbation of the zero-field Hamiltonian. This kind of approximation has been used by Damburg

and Kolosov [47] to obtain the field dependence of the energy of a specific Stark state $|n, k, m_l\rangle$,

$$\begin{aligned} E_{nm_lk}(F) &= -\frac{1}{2n^2} + \frac{3}{2}nkF - \frac{n^4}{16}[17n^2 - 3k^2 - 9m_l^2 + 19]F^2 \\ &+ \frac{3}{32}n^7k[23n^2 - k^2 + 11m_l^2 + 39]F^3 \\ &- \frac{n^{10}}{1024}[5487n^4 + 35182n^2 - 1134m_l^2k^2 + 1806n^2k^2 \\ &-3402n^2m_l^2 - 3093k^4 - 549m_l^4 + 5754k^2 - 8622m_l^2 + 16211]F^4 \\ &+ \frac{3}{1024}n^3k[10563n^4 + 90708n^2 + 220m_l^2k^2 + 98n^2k^2 + 772n^2m_l^2 \\ &-21k^4 + 725m_l^4 + 780k^2 - 830m_l^2 + 59293]F^5 + O(F^6). \end{aligned} \tag{1.31}$$

The above Eq. 1.31 clearly expresses that the energy of Stark states with different values of k will exhibit different dependencies upon the external field strength and thus will have different ionization characteristics when interacting with a high field or a surface. The energy states of neighbouring manifolds are in close proximity to one another as illustrated in Fig. 1.8, and the energy of each member of the manifold is calculated using the above Eq. 1.31.

At sufficient high field strength, the extreme blue-shifted Stark state (positive-k) of a n manifold will cross the extreme red-shifted Stark states (negative-k) of the adjacent Rydberg (n+1) manifold. The field at which the n manifold crosses the adjacent high-n manifold is known as the Inglis-Teller limit. The zero-field energy levels scale as n^{-3} for $m_l = 0$ states and the Inglis-Teller field is given by approximately

$$\begin{aligned} F_{IT} &= \frac{1}{3n^5} \text{ a.u.} \\ &= 1.798 \times 10^9 n^{-5} \text{ Vcm}^{-1}. \end{aligned} \tag{1.32}$$

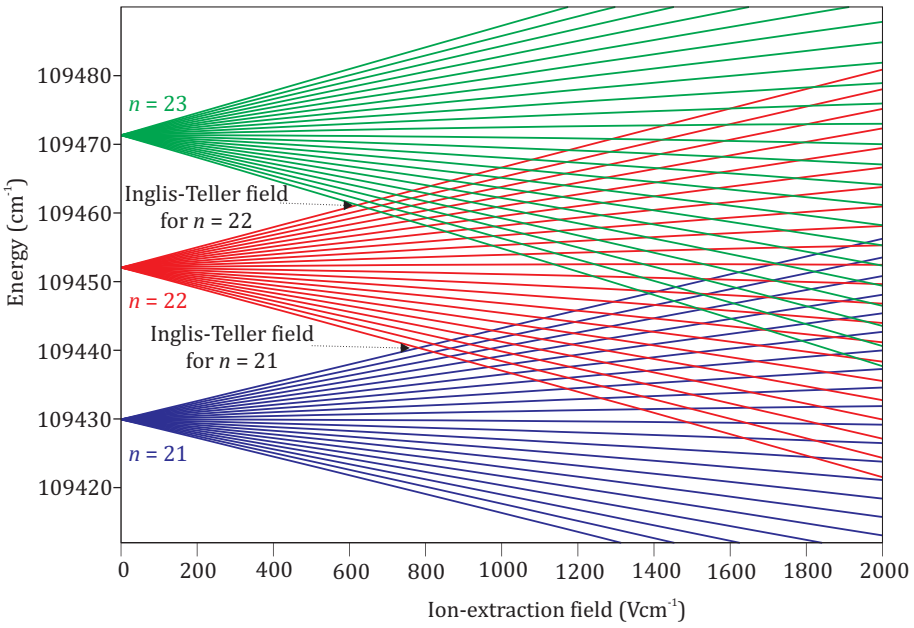

Figure 1.8: Stark map for $n = 21 - 23$ hydrogen Rydberg states ($|m_l| = 0$) energy level in the presence of an applied electric field. Inglis-Teller limits for the initially populated $n = 21$ and $n = 22$ Rydberg states also clearly marked.

Furthermore, Stark levels of the hydrogen atom corresponding to different n, but the same value of m_l, undergo direct crossing without interacting (at the Inglis-Teller limit as noted above).

1.4.2 Non-hydrogenic system

The Rydberg states of non-hydrogenic systems behave differently in the presence of an electric field from the situation previously discussed for the H atom. In non-hydrogenic systems, the core-electron interaction is not purely Coulombic in the short range region due to the finite size screening by other electrons of ionic core, and therefore the states exhibit a non-zero quantum defect. The Stark map of a non-hydrogenic Rydberg state in an external electric field is illustrated in Fig. 1.9 and the overall features observed are similar to the hydrogenic system (see section 1.4.1).

There are a number of important differences observed between the Stark effect in non-

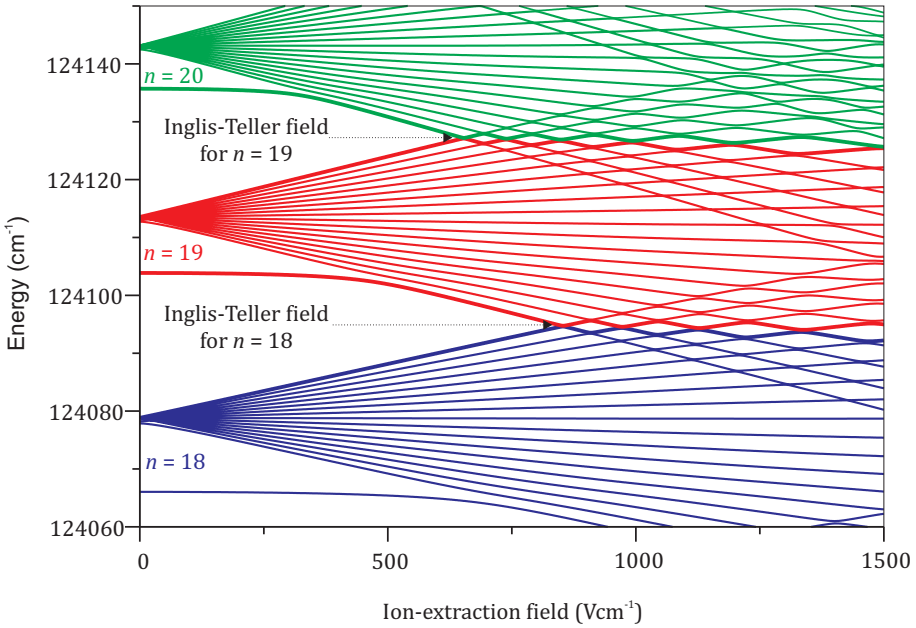

Figure 1.9: Adiabatic field ionization for $n = 18 - 20$, $N^+ = 2$ H_2 molecular Rydberg states energy levels ($M_J = 0$) in an electric field. The bold line represents the adiabatic path following by the avoided energy level crossing.

hydrogenic systems and the hydrogenic system due to the non-zero quantum defect of the low-l Rydberg states as summarized below. The low-l Rydberg states are no longer degenerate with the high-l Rydberg states at zero-field, are weakly mixed with the high-l Rydberg states in the presence of low electric field, and the low-l Rydberg states are gradually mixed into the hydrogenic manifold as the strength of applied field increases. The high-l Rydberg states, however, are non-penetrating to the ionic core and continue to follow hydrogenic behaviour even at low field strengths. The other behavioural differences exhibited by non-hydrogenic systems arise because of the additional symmetry provided by the z component of the Runge-Lenz vector (constant of the motion which allows construction of ladder operator solutions for the H atom's electron Eigenfunctions and energy Eigenvalues) in the hydrogenic system. This is again due to the deviation of the core-electron potential from a pure Coulombic form. As a result, states with the same m_l quantum number interact and all crossings where

$m_l = m_l^{'}$ are now avoided. In the case of low-m_l states, these avoided crossings are quite distinct where as at high-m_l they are too small to be observed. This is a consequence of the fact that as the low-l character of the Stark mixed states decreases (at higher-m_l) the potential becomes more Coulombic in character. These avoided crossings also influence the field ionization behaviour of non-hydrogenic Rydberg states. As the field is increased it is feasible that the Stark states will undergo many crossings on the way to ionization.

In the adiabatic field ionization limit, where every crossing is avoided, the population of an initial state will be ionized when it intersects a red-shifted state of a higher-n manifold above the saddle point, *i.e.* the lowering of the ionization limit is -6.1$\sqrt{F(\text{ Vcm}^{-1})}$ cm^{-1}. The magnitude of the energy splitting at the avoided crossing depends on principal quantum number (n) and the quantum defect (δ). The probability of that the energy level crossing between two n, k states will be traversed diabatically was calculated by Rubbmark et al. [48]; the approximate analytical expression of this probability is given by [49],

$$P_{diab} \cong \exp\left[\frac{-10^{27}\left(|\delta| - \delta^2\right)^2 n^{-10}}{dF/dt}\right]. \tag{1.33}$$

From Eq. 1.33, is clearly expressed that the probability for a crossing to be traversed adiabatically increases with slowly rising fields, low values for n and larger quantum defects. However, even for very high-n Rydberg states, where P_{diab} may be close to unity under typical experimental conditions, the cumulative effect of many thousands of crossings may still lead to significant adiabatic behaviour.

1.4.3 Field ionization

When the external field is applied along the z axis, for a state with zero angular momentum, the resultant potential experienced by the electron along the z axis (Eq.

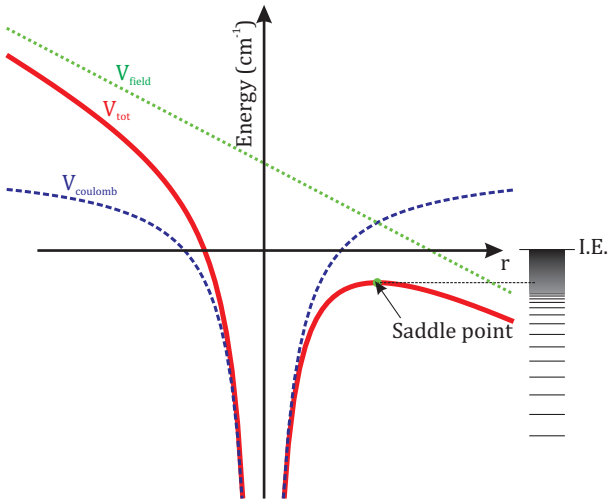

Figure 1.10: Schematic representation of the Coulombic and Stark potential, where the electric field is defined along the z axis.

1.22 and the separation of that equation into its two terms) which is illustrated in Fig. 1.10.

The saddle point lies -6.1$\sqrt{F(\text{ Vcm}^{-1})}$ cm^{-1} below the field-free ionization limit (shown in Fig. 1.10), and classically all states lying above this saddle point limit are expected to ionize with 100% efficiency. The electron remains bound for Rydberg states which appear below the saddle point energy. The blue-shifted Stark states reach the energy of the classical ionization threshold at relatively low field ($F \sim \frac{11-4\sqrt{7}}{9n^4}$, is calculated by using Eq. 1.31) but red-shifted Stark states will require a greater field ($F \sim \frac{1}{9n^4}$) to reach the classical threshold. Quantum mechanically, no states are strictly speaking bound, since there is always a non-zero probability that tunnelling through the barrier can lead to ionization. A useful formula for calculating the field ionization rate (Γ) of Hydrogenic Rydberg states was derived by Damburg and Kolosov

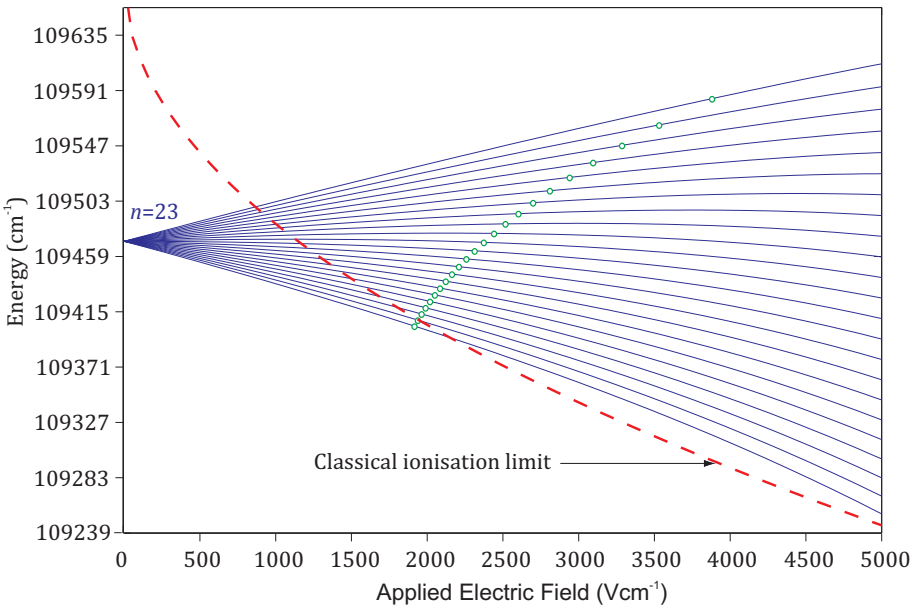

Figure 1.11: The hydrogenic Stark map of the $n = 23$, $m_l = 0$ Rydberg manifold. The classical field ionization limit is shown as the - - - line, and the open green circle represents the critical field for hydrogenic field ionization at a rate of 10^5 s^{-1}, which is calculated using Eq. 1.34.

using numerical solutions of the Stark Hamiltonian [47]:

$$\Gamma = \frac{(4R)^{2n_2+m_l+1}}{n^3 n_2!(n_2+m_l)!}\exp[-\frac{2}{3}R - \frac{1}{4}n^3F(34n_2^2+34n_2m_l +46n_2+7m_l^2+23m_l+\frac{53}{3})] \quad (1.34)$$

where $R = \frac{(-2E_{nm_lk})^{3/2}}{F}$, and E_{nm_lk} is the sixth order perturbative Stark energy and it can be calculated by using the formula given in Eq. 1.31. The rates of ionization for different states in an electric field as predicted by Eq. 1.34 can vary by ten orders of magnitude, or more, across a single manifold. The open circles in Fig. 1.11 indicate the value of the field strength at which different k states attain the value of 10^5 s^{-1} corresponding to a lifetime of ~ 10 μs, which is the classic timescale for a Rydberg surface experiment.

The wave functions of red-shifted states are located primarily in the region of the

saddle point, whereas the wave functions for blue-shifted states have their maxima located on the opposite side of the core from the saddle point. Consequently, although lying higher in energy, the blue-shifted states are kinetically more stable than the red-shifted states. In contrast, the red-shifted states are localized towards the saddle point and ionization is able to occur very much more rapidly.

1.4.4 Lifetime in an electric field

The lifetime of high-n, low-l Rydberg states is given to scale as n^3 but in the case of high-l states, the radiative lifetime will increase dramatically as n^{4-5} [49]. This lifetime variation between low-l and high-l Rydberg states can be explained by the strong mixing of l and m_l states by the Stark effect, the mixing of the near-degenerate l and m_l states in the presence of an inhomogeneous electric field. An inhomogeneous field can be generated from the dopant charges at the surface [50], and collisional interactions between the Rydberg states and the surface [51]. One of the particularly interesting aspects of the m_l mixing is the population of high-m_l Rydberg states which are kinetically stable during the lifetime of experiments.

1.5 Charge transfer processes at metal and semiconductor surfaces

The ionization of a Rydberg state takes place when the energy of the Rydberg electron exceeds the saddle point of the potential barrier between the Rydberg ionic core and the target surface. After the ionization of the Rydberg molecule near the surface, the resultant ion core is accelerated towards the surface due to its image-charge interaction [52] and unless the ion is drawn out before striking the surface, it will be neutralized at the surface (via Auger neutralization [53]). To avert the Auger neutralization of the

ions at the surface, a sufficiently strong electric field must be applied to the surface. The minimum extraction field ($F_{\min}$) required to pull the ion away from the surface should be large enough to overcome the combined effects of the initial momenta of the ions and the attractive image-charge force of them. In the case of semiconductor surfaces, the bottom of the conduction band lies below the vacuum level and the Rydberg electron tunnels directly into the conduction band [52, 54]. However, the image-charge fields at dielectric surfaces are reduced by the dielectric shielding (β) parameter via the shielding effect of their ionic cloud ($\beta = 1$, for the metal surface) [54–56]. The β parameter can be calculated by this equation:

$$\beta = \frac{\epsilon_{(\rho)} - 1}{\epsilon_{(\rho)} + 1} \tag{1.35}$$

where $\epsilon_{(\rho)}$ is the static dielectric constant.

It has been shown that charge exchange between the Rydberg electron and a metal surface is rapid and that a sizable fraction of the incident atoms can be detected as ions. Using the Jellium image-charge model, the total energy (U) of the ion at a perpendicular distance (D) from the surface in the presence of an applied electric field (F) is given by

$$U_{\perp} = \frac{-\beta}{4D_i} - FD_i + T_{\perp} \tag{1.36}$$

where the first term in the above equation describes the interaction between the ion core and its image-charge generated in the metal, the second term describes the potential due to the ion-extraction field, and $T_{\perp} = mv_{\perp}^2/2$ is the kinetic energy of the Rydberg molecule perpendicular to the surface at the point of ionization. Using the expression for the total energy, the perpendicular distance at which ionization occurs (D_{i}) can be found. The minimum ionization distance ($D_{\min}$) for which extraction will

occur can be calculated by rearranging Eq. 1.36 and is given below:

$$D_{\min} = \frac{T_\perp}{4F}\left[1+\sqrt{1+\frac{2\sqrt{F\beta}}{T_\perp}}\right]^2. \tag{1.37}$$

The minimum extraction field $F_{\min}$ required to pull the ions away from the surface for ionization at a given distance $D_{\rm i}$ is given by the following equation [54–56]:

$$F_{\min(\mathrm{D_i},\mathrm{T}_\perp)} = \left[\frac{\sqrt{\beta}}{2D_i}+\sqrt{\frac{T_\perp}{D_i}}\right]^2. \tag{1.38}$$

When the applied electric field is greater than the threshold field ($F_{\min}$), ions are accelerated away from the surface and detected by the MCP detector. $D_{\min}$ and $F_{\min}$ are affected by the ionization rate of the Rydberg molecule as a function of distance from the surface.

1.5.1 Jellium image-charge model

The Rydberg molecule is considered as a two-particle system consisting of an electron and an ion core. When the Rydberg molecules are relatively far from the surface, the image-charge interaction can strongly influence the motion of the excited electron [14, 56, 57]. The point charge images induced in the surface act in the same way as the other point charges so that the potential may be considered as interactions between the electron and ion point charges and the image point charges in the surface [58]. Let us consider a surface kept in the $z = -D$ plane and an ion core (charge Ze) kept at the origin of our coordinate system. The image ion core (charge -Ze) is located at the same distance on the other side of the surface plane. Similarly, the electron (charge -e) of the Rydberg molecule is situated at a distance r ($r = \sqrt{\rho^2 + d^2}$) from the ion core and the image electron (charge e) is located at the same distance on the other side of

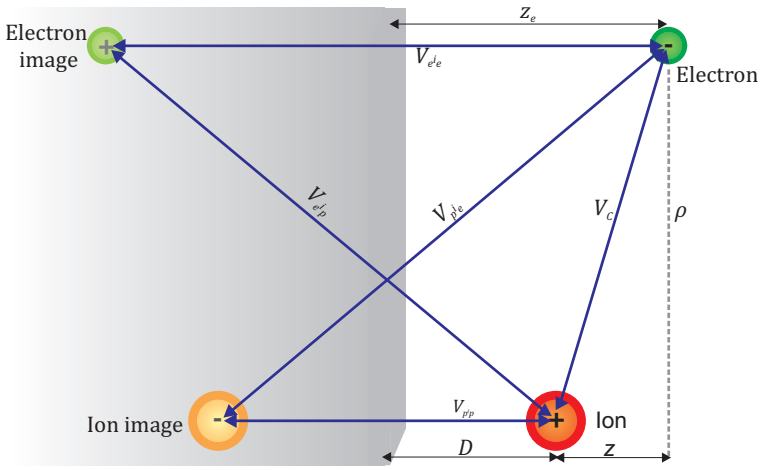

Figure 1.12: The pictorial representation of the classical image-charge interaction between the Rydberg states and its image near the surface and the contributions to the potential.

the surface plane. The geometry and contributions to the potential arising from the presence of the surface are represented in Fig. 1.12 [59].

As the problem has cylindrical symmetry, so we introduce the cylindrical polar co-ordinates which are defined as $x = \rho\cos\phi$, $y = \rho\sin\phi$ and $z = d$. The Coulomb interaction with the core ion (V_c), the interaction of the electron with its image-charge (V_{e^ie}), the interaction of the electron with the image-charge of the core ion (V_{p^ie} / V_{e^ip}) and the interaction of the core ion with its image-charge (V_{p^ip}) are given by the equation written below [60]

$$\begin{aligned} V_c &= \frac{-Ze^2}{r} \\ V_{p^ie} = V_{pe^i} &= \frac{\beta Ze^2}{\sqrt{\rho^2+(2D+z)^2}} \\ V_{e^ie} &= \frac{-\beta e^2}{2(D+z)} \\ V_{p^ip} &= \frac{-\beta Z^2e^2}{2D} \end{aligned} \tag{1.39}$$

where D is the ion core separation, (z, ρ) are the electron co-ordinates in the ion core

frame and $(D + z) = z_e$ is the electron-surface separation.

These interactions distort the Rydberg electronic wave function and lead to strong hybridization. For the hydrogen Rydberg molecule or the hydrogen atom, we set $Z = e = 1$; furthermore at the asymptotic limit, the overall one-electron potential in cylindrical co-ordinates, is given by the following equation

$$\begin{aligned} V_{\text{tot}} &= V_e + V_{e^ie} + V_{pe} + V_{p^ip} \\ V_{\text{tot}} &= -\frac{1}{|z|} - \frac{\beta}{4(D+z)} + \frac{\beta}{2D+z} - \frac{\beta}{4D}. \end{aligned} \tag{1.40}$$

The last three terms in Eq. 1.40 are called the electrical mirror image potential induced by the surface.

1.5.2 Electron-electron image potential

As the Rydberg molecule (or atom) approaches a metal surface, the attractive interaction between the Rydberg electron with its image-charge in the surface will strongly influence the motion of the Rydberg electron. However, the simple form of the potential above tends to -∞ when the electron comes close to the surface whereas, in reality, its energy should converge to the energy of the bulk electronic state of the metal. The electron-electron image potential can be modified as follows [61–63] to allow this smooth convergence:

$$V_{e^ie} = \begin{cases} \frac{-1+\exp[-\alpha((D+z)-z_o)]}{4((D+z)-z_o)} & \text{if } (D+z) > z_o \\ \frac{V_o}{A\exp[B((D+z)-z_o)]+1} & \text{otherwise} \end{cases} \tag{1.41}$$

where $A = -1 - \frac{4V_o}{\alpha}$, and $B = \frac{2V_o}{A}$ are constants, V_o is the bulk metal potential, z_o is the image plane of the metal surface and α is the interpolation parameter. The values of z_o, α and V_o are dependent on the type of surface and for an aluminium surface,

$z_o = 0.7$, $\alpha = 1.25$ and $V_o = -0.574$ [46, 62]. The above modified electron-electron image potential combined with the attractive Coulomb potential of the ion core leads to an overall potential that exhibits a saddle point and a finite-width-barrier on the surface side of the ion core (as shown in Fig. 1.1) [46, 64].

1.6 Previous experimental studies of Rydberg surface interactions

1.6.1 Previous studies involving a metal surface

The interaction of Rydberg atoms and molecules with metallic surfaces, and the associated resonant charge transfer process, has been the subject of many previous experimental and theoretical studies.

In recent years much attention has been focused on the dynamics of Rydberg atoms in external fields. The highly excited Rydberg states near a metal surface is an ideal system to investigate the instantaneous VDW interaction and an important example to reveal quantum chaos. The VDW interaction between a metallic surface and an atom is an important process in atomic physics. Anderson and co-workers have been the first to directly measure the VDW force by using the deflection of alkali Rydberg atoms (Cs and Na) towards a gold coated metallic surface [65]. The atoms were excited to Rydberg states ($n = 12 - 27$) at the entrance to a metalic tunnel and the transmission through the tunnel monitored by further laser excitation and field ionization at the exit. The results confirm that the VDW force is applicable to higher-n Rydberg states due to the large atom-surface separation.

The first experimental investigation of the atom-surface separation at which ionization occurs was obtained using alkali (Na (nd)) Rydberg atoms [66]. The transmission of

the Rydberg atoms through the slits in a metalic mesh was measured as a function of the principal quantum number, n. A linear relationship was found between the classical Rydberg orbital radius (n^2 a.u.) and the position at which the Na Rydberg atom ionizes (at $\sim 4n^2 - 5n^2$ a.u.). Kocher et al. extended these experiments to investigate the effects of adlayers on the surface, which affect the image-charge fields and hence the ionization probability of a Li Rydberg atom at a particular distance from a gold metal mesh surface [67]. The formation of a monolayer or alkali deposition can lead to the production of localized electric fields at the surface leading to the variation in the transmission of the Rydberg atoms through the mesh as function of time. More recently, Xe Rydberg atoms have been employed as these do not stick to or react chemically with a target surface [52, 68, 69], and it was found that the minimum ionization distance varies as $Z_{\rm i} = 4.5 \pm 0.9\ n^2$ a.u. in agreement with the earlier measurements [66].

The interaction of a Rydberg molecule with a metallic surface adds a new degree of complexity to the process of surface ionization. The core has vibrational and rotational degrees of freedom that might affect the ionization process via autoionization or predissociation [14], which may occur before the molecules arrive at the surface, or be induced by the fields at the surface. Lloyd et al. studied the surface ionization of H_2 Rydberg molecules at a metallic surface [70, 71]. McCormack extended this work to look at the gas-phase ionization profiles at the metal surface by using two external pulsed fields, which are created by applying a pulsed voltage to the surface and extraction electrode [72]. In these experiments, the hydrogen Rydberg molecules were excited such that they possessed ion core rotation ($N^+ = 2$), but no core vibration ($v^+ = 0$), where N^+ and v^+ are the rotation and vibration quantum numbers of the ion core respectively. The ionization distance inferred by using the effective principal number, ν_0, with respect to the $N^+ = 0$ limit was found to be in accordance with ear-

lier results with alkali [73] and Xe [52] atoms, $Z_{\rm i} = \sim 3\nu_0^2 - 5\nu_0^2$ a.u. Further studies comparing the surface ionization profiles (the surface ionization signal versus external electric field, see chapter 3 for detailed discussion) of hydrogen Rydberg molecules populated with no core rotation ($N^+ = 0$, $\nu_0 = 23.17 - 46.19$) and those with a core rotation ($N^+ = 2$, $n = 17 - 22$) verify that the rotation-electronic energy transfer process is occurring [71].

The Stark effect, in relation to surface ionization, has been investigated in more detail by populating different hydrogen Rydberg molecule Stark states of a given principal quantum number: the ionization profiles were recorded for states across the full width of the $n = 17$ Stark manifold with electron distributions that range from being initially surface-oriented (red-shifted) to those that are vacuum-oriented (blue-shifted) [72, 74].

1.6.2 Previous studies involving a semiconductor surface

The dielectric Si surface has a narrow electronic band gap where the bottom of the conduction band lies below the vacuum level, and so charge transfer of the Rydberg electron is possible into the conduction band. Experiments with p- and n- type Si surfaces were performed by Dunning et al. [54–56]. Ionization rates and distances for incident Xe Rydberg atoms were found to be similar to that on Au, except at lower external applied fields where a higher surface ionization signal was recorded. This behaviour is attributed by the presence of '*patch*' charges in the surface region, and by modeling a surface that has feature sizes of ~ 2 μm and a simple periodic variation in the potential that varies by $\pm$ 80 mV, the differences in the experimental profiles can be accounted for. This shows that small differences in the potential difference across a Si surface can have a large effect on the ionization of the Rydberg atoms. The range of fields experienced by the atoms is thus broadened and the barrier for ionization lowered; more ions are detected at lower external applied fields.

The previous studies only concerned heavily doped Si surfaces [54–56], but this experimental study is more concerned with a wide range of dopant densities. Therefore, dopant charge or stray field effects on the surface ionization processes affect this experimental investigation most prominently.

Our particular interest is to study the charge transfer processes between highly excited Rydberg states and metal or semiconductor surfaces due to the large spatial extent of highly excited Rydberg states. The present experiments involve the interaction of atomic H and molecular H_2 Rydberg states with Si semiconductors doped by different dopant densities and types. Particularly for the resonant electron transfer, a quantitative description of experimental data has been successfully performed.

1.7 Thesis outline

The work involved in this thesis provides a detailed understanding of charge transfer processes between the H_2 Rydberg molecule and H Rydberg atom with various doped Si surfaces. Furthermore, it involves the development of a simple trajectory simulation to compare with experimental surface ionization profiles.

Chapter 2 outlines the experimental setup for generating hydrogen Rydberg molecules at Si surfaces and characterization of the time-of-flight signal. The results discussed in chapters 3 and 4 are obtained with this experimental setup.

The outcomes of the experimental research into the ionization dynamics of hydrogen molecular Rydberg states at various doped Si surfaces are presented in chapter 3. Furthermore, the effect of dopant density and dopant type are clearly compared via the ion detectability method.

Chapter 4 focuses on the analysis the surface ionization profiles via the ion and electron detection methods in the presence of the Stark polarization. The comparison of these

two different detection schemes following surface ionization of H_2 Rydberg states is also discussed here.

The new experimental setup used to investigate the surface ionization profiles of the incident hydrogen atomic beam on the Si surfaces is clearly explained in chapter 5. The ion detectability method is used to directly compare many surface ionization profiles and the outcome of this study shows the influence of the dopant density and dopant type on the ionization profiles.

In chapter 6, theoretical trajectory simulations based on the simple OTB model have been developed using the new *2D* surface model for various doped Si surfaces taking into account the effects of dopant charges. The output of this trajectory simulation is compared with and helps to explain the experimental surface ionization profiles.

Chapter 7 summarizes the main facts of this work and outlines potential opportunities to promote these studies in the future providing some more characteristic features of the surface structure and the properties of the Rydberg states.

Chapter 2

Experimental details

The H_2 molecule has a non-polar non-magnetic ground state, and unusually large rotational constant (B); as a two-electron system its simple electronic and geometrical framework has led to fundamental interest in both experimental and theoretical studies in chemical physics. For the Rydberg states of H_2, the rotational and vibrational degrees of freedom of the ionic core lead to the overlap of Rydberg series with different ion core states and also with possible dissociating channels, with the result that autoionization and predissociation can occur [14]. For the case of the Rydberg surface interaction, these competing processes may take place before the molecules approach the surface, or may even be induced by the fields at the surface.

Using the pulsed field ionization (PFI) method, Softley and co-workers [29, 70, 71, 75, 76] demonstrated that the state-selective population of para-H_2 Rydberg states with specific rovibrational core excitation could be achieved using a Vacuum Ultra Violet (VUV)-Ultra Violet (UV) two-photon excitation scheme. Recently, Mc Cormack [72] has used this excitation scheme and the PFI method to investigate the effects of level crossings in the ionization of hydrogen Rydberg molecules at metal surfaces. The experimental work presented in the following two chapters utilises the same experimental scheme [72], and focuses on the interaction of para-H_2 Rydberg molecules lying in the

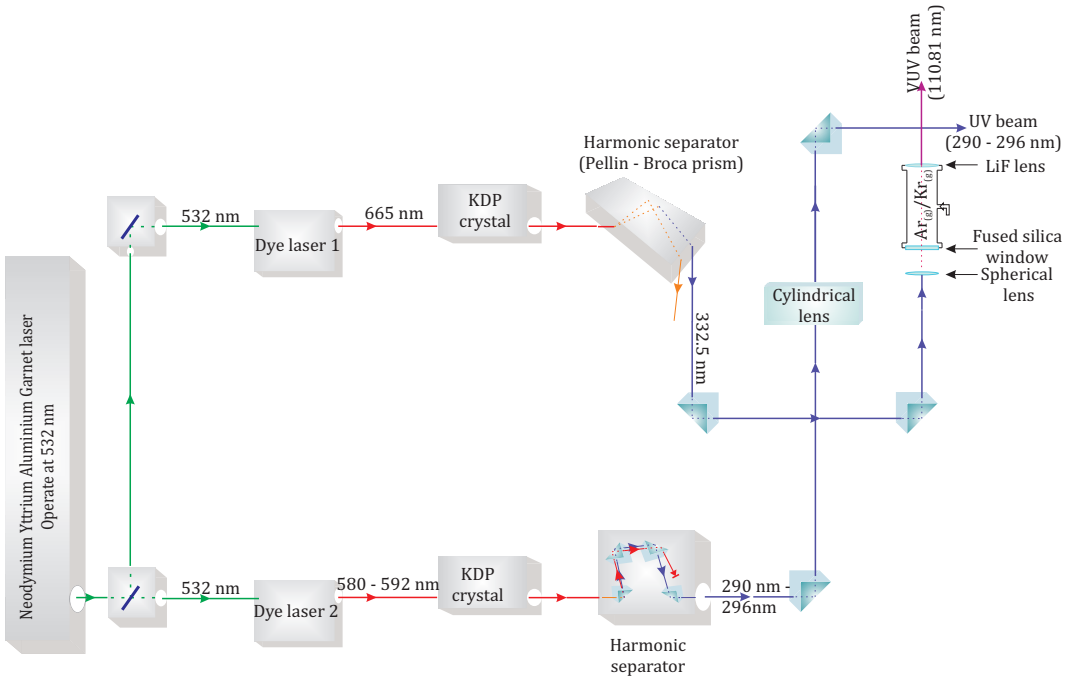

Figure 2.1: Schematic diagram of the Rydberg surface experimental laser setup showing optical conversion.

vicinity of the first ionization threshold limit with doped Si semiconductor surfaces.

2.1 Experimental setup

The experimental apparatus comprises two differentially pumped vacuum chambers, a source chamber, and an experimental chamber.

2.1.1 Laser System

The laser systems consist of a Nd:YAG (Neodymium-doped Yttrium Aluminium Garnet; $NdY_3Al_5O_2$) laser (Spectra Physics GCR 290) and two different dye lasers. The hydrogen molecules are excited into the Rydberg states via a VUV-UV doubly resonant excitation process. The main optical conversion scheme of the laser setup is illustrated schematically in Fig. 2.1.

The first step in the excitation scheme involves a single photon ($R(0)$ $B^1\Sigma_u^+(\nu' = 0) \longleftarrow X^1\Sigma_g^+(\nu'' = 0)$) transition from the ground state to the intermediate state. This transition requires laser radiation in the VUV region at $\sim$ 110.81 nm. It was generated by non-resonant frequency tripling of strongly focused UV laser radiation in a mixture of krypton and argon gases (BOC special gases 99.9% - see below for detailed discussion). The required UV laser radiation was obtained by frequency doubling the output of a pulsed dye laser ((Spectra Physics, PDL3), hereafter called laser 1) in a crystal of KDP (Potassium Dihydrogen Phosphate). An auto-tracker (INRAD II) was used to maintain the crystal at the optimum crystal angle for frequency doubling. The output of the dye laser 1 was maintained at 664.86 nm. Dye laser 1 was operated using a mixture of DCM and LDS 698 laser dyes in the ratio 10 : 2 (84% by mass of DCM and 16% by mass of LDS 698) in the oscillator and preamplifier cells, and pure DCM in the amplifier (20 mg/l); the concentration was selected by optimising the power output of the UV beam. The dye laser was pumped using $\sim$ 350 mJ/pulse of the second harmonic from a Nd:YAG laser operating at a repetition rate of 10 Hz. Under optimal working conditions, there was $4 - 7$ mJ of UV radiation ($\lambda = 332.42$ nm) available per pulse.

The wavelength of the laser beam was calibrated to a precision of 0.001 nm using a Burleigh wavemeter (WP 4500). Conversion of the wavelengths from their values in air to vacuum is required, because while the wavelengths required to excite the molecular energy levels are presented in the literature in vacuum conditions [77], the Burleigh wavemeter measurement was given in atmospheric conditions. The wavelength conversion from vacuum to air is given by the following equation,

$$\lambda_{(air)} = \frac{\lambda_{(vac)}}{1 + 2.73518e^{-4} + 131.4182/\lambda^2_{(vac)} + 2.76249e^8/\lambda^4_{(vac)}} \tag{2.1}$$

where $\lambda_{(vac)}$, $\lambda_{(air)}$ are the vacuum and air wavelength, respectively, in units of angstroms.

Finally, a Pellin-Broca prism was used to isolate the residual light from the fundamental frequency of laser 1.

Frequency tripling was achieved via a nonlinear process in which the UV laser beam was focused, using a 191 mm spherical focal lens, into a 200 mm long stainless steel tube ('*tripling cell*') and this tripling cell contained a mixture of the Kr/Ar gas mixture (see Fig. 2.2). The intensity of the frequency tripling in a rare gas medium depends upon the third-order nonlinear susceptibility, $\chi^{(3)}$, and the intensity of the generated third harmonic wave is described by [78],

$$I_{3\nu} = N^2 \left|\chi^{(3)}(3\nu)\right|^2 I_\nu^3 F(b\Delta k) \tag{2.2}$$

where I_ν is the intensity of the input laser beam, ν is the frequency of the input laser beam, and N is the number density of the nonlinear medium. The phase matching function $F(b\Delta k)$, where b is the path length and Δk the wave vector mismatch, depends on the macroscopic properties of the medium and the focusing of the fundamental, and represents the phase matching between the input light and the generated VUV. Phase matching means the constructive interference of the contributions generated in different volume elements of the medium to the output wave. This is described by a generally complicated function, which can be written for the limiting case of a plane wave in a weak focusing limit regime and neglecting absorption as [79]

$$F(b\Delta k) = F(L\Delta k) \cong \left(\frac{\sin(L\Delta k/2)}{L\Delta k/2}\right)^2 \tag{2.3}$$

which is similar to the second order processes in nonlinear crystals [80]. The optimum power conversion efficiency in a phase matched system is given typically for $b \cong L$ [79]. Furthermore, Δk is required to be negative (where $\Delta k = k_{3\nu} - 3k_\nu$) [78, 81], such that

the refractive index n at 3ν is less than the refractive index at ν:

$$k_\nu = \frac{\nu n_\nu}{c}, \tag{2.4}$$

$$\Delta k = \frac{3\nu}{c}(n_{3\nu} - n_\nu) < 0. \tag{2.5}$$

Since the refractive index normally increases with frequency, this behaviour ($n_{3\nu} < n_\nu$) is called negative dispersion. Argon is negatively dispersive medium in this region [82] and the VUV output can be increased by phase matching with a gas such as krypton [82, 83], which is positively dispersive at 110.81 nm, and is consistent with known refractive indices [84, 85]. Procter [86] has studied the efficiency of the VUV generation via frequency tripling as a function of wavelength (in the 110.0 nm to 111.5 nm range) for the various gas mixture ratios by directly measuring the VUV intensity using ionization of acetone seeded in an atomic beam of helium gas. It was found that a mixture consisting of argon and krypton in the ratio 200 : 1080 mbar resulted in the maximum intensity at 110.81 nm.

In the experimental setup, the VUV radiation at 110.81 nm was focused by the LiF lens (70 mm focal length at 110 nm) and directed into the vacuum chamber, where it intersected the molecular beam. The polarisation of the VUV beam was aligned horizontally. It is not be possible to separate the VUV output of the rare gas mixing cell from the residual UV in this experimental setup (in principle it could be separated by adding an extra dispersive prism or a diffraction grating, but this adds an unnecessary layer of complexity), and this is one of the disadvantages of the VUV generation step. However, since the focal length of the LiF lens varies significantly as a function of wavelength, it was possible to choose the position of the UV focus within the gas cell so that the resulting VUV was focused into the vacuum chamber but the remaining UV radiation was not. This situation, which reduces the probability of any unwanted

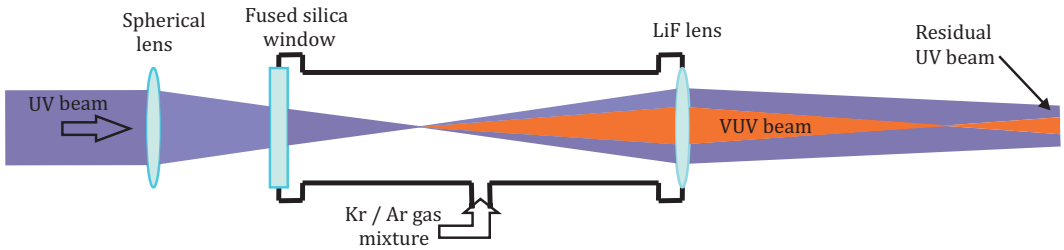

Figure 2.2: Rare gas mixing cell used for the tripling frequency of the UV beam.

UV multi-photon processes occurring, is shown schematically in Fig. 2.2.

In addition, the summation of the UV one-photon energy and VUV photon energy lies well below the adiabatic ionization threshold of H_2 and cannot directly bring about any background ionization. However, there is a risk of the residual UV striking electrodes; these cause electron photoemission and create some unwanted signals. The absolute power of the VUV light was not measured, but, based on similar work [87], it is likely that the available power was in excess of 10^9 photons/pulse.

The second excitation step was performed through the one-photon transition from the intermediate state to the Rydberg state. It was achieved by using a UV laser beam in the wavelength range of $291 - 296$ nm. This UV wavelength was provided by the frequency doubled output of another dye laser (Quanta Ray PDL 3), which was pumped using the output of the same Nd:YAG laser (Spectra Physics CR290), providing nearly 350 mJ/pulse at 532 nm. This dye laser (laser 2) was operated using 175 mg/l of Rhodamine 610 in an oscillator with preamplifier cells, and the same dye at a concentration of 24 mg/l in the amplifier cell. The fundamental radiation was measured by the Burleigh wavemeter (WP 4500), and the frequency doubling was carried out by a KDP crystal. When scanning the laser wavelength, the optimum angle for the doubling crystal was maintained by an auto-tracker (INRAD) and any residual fundamental light was separated by using a four-prism harmonic separator (INRAD). The resultant UV radiation ($3 - 4$ mJ/pulse) was focused by a cylindrical

lens (f = 285 nm) into the main chamber with its polarisation vertically aligned; it crossed the VUV beam at an angle of 90° and intersected the hydrogen molecular beam at an angle of 135°. The polarisation of the UV beam could be set either parallel or perpendicular to the molecular beam axis by the addition or removal of an extra prism from the beam line. By adjusting the individual path lengths of the laser beam, it was possible to achieve temporal synchronisation between the VUV and UV pulses, which was essential for the efficient population of the Rydberg states due to the short lifetime of the $B^1\Sigma_u^+$ ($\sim$ 0.5 ns) intermediate [88].

2.1.2 Hydrogen molecular beam

Hydrogen gas (BOC 99.99%) at a backing pressure of 2 bar was introduced into the source chamber through a pulsed-solenoid valve (General Valve, Series 9, Orifice diameter 0.5 mm) to create a pulsed supersonic expansion of $\sim$ 200 μs duration. The nozzle was operated synchronously with the excitation lasers at a repetition rate of 10 Hz. The pulsed valve was triggered so that it opened $\sim$ 210 μs before the lasers were fired, ensuring that the excitation happened at the front of the gas pulse. The vacuum in the source chamber was kept at a background pressure of $\sim 2\times10^{-8}$ mbar, which increased to $\sim 2\times10^{-6}$ mbar during the operation of the pulsed valve. The base pressure in the main chamber was maintained at $\sim 6\times10^{-9}$ mbar, and the pressure during operation was $\sim 9\times10^{-7}$ mbar. These pressures were maintained using two turbo molecular pumps (Leybold 620 $l\mathrm{s}^{-1}$) backed by rotary pumps (Edwards EM series 1100 $l\mathrm{s}^{-1}$).

The central part of the molecular beam was then passed into the main chamber through a skimmer (Beam Dynamics Inc.) of 1 mm diameter located 3 cm from the opening of the pulsed valve. The pulsed valve and the skimmer were mounted such that the resulting collimated beam was incident on the horizontally mounted surface at an

angle of 7°. After passing through the skimmer, the hydrogen molecular beam was intersected at right angles by the two laser beams in the centre of the main chamber, 170 mm from the skimmer face (as seen in Fig. 2.1).

2.1.3 Diatomic molecular Rydberg states

Before considering the details of the excitation scheme it is useful to understand the angular momentum coupling for a diatomic molecule. For diatomic molecular Rydberg states, the angular momentum can be described by using either Hund's case (b) or Hund's case (d). The vector coupling schemes for the two Hund's cases are illustrated in Fig. 2.3. The orbital angular momentum of the electron, L, the spin angular momentum of the electron, S, the nuclear rotational angular momentum, N^+ for the ion core in Hund's case (d) or R for the whole molecule in Hund's case (b), and the nuclear spin, I, are the four contributions towards the total angular momentum of the diatomic molecules, I will be ignored in this discussion. The choice of the two Hund's cases (b or d) to provide the best description for a particular system depends upon the strength of the coupling between the orbital angular momentum of the excited electron and the internuclear axis. For the low-n case, the Rydberg electron spends more time in the ionic core region and the electronic angular momentum is strongly coupled to the internuclear axis and, therefore, Hund's case (b) is most appropriate. In contrast, in the high-n case, the strength of the electron-ion core coupling is considerably weaker, due to the large distance between the Rydberg electron and the ionic core, and the relatively short time that the Rydberg electron spends near the ionic core: the electronic angular momentum is therefore decoupled from the symmetry axis and is most appropriately described by Hund's case (d).

For Hund's case (b), the projection, Λ, (L processes very rapidly about the internuclear axis with a well characterised component Λ) is coupled to nuclear rotation R to form

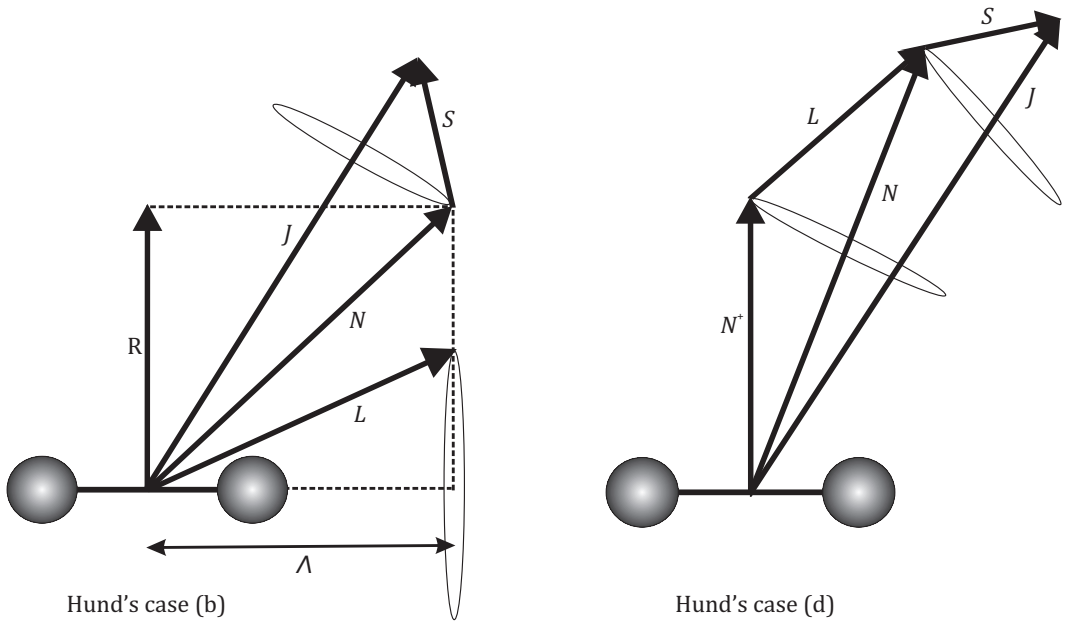

Figure 2.3: Vector coupling diagram for Hund's case (b) and Hund's case (d).

N; and N couples with S to form the total angular momentum, J. The molecular states are labelled as ${}^{(2S+1)}\Lambda^{+/-}_{g/u}$, where Λ is labelled Σ, Π and Δ for the values of 0, 1 or 2 respectively. The superscript of +/- specifies the symmetry of the electronic wave function on reflection through a plane containing the nuclei. The subscripts g/u indicate the overall parity of the state (gerade or ungerade) with respect to inversion of the electronic coordinates.

For Hund's case (d), the coupling between L and the nuclear rotation of the ion core N^+ is much stronger than that between L and the internuclear axis. The coupling between L and N^+ results in N, which can be further coupled with S (in the appropriate open shell system), resulting in the total angular momentum, J.

Assuming S is equal to zero for para-H_2 molecules, since these two electrons spin in opposite directions (singlet state), the value of total angular momentum ($J \equiv N$) is given by [89]

$$J = \left|L + N^+\right|, \left|L + N^+ - 1\right|, ..., \left|L - N^+\right|. \tag{2.6}$$

It follows that there are $(2L+1)$ or $(2N^{+}+1)$ states, depending on whether $N^{+} > L$ or $N^{+} < L$, respectively. The rotational energy in Hund's case (d) is given by

$$E_{rot} = BN^{+}(N^{+}+1) \tag{2.7}$$

where B is the rotational constant, and each level is then further split into $(2L+1)$ or $(2N^{+}+1)$ components. The transition from Hund's coupling case (b) to case (d) has been shown to occur for np states of H_2 molecule at approximately $n = 9$ [6], while for the high-l states $l \geq 3$, case (d) is already well characterised with $n \geq 4$ [90]. For the work presented below, Rydberg states with $n = 17-21$ are considered. Therefore, Hund's coupling case (d) is the most appropriate description for the $n = 17-21$ H_2 molecular Rydberg states, but the intermediate $B^{1}\Sigma_{u}^{+}$ state behaves as Hund's case (b).

2.1.4 The excitation scheme

The experimental work presented in this thesis focuses on molecular hydrogen Rydberg states with no core vibrational motion ($\nu^{+} = 0$). The two-colour photon excitation scheme is shown in Fig. 2.4.

B - state excitation

The VUV frequency radiation (laser 1) is resonant with the $R(0)$ $B^{1}\Sigma_{u}^{+}(\nu^{'} = 0) \longleftarrow X^{1}\Sigma_{g}^{+}(\nu^{''} = 0)$ transition, leading to population of the $J^{'} = 1$ level of the $^{1}\Sigma_{u}^{+}(\nu^{'} = 0))$ intermediate state, which generates a one-photon transition of para-hydrogen (the nuclear spin of the two hydrogen atoms are anti-parallel) at an excitation energy of 90242.33 cm^{-1} [77]. The VUV spectroscopy of these transitions has been studied in detail by Rottke and co-workers [87].

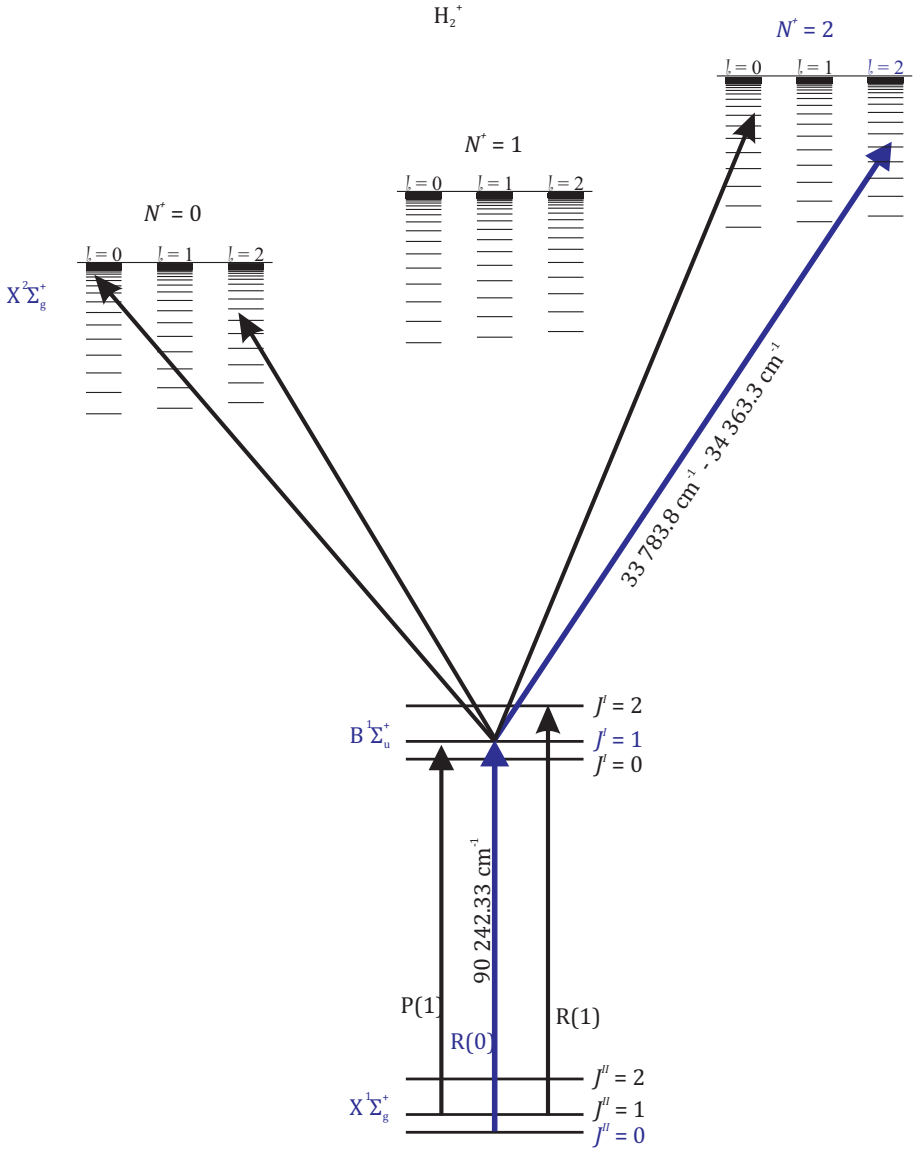

Figure 2.4: VUV and UV doubly resonant two-photon excitation scheme to excite ns/nd Rydberg states of H_2.

Rydberg state excitation

The second resonant one-photon transition is from the intermediate state ($B^1\Sigma_u^+(\nu' = 0)$), to the Rydberg series, converging on the ionization thresholds corresponding to the $\nu^+ = 0$, $N^+ = 0$ and $N^+ = 2$ rovibrational levels of the H_2^+, $X^2\Sigma_g^+$ ground ionic state. The overall energy of the transitions is approximately 124000 cm^{-1} with the lowest ionization threshold located at an energy of 124417.50718 cm^{-1} above the ground state ($X^1\Sigma_g^+$) [91]. The transition from the intermediate state ($J' = 1$, $2p$ level), which has ungerade symmetry, must be accompanied by a change in parity, allowing population only of the final states which are gerade in character. Since the H_2^+ ion core has $^2\Sigma_g^+$ electronic symmetry, overall gerade symmetry is only accessible for states which have even l, and the allowed transitions are primarily to ns and nd Rydberg series. In addition, the $\Delta J = 0, \pm 1$ selection rule further restricts the states accessible from the $J' = 1$ level of the intermediate B states allowing excitation only to states with total angular momentum $J = 0$, 1 or 2. Therefore, there are seven series accessible from the intermediate level populated via $B^1\Sigma_u^+$ ($\nu' = 0$, $J' = 1$); using Hund's case (d) notation, $(nlN^+)_J$, these are $(ns0)_0$, $(ns2)_2$, $(nd0)_2$, $(nd2)_0$, $(nd2)_1$, $(nd2)_2$ and $(nd4)_2$. However, all states are not accessible experimentally; in particular, the $(nd4)_2$ state excitation process is unlikely to be observed in experimental studies due to the very small transition intensity [87].

On the other hand, for these experimental studies, the effect of the polarisation of the VUV and UV photons, which were set to be mutually perpendicular, must also be considered. Under the field-free conditions, the quantisation axis could be defined with respect to one of the laser polarisation axes. In this framework, given the initial $J = 0$ and $M_J = 0$ state and an overall selection rule of $\Delta M_J = \pm 1$ from both steps of the excitation scheme (one step parallel to quantization axis, one perpendicular), this leads to the final projection of $M_J = \pm 1$. Consequently, the final state total

angular momentum, (J) quantized along either VUV or UV direction of polarisation, must be greater than zero ($J = 1$ or 2). This means the transitions to the $(ns0)_0$ and $(nd2)_0$ states are forbidden in this excitation scheme. Furthermore, Rottke et al [87] have suggested that the $J = 2$, $(ns2)_2$ and $(nd2)_2$ Rydberg series can rapidly decay via electronic coupling to the predissociative and autoionizing channels, accounting for the very low intensity of the $(ns2)_2$ and $(nd2)_2$ Rydberg series observed experimentally in Ref [87]. Hence, the $(nd2)_1$ and $(nd0)_2$ Rydberg series are likely to be dominantly observed in this experimental setup. These two Rydberg series are also well separated energetically. The zero-field excitation spectra of those two different series are discussed briefly in section 2.3.1.

2.1.5 The excitation region

The configuration of the apparatus within the main chamber, the alignment of the laser beam, and the H_2 molecular beam are illustrated in Fig. 2.5.

The H_2 molecular beam travels with a mean velocity of 2535 $\pm$ 50 m/s (this narrow range of velocity, characteristic of a low temperature, is attributed to the narrow diameter of the skimmer) and at an angle of 7° with respect to the surface, such that the perpendicular mean velocity of the hydrogen molecular beam was $\sim$ 309 ms^{-1} [92]. Consequently, it was expected that the central portion of the molecular beam would intersect with the surface $7 - 10$ μs after passing through the excitation region, corresponding to the vertical distance above the surface of $2.5 - 3.0$ mm.

2.1.6 The detection of H_2^+ ion

As the Rydberg molecule approaches a metallic or semiconductor surface, the interaction between the Rydberg electrons, with the image-charges in the surface, will strongly influence their trajectory (as discused in section 1.5). The effect of the image-charge

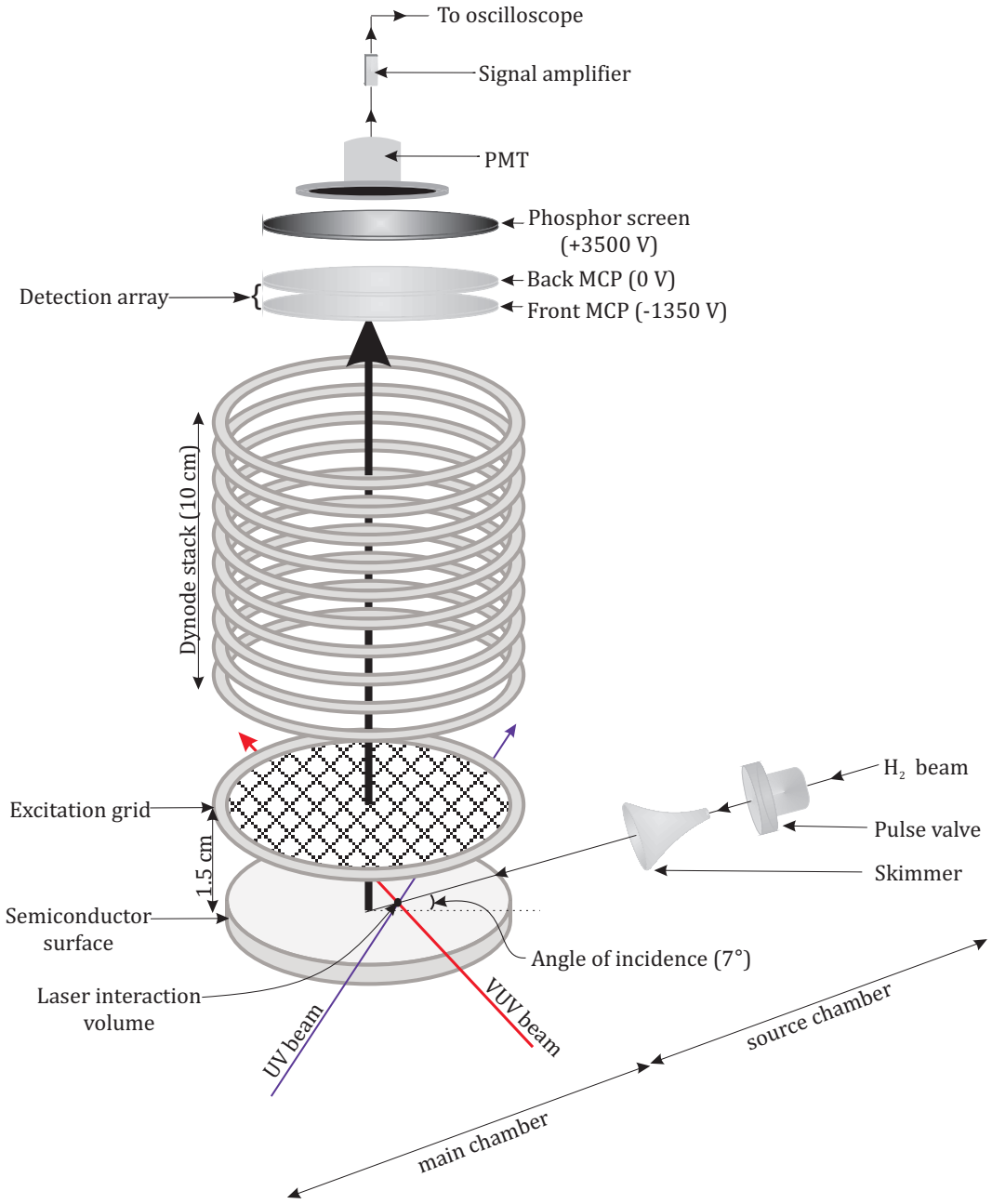

Figure 2.5: Schematic diagram of the experimental apparatus showing the geometry of the surface, extraction grid, dynode stack, MCPs, PMT and the molecular beam in the region between the surface and the mesh.

attraction is to lower the barrier for escape of the Rydberg electron and at a critical distance from the surface, the Rydberg electron is able to tunnel into the conduction band of the surface and ionization will occur. After the Rydberg molecule is ionized near the surface, the resultant molecular ion is repelled from the surface by an applied field, and pushes towards the mesh grid when a sufficient magnitude of negative external potential is applied to the extraction grid.

In earlier experimental studies of metal surfaces, a variable positive potential was applied to the surface [70, 93, 94]. However, in the case of a semiconductor surface, there is a band gap between the valence and conductance band such that the semiconductor surface would suffer from the effect of charging: if the applied potential is rapidly switched off, there would be a time delay before the surface is discharged. For this reason, in all these experimental studies, a large variable negative pulsed potential (up to 5000 V) was applied to the extraction grid (maintaining the charge difference between the surface and the mesh grid) at a time of 1 μs after laser excitation, while the surface was kept grounded (in order to achieve the same field as applying a positive potential to the surface). The magnitude of the homogeneous electric field generated by this potential was determined by the separation of the mesh electrode and the silicon surface.

Typically, the distance between the surface and the mesh electrode was confirmed to be 15 mm via the comparison of the experimental study of excitation spectra of the Rydberg states in the presence of a field and the theoretical Stark spectra [95]. The applied field can be varied from 30 Vcm^{-1} to 3300 Vcm^{-1}. Above a certain minimum required field, the H_2^+ ions were accelerated perpendicularly away from the surface (either those formed by pulsed field ionization or surface ionization) and travelled through the mesh electrode. Then they passed through a series of ring electrodes spaced 10 mm apart (a dynode stack); all of these ring electrodes (10) were maintained at the same potential

to provide a field-free flight region. A pair of 40 mm diameter multi-channel plates (Galileo, Chevron configuration) coupled to a phosphor screen detected the accelerated H_2^+ ions (the MCP detectors provided high temporal resolution, direct conversion, high physical charge amplification, low-noise, and pulse-counting capabilities). Potentials of -1350 V, 0 V and +3500 V were applied to the front MCP, back MCP and phosphor screen, respectively. The potential of the dynode stack was maintained at -1250 V ($\sim$ 100 V lower than the potential of the front MCP). The resulting fluorescence emitted from the phosphor screen was collected by the photo multiplier tube (PMT), and the amplified output of the PMT was connected to a digital oscilloscope. Finally, automated data acquisition from the oscilloscope to a personal computer was carried out by using custom-built LabVIEW^{TM} programmes, which allowed a time-of-flight (TOF) spectrum (ion-signal versus time delay from laser trigger) to be obtained. The fast response time of the MCPs, phosphor screen and PMT allowed for a well-resolved TOF spectrum, as shown in Fig. 2.6.

2.2 Assignment of the TOF spectrum

The specific LabVIEW^{TM} based programme developed for scanning the laser wavelength is used in the application of the field pulses and synchronised recording of the input and output data and it controls the whole data acquisition process. The experimental TOF illustrated for surface ionization and field ionization of H_2 Rydberg states is shown in Fig. 2.6. This profile is obtained at a particular wavelength for both laser beams, and the extraction field is chosen in between the limit of the surface ionization and field ionization signals.

The ion-signal produced by the field ionization occurs before the surface ionization signal because the direct-field ionization takes place in the gas-phase region, and the surface ionization takes place in the surface region, which is much further down along

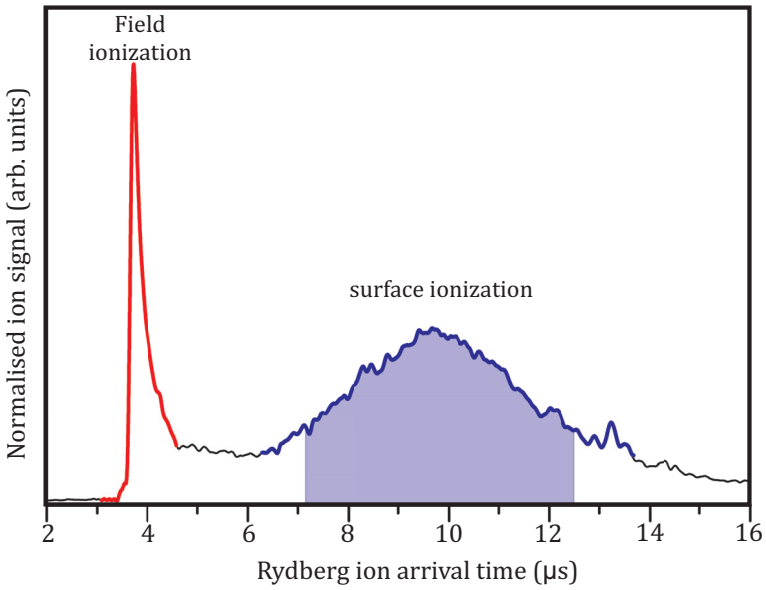

Figure 2.6: Experimental TOF displaying the detected ion-signals.

the molecular beam axis. The field ionization appears as soon as the extraction field is turned on, but in the case of the surface ionization signal it is independent of the pulse time of the electric field (as long as this occurs before interaction with the surface). Furthermore, the time of ionization of the Rydberg states is dispersed because of their range of arrival times at the surface, hence a broader time of flight signal appears.

2.2.1 Determining the excitation point

The laser beams (VUV and UV) intersect the H_2 molecular beam at a point a few mm above the Si surface. The height of the intersection position above the surface can be changed by adjusting the alignment of the VUV and UV laser beams, while keeping the incident angle of the H_2 molecular beam constant ($\sim 7°$). A typical time of flight distribution is shown in Fig. 2.7, for $n = 19$, H_2 Rydberg molecules at an applied field of $\sim$ 570 Vcm^{-1} with excitation occurring at five different intersection positions ($\sim$ 2.50 mm, $\sim$ 2.75 mm, $\sim$ 3.00 mm, $\sim$ 3.25 mm and $\sim$ 3.5 mm up the beam line from the surface). The two different ionization processes are immediately apparent. The

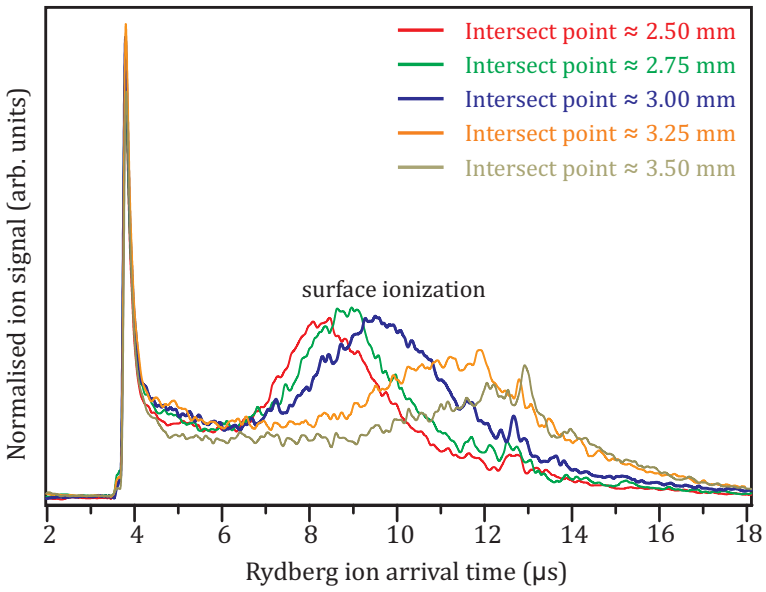

Figure 2.7: The arival time distribution of the H_2^+ ion for different excitation points.

position of the first signal remains constant whereas that of the second signal moves noticeably in the time of flight profile with the different extraction points as clearly shown in Fig. 2.7.

The direct-field ionization in the gas-phase is generally unaffected by the exact intersection position of the laser beams and molecular beam. The ions from field ionization are accelerated towards the MCPs instantaneously after the negative pulsed potential is applied to the extraction grid and the flight time towards the detector is relatively short, at ~ 3.7 μs. This '*early*' ion-signal is detected at all fields above the ionization threshold for the given populated Rydberg states.

The second feature appears from ionization at the surface, and the arrival time of the signal is strongly dependant upon the height of the intersection position above the surface. The time taken for the Rydberg molecules to reach the region in which surface-induced ionization can occur is varied by lowering or raising the intersection point and is much longer (~ 10 μs) than the flight time of the H_2^+ ions towards the

detector ($\sim$ 3.7 μs). Typically the beam crossing position is chosen such that the surface-induced ionization signal is centred at $\sim$ 10 μs corresponding to $\sim 2.75 - 3.25$ mm above the surface. Note (as stated above) that this surface ionization signal is independent of the time at which pulsed field is switched on [70, 71].

2.2.2 Determining the time gates

The time of arrival of the ions from the point of ionization of the Rydberg state has some dependence on the strength of the extraction electric field. In order to determine the time gate for the integration of the field ionization and surface ionization signals, the time of flight profiles were taken over a range of applied electric fields appropriate for a given principal quantum number, and the optimum time gate for the discrimination of the surface-induced and the direct-field ionization signal was chosen. At the highest extraction field strength ($\sim$ 550 Vcm^{-1}), the accelerated ions arrived at the detector in a time period of $\sim$ 3.7 μs. But in the case of low strength of extraction field, the arrival time of the ions can be much longer ($>$ 3.7 μs) (see Eq. 2.10). This is illustrated in Fig. 2.8, which shows the distribution of ion arrival times (relative to the laser excitation timing) that was observed at electric fields of 350, 450 and 550 Vcm^{-1}. The selected field ionization and surface-induced ionization time gates are shown also in the Fig. 2.8. Note that the different sensitivity of the time of arrival of the surface ion-signal compared with direct-field ion-signal is due to the longer time spent in the accelerating field region for ions that are formed at the surface.

The detection time for the surface-induced ionization signal T_T, is given by [96]

$$T_T = T_S + T_A + T_D \tag{2.8}$$

where T_S is the time taken from excitation for the molecules to arrive at the point

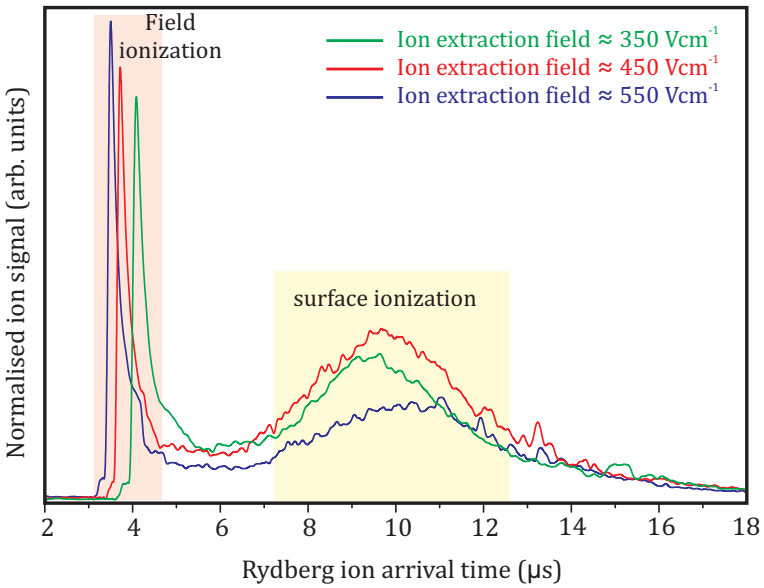

Figure 2.8: The arrival time distribution for population of the $n = 19$ Rydberg states for the various magnitudes of the ion-extraction fields.

above the surface at which they are ionized, T_A is the time during which the resulting ions experience an accelerating force, and T_D is the time required for the ions to arrive at the detector once they have left the region between the surface and extraction. T_S is dependent upon the excitation position, incidence angle and the mean beam velocity, and is given by

$$T_S = \frac{d}{v \sin\theta} \tag{2.9}$$

where d is the excitation distance from the surface, θ is the molecular incidence angle and v is the mean beam velocity. T_A and T_D are dependent upon the magnitude of the applied pulsed field on the extraction grid, and Eq. 2.8 may be rewritten thus

$$T_T = \frac{d}{v \sin\theta} + \frac{\sqrt{v_i^2 - 2ax} - v_i}{a} + \frac{L}{\sqrt{v_i^2 - 2ax}} \tag{2.10}$$

where x is the separation between the surface and the mesh grid, L represents the distance from the extraction grid to the detector (19.7 cm), a is the acceleration due

to the pulsed field and v_i is the incident mean beam velocity. Previous studies by Lloyd et al. [70] has shown that the sum of T_A+T_D varies by less than 0.1 μs.

2.2.3 Determining the mean beam velocity

Previous measurements of the velocity distribution of the pure H_2 molecular beam used in this experiment have been shown to exhibit a mean velocity of 2535 ms^{-1}, with a spread of 50 ms^{-1} [92]. However, the mean beam velocity observed for these experimental studies will be affected to a very small degree by the change in the excitation position of the Rydberg molecule, which will give rise to small changes in the time of flight profiles observed for surface-induced and direct-field ionization signals. Lloyd et al. [70] found that a change of incidence angles has a small effect on the surface-induced and direct-field ionization profiles through the study of the time of flight profile changes versus the incidence angle of the H_2 molecular beam. This molecular beam velocity distribution also varies with temperature. However, all of our experimental studies were carried out with the backing gas at room temperature. Furthermore, the incidence angle of the molecular beam also remains constant. Therefore, the time of flight profiles are generally unchanged from one experiment to another.

2.3 Ionization spectrum

2.3.1 Field-free spectrum

Figure 2.9 shows the Rydberg spectrum for field-free excitation of the H_2 Rydberg states. The VUV laser wavelength was fixed to the transition to the $\nu' = 0$, $J' = 1$ B-state intermediate (described in section 2.1.4) and the UV laser beam was scanned across the range of $291 - 295$ nm. This spectrum was obtained by detecting the total ion-signal by PFI at a delay of 3.7 μs after excitation and only those states

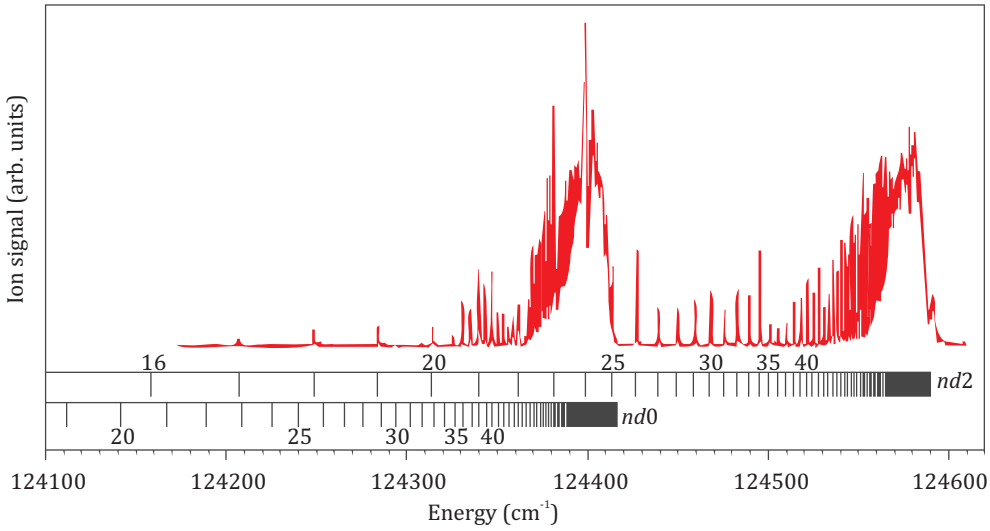

Figure 2.9: Field-free spectrum of the nlN^+ gerade Rydberg states of para-H_2 using pulsed-field ionization with 3.7 μs delay time, adapted from [86].

.

which survived decay by predissociation or autoionization contributed to the observed intensity.

Two principal series of Rydberg states were visible in the spectrum associated with nd states, which are labelled in Fig. 2.9 and converge to either the $N^+ = 0$ or $N^+ = 2$ ionic threshold. The ionization threshold for the $N^+ = 0$ series lies at 124417.50718 cm^{-1} above the ground state and the series of $N^+ = 2$ states lies at 124592.75109 cm^{-1} [91]. Rydberg states below the $N^+ = 0$ threshold in the region around 124200 cm^{-1} belong to one of the $(nd2)_J$ series with $J = 1$ or 2, and $(nd0)_2$ states were not observed below $n = 35$. The work of Osterwalder and co-workers [97] and other groups [87, 98] has shown that there is a fast predissociation of the $(nd0)_2$, $(nd2)_2$ and $(ns2)_2$ series in the region around 124200 cm^{-1} due to the interaction with a broad predissociated low-n, $J = 2$ interloper state corresponding to a vibrationally excited ion core. As a result, the main peaks apparent in this region were associated with the $(nd2)_1$ series rather than the $(nd0)_2$ series converging to the $N^+ = 0$ threshold.

For the Rydberg states observed above the $N^+ = 0$ threshold, at least one of the $(nd2)_J$ series (with $J = 1$ or 2), or perhaps both series, might be expected to be lost through the rotational autoionization during the time delay period (3.7 μs) [87]. However, the $(nd2)_1$ states cannot autoionize because at zero-field autoionization is governed by a $\Delta J = 0$ selection rule and there are no $J = 1$ continuum channels of gerade symmetry associated with $N^+ = 0$. Therefore, the Rydberg series observed above the $N^+ = 0$ continuum arises from the $(nd2)_1$ ($J = 1$) states, which are metastable with respect to autoionization.

2.3.2 Surface ionization spectrum

To detect the surface-induced ionization, a field must be applied that is sufficient to draw the ions away from the surface; this field must also be applied before the surface-induced ionization occurs, even though the field must be lower than the field ionization threshold for the Rydberg states.

Previous studies with H_2 Rydberg molecules have only considered the characteristic behaviour of the surface ionization profiles with different quantum numbers and different surfaces [32, 70–72, 93], and not the absolute (quantitative) surface ionization profiles. As a result, all the surface ionization profiles presented previously are normalized to a peak height of one. However, in the current experimental studies, the surface ionization profiles are compared qualitatively and quantitatively for different surfaces and different principal quantum numbers. Therefore, the absolute quantity of the surface ionization signal is of greater important in the current analysis. The absolute efficiency of the surface ionization process can be calculated by comparing the integrated surface ionization signal within the appropriate time gate region with the corresponding integrated field ionization signal at the high field. For each experimental study carried out, a detection efficiency ratio between the integrated surface ionization

and field ionization was calculated. This detection efficiency ratio fluctuated in every experimental study even when both laser beam and molecular beam alignments were unchanged.

The surface ionization profiles (detected ion-signal in the time gate corresponding to the Rydberg surface collision as a function of the ion-extraction field) presented in this thesis are normalized with respect to the maximum integrated field ionization signal. The profiles are recorded as a function of the ion-extraction field with steps of 2 $\mathrm{Vcm^{-1}}$, and the data are smoothed with a five-point FFT (Fast Fourier Transform) filter. The normalized surface ionization profiles may or may not have the same maximum peak between the different surfaces or different principal quantum numbers because of their relative normalization with the integrated field ionization signal. The ion detectability method is the best method to compare many surface ionization profiles for the variety of surfaces studied, see more details in section 3.3.

2.4 Surfaces

This research work involved investigation with different doped Si surfaces and an atomically flat gold surface.

2.4.1 Silicon semiconductor surfaces

The silicon semiconductor surfaces used in the experiments comprised a selection of *p*- and *n*- type doped silicon wafers, with different dopant concentrations ranging from 10^{19} $\mathrm{cm^{-3}}$ to 10^{14} $\mathrm{cm^{-3}}$, (PI-CHEM industry, United Kingdom). The characteristic details for the ten selected silicon-based semiconductor surfaces are given in table 2.1. The dielectric shielding parameter (see section 3.2.1), and mean dopant spacing (see section 3.2.2) are particularly important for the studies carried out here. An

Type of Si surface	**Dopant element**	**Resistivity (Ωcm)**	**Dielectric shielding parameter (β)**	**Dopant concentration (cm^{-3})**	**Mean dopant spacing (nm)**
n- type	Phosphorus	10-20	0.8413	3.00×10^{14}	149.3802
	Phosphorus	1-5	0.8414	1.88×10^{15}	81.0241
	Phosphorus	0.1-1.0	0.8421	9.52×10^{15}	47.1832
	Phosphorus	0.01-0.1	0.8485	2.04×10^{17}	16.9873
	Arsenic	< 0.005	0.8893	1.30×10^{19}	4.2529
p- type	Boron	10-20	0.8413	9.00×10^{14}	103.5744
	Boron	1-5	0.8414	5.65×10^{15}	56.1458
	Boron	0.1-1.0	0.8421	2.90×10^{16}	32.5487
	Boron	0.01-0.1	0.8485	6.21×10^{17}	11.7211
	Boron	< 0.005	0.8893	2.10×10^{19}	3.6246

Table 2.1: The specific characterstics for all ten surfaces; all of these values are calculated from the equations below (2.11 and 2.12).

approximate calculation of the static dielectric constant is given by equation 21 of reference [99],

$$\epsilon_{(\rho)} = \frac{0.0125 + \epsilon_{(Si)} \times \rho}{9.15 \times 10^{-5} + \rho} \tag{2.11}$$

where ϵ_{Si} is the dielectric constant of the intrinsic silicon surface (~ 11.6) and ρ is the resistivity of the doped silicon surface.

The mean dopant spacing (λ) depends on the dopant concentration (N_{D}) and it is calculated using the following equation [100, 101],

$$\lambda = \left(\frac{1}{N_D}\right)^{1/3}. \tag{2.12}$$

The native oxide (SiO_2) formation is related to the time period, and has been measured

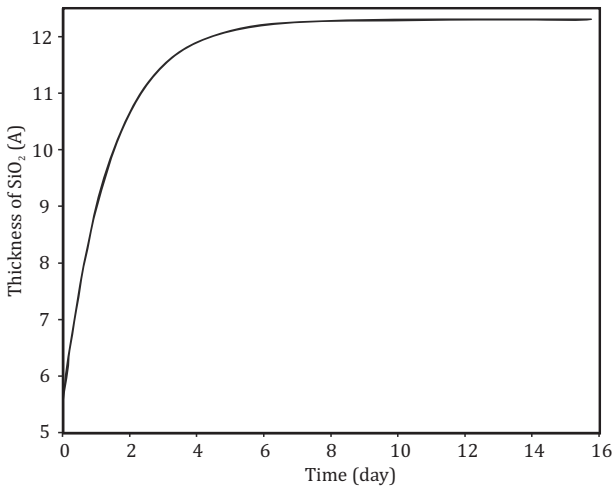

Figure 2.10: The native oxide forms on a silicon wafer were measured over time on the same Rudolph ellipsometer, as captured from [102].

using a Rudolph ellipsometer, which is shown in Fig. 2.10 [102]. The formation of SiO_2 thickness ($\sim$ 1.2 nm) is small compared to the Rydberg orbital dimension (10 nm). In addition, it was very difficult to maintain chemically clean conditions in the experimental setup due to the rapid oxidation with the atmospheric air. Therefore, all of these experimental studies were carried on different dopant concentrations of *p*- and *n*- type 3" Si semiconductor surfaces, which were placed on the surface holder from a vacuum-sealed pack immediately without further cleaning processes.

2.4.2 Gold surfaces

The 3" diameter polished Si wafer was coated with a gold layer via metal vapour deposition in a BOC Edwards Auto 306 vacuum coater. First, a 5 mm thick layer of chromium was deposited onto the Si wafer and then succeeding gold (99.99%, Alfa) deposition was continued via evaporation processes until the gold thickness was 200 nm. Finally, the resulting evaporated gold surface was permitted to cool to room temperature. Its roughness was less than 1 nm, as measured by atomic force microscopy (AFM) [71].

Chapter 3

Surface interaction of molecular hydrogen Rydberg states at zero field

This chapter presents the experimental results of the surface-induced ionization of H_2 Rydberg molecules incident at *p*- and *n*- type doped Si semiconductor surfaces at various dopant concentrations. The aim of this chapter is to provide an understanding of the effects of the dopant type (*p* or *n*) and their different dopant concentrations on the surface-induced ionization of Rydberg H_2 and the subsequent detection of the H_2^+ ion.

3.1 Surface-induced ionization profiles

The integrated direct-field ionization and surface-ionization signal from the TOF profiles (see section 2.2) for the H_2 Rydberg molecular beam incident on the Si surface is recorded as a function of the applied extraction field. The characteristic behaviour of both types of ionization signals (direct-field and surface-induced) for an initial popu-

lation of $(nd2)_1$ Rydberg molecules with the principal quantum number $n = 17 - 21$ is shown in Fig. 3.1 for a n-type phosphorus doped Si surface. Each data point presented is typically averaged over $30 - 50$ laser shots, and the error bars associated with the data points are also presented in Fig. 3.1. The error bars are relatively small in comparison to the variation of signal due to the resonance effects (see section 3.2). The shot to shot variations of the experimental signal can be attributed to fluctuations in laser power, variation in gas density from the pulsed valve and temperature fluctuations.

The surface-induced ionization signal is not detected at very low extraction field because the field is not adequate to pull the ions away from the surface. The surface ionization profiles increase with increasing external pulsed field until they reach the onset of direct-field ionization. At high electric field, the surface ionization process competes with gas-phase direct-field ionization, and this high field removes the Rydberg molecules before interaction with the surface. Therefore, no surface ionization signal is detected after this cut-off limit.

Previous studies of surface ionization of H_2 Rydberg molecules at a metal surface [70, 71] showed that the surface ionization profiles show a progression of sharp resonances as seen in Fig. 3.1. These sharp resonances are experimentally reproducible and represent an enhancement in the surface ionization probability. This was attributed to the initially populated $N^+ = 2$ energy level states crossing in the Stark map with higher-n levels belonging to the $N^+ = 0$ series, which give the sharp resonance at particular extraction fields. Since the higher-n $N^+ = 0$ states are ionized further from the surface, the detection probability of the subsequent ion is much higher at a given field. The time required to transfer energy between the Rydberg electron and the rotating ion core is therefore much less than, or on the order of, the time scale for which the molecule approaches the surface. The time scale has been studied in detail

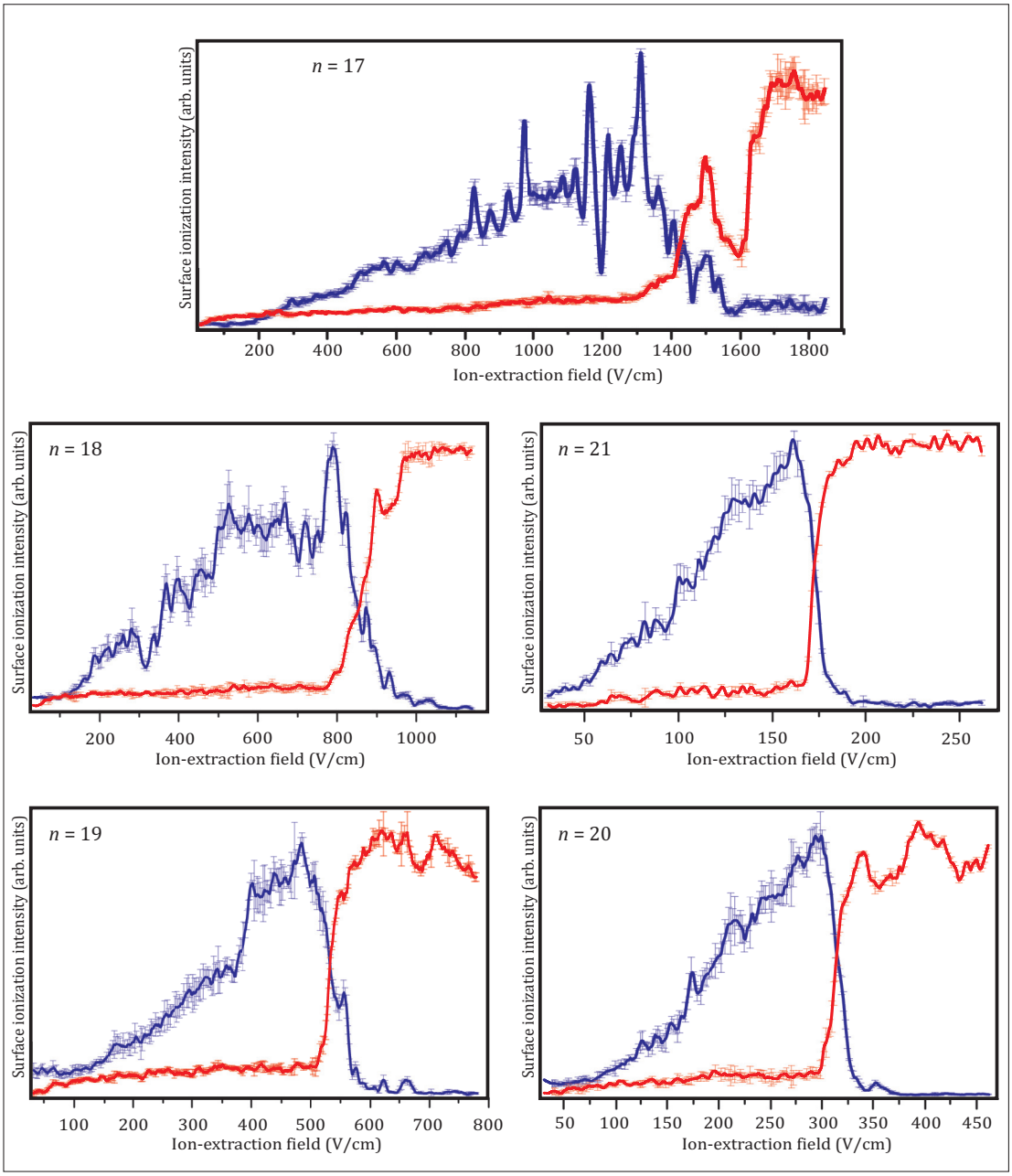

Figure 3.1: Surface ionization profiles (blue line) and direct-field ionization (red line) for population of the $(nd2)_1$, $n = 17 - 21$ Rydberg states incident on the n-type (phosphorus ($N_D = 3.00\times10^{14}$ cm^{-3})) silicon surface, recorded as a function of applied ion-extraction field.

by McCormack using pulsed field ionization (PFI) at different time delays from initial laser excitation [72, 95].

The effects of redistribution of population between Rydberg states with adjacent principal quantum numbers have also been studied previously [103]. It was suggested that the ion signal at low extraction field (the long tail that does not follow the general cumulative normal distribution of the overall profiles) is the result of black-body radiation (BBR) stimulated redistribution (see section 1.3.1).

The observed direct-field ionization thresholds for the $(nd2)_1$ Rydberg states are associated with the $N^+ = 0$ ionization threshold. Field ionization occurs through the coupling between the $N^+ = 2$ and $N^+ = 0$ channels leading to field induced rotational autoionization, and it happens on a sub-microsecond time scale [72]. This field ionization mechanism involves the complete transfer of rotational energy from the H_2^+ ion core to the Rydberg electron. In section 2.3.1, it was discussed that the field ionization process is dominated by the $N^+ = 2 \longrightarrow N^+ = 0$ rotational autoionization process leading to strong resonances observed.

For a given Rydberg state n belonging to the $N^+ = 2$ series, the effective principal quantum number, ν_o, with respect to the $N^+ = 0$ threshold is given below,

$$\nu_0 = \left[\frac{1}{n^2} - \frac{I_2 - I_0}{\Re_{H_2}}\right]^{-1/2} \tag{3.1}$$

where I_2 and I_0 are the ionization thresholds for the $N^+ = 2$ and $N^+ = 0$ Rydberg series respectively [91] and $\Re_{H_2}$ is the Rydberg constant for the hydrogen molecule. It has been shown previously [32, 93] that the midpoint of the rise of the surface ionization signal corresponds to ionization distances of 3.1 ν_o^2 a.u. (shown in Fig. 3.2 as vertical - - - lines), demonstrating that detected ion signal from surface ionization comes solely from $N^+ = 0$ states, via population transfer at the $N^+ = 2$, $N^+ = 0$ level crossings.

3.1.1 Effect of the principal quantum number

As explained in sesction 1.3, the lifetime of the Rydberg states is strongly dependent on the principal quantum number. In order to study the interaction of Rydberg states with surfaces, the lifetime is required to be of the order of, or greater than, the time between Rydberg excitation and when the Rydberg molecule collides with surface ($\sim$ 10 μs). Thus, all of our experimental studies are carried out for the range of the principal quantum number $n \geq 17$. The limitation of carrying out experiments at higher-n is a consequence of the minimum field resolution or field increments ($\sim$ 2 Vcm^{-1}) that can be provided by the instruments. For principal quantum number $n > 21$, the number of field steps for which profiles can be recorded before the onset of field ionization is limited, and resonance effects may therefore be missed by the relatively large field step. Clearly, the field resolution can be increased by increasing the separation between the surface and the extraction mesh grid. However, for the current study, the surface-mesh grid is kept at a distance of 1.5 cm as in Ref. [71], and this limits the highest Rydberg states studied to $n = 21$.

The ionization of the Rydberg molecules arises from the loss of the Rydberg electron, which is weakly-bound to the ion core, to the conduction band of the semiconductor surface. This charge transfer process occurs at a separation at which there is significant overlap between the Rydberg electron wave function and the surface. The classical radius of the Rydberg orbital increases with principal quantum number, and scales as n^2 (see more details in section 1.2.2). The ionization distance between the molecule and the surface will therefore rise with increasing principal quantum number. For that reason, the onset potential of the observed surface-induced ionization profiles decreases with increasing principal quantum number (see Eq. 1.38). This is shown in Fig. 3.2. In fact, hydrogenic theory [104] and previous experimental studies of the ionization of xenon Rydberg atoms at a metal surface [52] have shown that the minimum required

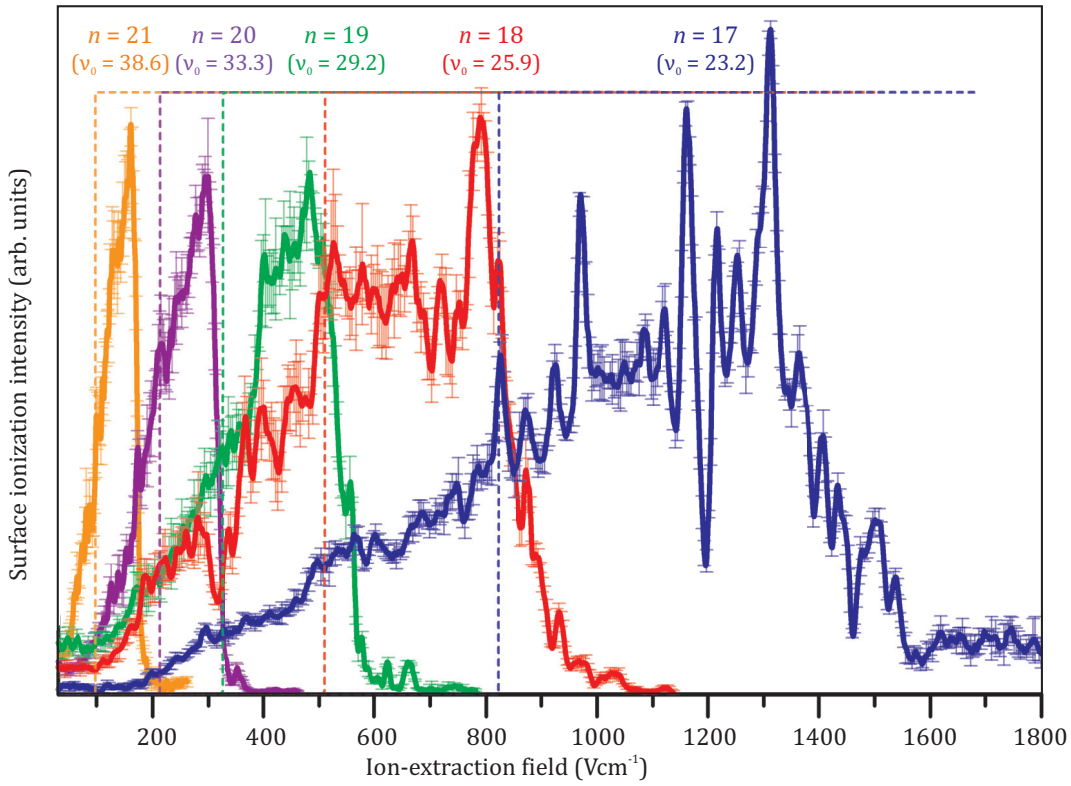

Figure 3.2: Surface ionization signal as a function of applied extraction field for population of the $n = 17-21$ H_2 Rydberg states incident on the n-type (phosphorus doped ($N_D = 3.00\times10^{14}$ cm^{-3})) Si surface. The - - - lines show the results of the OTB trajectory calculations with fixed minimum ionization distance as 3.1 ν_o^2 a.u. (see section 6.4).

field ($F_{\min}$) scales as approximately n^{-4}.

3.2 Comparisons of the surface ionization profiles

The surface-induced and direct-field ionization data were recorded for an initial population of $(nd2)_1$ Rydberg states, over the range of principal quantum number $n = 17-21$ Rydberg states, as a function of the applied extraction field for a variety of doped Si surfaces. To illustrate the large differences in the detected ion signal that can be ob-

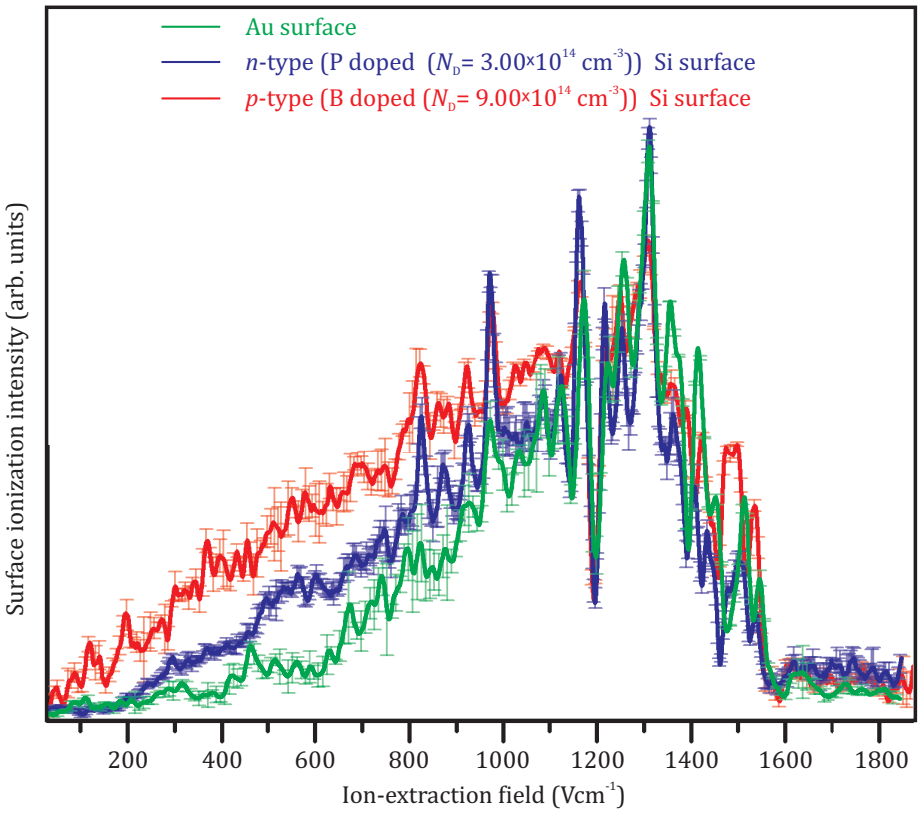

Figure 3.3: Comparing the surface ionization profiles of the $n = 17$ Rydberg states incident on the Au surface (green line), n-type (phosphorus doped ($N_D = 3.00\times10^{14}$ cm^{-3}), blue line) and p-type (boron doped ($N_D = 9.00\times10^{14}$ cm^{-3}), red line) Si surfaces, recorded as a function of applied ion-extraction field.

served between the different Si surfaces and the previously studied metal conductor surfaces [71], the surface ionization profiles for p- and n- type doped Si surfaces with similar dopant densities and an atomically flat gold surface are shown in Fig. 3.3 for the H_2 $n = 17$ Rydberg states.

The three surface ionisation profiles show some similar behaviour. First, the detected ion signals increase with increasing ion-extraction field until the high-field cut-off limit where the surface ionisation signal for all three profiles drops sharply at the same field ionisation threshold. Secondly, the field positions of resonance structures which the three surface ionisation profiles exhibit appear to coincide with one another, and are

independent of the nature of the target surface. As explained before, the experimentally reproducible resonances are attributed to the evolution of population from the initially populated $N^+ = 2$ Rydberg state to states belonging to the adjacent $N^+ = 0$ channel, when the ion-extraction field is held at the field positions of the energy level crossings. Thus the resonance structures are not expected to be dependent the nature of the target surface, but only on the magnitude of the applied electric field. However, the intensity of the detected ion signal clearly shows some variation.

Despite the similarity between the surface ionisation profiles shown in Fig. 3.3, the overall magnitudes of the detected ion signal at a given electric field for the three surfaces are clearly very different. The ion-signal for the Si surfaces is considerably higher than for the Au surface, and the *p*-type Si-surface has noticeably higher ion detection than the *n*-type Si surface. The differences between the profiles are greatest at low ion-extraction fields. The differences between these three surface-induced ionisation profiles cannot be attributed to the difference in surface roughness, because the surface roughness of the doped Si surfaces and the gold surface are very similar and are nearly atomically flat (< 1.2 nm [102, 105]), and previous studies where a noticeable difference in the surface ionization profiles was observed had a roughness spanning $\sim$ 2 orders of magnitude (1 nm vs 231.9 nm) [70, 71]. The variation in ionization profile must therefore arise from differences in the electronic band structure of the surface, or other characteristics of the doped surfaces other than geometrical.

As will be shown below, it is possible to account for the different ion detectabilities at the semiconductor surfaces by considering the possible presence of localized dopant charges at the surface-vacuum interface.

3.2.1 Electronic structure of the surfaces

Experimental studies of the interaction of hydrogen Rydberg molecules with gold and aluminium surfaces [70–72] has shown that, for free-electron metallic conductors, the charge transfer process is independent of the type of the target metal surface, since the energy of the Rydberg state is degenerate with the continuum of energy states of the metal and therefore is not sensitive the exact electronic structure of the metal. For the case of a semiconductor however, the presence of a band gap could play an important role in the Rydberg surface charge transfer (if the energy of the Rydberg state is in the same range). However, in the case of Si semiconductor surfaces, the bottom of the conduction band lies below the vacuum level [52, 54–56] and also below the energies of the typical Rydberg energy levels ($n > 15$) of interest, *i.e.* energetically, the band gap is located far below that of the Rydberg states. Therefore, the Rydberg electrons can tunnel directly to the conduction band of the Si surfaces, just like the case of a free-electron metal surface. However, the image-charge fields experienced by a charged ion outside a dielectric surface are reduced by factor of β, such that the attractive image potential is smaller than for a '*true*' metal [54–56].

The β-factor is related to the dielectric constant (see Eq. 1.35) [54–56], which is a measure of the ability of a dielectric material to store electrical potential energy under the influence of an electric field, and provides a quantitative measure for the dielectric screening of the image-charge attraction. The dielectric constant is known to vary with the dopant density (see Eq. 2.11) [99]. A low dielectric constant is found for intrinsic (or lower dopant density) Si semiconductors, and as the dopant density increases, the dielectric constant increases, and approaches the value of a metal surface (∞), giving a corresponding β value of 1. As the image-charge attraction varies with the dielectric constant, the minimum detectable ionization distance at a given electric field also changes (see Eq. 1.37). The variation of dielectric shielding factor and

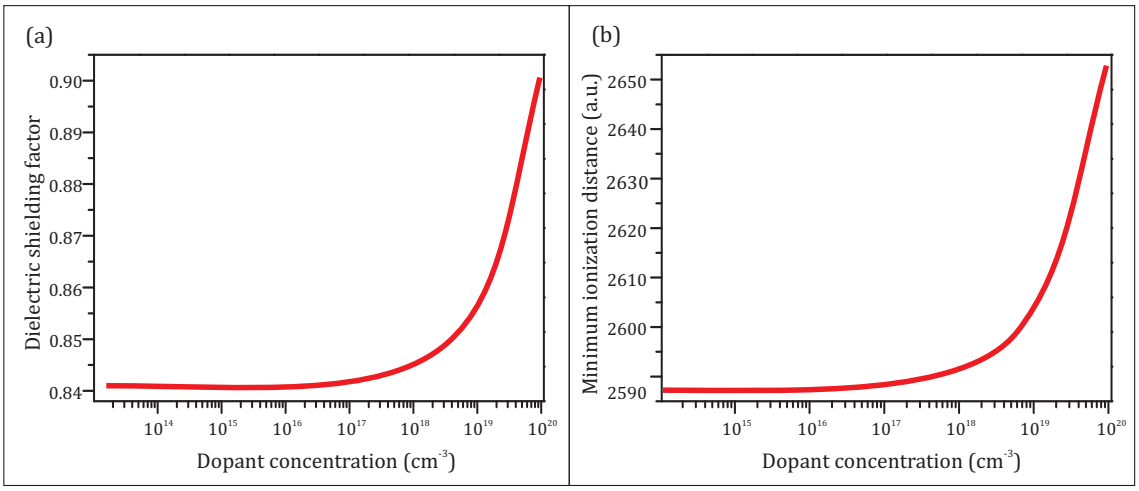

Figure 3.4: (a) The β-factor changes as a function of dopant concentration of Si surface (b) The minimum ionization distances for the $n = 19$ Rydberg state at a particular electric field is related to the dopant concentration.

the corresponding minimum detectable ionisation distance with the range of dopant densities studied in this work is illustrated in Fig. 3.4.

Figure 3.4 (a) shows that for the surfaces used in these experimental studies ($N_{\mathrm{D}} \sim \times 10^{14}$ cm^{-3} to $\times 10^{19}$ cm^{-3}), the β-factor varies from ~ 0.84 to ~ 0.90 in these experimental studies, and the corresponding change in the range of minimum detectable distance is relatively small: from ~ 2590 a.u. to ~ 2650 a.u. for $n = 19$ Rydberg state at particular ion-extraction field (shown in Fig. 3.4 (b)). Thus, the effect of the dielectric constant on the shielded image-charge predicts a small shift of the onset of ion signal towards higher fields as the dopant concentration increases approaches the free-electron metal limit (*i.e.* higher dopant concentration leads to a larger dielectric constant, which accounts for the higher image-charge attraction and the higher field required to extract ions formed at a given distance from the surface, so it give lower ion detection probability). Although this is somewhat consistent with the observed differences between ionisation profiles of the Si semiconductors and the Au surface shown in Fig. 3.3: the onset of the Au surface is at a higher field than Si surfaces with

lower dielectric constants, the magnitude of the shift is much larger than expected from the shift of detectable distance shown in Fig. 3.4 (b). Furthermore, the significant difference between the ionisation profiles of the *p*- and *n*- type Si surfaces shown in Fig. 3.3 cannot be explained by considering only the dielectric constants, since they are roughly the same (the dopant concentration of the *p*- and *n*- type surfaces are of the same order of magnitude).

The difference can be attributed purely to the difference in the dopant density in this case; similar size differences of ion signal can be seen when comparing *p*- and *n*- type doped Si surfaces of similar dopant concentration. The conduction band minimum is energetically far below that of the Rydberg states. Therefore, it was initially thought that the changes in the electronic band structure of the semiconductor due to the different dopant concentration might cause the difference in the observed ionization profiles. However, only at very high dopant densities ($N_{\mathrm{D}} > 10^{21}$ cm^{-3}) does the band gap shrink (or start to disappear) due to the wave functions of the electrons located on the dopant atoms beginning to overlap, and behave as metal surfaces. All these experimental studies are carried out in this work on Si surfaces with dopant concentration of $N_{\mathrm{D}} = 10^{14}$ cm^{-3} – 10^{19} cm^{-3}.

In previous studies of the surface ionisation of Xe Rydberg atoms at Au and Si surfaces, it was shown that the stray field at the surface plays an important role on the charge transfer and ion detection process [50, 54–56, 106]. The stray fields affect both the ionisation distance and the ion detection probability. However, in some of that work the stray fields arose from surface imperfections and adsorbates rather than a deliberate variation of dopant density as in this work. It will be shown in the following sections and chapter 6 that the experimental observations at *p*- and *n*- type surface can be adequately explained only when presence of the surface dopant charges at the semiconductor surfaces (due to the dopant's local charges) is considered.

3.2.2 Surface dopant charges

Previous studies of the surface ionization of Rydberg Xe atoms at Si surfaces show that the Si surface potential may be modelled by regular positive and negative patch charges [54–56]. But for the surfaces used in this research work, the polarity and dimensions of the local charges depends on the dopant type and dopant concentration, and it should affect both the distance at which ionization occurs, as well as the detection probability of the positively charged ion core.

Surface charge distribution in p- and n- type Si surfaces

In general, a doped Si semiconductor can be one of two types, p- or n- type, depending on the doping atom. When the Si semiconductor is doped with acceptor atoms that '*accept*' electrons, typically III A group element in the periodic table, *e.g.* boron, the semiconductor is categorized as p-type doped Si semiconductor, and if it is doped with donor atoms which '*donate*' electrons, typically V A group element in the periodic table, *e.g.* phosphorus, it is categorized as a n-type doped Si semiconductor. The addition of donor atoms produces states near the conduction band while acceptor atoms create states near the valence band. The simple energy level diagram of the p- and n- type Si surfaces are illustrated in Fig. 3.5 (a).

The majority of the charge carriers of the p-type doped Si surface are holes, which are created in the valence band when the acceptor dopant atoms accept electrons from the Si substrates, *i.e.* each hole (positive charge) on Si is associated with a negatively point charged dopant ion, such that the semiconductor surface remains electrically neutral as a whole. The majority of carriers are near the valence band and the Fermi energy level is also near the valence band (see Fig. 3.5 (a)). The charge distribution at the surface can therefore be seen as repeating units of a positive delocalized surface charge (from the holes) and a negative point charge (representing the dopants), as

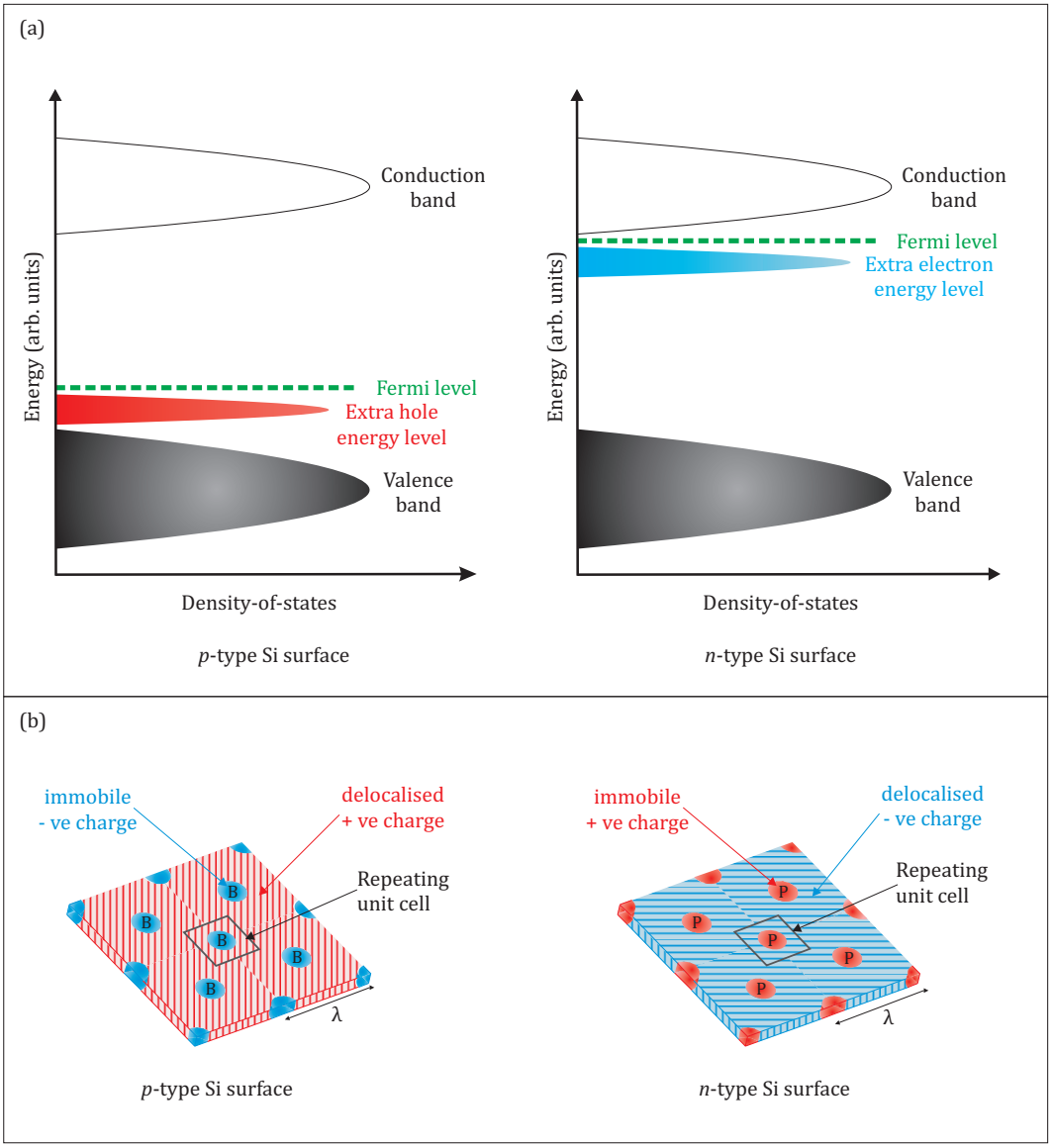

Figure 3.5: (a) Density of states diagram of p- and n- type doped Si surfaces. Shaded area represents the energy levels filled at 0 K below the Fermi level. (b) p- and n- type doped Si surfaces and their surface charges such as to maintain surface neutrality due to the presence of the point charged dopants, λ is the mean dopant spacing between dopants. Note that in reality the spacing of dopants is not regular as illustrated, even though we model in that way.

illustrated in Fig. 3.5 (b).

In the case of *n*-type doped Si surface, the majority of the charge carriers are mobile electrons, which are created in the conduction band when the donor dopant atom donates an electron to the Si substrate, resulting in a negatively charge cloud '*delocalized*' around the positive point charged dopant ion. The majority of the charge carriers appear near the surface and the Fermi energy level appears closer to the conduction band (as shown in Fig. 3.5 (a)). The charge distribution of the surface can be seen as repeating units of a negative delocalized surface charge (from the mobile electrons) and a positive point charge (representing the donor dopants) as illustrated in Fig. 3.5 (b). These occupied dopant sites in the surface have been observed previously using STM [100, 107].

Effects of dopant charges on the surface ionization profiles

Now let us consider the effect of these surface dopant charge distributions on the experimental surface ionization profiles. The surface dopant charges will affect both the distance at which surface ionisation occurs and the ion detection probability of the resultant ions. The detailed quantitative analysis of both these factors and quantitative comparison of theoretically predicted profiles with the experiment will be given in chapter 6. It will be shown in chapter 6, that the main contribution to the changes in the ionisation profiles from the dopant charges are due to the changes in the ion detection probability, and will be the basis of qualitative discussions below.

Considering only the effect on the ion detection probability (not the minimum ionization distance), it is easy to see that a positive charge at the surface increases the ion detection probability as it repels the H_2^+ ion away from the surface, while a negative charge decreases the ion detection probability by pulling the H_2^+ ion towards the surface. When ion trajectories approach the *p*-type doped Si surface, the ion is more

likely to encounter the delocalized positive surface charges than the localized negative charges at the doping atom, and for n-type surfaces, the delocalized negatively charged region is more likely to be probed. Thus, from this simple argument of surface charge distributions, it is expected that a p-type doped Si surface (with large areas of delocalized positive dopant charges) would provide a higher detected ion-signal than for the n-type doped Si surface (with delocalized negative dopant charges), as illustrated by the experimental ionisation profiles shown in Fig. 3.3. The effect of variation of dopant charge distribution with dopant density will be explained in the next section.

It is important to note that the dopant charge potential experienced by the Rydberg state and the resultant ion is strongly dependent on the distance from the surface. This is because the potential due to the dopant charge decays exponentially with distance. This is illustrated in Fig. 3.6, which shows the model potential (which is employed in chapter 6) at two distances from the surface, for a repeating unit of a n-type Si surface. Therefore, the higher-n Rydberg states, which have a large ionization distance, enter the slow decay potential of the additional dopant charges. On the other hand, lower-n Rydberg states enter the region of rapid decay of the dopant charge potential, as shown in Fig. 3.6. Thus, the magnitude of change between the ionisation profiles for different Si semiconductor surfaces are expected to vary with the principal quantum number of the Rydberg state studied, as this provides a probe of the dopant potential at various distances from the surface (surface ionisation distance scales as n^2). The effect of varying the principal quantum number of the Rydberg state will be investigated in the following sections.

Surface charge distribution in different dopant density Si surfaces

These experimental studies were carried out not only for the various dopant types of the Si surface but also carried out with various dopant densities. It is shown in

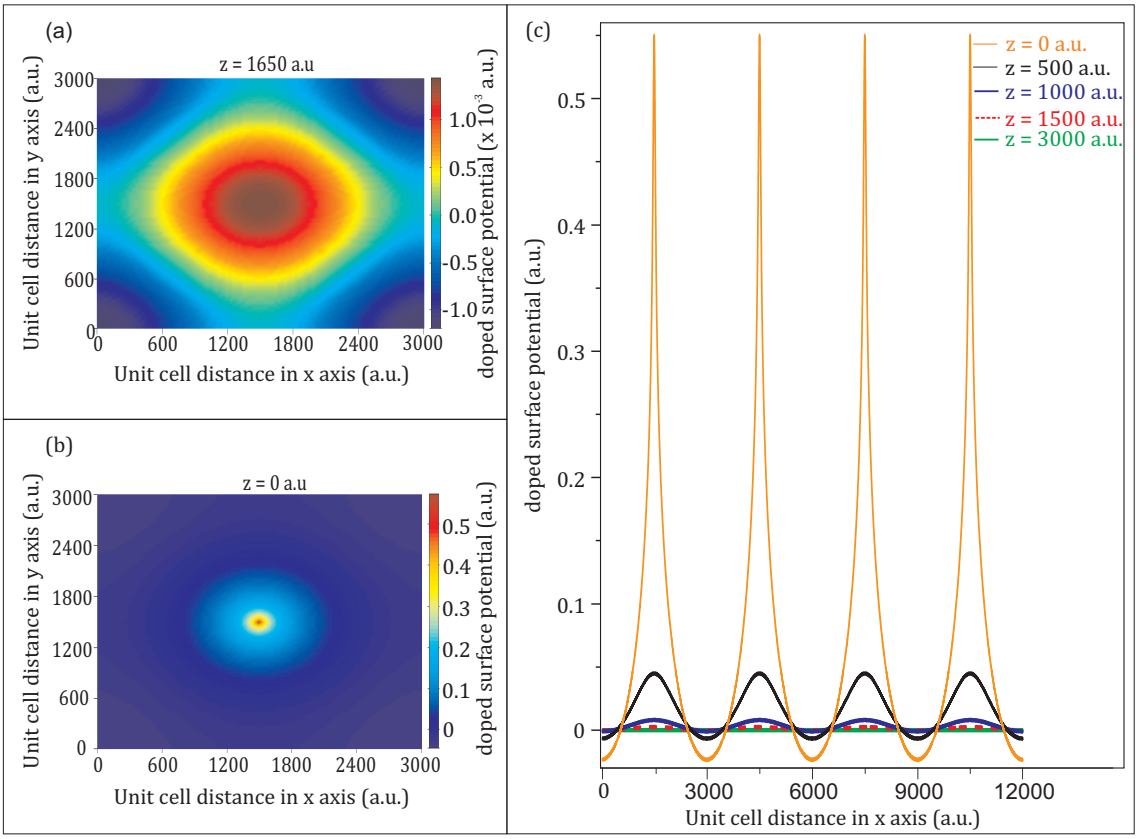

Figure 3.6: Potential decay of surface dopant charges at (a) long, (b) short, and (c) various distances from the n-type (phosphours doped ($N_{\mathrm{D}} = 3.00{\times}10^{14}$ cm^{-3})) Si surfaces, which are calculated by solving the Poisson's equation 6. The *1D* doped surface potential is taken at y = $\lambda/2$ on the *2D* potential distribution.

section 3.2.1 that varying the dopant density affects the ion detection probability by the changes in the dielectric shielding of the image-charge potential. However, varying the dopant density also has a signifcant effect on the dopant charge distribution at the Si surfaces.

The *p*-type Si surfaces have a positive delocalized surface charge and negative point charges in their surface region. These positive delocalized charge areas create fields which repel the H_2^+ ions, and accelerate the H_2^+ ion towards the detector, so detected ion signal is higher for incidence of the ion over these positively charged regions at the surface. The area spanned by these delocalized positive charges becomes wider with decreasing dopant density, and thus, the probability of the H_2^+ ions sampling these areas of higher ion detectability also increases. As a result, the detected ion signal will tend to increase with decreasing dopant density. And as shown quantitatively in section 6.3.2 (as see in Fig. 6.5), the potential at a distance from the surface is actually higher for lower dopant density. An *n*-type Si surface, has a negative delocalized surface charge and positive point charges on its surface. The large area of delocalized negative charge creates a supplementary attractive force, so that the resultant ions are attracted to the surface, and the efficiency of the ion detection becomes smaller. However, the ionization distance increases with the presence of positive surface charges, but decreases in regions of negative surface charges. Thus, the '*ionization surface*' (the spatial distribution of the most probable ionization distance) is corrugated with the periodicity of the dopant atom, and the amplitude of this corrugated '*surface ionization distance*' also decreases with increasing the dopant density, as shown in Fig. 3.7

The H_2 Rydberg molecules fly at a 7° angle to the surface, and a visualization of this corrugated surface ionization distance is shown in Fig.3.8. Most of the H_2 Rydberg molecules are ionized at the top of the '*hill*' on the corrugated surface ionization distance and it clearly shows that positive charges present in the surface regions have

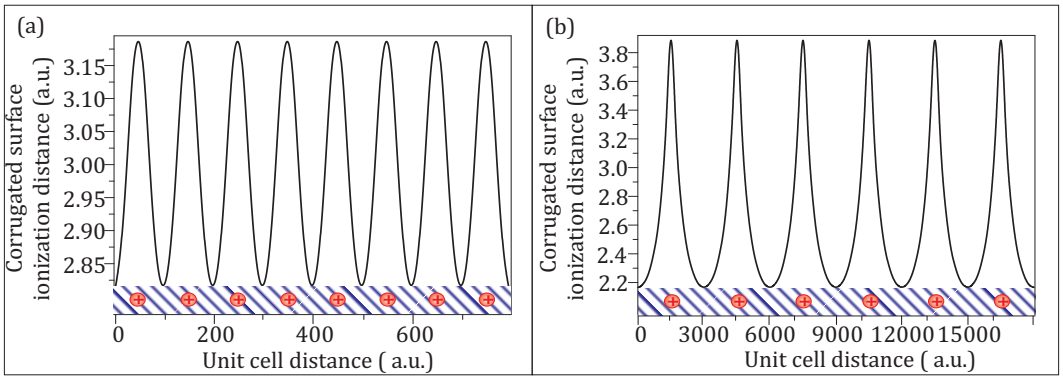

Figure 3.7: The variation of corrugated surface ionization distances, which is created from surface dopant charges, for the (a) high dopant density ($N_{\mathrm{D}} = 1.30\times10^{19}$ cm^{-3}), and (b) low dopant density ($N_{\mathrm{D}} = 3.00\times10^{14}$ cm^{-3}) of n-type Si surface.

the predominant effect on the Rydberg ionization processes rather than the presence of the negative charges. As the dopant density is increased the dopant charges become smaller in size and come closer together (see Eq. 2.12). Additionally, the decay length of these dopant charges also decreases with increasing dopant density (as a function of x, y direction); *i.e.* rapid potential decay occurs at the high dopant density (see more details in section 6.3.2). Therefore, as the dopant density increases, the enhancement of the minimum ionization distance in the presence of the positive charges become lower and the positive-potential area in which the Rydberg molecule is ionized becomes narrower, and it will give a lower efficiency of the detected ion signal. For very high dopant density, the dopant charges present in the surface region appear effectively '*more neutral*' like a metal surface. For that reason, the experimental surface ionization profile for a metal surface is noticeably of lower intensity than the p- and n- type Si surfaces. The effect of dopant density and type on surface ionization profiles is discussed further in the next section.

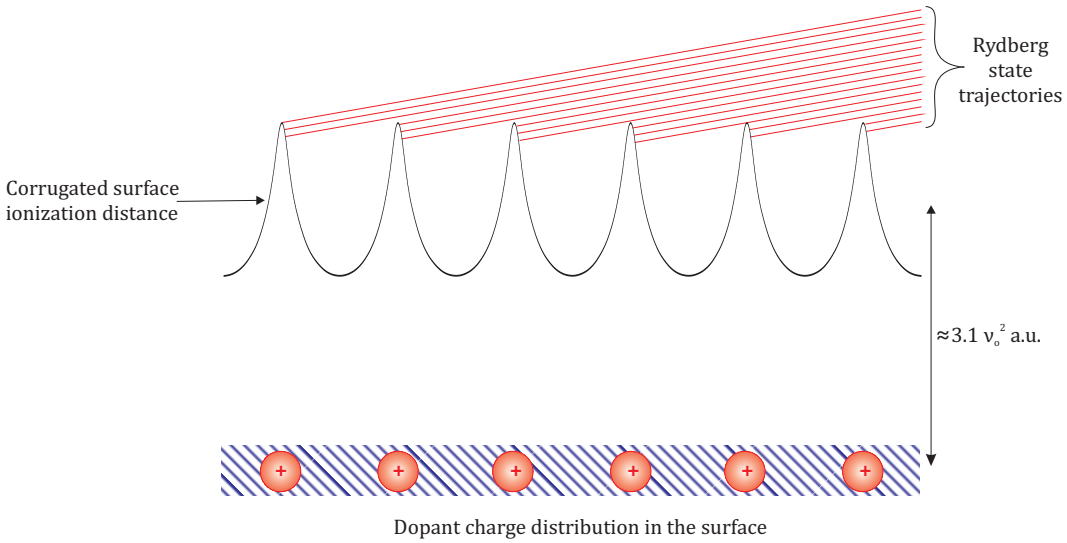

Figure 3.8: The pictorial illustrate H_2 Rydberg molecular trajectories hit only at the hill of the corrugated surface ionization distances.

3.3 Ion detectability

In order to compare directly the surface-induced ionization profiles for Si surfaces with various dopant types and dopant densities, and to ease the analysis of this difference, one can simply consider the overall integrated surface ionization profiles as a function of applied electric field. This is calculated by integrating the surface ionization profiles between the two points where the surface ionization arises and the direct-field ionization begins (as shown in Fig. 3.9). This integrated value will be referred to as the overall '*ion detectability*' (*i.e.* the total ions detected from the surface ionization from low field up to the high-field cut-off limit).

For convenience, the ion detectability values are further normalized relative to the predicted values for a '*standard*' surface, which can be interpreted as a heavily doped Si semiconductor whose values are the average of the extrapolated values of the ion detectability for the *p*- and *n*- type doped Si semiconductors with various dopant densities. As expected, these values are very similar to the values obtained for the

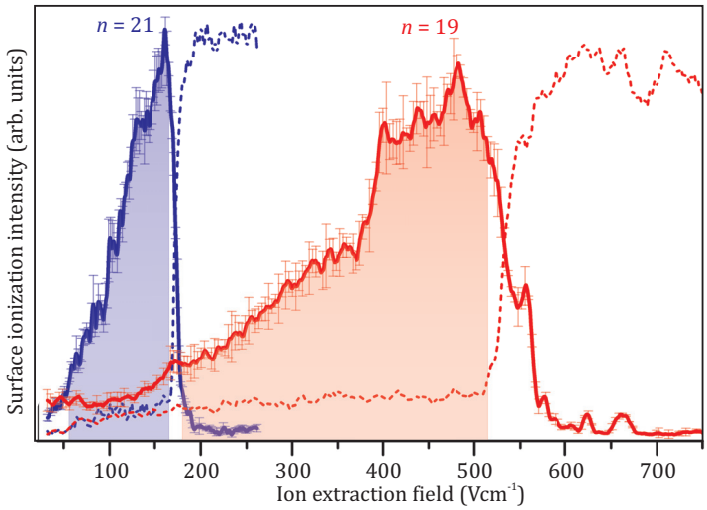

Figure 3.9: Integrating surface ionization profiles (shaded area) for population of the $(nd2)_1$, $n = 21$ & 19 Rydberg states incident on the n-type (phosphorous doped ($N_D = 3.00\times10^{14}$ cm^{-3})) doped silicon surface, recorded as a function of applied ion-extraction field. The dashed lines show the field ionization signal used to normalize.

integrated surface ionization profiles of a gold surface since the metal surface is the equivalent to the infinite dopant concentration limit.

The ion detectability is used as a tool to compare many surface ionization profiles quantitatively and also qualitatively in the following sections.

3.3.1 Effect of dopant type

In order to investigate the effect of dopant-type, p- and n- type doped Si surfaces at equivalent dopant densities were selected to avoid the possible effects of different dopant density. Data were collected for an initial population of $(nd2)_1$ H_2 Rydberg states, for the range of principal quantum numbers $n = 17 - 21$, using the same experimental methodology outlined in the chapter 2. The ion detectabilities (see section 3.3) for the p- and n- type doped Si surfaces are shown with their error bars in Fig. 3.10. The main source of uncertainty arises from the integration of the surface

ionization profiles, where the lower and upper bounds are estimated by calculating the area under the lower and higher error bars of the surface ionization profiles (as shown in Fig. 3.9).

Figure 3.10 shows some important features in this study: (1) p-type Si surfaces show higher ion detectability than n-type Si surfaces, (2) the ion detectability for high-n Rydberg states is greater than for low-n Rydberg states, (3) the difference between the high-n and low-n Rydberg states, ion detectability decreases as dopant density increases, and (4) ion detectability for both p- and n- type doped Si surfaces decreases with increasing their dopant density. The above first two observable variations are purely depending on the dopant type, and are explained here. The rest of the above recognizable differences depend on the dopant density, and will be described in the next section (see section 3.3.2).

As expected from the discussion of the surface charge distribution of p- and n- type doped Si surfaces above (as shown in Fig. 3.5 (b)), the experimental results clearly show that the ion detectabilities of the p-type doped Si surfaces are greater than those from the n-type doped Si surfaces (except for the $n = 19$ Rydberg states at $N_{\rm D} \approx 10^{15}$ cm^{-3}). This is attributed to the delocalized positive charge of a p-type doped Si surface repelling the H_2^+ ions away from the surface, more than the positive (but more localized) regions of the n-type surface. However, it is less straightforward to explain the observed variation of ion detectability with principal quantum number as shown in Fig. 3.10 for both p- and n- type doped Si surfaces. Note also the scale on the y axis; the variation of ion detectability with principal quantum number decreases with increasing dopant density, such that at the highest dopant density of 10^{19} cm^{-3} the ion detectability is less than half of that at the lowest dopant density studied at 10^{14} cm^{-3}. The effect of dopant density on ion detectability will be discussed in the next section.

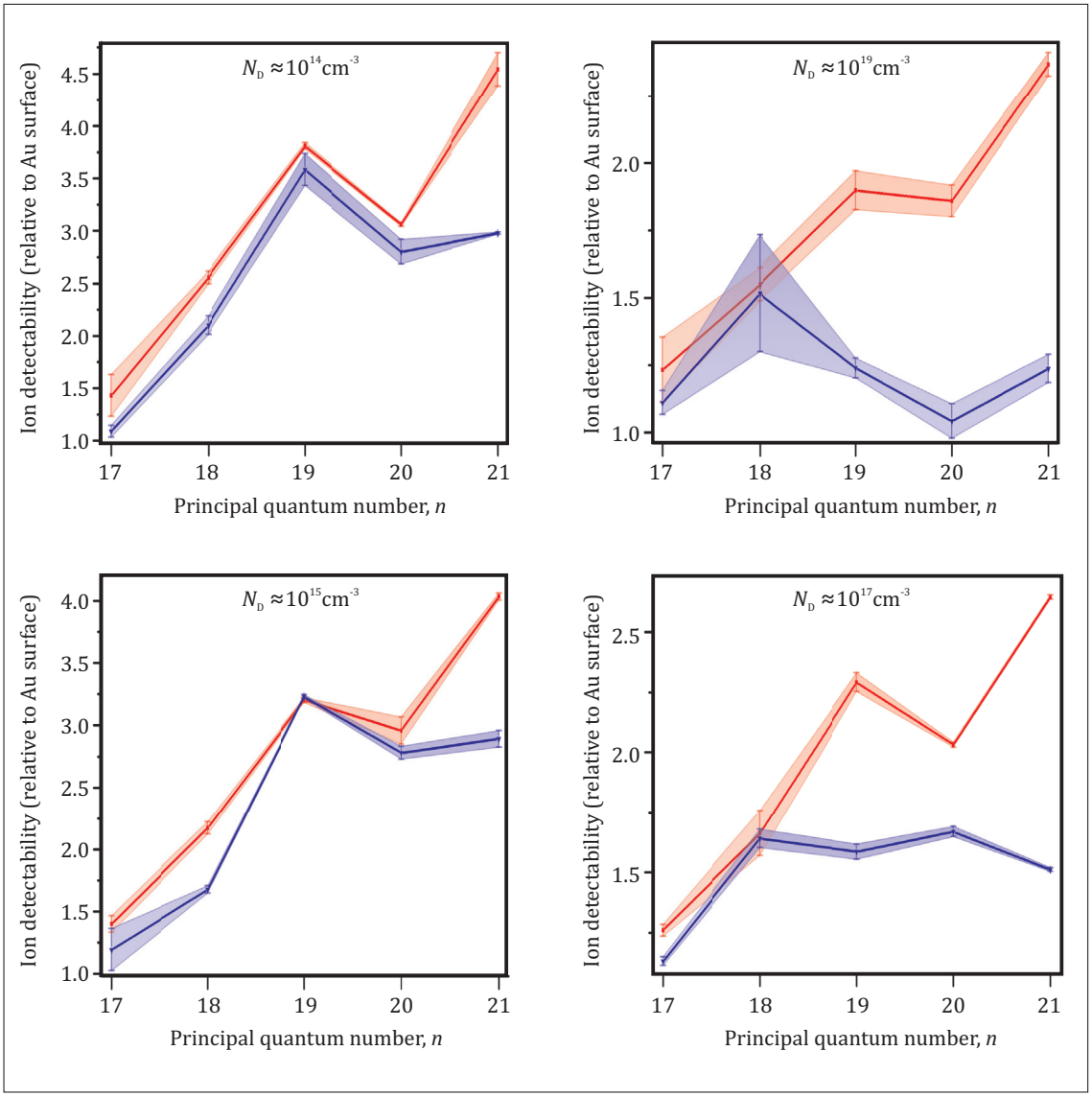

Figure 3.10: Ion detectability for population of the $(nd2)_1$, $n = 17-21$ Rydberg states incident on the p-type (red line) and n-type (blue line) doped Si surfaces, recorded as the function of the principal quantum numbers. The shaded area joins the upper and lower error bar points for each principal quantum number, and the solid line was connected to the mean values.

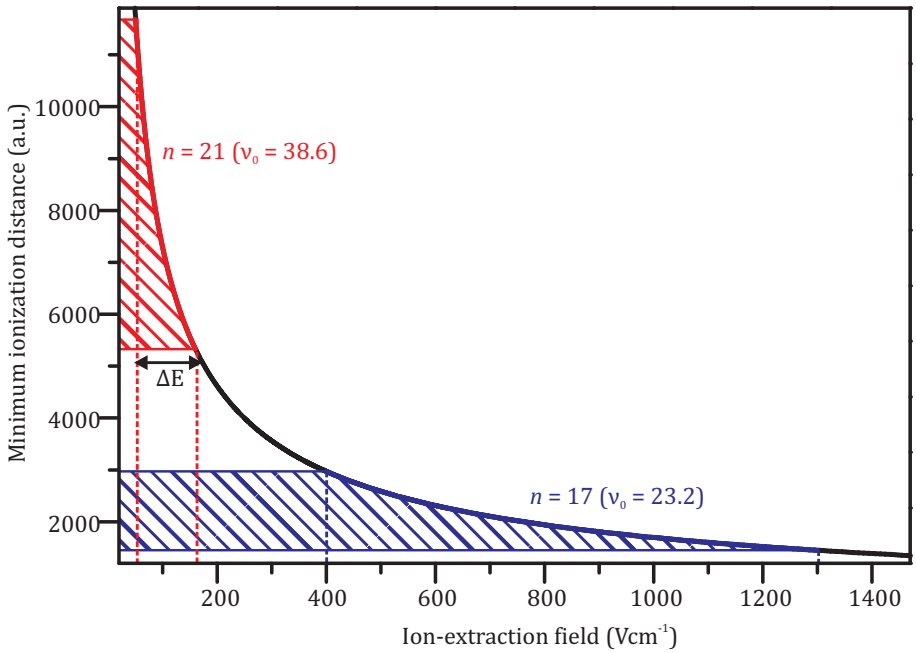

Figure 3.11: Illustration showing how the minimum ionization distance changes as a function of applied electric field, which is based on the Eq. 1.37; the shaded area represents the integrated area of the ion signal.

The increase of ion detectability with principal quantum number can be attributed to the dependence of the minimum ionization distance on extraction field, given by Eq. 1.37. Figure 3.11 shows a plot of the minimum ionization distance as a function of electric field. It can be seen that the gradient at lower fields is significantly larger than at high fields. Treating the effect of the surface dopant charge fields as an uncertainty of the electric field experienced by the molecule, it is possible to see that the range of detected distance introduced by the dopant charges is much larger at lower applied extraction fields, because the dopant charge field is a greater proportion of the applied electric field. Thus the increase in detected ion-fraction is greater for high-n values which have an onset of ion signal at low ion-extraction field.

On the other hand, the effect of the surface dopant charge field is noticeably smaller at higher ionization distance than at shorter ionization distance (as show in Fig. 3.6), so that the effect of surface dopant charges on detected ion signals of the higher-n

Rydberg state may be expected to be considerably smaller than detected ion signals of the lower-n Rydberg state. However, the former effect due to the gradient of the applied ion-extraction field against the ionization distance dominates, and the detected ion-fraction is greater for high-n Rydberg states than low-n Rydberg states.

3.3.2 Effect of dopant density

The effect of the different (p- and n-) types of Si surfaces on the ion detectability was discussed in the previous section 3.3.1, and a qualitative argument based on the dopant charges introduced by the dopant atoms at the surfaces accounted qualitatively for the experimental observations. In this section, the effect of varying the dopant density of the p- and n- type doped Si surfaces will be considered. The dopant density determines the mean dopant spacing (λ) between the adjacent dopant atoms, *i.e.* the mean dopant spacing decreases with increasing dopant density (see Eq. 2.12). Therefore, in terms of the surface dopant charge model discussed in section 6.3.2, the size of the '*unit cell*' of the delocalized surface charge and the point charge of opposite sign (representing the dopant atom) becomes smaller when increasing the dopant density. This change in the period of the charge distribution at the surface should have a noticeable effect on the ion detectability given that the corresponding surface dopant charge field sampled by the Rydberg states and positive ion will be significantly different.

Figure 3.12 shows the ion detectability for the surface ionization of the H_2 Rydberg molecule incident on various dopant densities of p-type boron doped Si surfaces with N_D = 9.00×10^{14} cm^{-3}, 5.65×10^{15} cm^{-3}, 2.90×10^{16} cm^{-3}, 6.21×10^{17} cm^{-3} and 2.10×10^{19} cm^{-3}. The error bars are also shown in the figure, and the shaded areas correspond to the values bound by the upper and lower limits of the error bars. The mean values are connected to solid lines to help the analysis of different Si surfaces, and clearly show significant differences in the overall ion detectability between each

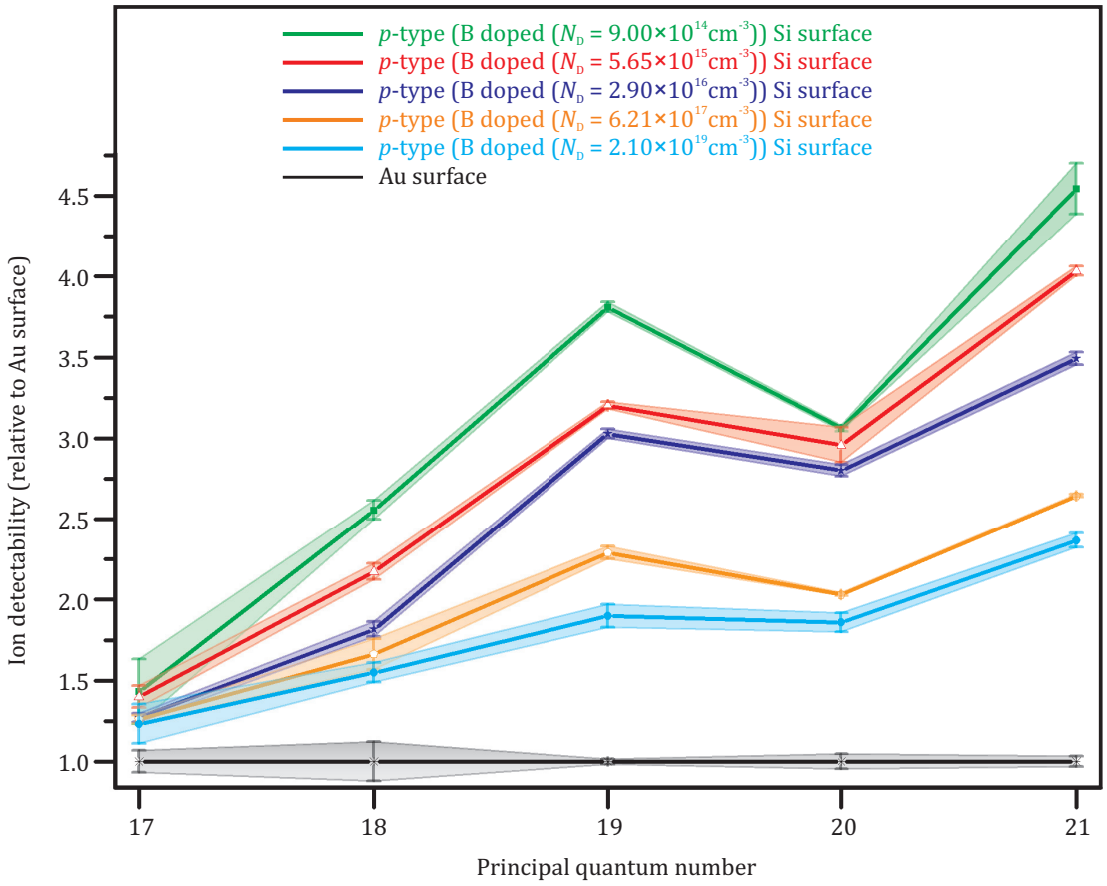

Figure 3.12: Ion detectability for population of the $(nd2)_1$, $n = 17 - 21$ Rydberg states incident on the boron doped $N_D = 9.00\times10^{14}$ cm^{-3}, 5.65×10^{15} cm^{-3}, 2.90×10^{16} cm^{-3}, 6.21×10^{17} cm^{-3} and 2.10×10^{19} cm^{-3} Si surfaces, recorded as the function of the principal quantum numbers. The shaded area joins the upper and lower error bar points for each principal quantum number, and the solid line is connected to the mean values.

surface of different dopant density.

Figure 3.12 shows that the lower dopant density p-type doped Si surfaces have noticeably higher ion detectability compared to the higher dopant density Si surfaces. This effect can be rationalized by considering the dopant charge distribution and the changes of the dielectric constant (ϵ_{Si}) with dopant density. Once again, the ion detectability from each surface increases significantly with principal quantum number of the Rydberg state.

There is a further factor that may contribute to the greater sensitivity of high-n Rydberg states to the change in dopant density. As the dopant density increases, the frequency of the charge variation at the surface also increases, and the exponential surface potential decay length in the x, y plane is dependent on the surface charge distribution. This point is discussed in detail in section 6.3.2. Furthermore, the exponential surface potential decay experienced by the higher-n Rydberg states covers a broader region than the low-n Rydberg states, as shown in Fig. 3.6.

The mean dopant spacing (λ) between two neighbouring dopant atoms in a p- or n- type doped Si surface measured by STM depends on the dopant density ($N_{\rm D}$) (see Eq. 2.12) [100, 101, 107]. For large dopant spacing, low dopant density, the positive and negative charges are widely distributed, and the Rydberg molecules are ionized only at the positive '*probe*' area. The principal quantum number controls the distance that the H_2^+ forms above a positive charge island; typically surface ionization occurs at $\approx 3.1\ \nu_o^2$ a.u. from the surface. H_2^+ formed far above the surface, from a higher-n Rydberg state, is rapidly repelled and this effect increases the detection probability. On the other hand, H_2^+ produced near the surface can interact with negative charge islands as it leaves the surface, reducing the detection efficiency (as shown in Fig. 3.13). Therefore, the ion detectability of the higher-n Rydberg states is noticeably higher than the lower-n Rydberg states. However, in the case of a small mean dopant spacing of both p- and n- type doped Si surfaces, these will tend to behave as conductors because they are heavily doped with donor/acceptor atoms with a distribution of positive and negative dopant charge islands arranged more closely together. Therefore, the horizontal area (parallel to the surface) sampled by the H_2^+ ions become effectively more neutral, at high dopant density, and the ion detectability difference between the higher-n and lower-n Rydberg state is negligible. Furthermore, the ion detectability variation between the higher-n and lower-n Rydberg states also

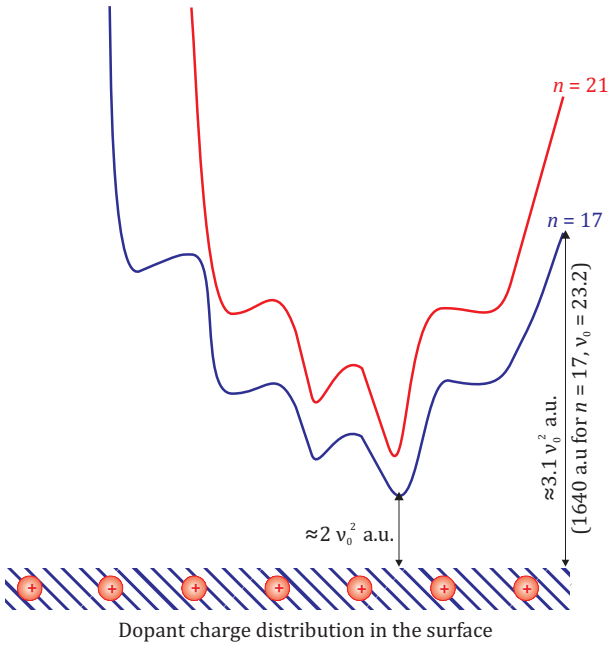

Figure 3.13: Illustration of the higher-n and lower-n H_2^+ ion trajectories above the surface for an ion-extraction field which is enough to pull the ion far from the surface.

arises from the variation of the minimum ionization distances which is related to the ion-extraction field, as explained in previous section 3.3.1.

Having studied the effect of dopant density on the ion detectability of Rydberg states for the p-type Si surface, it will be of interest to find whether the ion detectability variation with dopant density for a n-type Si surface also behaves in the same way as p-type doped Si surfaces. The polarity of the delocalized surface charges and point charges is the opposite of those of p-type Si surfaces. Figure 3.14 shows the ion detectability for the surface ionization of H_2 Rydberg states incident on n-type doped Si surfaces of various dopant densities. First, it can be noted that, as shown in section 3.3.1, the ion detectability for n-type doped Si surface is lower than that of the p-type doped Si surface with the same dopant density.

Like the p-type surfaces, the n-type Si surfaces show that ion detectability increases with decreasing dopant density. As explained above, the dielectric shielding of the

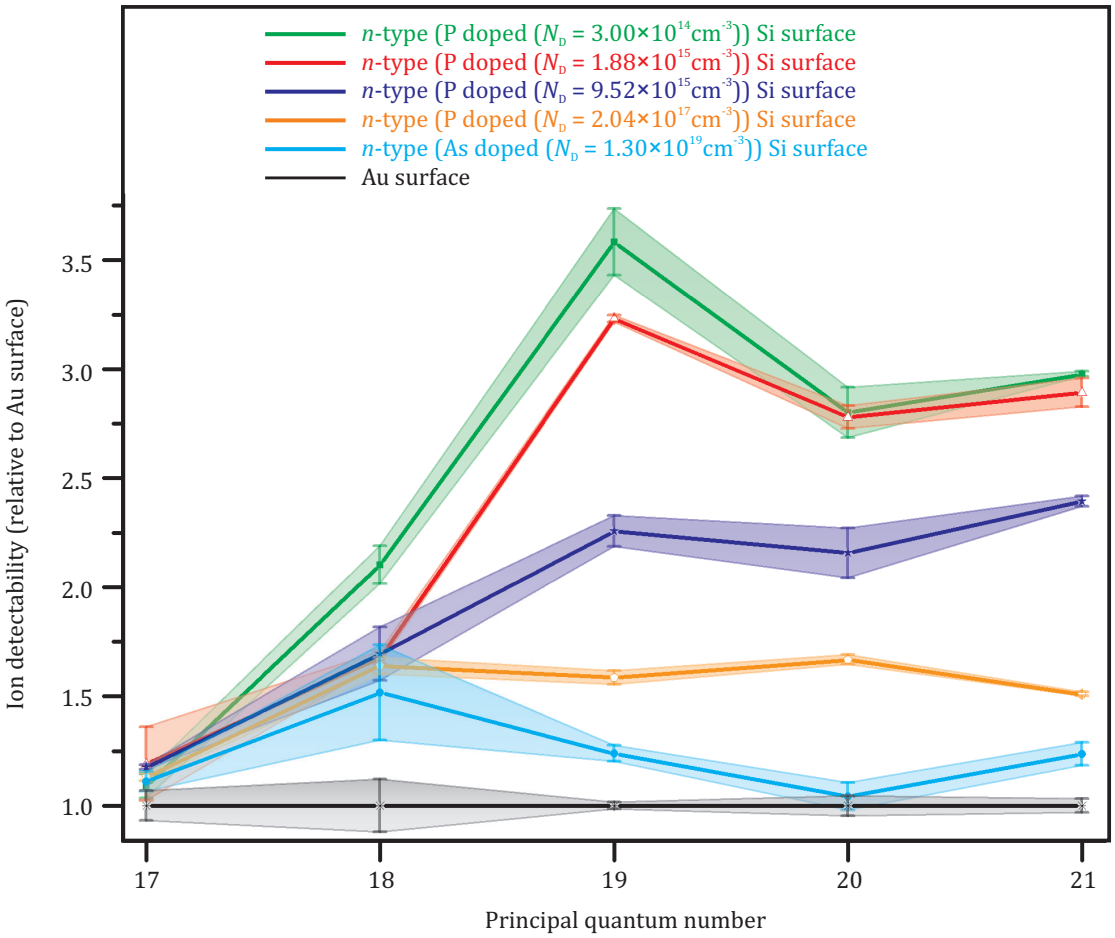

Figure 3.14: Ion detectability for population of the $(nd2)_1$, $n = 17-21$ Rydberg states incident on the phosphours doped $N_D = 3.00\times10^{14}$ cm^{-3}, 1.88×10^{15} cm^{-3}, 9.52×10^{15} cm^{-3}, 2.04×10^{17} cm^{-3} and arsenic doped $N_D = 1.30\times10^{19}$ cm^{-3} Si surfaces, recorded as the function of the principal quantum numbers. The shaded area is linked up with the upper and lower error bar points for each principal quantum number, and the solid line is joined to the mean values.

image-charge effect is relatively small and does not fully account for the significant change in ion detectability. Instead, the increase of ion detectability can be attributed to the small local areas of the positive charge probed by the Rydberg states approaching, and H_2^+ leaving, the surface. The positive charges near the dopant atoms will promote both ionization and subsequent ion detection, such that the Rydberg states effectively only probe the areas of positive potential. As the dopant concentration increases, the field experienced by the Rydberg states decreases due to the increased frequency of charge variation at the surface leading to a more rapid decay with x and y distance (see section 3.2.2). Thus, the overall ion detectability decreases with increase dopant density of both *p*- and *n*- type doped Si surfaces.

In summary, the overall ion detectability of the doped Si surfaces highlights the combined effect of the following factors: (i) the charge distribution due to the dopants, which depends on the dopant type and dopant density of the Si surfaces, and (ii) the β-factor (to a smaller effect).

3.4 Conclusions

This chapter has presented a study of the surface interaction and charge transfer process of H_2 Rydberg molecules at various doped Si surfaces. The behaviour of Rydberg states with different principal quantum number was studied and the ionization distance of the Rydberg states scales approximately with 3.1 ν_o^2 a.u. The experimental surface ionization profiles also exhibit the sharp resonance peaks previously discussed for a metal surface and are attributed to the level crossings of the Rydberg states with different ion core rotattional states, which are resonant at particular ion-extraction fields.

So far, relatively simple qualitative arguments based on the surface dopant charges on

the surface and mainly their effect on ion detection has been discussed. In chapter 6, this effect will be modelled theoretically and a full discussion addressing the effect of dopant type and dopant density on both the ionization distance and ion detection probability will be presented there.

To compare the surface ionization profiles of multiple Si surfaces, the ionization profiles are integrated as a function of applied electric field, and the integrated values, referred to as the ion detectability, are used for direct comparison. For similar dopant density, the ion detectability is higher for a p-type doped Si surfaces compared with a n-type doped Si surface. The p-type doped Si surfaces have large regions of positively dopant charge that can repel the H_2^+ ion whereas n-type doped Si surfaces have large regions of negatively dopant charge that attract the ions. As the dopant density increases, the dopant spacing at the surface decreases. The area sampled by the H_2^+ ion becomes effectively more neutral, and the dielectric constant also increases such that detected signal decreases and tends to that of Au surface. Furthermore, the ion detectability, for the case of large mean dopant spacing of both p- and n- type doped Si surfaces has shown a more significant variation between the lower and higher-n Rydberg states than the small mean dopant spacing (higher dopant density) of both p- and n- type doped Si surfaces.

In summary, for nearly all cases of dopant concentration there is a tendency for the ion detectability to increase with principal quantum number. But, that tendency is less marked for the n-type than the p-type and hence as the dopant concentration increases (which always tends to decrease this effect), the effect falls off more quickly for the n-type than the p-type. This is all explained by the effect of positive charges having the gratest effect, and for the lowest applied fields.

Chapter 4

Surface ionization of molecular hydrogen Stark states

4.1 Introduction

Rydberg molecules have a strong dipole coupling with an externally applied electric field, which is generally important in the study of Rydberg surface interactions. At zero field, the angular momentum of a Rydberg molecule gives rise to degenerate energy levels, and as they are subjected to an applied field, they are shifted from their initial energy, and the degeneracy is split; this is called the Stark effect (see section 1.4). The Stark effect on molecular Rydberg states has been well studied both theoretically and experimentally [72, 93, 108, 109]. On the theoretical side, Stark maps can be generated following the energy matrix diagonalization of the Stark Hamiltonian with a basis set of the form $\{N^+, n, l, J, M_J\}$ [93, 110]. The resultant energy levels of the Stark states have also been calculated by high order perturbation theory [111–113]. On the experimental side, there have been a number of spectroscopic studies carried out on the Stark effect of molecular Rydberg states [49, 71, 72, 109, 110, 114–116]. The Stark effect on the Rydberg energy levels just below the $N^+ = 0$ ionization threshold limit

of H_2 has been initially reported by Glab and Hessler [117]. For non-hydrogenic atoms (*e.g.* He) or molecules (*e.g.* H_2), the Stark states are coupled leading to avoided level crossings between Stark states in the presence of electric field strengths beyond the Inglis-Teller limit [11], as shown in Fig. 1.9.

In the previous chapter (chapter 3), it was shown that the surface ionization profiles under field-free conditions are strongly dependent on the principal quantum number due to the variation of the molecule-surface separation where surface ionization takes place, and surface ionization profiles behave differently for differently doped Si surfaces. This chapter is extended to study the interaction of different H_2 Stark states belonging to the same n manifold, incident at the doped Si surfaces in the presence of a homogeneous electric field. An electric field is applied across the ionization region with a dual purpose, *i.e.* extracting the ions and also assigning the Stark field. The polarization of the Rydberg electron wavefunction is altered with different Stark states, opening up a new route to investigate how the surface ionization profiles of each Stark state are affected by the nature of the target surfaces, *e.g.* the dopant type or concentration. Furthermore, the Stark effect of the molecular Rydberg states may lead to further information about the core charge distribution.

4.2 Ion detected surface ionization profiles

A similar experimental setup to that described in chapter 2 was used to investigate the surface-induced ionization profiles for population of $n = 17$, $(nd2)_1$ Rydberg states, incident on the doped Si surfaces in the presence of a Stark field. The Stark field is formed by applying a high voltage to the surface with the extraction plate at a less positive voltage. For all the experimental studies carried out in this chapter the field was typically maintained at $+600\ \mathrm{Vcm^{-1}}$ (static field) with a positive potential applied to the surface, and the ion-extraction pulsed field is applied using a potential on the

mesh grid as in section 2.1.6. The charging or discharging effect on the semiconductor surfaces could be ignored (more details in section. 2.1.6) in the presence of the fixed Stark field. The ionization profiles are compared using the ion detectability method described in section 3.3.

4.2.1 Surface ionization of $n = 17$ Stark states

In the presence of the static Stark field, the Rydberg states for a particular n manifold are no longer degenerate, and the manifold is split into different energy level states. The parabolic quantum numbers (n_1, n_2 and m_l) are the best quantum numbers to describe the Stark states. The effective parabolic quantum number ($k = n_1 - n_2$) physically stands as a measure of the projection of the charge distribution along the field axis when Stark states are considered as fixed dipoles. This effective parabolic quantum number is only strictly defined for the hydrogen atom, but it is approximately a good quantum number for the H_2 molecule especially at high field. The effective parabolic quantum number gives a useful indication of the orientation of the electronic distribution of the Rydberg states with respect to the field direction, *i.e.* whether the dipole moment alignment is parallel or anti-parallel to the applied field [118]. Red-shifted Stark states occur when the dipole moment alignment is parallel to the applied field, the k value is negative, and the electronic distribution is oriented towards the surface. Ionization of these Rydberg molecules would be expected to occur at larger surface separation. Extreme blue-shifted Stark states occur when the dipole moment is aligned anti-parallel to the applied field (*i.e.* the electronic distribution is oriented in the vacuum direction) and the k value is positive. Ionization would be expected to occur closer to the surface. Therefore, red- and blue- shifted Stark states are seen to have a different surface ionization profile and different field ionization threshold.

In the homogeneous low field limit, the energy level splitting arises from the coupling

between the orbital angular momentum, l, of the Rydberg electron and the rotational angular momentum ($N^+ = 2$) of the H_2^+ ionic core. These low field Rydberg states are described by using the coupled states $|N^+lJM_J\rangle$ [95]. At high field strength, the angular momenta becomes decoupled so that the Stark states can effectively be characterized by a linear combination of decoupled states $|N^+M_{N^+}lm_l\rangle$ [95]. There are five states for each k value that can be divided into two different sets of degenerate states (a and b), which are better resolved at higher field strength. Three higher energy states (a) correspond to $m_l = 0, \pm 1$ components having an admixture of $N^+ = 2$, np character; the two lower energy states (b) correspond to $m_l = \pm 2$ components having no admixture of states with $l < 2$ ($l \geq m_l$) [72].

For the a states, the high-field end of the surface ionization profiles shows a high-field cut-off due to field-induced rotational autoionization occurring at, or close to, the field at which the $N^+ = 2$ energy level crosses the classical field ionization threshold limit for the $N^+ = 0$ states. The b states are more stable with respect to field ionization so that they show surface ionization signal at fields considerably higher than the a state for a matching k value [72]. In recent experimental studies, a metal surface was investigated for two different near-degenerate (a and b) levels for some of the k states [72]. However, this chapter only deals with the a Stark manifolds because the b Stark manifolds could not be optically detected under all conditions.

A linear Stark effect is observed until, at high fields, the adjacent Stark manifolds converge. If a pair of adjacent Stark manifolds having the same core rotational angular momentum (*i.e.* $N^+ = 2$) bisect each other, then the Stark splitting avoids that level crossing via the coupling between states with the same $|m_l|$ [48, 119–121], resulting from the presence of non-Coulombic terms in the Hamiltonian [112, 122]. These avoided crossing are more noticeable for the $m_l = 0$ than for the $|m_l| = 1$ states [118]. The minimum energy separation at an avoided crossing is very small for b state which

is not strongly coupled with other states; there is a high probability for the avoided crossing to be navigated diabatically when the electric field is increased. Higher-n Rydberg states have revealed less interaction at level crossings. Hence, the probability of adiabatic passage to ionization will increase with $|m_l|$ and n.

4.2.2 General features of the surface ionization profiles with population in the Stark field

All the experimental studies were carried out at a Stark field strength of 600 $\mathrm{Vcm^{-1}}$. The surface ionization profiles for a range of effective parabolic quantum numbers $k = -14$ to $+16$ of the H_2 Rydberg molecule incident at the n-type arsenic doped $N_\mathrm{D} = 1.30 \times 10^{19}$ $\mathrm{cm^{-3}}$ were recorded as a function of an applied ion-extraction field, and is shown in Fig. 4.1. The profiles are normalized with respect to the integrated field ionization signal as discussed in section 2.3.2. The error bars corresponding to the data points are also indicated.

The surface ionization profiles shown in Fig. 4.1 have experimentally reproducible sharp resonance features, which are an enhancement in the surface ionization (or detection) probability. These sharp resonances arise from the energies of the populated $N^+ = 2$, $n = 17$ Rydberg states crossing with the higher-n Stark manifold ($n = 22 - 25$) belonging to the $N^+ = 0$ series. Following such a level crossing, the electron wave function of that specific Stark state will be shifted to show a higher-n $N^+ = 0$ character. These states are ionized further from the surface and require lower ion-extraction field to extract the H_2^+ ion. It has been shown previously that the surface ionization signal is almost entirely due to such level crossing effects [72]. Therefore, the onset of the surface ionization profile with the effective parabolic quantum number, k, not only depends on the minimum ionization distance (D_min) of the initially populated states, but also it depends on the minimum ion-extraction field at which the level

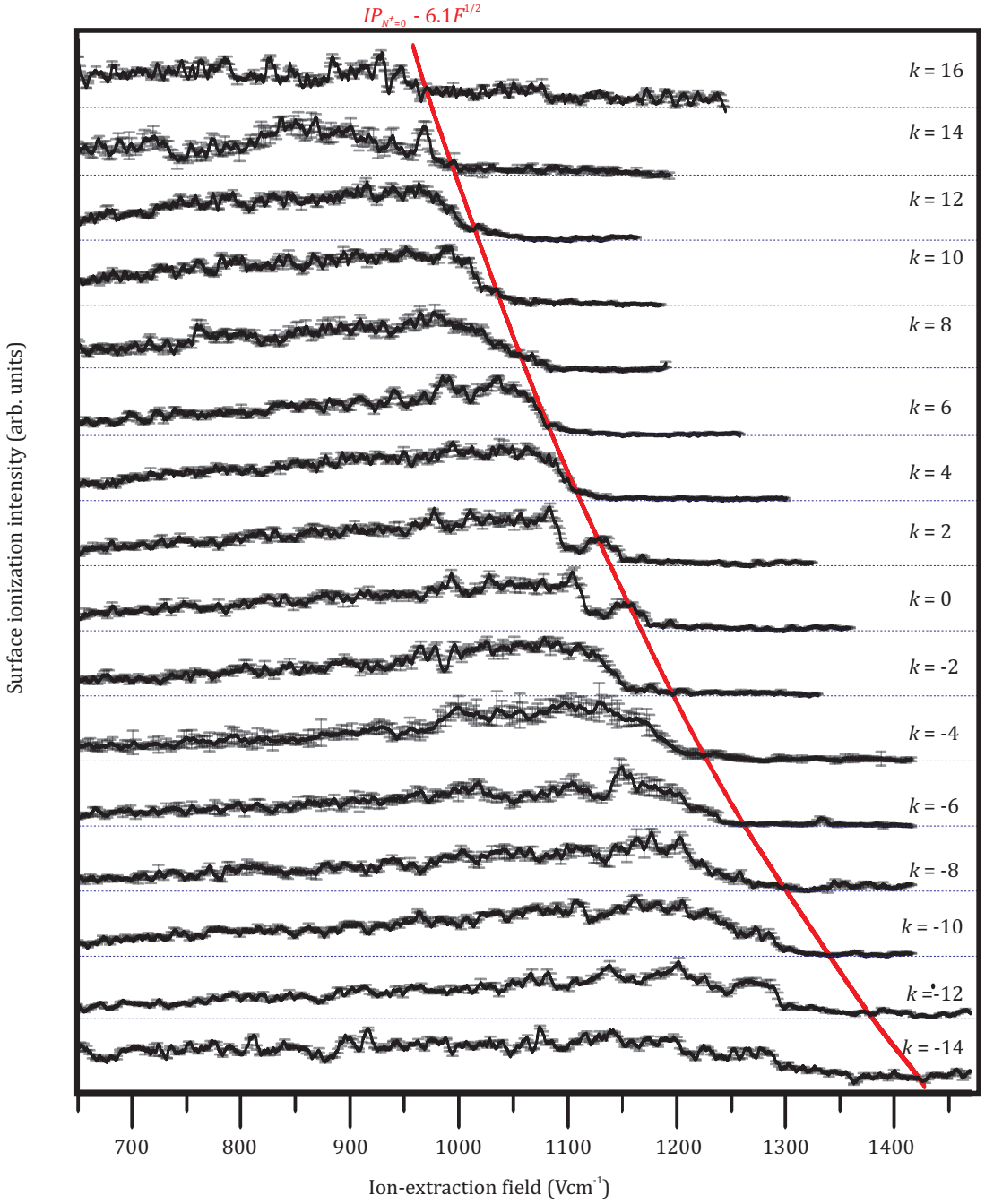

Figure 4.1: The surface ionization profiles for the red- to blue- shifted $n = 17$, $N^+ = 2$ Stark states (Stark field at 600 Vcm^{-1}) of the H_2 Rydberg molecule incident at the n-type arsenic doped $N_D = 1.30 \times 10^{19}$ cm^{-3} Si surface, recorded as a function of the ion-extraction field (black line) and classical ionization threshold limit for the $N^+ = 0$ channel also illustrated (red line).

crossing occurred between the $N^+ = 2$ and $N^+ = 0$ Rydberg states. Figure 4.1 clearly shows that the surface ionization profiles at low ion-extraction field generally increase from red-shifted (negative-k) to blue-shifted (positive-k) Stark states due to this level crossing effect between the $N^+ = 2$ and $N^+ = 0$ characters, *i.e.* the first level crossing occurs at lower field for the blue-shifted states.

The character of the initially excited $n = 17$, $N^+ = 2$ states and the neighbouring n ($n = 16$ and $n = 18$), $N^+ = 2$ Stark manifold levels will adiabatically follow a level switching between red- and blue- shifted character, taking a near-horizontal path across the Stark manifolds as the field rises. This behaviour may facilitate population of levels, which are metastable with respect to field-induced autoionization. Nevertheless, there is a fairly sharp cut-off for all levels when the field reaches the classical field-ionization threshold for the $N^+ = 0$ channel. Above this threshold, any transfer from $N^+ = 2$ to $N^+ = 0$ results in the population of a state that rapidly ionizes.

The electronic distributions of the negative-k red-shifted Stark states are oriented towards the surface. Therefore, the charge transfer process might be expected to be faster for the red-shifted Stark states and the surface ionization profiles for the surface-oriented red-shifted Stark states would be detected at considerable lower ion-extraction fields compared to the vacuum-oriented blue-shifted Stark states. This behaviour is clearly observed in the experimental study of the H atom system [123]. However, in the case of the H_2 molecule, the behaviour is dominated entirely by the $N^+ = 0 - N^+ = 2$ level crossings. Once population is transferred to the $N^+ = 0$ manifold there will be many avoided crossings between red- and blue- shifted states as the molecule approaches the surface, and the polarization is lost [68, 72]. Therefore, the ionization profiles of red- and blue- shifted Stark states show nearly similar intensity to the surface ionization profiles observed in the previous experimental studies [72]. In addition, $N^+ = 0$ Rydberg series are also expected in this spectral region, but they

are not observed in these experimental studies, because predissociation processes may be occurring before $N^+ = 0$ field ionization [98].

4.2.3 Comparison between Au and Si surfaces

The previous section clearly explained the fact that the energy levels of $n = 17$ Rydberg states belonging to the $N^+ = 2$ series can be shifted upward (blue-shifted) and downward (red-shifted) in the presence of the static Stark field and this energy level shift originates from the orientation of the Rydberg electron distribution. There is an interesting question arising from this Stark splitting, *i.e.* whether the surface ionization profiles of the red- and blue- shifted Stark states depend on the nature of the target surface, and whether the dependence on target surface is different for red- and blue- shifted states. For this study, the surface ionization profiles of the $k = -6$ to $+6$ Stark states of the $n = 17$, $N^+ = 2$ Rydberg states incident on the n-type arsenic doped Si surface are compared with the metal (Au) surface. These surfaces are atomically flat so that the effect of roughness on the surface ionization profiles is negligible. All these Stark states are populated in the presence of a 600 Vcm^{-1} static Stark field and these surface ionization profiles are recorded as a function of the applied ion-extraction field, as shown in Fig. 4.2.

The surface ionization profiles for all Stark states show again a sequence of sharp resonant features (as illustrated in section 3.1). However, the overall ionization profiles behave similarly for all the Stark states meaning that the surface ionization profiles increase with increasing ion-extraction field until they reach the high-field cut-off limit. Each Stark state has a specific direct-field ionization cut-off limit, which is independent of the target surfaces, depending only on the red- and blue- shifted nature of the Stark states. However, at low ion-extraction field, the n-type arsenic doped Si surface shows slightly higher surface ionization efficiency than the metal surface for all the Stark

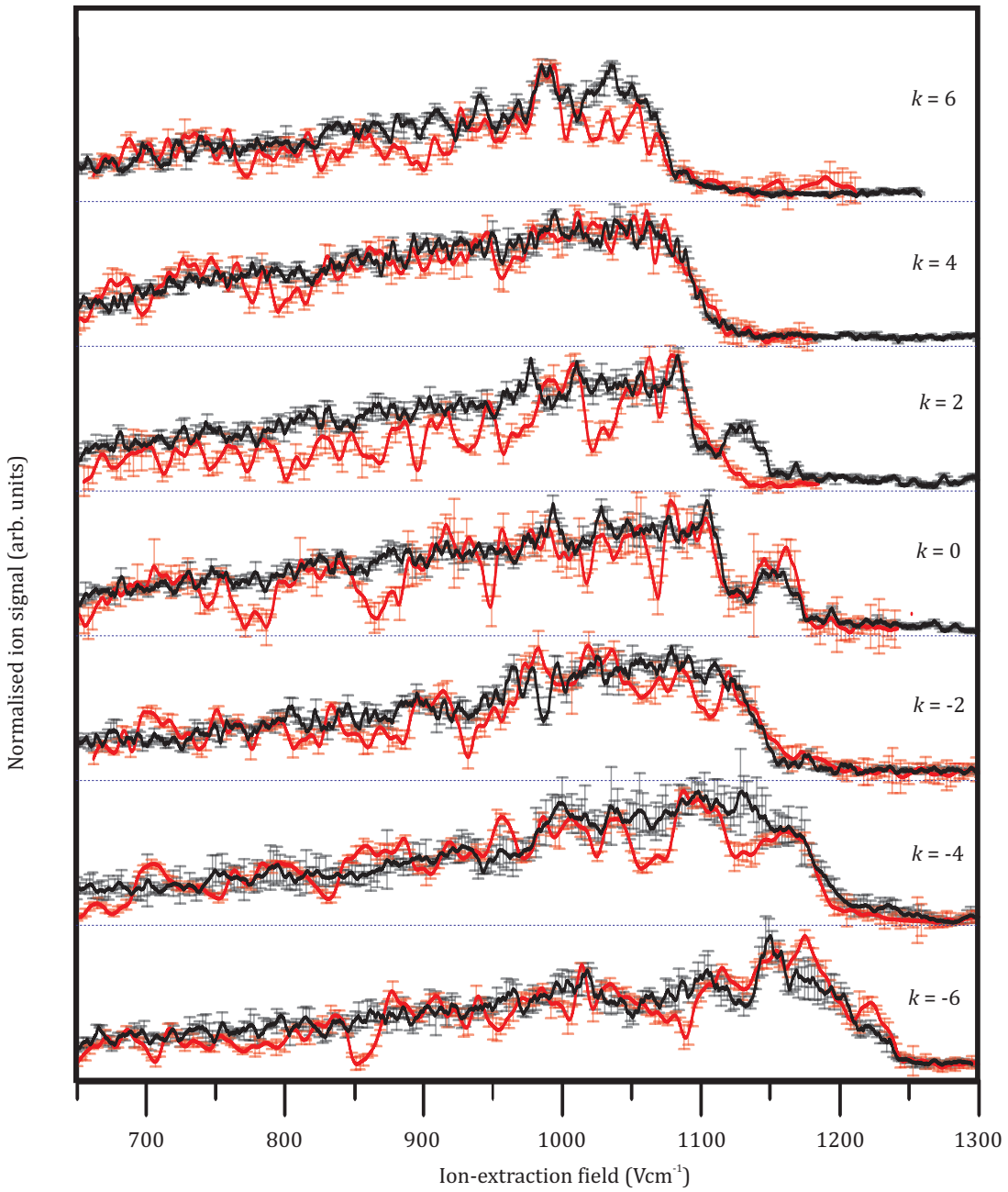

Figure 4.2: Surface ionization profiles for the blue- and red- shifted $n = 17$, $N^+ = 2$ Stark states (Stark field at 600 Vcm^{-1}) of the H_2 Rydberg molecule incident at the n-type arsenic doped ($N_\mathrm{D} = 1.30 \times 10^{19}$ cm^{-3}) Si semiconductor surface (black line) and metal (Au) surface (red line).

states due to the effect of the distribution of the surface dopant charge fields and the electronic shielding effect in the target surface. Furthermore, the Au surface shows sharp dips in its surface ionization profile, which is not seen with the Si surface. This difference may also arise from the surface dopant charge field distribution in the surface layer. An additional repulsive force is produced by the asymmetrically and widely distributed dopant charge fields on the Si surface, which not only changes the ion detection probability and minimum ionization distance (as discussed in section 3.2.2) but also affects the relative intensity of resonances enhancing some resonances not seen (in the '*dips*') for the Au surface. For this reason, the Si surfaces do not show any sharp dips in their surface ionization profiles as these are filled in by additional resonances. Therefore, the variation of the surface ionization profiles for every single Stark state depends on the nature of the target surfaces and the magnitude of the Stark field.

4.2.4 Ion detected surface ionization signal variation for different doped Si surfaces

The previous chapter (chapter 3) clearly shows that the surface ionization profiles of differently doped Si surfaces have significant variation in their ionization profiles (especially at low ion-extraction field) due to the electron shielding effect (β) and the presence of distributed charges in the surface layer due to the dopant atoms. The present chapter deals with the effect of β-factor and surface dopant charge distribution on the surface ionization profiles in the presence of the Stark polarization. The main focus of this study is to investigate the effect of orientation of the electronic wave function on the surface ionization profiles for different doped Si surfaces and to see whether different orientations lead to different dependences on the nature of the surface. For this, the experimental studies were carried out with the $k = -8$ to $+8$

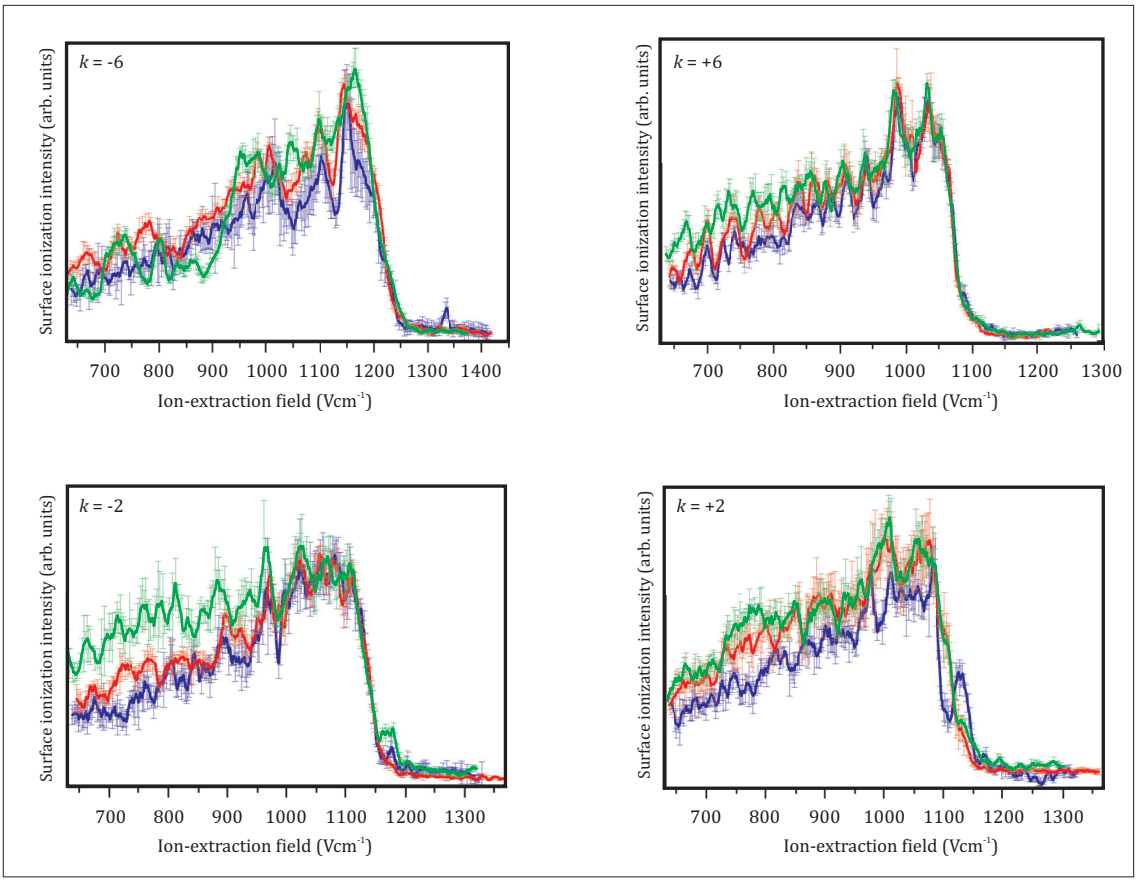

Figure 4.3: A comparison of the experimental surface ionization profiles for the $n = 17$, $N^+ = 2$ Stark states ($k = -6$, -2, +2, and +6) of the H_2 Rydberg molecules incident on the n-type arsenic doped ($N_D = 1.30 \times 10^{19}$ cm^{-3}) (blue line), n-type phosphorus doped ($N_D = 3.00 \times 10^{14}$ cm^{-3}) (green line) and p-type boron doped ($N_D = 2.10 \times 10^{19}$ cm^{-3}) (red line) Si surfaces.

Rydberg states of the $n = 17$, $N^+ = 2$ manifolds incident at the various doped Si surfaces in the presence of a field of 600 Vcm^{-1}. Figure 4.3 shows the surface ionization profiles of selected Stark states ($k = -6$, -2, +2 and +6) of the $n = 17$ manifolds incident at the n-type arsenic doped ($N_D = 1.30 \times 10^{19}$ cm^{-3}), n-type phosphorous doped ($N_D = 3.00 \times 10^{14}$ cm^{-3}) and p-type boron doped ($N_D = 2.10 \times 10^{19}$ cm^{-3}) Si surfaces, recorded as a function of the ion-extraction field.

Figure 4.3 shows that all the surface ionization profiles for the Stark states increase with increasing ion-extraction field until they reach the high-field cut-off limit. The

surface ionization profiles for all the Stark states incident at the p-type (red line) doped Si surface have higher ionization profiles than those for incidence at the n-type (blue line) doped Si surface at low ion-extraction field due to the presence of comparably wider distribution of positive delocalized surface dopant charges present in the p-type doped Si surface than the n-type doped Si surfaces (as discussed in section 3.2.2). These widely distributed positive surface charges increase the minimum ionization distance and increase the acceleration of H_2^+ ions towards the detector and are also likely to enhance the transfer of population at the level crossings or enhance the ionization after the transfer.

For the quantitative analysis of differences with dopant type and density, the relative integrated surface ionization signal (ion detectability) was calculated as described in the section 3.3 and the ion detectability for various Stark states was compared for various doped Si surfaces. The calculated ion detectability variation between different dopant types at similar dopant density of the Si surfaces is illustrated in Fig. 4.4. The primary source of the error bars in Fig. 4.4 arises from the calculation of the integrated upper and lower error bar limit of the surface ionization profiles. Furthermore, a solid line is connected through the mean value of the ion detectability for all the Stark states. Figure 4.4 clearly show that the overall ion detectabilities of the p-type doped Si surfaces are higher than the n-type doped Si surfaces.

As discussed in section 3.2.2, the surface dopant charge fields become smaller when increasing the dopant density due to the smaller distance between adjacent doping atoms so that the surface dopant charge field effect becomes weak, and the detection probability of H_2^+ ions becomes smaller. In addition, the image-charge attraction is reduced with the reduction of the dielectric shielding (β) factor (see Eq. 1.40) [54–56] and this factor is directly correlated with their dopant densities (*i.e.* $\beta \propto N_D$) [99]. Due to reduced image-charge attraction, the resultant H_2^+ ions are easily pushed

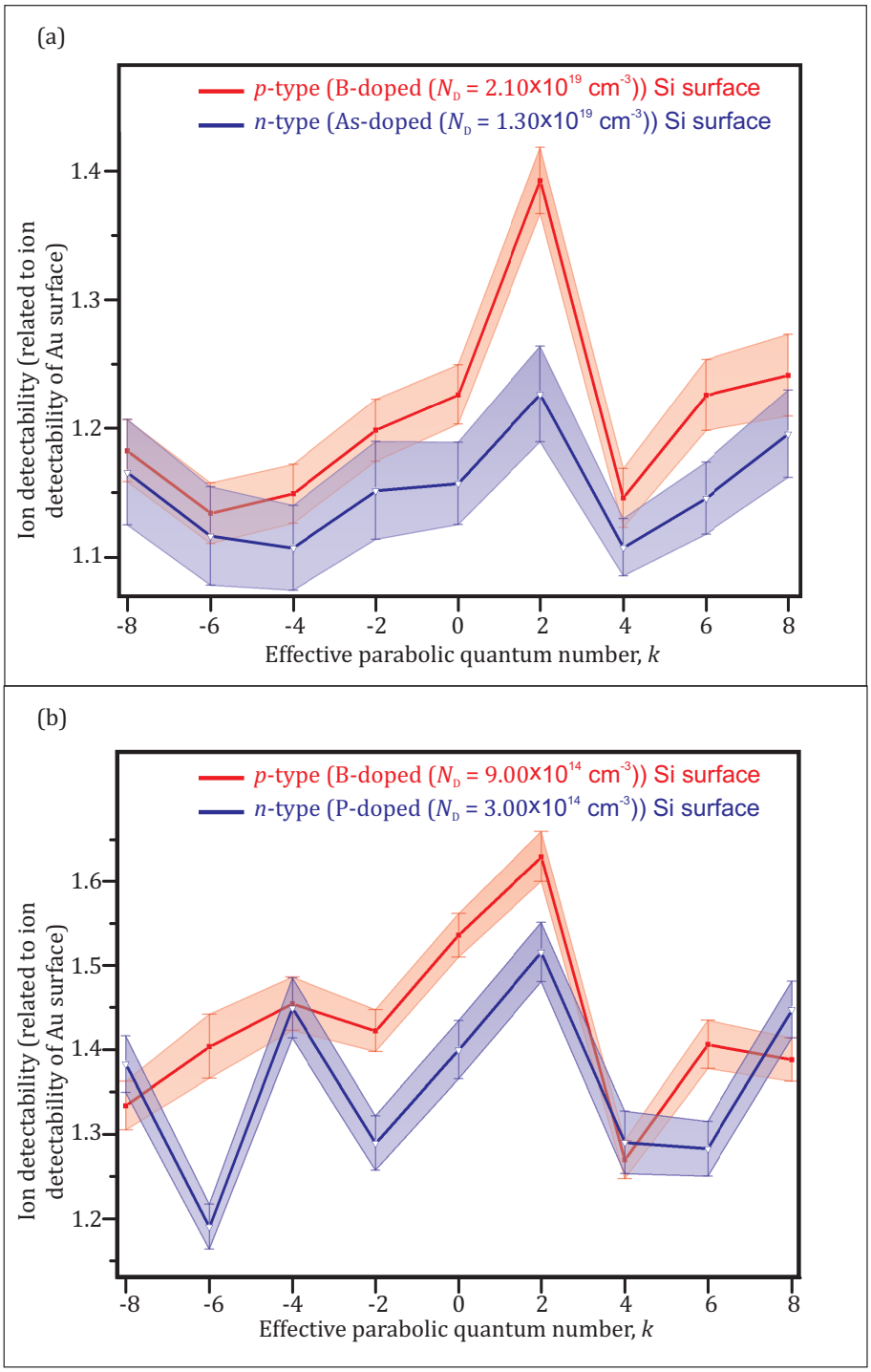

Figure 4.4: The ion detectability variation for the red- and blue- shifted Stark states ($k = -8$ to $+8$) of the $n = 17$ Rydberg manifold incident at the (a) high and (b) low dopant density of the n-type (blue line) and p-type (red line) Si surfaces. The shaded area is linked up with the upper and lower error bar points for each principal quantum number, and the solid line is connected to the mean values.

towards the detector at the lower extraction field. Due to the above reasons, the surface ionization profile is slightly shifted down in both red- and blue- shifted Stark states when the dopant density increases, *i.e.* the red and blue line curves are below the green one, as shown in Fig. 4.3. This effect is seen more clearly in the calculated ion detectability variation for different dopant densities of the *p*- and *n*- type doped Si surfaces as illustrated in Fig. 4.5. Ion detectability for red- and blue- shifted Stark states behaves similarly with different dopant density of *p*- and *n*- type doped Si surfaces. However, the $k = +2$ Stark states show considerably higher and $k = +4$ Stark states show slightly lower ion detectability variations than other Stark states. These unusual behaviors may arise because the surface dopant charges have a greater effect in enhancing transfer at the $N^+ = 2 - N^+ = 0$ level crossings in this case, *i.e.* the observed behaviour depends on the specific details of the transition rates at the level crossings.

The quantitative analysis is used to investigate the effect of delocalised surface dopant charge with red- and blue- shifted Stark states, and they are presented here. As discussed in section 3.2.2, the *p*-type Si surface has a considerably wider distribution area of the delocalized positive surface dopant charge than the *n*-type Si surfaces. These positive surface dopant charges apparently have a greater influence on surface-oriented red-shifted Stark states than the vacuum-oriented blue-shifted Stark states. Therefore, the ion detectability variation between the red- and blue- shifted Stark states becomes more distinguishable in *p*-type Si surfaces than *n*-type Si surfaces. The experimental analysis of the ion detection variation of red- and blue- shifted Stark states for the *p*- and *n*- type doped Si surfaces is shown in Fig. 4.6.

Figure 4.6 clearly shows that ion detectabilities of blue-shifted Stark states are slightly shifted up compared to red-shifted Stark states because blue-shifted Stark states are ionized a little earlier than the red-shifted Stark states as shown in Fig. 4.1. This

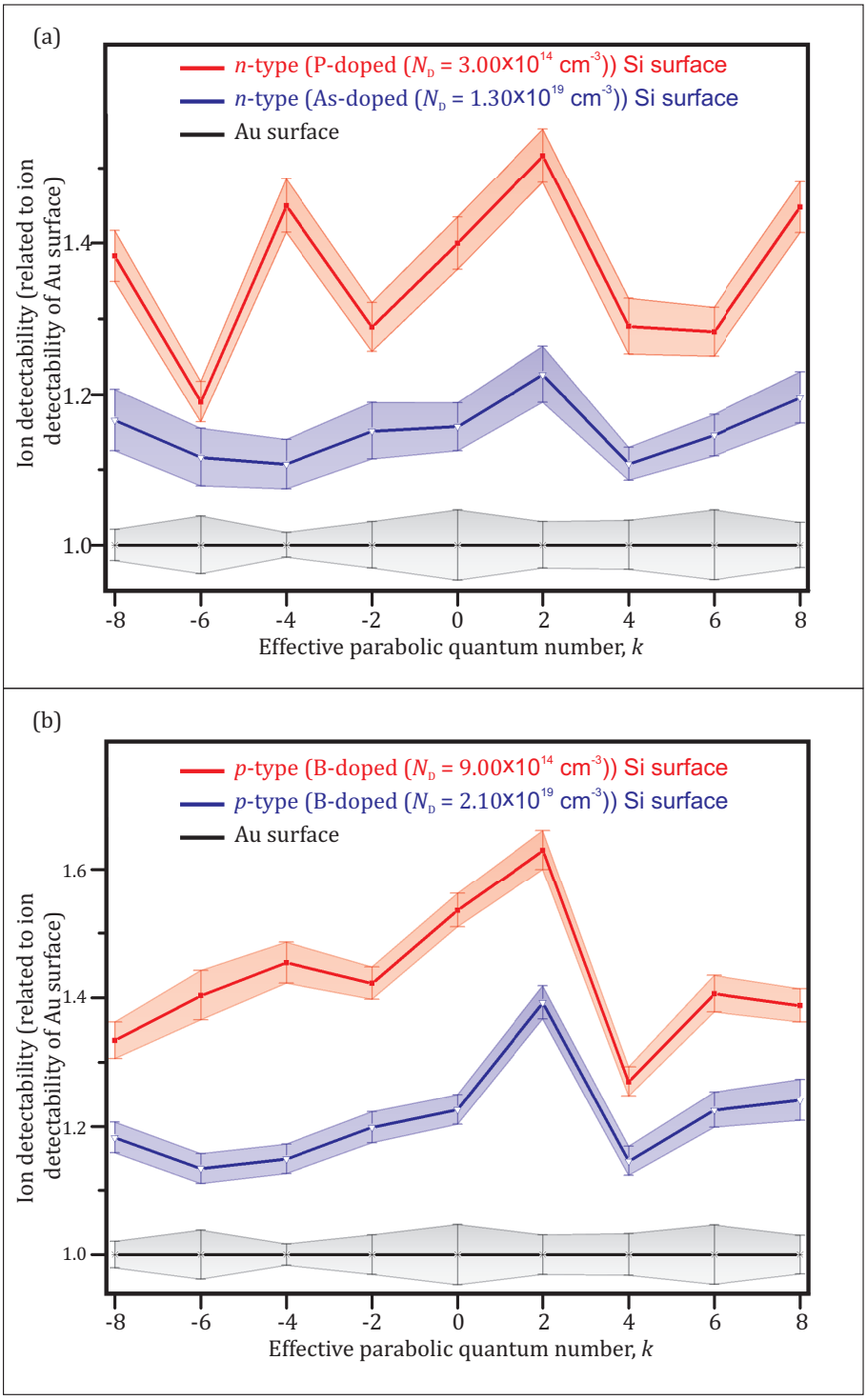

Figure 4.5: The ion detectability variation for the red- and blue- shifted Stark states ($k = -8$ to $+8$) of the $n = 17$ Rydberg manifold incident at the (a) n-type (b) p-type Si surfaces. The shaded area is adjoined the upper and lower error bar points for each principal quantum number, and the solid line is connected to the mean values.

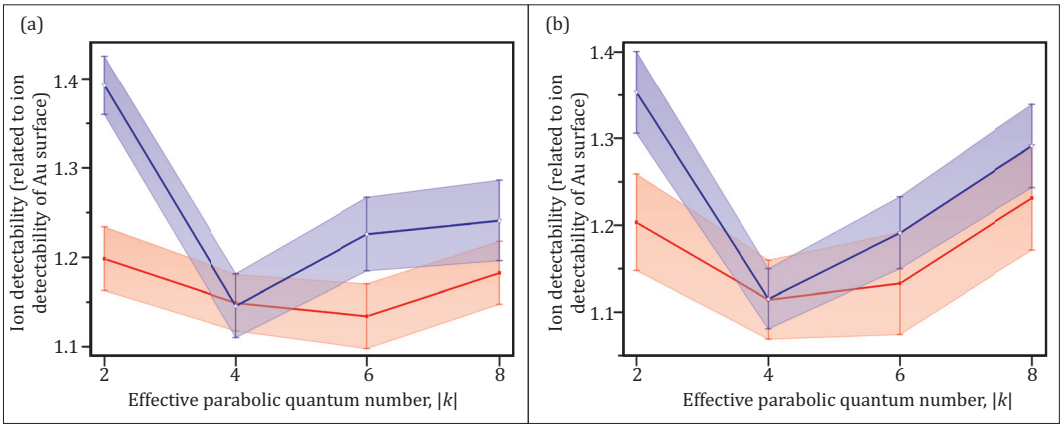

Figure 4.6: The ion detectability variation for the red- (red line) and blue- (blue line) shifted Stark states ($k = -8$ to $k = +8$) of the $n = 17$, $N^+ = 2$ Stark manifolds incident at the (a) p-type boron doped ($N_D = 2.10 \times 10^{19}$ cm^{-3}), (b) n-type arsenic doped ($N_D = 1.30 \times 10^{19}$ cm^{-3}) doped Si surfaces. The shaded area is connected to the upper and lower error bar points for each principal quantum number, and the solid line is connected to the mean values.

experimental observation does not agree with what would be predicted for a hydrogenic system due to the strong level crossings between the adjacent Stark manifold of $N^+ = 0$ rotational channels and the loss of their initial populated Stark state character.

The atomic hydrogen Rydberg states would be a suitable candidate to investigate the ion detectability variation between the red- and blue- shifted Stark states arising from the p- and n- type doped Si surface because hydrogen atomic Stark states do not lose their initial character of the originally populated states (weaker interaction between the adjacent Rydberg manifolds) [123]. Therefore, in future, the investigation of the surface ionisation profiles of the H atomic Rydberg states in the presence of a Stark field will help to understand the dopant type effect on the red- and blue- shifted Stark states.

4.3 Electron detected surface ionization profiles

Most previous work on Rydberg surface interactions deals with the surface ionization profiles of the Rydberg molecules or atoms via the ion detection process [68, 72, 109, 110, 114, 124, 125]. More recently, McCormack et al. [74] studied the electron detection scheme to investigate the surface ionization profiles of the incident hydrogen Rydberg atoms and molecules at a metal surface. This section also covers the electron detection method with the incidence of hydrogen Rydberg molecules at different doped Si surfaces. This study will investigate the variation of the electron detected ionization profiles with various dopant types and various dopant densities and it will give an opportunity to compare the ion and electron detected surface ionization profiles at Si surfaces.

In the case of the electron detection scheme, the experimental setup was modified by reversing the direction of the applied field. The detailed experimental modification is described below: a positive variable potential was applied to the mesh grid and potentials of 0 V, +1650 V, +4500 V were applied to the front MCPs, back MCPs and phosphor screen respectively, as shown in Fig. 4.7. The potential of the dynode stacks was maintained at 0 V. The negative static Stark field (-600 Vcm^{-1}) was applied to the surface to generate a homogeneous Stark field at the time of extraction.

The mass of the electron is considerably smaller than the H_2^+ ions (mass ratio between $e^n : H_2^+ = 1 : 3680$), but the kinetic energy would be the same for acceleration in the same field so that the velocity of the electron is much higher than H_2^+, and the electron bunch spreads over a smaller microsecond time scale in the TOF region. In the previous experimental studies [74], the pulsed extraction field was applied to the surface and dynode stacks and the MCP front plate were maintained at 0 V to pull the electrons up to the detector. In the case of the Si surface studies presented here, a positive pulsed potential was applied to the mesh grid, and the front MCP, and the

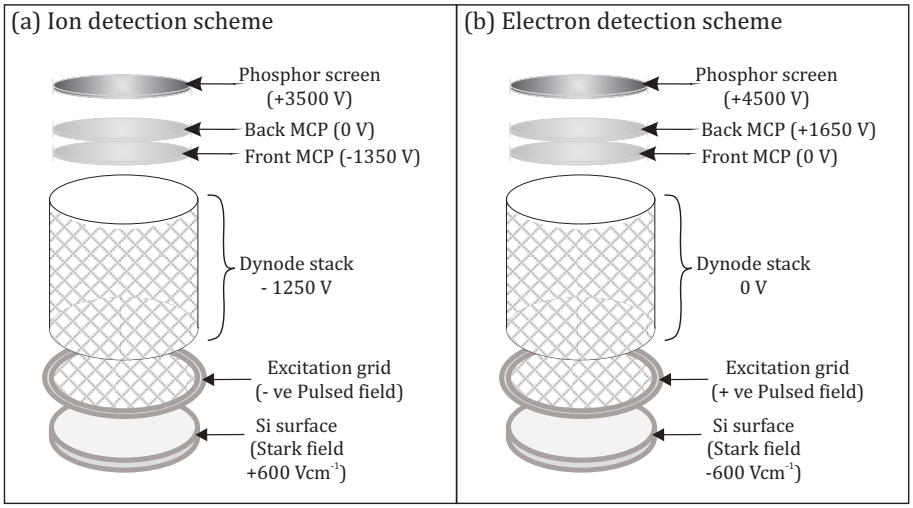

Figure 4.7: Schematic diagram represents the applied field into the surface, mesh, MCP and phosphor screen for (a) ion and (b) electron detection scheme.

surfaces were maintained at ground potential (0 V). Therefore, the acceleration force of ejected electrons towards the detector was reduced by the (zero field) surface. For that reason, the majority of the ejected electrons are not reaching MCP detector, as illustrated in Fig. 4.8, and it gives a lower signal to noise ratio in the surface ionization profiles.

However, in the presence of a negative static Stark field, applied as a negative potential to the surface, an additional acceleration force is provided towards the MCP detector. Therefore, ejected electrons fly easily towards the detector, and give a clear surface ionization signal (see Fig. 4.8). The energy levels of the particular Rydberg manifold are split by the Stark field as discussed previously [126], and the Stark state mixes with a vacuum-oriented state as it approaches the surface which result in backscattering of the Rydberg electron [126]. The Stark state mixing becomes more favourable as the electron-extraction field increases. Therefore, the electron detection experimental studies are carried out with the presence of a 600 Vcm^{-1} Stark field.

The study of the electron detection method is different from the ion detection scheme

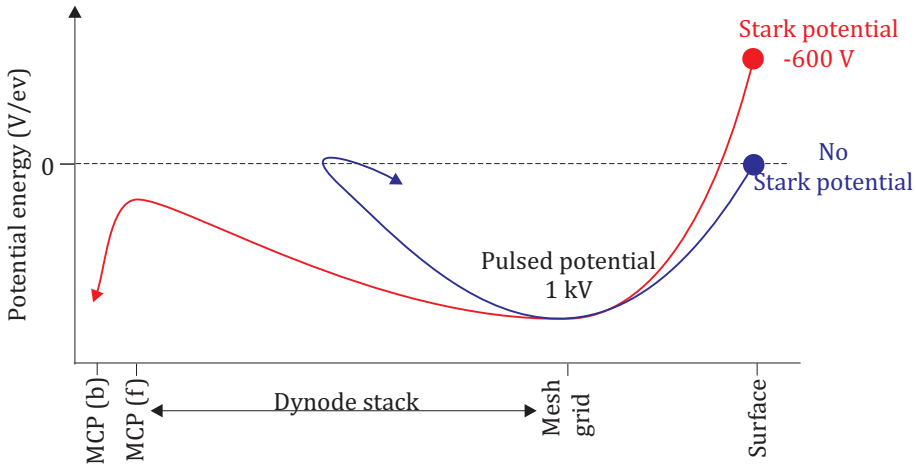

Figure 4.8: Schematic diagram represents the path of travel produced for the electron with the presence (red line) and absence (blue line) of the Stark field.

and this difference manifests itself not only in the reverse field but also in the arrival time of the ion/electron at the detector. The electron arrival time at the detector is shorter than the arrival time for ion detection (1 μs), as shown in Fig. 4.9. This observation clearly indicates that the ionization profiles were not generated for example from the H_2^- ion, because in that case the surface and field ionization profiles would appear with the same flight time as H_2^+. The electron detection could be created by various mechanisms such as (i) '*backscattered*' Rydberg electrons, (ii) Auger electrons from ion incidence at the surface [53, 127] and (iii) secondary electrons from the surface [128, 129]. The arrival time of the produced electron from these three different mechanisms would be expected to be approximately similar.

As discussed by McCormack et al [74] electrons produced by Auger or secondary processes would not be likely to show sharp resonances in the surface ionization profiles. However, these experimental surface ionization profiles do show sharp reproducible resonance signals (shown in Fig. 4.10), and therefore, the Auger process can be discounted. In addition, wave-packet propagation studies for the fraction of backscattered electrons as a function of electron-extraction field provide a plausible qualitative ex-

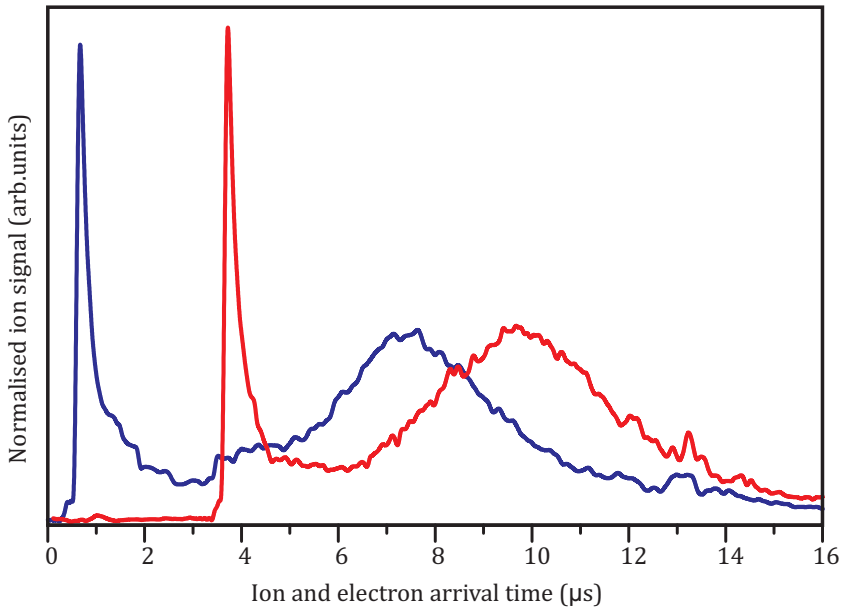

Figure 4.9: Experimentally detected ion (red line) and electron (blue line) time-of-flight (TOF) signals.

planation for the electron detection signal [126]. Therefore, the main mechanism for electron detection is backscattered Rydberg electrons, *i.e.* the Rydberg electron which is ejected as the molecule approaches the surface is the one detected.

4.3.1 General features of the surface ionization profiles

In the electron detection scheme, the direction of the applied electric field is reversed. Therefore, the electron distributions of the blue-shifted Stark states are surface-oriented and the red-shifted Stark states are vacuum-oriented, so the higher energy states are now surface-oriented [126]. The surface ionization profiles for a range of Stark states ($k = -14$ to $+16$) incident at the Si surface are recorded as a function of the applied electric field in the presence of the homogeneous static Stark field (-600 Vcm^{-1}). The results are shown in Fig. 4.10.

Figure 4.10 shows the sharp reproducible resonances again arising from the level crossings between the neighbouring rotational channels ($n = 17$, $N^+ = 2$ and $n = 22 - 25$,

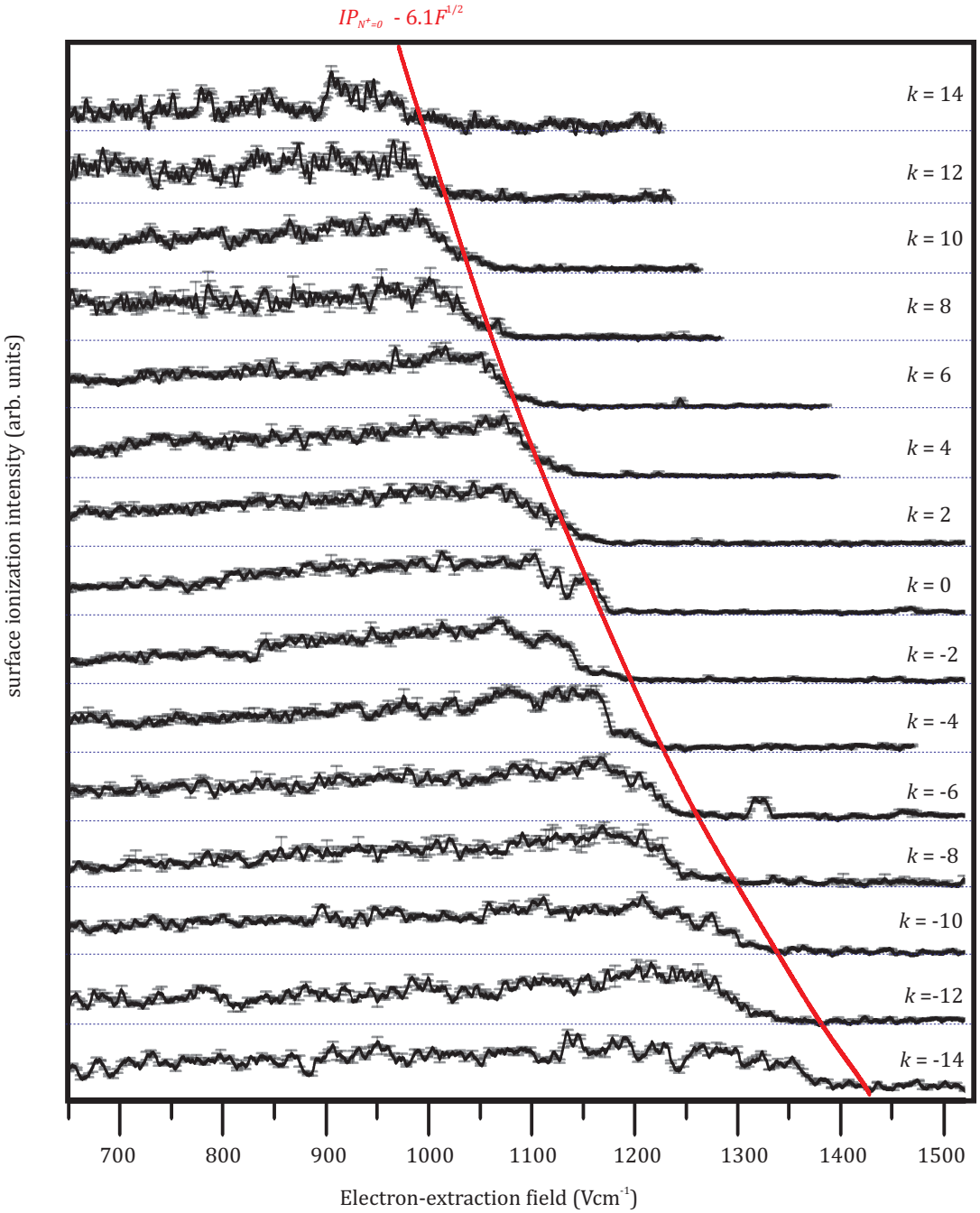

Figure 4.10: The surface ionization profiles for the red- to blue- shifted $n = 17$, $N^+ = 2$ Stark states (Stark field $\approx$ -600 Vcm^{-1}) of the H_2 Rydberg molecule as a function of the electron-extraction field. The ionization profiles are normalized with respect to the integrated field ionization signal.

$N^+ = 0$). The surface ionization efficiency generally increases with increasing applied electric field until it reaches the high-field cut-off limit. Furthermore, the high-field cut-off limit of the surface ionization profiles for the electron detected molecular hydrogen Stark states behave in the same way as discussed in section 4.2.2 for detected ion-signals.

4.3.2 Comparison between ion and electron detected surface ionization profiles

A comparison of the surface ionization profile for the population of the $n = 17$, $N^+ = 2$ Stark manifold incident at the n-type doped Si surface by the ion and electron detection methods is shown in Fig. 4.11. Both surface ionization profiles are normalized with respect to the field ionization signal as discussed in section 2.3.2. The surface ionization profiles have very similar characteristic behaviour for both detection schemes (as discussed previously in section 4.2.2 and 4.3.1), and both detection schemes show the progression of sharp resonances in the surface ionization profiles, which arises due to the population transfer from $N^+ = 2$ to $N^+ = 0$ rotational channel. The noticeable difference between these two different detection schemes is observed in the intensity of the resonance signal; stronger resonance signals appear via the electron detected method due to the effect of enhanced probability of extraction after the surface ionization process (as similar observation was made in the previous study with a metal surface [74]).

Figure 4.11 shows some distinguishable qualitative variation between ion and electron detected surface ionization profiles. The ion and electron detectabilities are used to show the quantitative difference of the surface ionization profiles in Fig. 4.12. Note that, the integrated ion and electron signals are further normalized relative to the ion detectability of the Au surface, helping to make a clear comparison between the

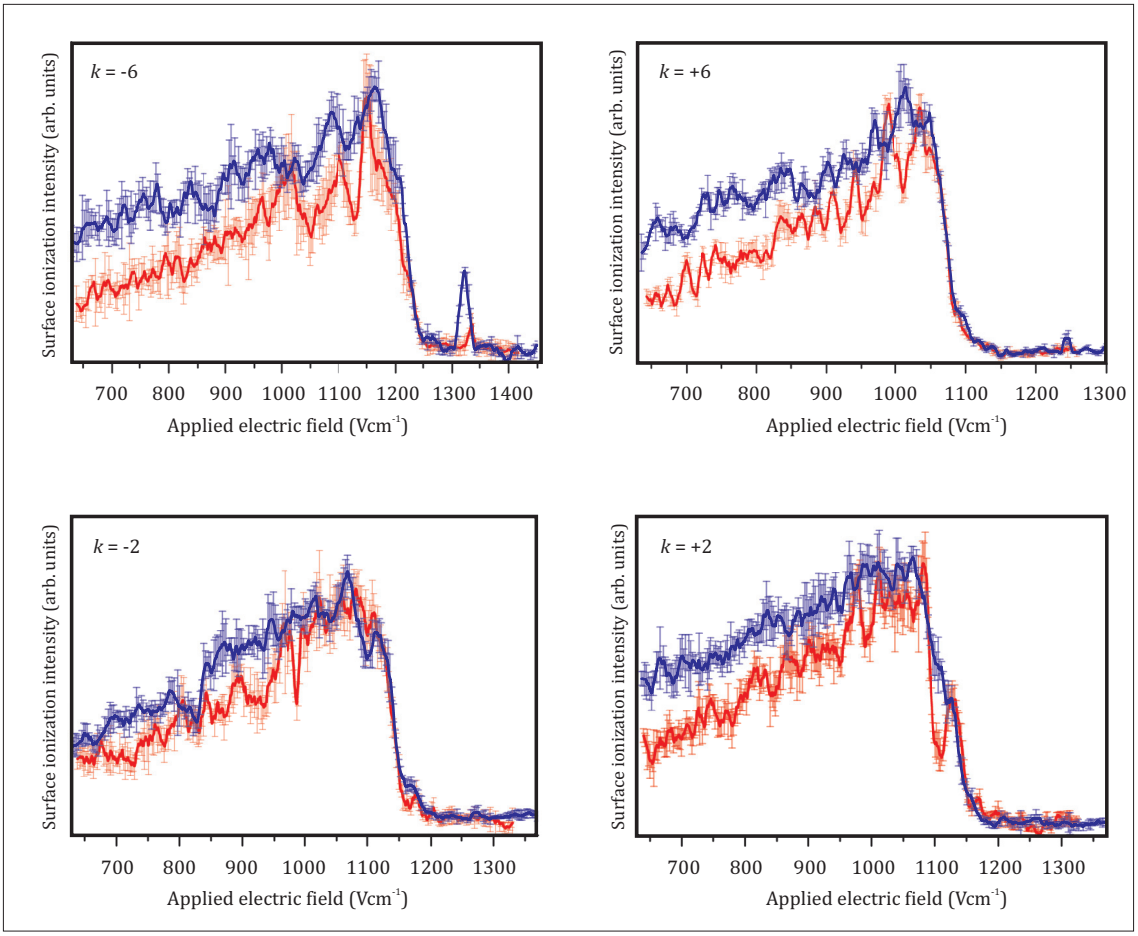

Figure 4.11: A comparison of the ion (red line) and electron (blue line) detection surface ionization profiles for the $n = 17$, $N^+ = 2$ Stark states ($k = -6$, -2, +2, and +6) of the H_2 Rydberg molecules incident on the n-type arsenic doped ($N_D = 1.30 \times 10^{19}$ cm^{-3}) Si surface.

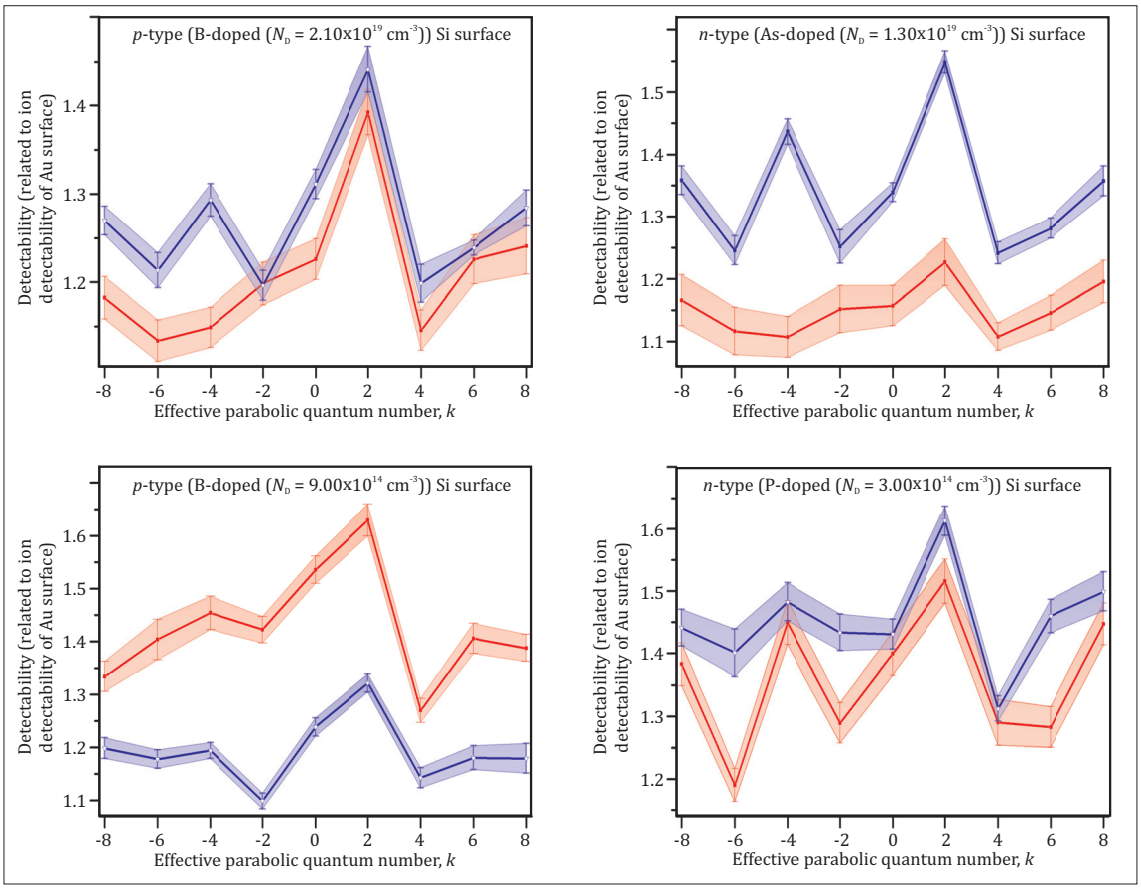

Figure 4.12: A comparison of the ion (red line) and electron (blue line) detectability variation for the red- and blue- shifted Stark states ($k = -8$ to $+8$) for the $n = 17$ Rydberg manifold incident at the n-type arsenic doped ($N_D = 1.30 \times 10^{19}$ cm^{-3}), n-type phosphours doped ($N_D = 3.00 \times 10^{14}$ cm^{-3}), p-type boron doped ($N_D = 9.00 \times 10^{14}$ cm^{-3}) and p-type boron doped ($N_D = 2.10 \times 10^{19}$ cm^{-3}) Si surfaces. The solid line is connected to the mean values.

related ion and electron detectabilities simultaneously. The electron detectabiity is also calculated by using the same integration region of the surface ionization profiles as discussed in section 3.3.

Figure 4.12 clearly shows that Stark states from the electron detection scheme have slightly higher detectability than the ion detection method, and this observable variation between the ion and electron detectabilities varies with dopant type and dopant density of Si surfaces. These clear variations on electron detectabilities are discussed

further in next section. Surprisingly, the p-type boron doped ($N_{\mathrm{D}} = 9.00 \times 10^{14}$ cm^{-3}) Si surface shows different behaviour when comparing electron and ion detection, *i.e.* the relative detected signal from the electron detection method is considerably lower than the ion detection method. This may arise from the widely distributed positive delocalized surface charge, which strongly opposes creating backscattered electrons, attracting them towards the surface. Therefore, the ion detection scheme is more favourable than the electron detection scheme at the low dopant density of the p-type doped Si surfaces and the converse also applies, *i.e.* the electron detection scheme is more favourable to low dopant density n-type Si surfaces, but this effect is less dramatic.

4.3.3 Electron detected signal variation at doped Si surfaces

The backscattered Rydberg electrons are repelled from the target surface and travel towards the detector in the presence of sufficiently strong extraction fields. Negative and positive surface dopant charge fields distort the repulsive force and modify the probability of the detected electron. For the electron detection scheme, the surface ionization mechanism effectively leads to a high probability of detection because the electron ejection takes place on the vacuum side of the Coulomb potential, *i.e.* the opposite side compared to the ion detection. For this reason, the next two subsections consider the effect of the surface dopant charge field distribution on the electron ejection processes, and how they affect the probability of detecting the electron.

Effect of dopant type

The electron detectability for the $n = 17$, $N^+ = 2$ Stark manifold of p- and n- type doped Si surfaces with equivalent dopant density is displayed in Fig. 4.13. Note that the relative electron detectability was determined relative to the electron detectability

of the Au surface in the same way as in the relative ion detectability (see section 3.3).

Figure 4.13 clearly shows that the n-type doped Si surfaces have higher electron detectability than the p-type doped Si surfaces. This difference arises from the distribution of the negative and positive surface dopant charges in the surface region. As discussed in section 3.2.2, for the n-type doped Si surfaces, the negative delocalized surface charge and positive point charges appear near the surface. As a result, the n-type doped Si surfaces exhibit more negative delocalized surface dopant charge fields. However, in the case of p-type doped Si surface, the more positive delocalized surface dopant charge field appears near the surface region. A negative surface dopant charge field produces an additional repulsive force and an increase in the electron detection probability, but the presence of a positive delocalized surface charge field opposes the production of backscattered electrons and also attracts the produced electrons, so that the electron detection probability become less. Therefore, the electron detectabilities show higher detectability on n-type doped Si surfaces than the p-type doped Si surfaces. This effect is evidently more distinct than that seen with ion detection, and it also shows the opposite dependence on dopant type (see Fig. 4.4).

Effect of dopant density

For the n-type doped Si surface, the electron detectability becomes more favourable when decreasing the dopant density, because the area spanned by these delocalized negative surface dopant charge become wider with decreasing dopant density, and it gives a greater repulsive force to the ejected electrons. Figure 4.14 (a) shows the electron detectability variation relative to electron detectability of the Au surface at the higher and lower dopant density of the n-type doped Si surfaces for a selection of the Stark states from the $n = 17$, $N^+ = 2$ Rydberg manifolds which are populated in the presence of a 600 Vcm^{-1}. This figure clearly shows that the lower dopant density

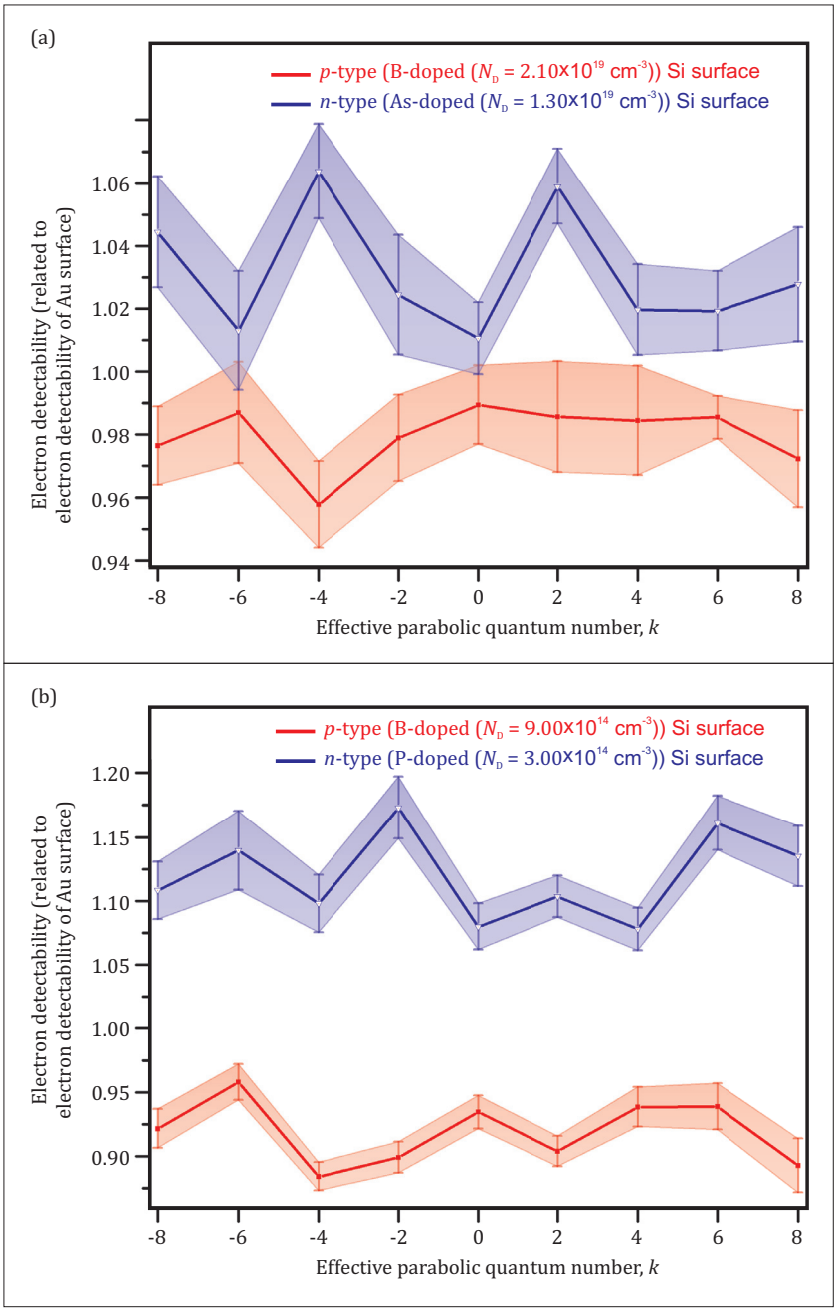

Figure 4.13: The electron detectability variation for the red- and blue- shifted Stark states ($k = -8$ to $+8$) of the $n = 17$ Rydberg manifold incident at the (a) high and (b) low dopant density of p- (red line) and n- (blue line) type doped Si surfaces. The shaded area is linked up to the upper and lower error bar points for each principal quantum number, and the solid line is connected to the mean values.

of the *n*-type surface has higher electron detectability than the higher dopant density. Furthermore, the charge variations are much less on an atomically flat Au surface (see section 3.2.2), so that it has shown less electron detectability than that of the *n*-type doped Si surfaces (shown in Fig. 4.14 (a)).

As discussed in section 4.3.2, positive delocalized surface charges oppose the ejection of backscattered electrons. As a result, the electron detection probability becomes lower. Furthermore, the efficiency of the electron detection probability decreases with decreasing the dopant density of *p*-type doped Si surfaces, because the distribution area of the positive delocalized surface charge becomes wider as discussed in section 3.2.2). Due to the above reason, the lower dopant density of the *p*-type doped Si surface has shown comparably lesser electron detectability than the heavily doped *p*-type Si surface, as shown in Fig. 4.14 (b). This is the only example in this thesis where the doped Si surfaces show lower detectability than an Au surface.

The various trends in electron detectability with dopant density of *p*- and *n*- type doped Si surface have clearly shown that the electron detection probability strongly depends on the magnitude and distributed area of the both positive and negative dopant charge fields. However, in the case of the ion detection scheme, the ion detectability variation is mostly affected by the distribution of the positive dopant charge field. The variation in detectability from a *p*-type Si surface is the opposite for the ion and electron detection schemes for comparing different dopant densities (see Fig. 4.5 and Fig. 4.14), indicating that the nature of the ionization process is different in the two cases.

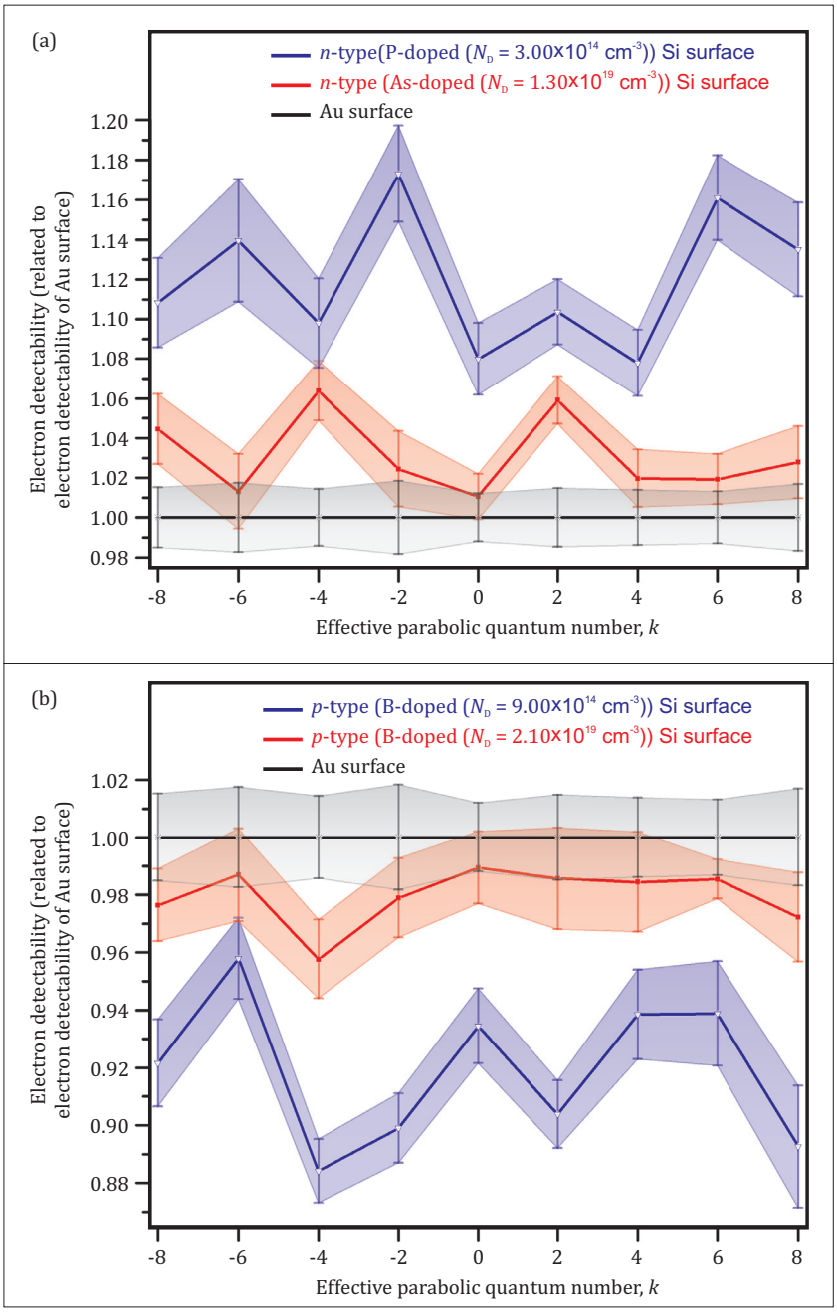

Figure 4.14: The electron detectability variation for the Stark states ($k = -8$ to $+8$) for the $n = 17$ Rydberg manifold incident at the (a) n-type and (b) p-type doped Si surfaces. The shaded area is links the upper and lower error bar points for each principal quantum number, and the solid line is connected to the mean values.

4.4 Conclusions

The experimental study of the surface ionization profiles of the $n = 17$, $N^+ = 2$ Stark states with respect to the Si surface with ion and electron detection schemes are presented in this chapter.

The overall trend of the ion detectability of Stark states behaves similarly to that described in the previous chapter (chapter 3), *i.e.* p-type doped Si surfaces have shown higher ion detection signal than n-type doped Si surfaces, and ion detectability decreases with increasing dopant densities for both p- and n- type doped Si surface. The ion detectability of the blue-shifted Stark states appears slightly higher than that of the red-shifted Stark states, because blue-shifted Stark states are ionized a little earlier than the red-shifted Stark states. Some of the k states (*e.g.* $k = +2$) show considerably higher ion detectability variations than that of the other k states.

For the electron detection scheme, the detected electrons are produced via a backscattered mechanism. The overall electron detection profiles of $k = -8$ to $+8$ Stark states for the n-type Si surface have higher detectability than the p-type doped Si surfaces at a particular dopant density. This variation arises from the distribution area of the negative surface dopant charge field islands in the surface region. For the n-type Si surfaces, the overall electron detection decreases with increasing the dopant density. However, in the case of p-type doped Si surfaces, the overall electron detection increases with increasing the dopant density (it behaves opposite to the ion detection scheme) because widely distributed positive surface dopant charge field islands oppose the electron escaping towards the vacuum at the point of ionization.

Comparing the ion and electron detection schemes, the surface ionization profiles show resonance structure at the same extraction fields, but the relative intensity for the electron detection scheme is considerably higher than the ion detection scheme. However,

the ion detection scheme shows slightly higher efficiency at low p-type dopant densities due to the presence of widely distributed positive surface dopant charge field islands in the surface region.

The ion detection ionization scheme is favoured at low dopant density, p-type Si surfaces, and the electron detection scheme is favoured at low dopant density, n-type Si surfaces.

Chapter 5

Surface interaction of atomic hydrogen Rydberg states

5.1 Introduction

Following the study of the ionization of H_2 Rydberg molecules at Si semiconductor surfaces presented in the previous two chapters (chapters 3 and 4), in the following chapter a study of the interaction of the H Rydberg atom with Si semiconductor surfaces will be presented. This will provide an opportunity to compare the interactions of non-hydrogenic (H_2) and hydrogenic (H) systems with Si semiconductor surfaces. The Rydberg states of H_2 molecules differ fundamentally from those of the H atom. The presence of core electrons for non-hydrogenic systems leads to a loss of the spherical symmetry and the introduction of non-zero quantum defects for low-l Rydberg states. The lifting of the zero-field l-degeneracy (for the same n) leads to avoided level crossings when adjacent principal quantum number manifolds (of the same m_l) overlap on the Stark map, while for the H atom system levels may cross without interactions. It has been shown, however, that in the presence of a metal surface, avoided level crossing may occur even for the H atom. Thus, it is of interest to investigate how these

intrinsic differences between hydrogenic and non-hydrogenic systems can affect their interactions with target surfaces. Furthermore, the interactions of an H Rydberg atom with a surface, and its accompanying charge transfer process have gained much theoretical interest [60, 130–136] because of the simple structure and inherent symmetry of the system [24, 137], and recently the first experimental study of Rydberg H atom with a metal surface has been carried out [123]. The work presented here focuses on the interaction of the Rydberg states of the H atom with Si surfaces following the work of So et al [123]. These atomic H Rydberg states are populated using the two-photon VUV-UV excitation scheme of Merkt and co-workers [138–140].

5.2 Experimental details

The experimental work presented in this section is carried out using the ultra-high vacuum setup of Ref. [123] (a different apparatus than used for the H_2 work), but the target surfaces are the same as those used for the H_2 experimental work presented in the previous two chapters (chapters 3 and 4).

5.2.1 Atomic hydrogen beam

In the present experimental study NH_3 seeded in He (NH_3 : He = 1 : 4) was used to generate the H atoms, following the work of So [46]. The backing pressure of the gas mixture was maintained at $\sim$ 2 bar, and a pulsed supersonic expansion of the seeded beam ($\sim$ 100 μs width) was generated by pulsed-solenoid valve (General valve, series 9, orifice diameter 1 mm) working at 10 Hz. A 15 mm long, 1 mm inner diameter quartz capillary tube (Vitrocom CV1012S) was mounted on the faceplate of the pulsed nozzle. An ArF excimer laser working synchronously with the pulsed nozzle at 10 Hz (with pulse duration of $\sim$ 8 ns and a spectral band width of 0.23 nm) and produces

the atomic H beam via photodissociation of NH_3 at 193.34 nm [141–143],

$$NH_3(\widetilde{X}^1A_1) \xrightarrow{h\nu} NH_2(\widetilde{X}^2B_1) + H(^2S). \tag{5.1}$$

The power of the ArF excimer laser is typically maintained at around $5-7$ mJ/pulse, and it is weakly focused into the capillary tube using a fused silica spherical lens ($f = 200$ mm). The generated hydrogen atomic beam is passed into the main chamber through a 1 mm diameter skimmer, located 3 cm from the end of the capillary tube. The H atomic beam is excited to Rydberg states by two-photon (VUV-UV) excitation in the centre of the main chamber 40 ± 0.8 cm from the skimmer face. The base vacuum pressure of the source chamber (before the skimmer) is kept at $\sim 1\times10^{-8}$ mbar and it increases to $\sim 7\times10^{-5}$ mbar during the operation of the pulsed valve. When the pulsed valve opens, the vacuum pressure of the main chamber (after the skimmer) changes from $\sim 4\times10^{-9}$ mbar to $\sim 1\times10^{-8}$ mbar.

5.2.2 Excitation region

The main features of the UHV apparatus and the alignment of the laser beams with respect to the molecular beam are illustrated schematically in Fig. 5.1.

The H atomic beam, seeded in He, is guided close to the target Si surface and intersects the both laser beams (VUV & UV) at a distance of ~ 46 cm from the capillary tube. Typically, a central portion of the H atom pulse arrives in the excitation volume ~ 300 μs after the photodissociation processes and at ~ 2.5 mm above the surface. The separation between the surface and mesh grid (Precision Eforming nickel mesh, 86.1% transmission) was always maintained at 10 mm.

The Si surface is mounted on a xyz vacuum manipulator and a rotation stage. Hence the location of the excitation and the distance of the mesh grid with respect to the

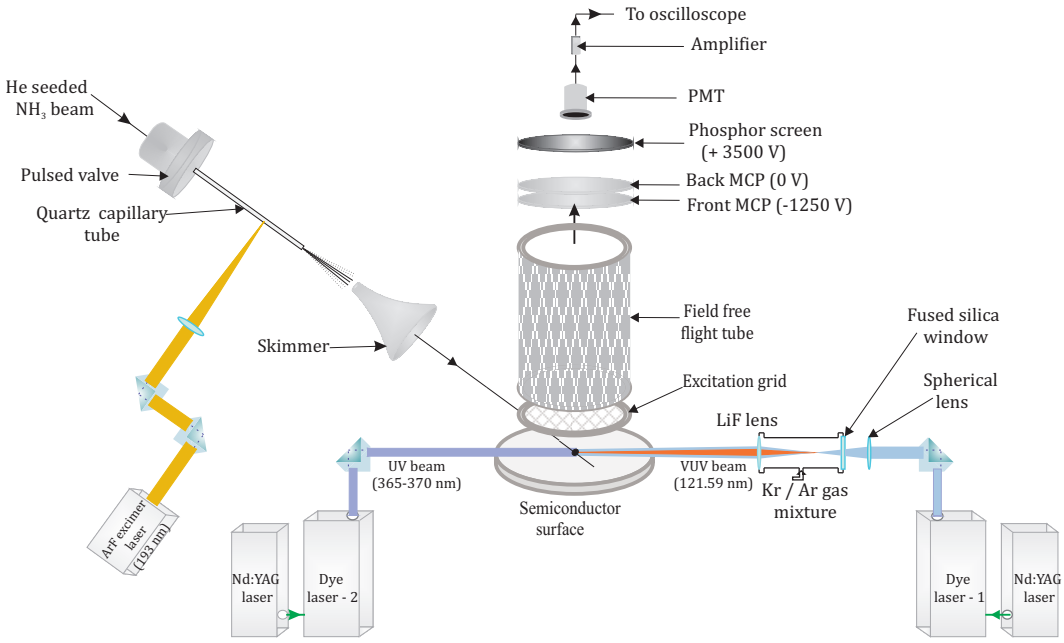

Figure 5.1: Schematic diagram of the modified new UHV experimental apparatus.

surface and the grazing incidence angle of the atomic beam can be varied. For the experimental work presented below, the incidence angle is kept constant at 15°. The excitation position, and surface position is varied by $\sim \pm 0.1$ mm in the routine alignment and signal optimization in between changing sample surfaces. The gap between the mesh grid and the surface (and thus the absolute electric field applied) is calculated by taking the Stark spectra of the $n = 23$ Stark manifold (see Fig. 5.5) and comparing directly with the calculated Stark splitting (see Eq. 1.31).

The collision velocity of the atomic beam can also be altered by changing the time delay of the Rydberg laser excitation with respect to the ArF excimer laser. The velocity of the resultant H atomic beam seeded in He is maintained at 1505 ± 15 ms^{-1} and the perpendicular mean velocity to the surface is 390 ± 3 ms^{-1}, with a characteristic translational temperature 20 K [46]. The narrow diameter skimmer (1 mm) removes the more extreme velocity components from the original seeded beam. Furthermore, the use of nanosecond Rydberg excitation lasers permits a tight velocity choice, with

1% standard deviation, so that the velocity distribution does not create a problem in this experimental study.

5.2.3 Rydberg excitation

The H atoms are excited to Rydberg states using a resonant two-photon VUV + UV scheme via the $2p$ intermediate state.

Excitation scheme

The VUV frequency is resonant with the one-photon transition from the H atomic ground state ($^2S_{1/2}$) to the $2p$ ($^2P_{3/2}$) intermediate state, at an energy of 82259.2850 cm^{-1} [77]. It is difficult to populate only a single intermediate state ($^2P_{3/2}$ or $^2P_{1/2}$) experimentally because the small spin-orbit splitting (0.365 cm^{-1}) between the two neighbouring states [45], is narrower than the VUV linewidth of 0.3 cm^{-1}. However, it is possible to tune the VUV wavelength to populate predominately a single intermediate state [46]. The second excitation step from this $^2P_{3/2}$ intermediate state to the Rydberg states in the range of $n = 20 - 40$ is achieved by tuneable UV radiation in the range of $365 - 370$ nm, as shown in Fig. 5.2. The overall energy of these two-colour two-photon transitions is approximately 109570 cm^{-1} and lies below the ionization threshold at an energy of 109678.772 cm^{-1} above the $^2S_{1/2}$ energy level [77].

The second excitation step leads to population of $^2S_{1/2}$, $^2D_{3/2}$ and $^2D_{5/2}$ Rydberg states in zero-field due to the selection rule $\Delta l = \pm 1$ and $\Delta J = 0, \pm 1$. In theory, the ^2D state should be more populated than the ^2S state due to the transition probability difference of those two states ($^2D : {}^2S = 4\sqrt{2} : 1$) [144]. However, the spin-orbit coupling is negligible in the high-n Rydberg states, and the separate levels cannot be observed experimentally (cannot be resolved energetically) [145].

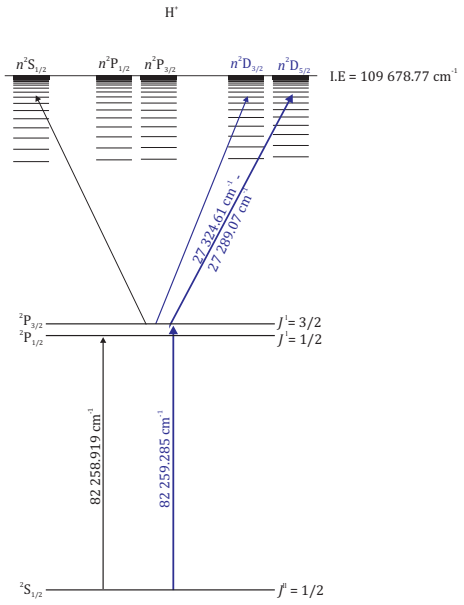

Figure 5.2: VUV and UV doubly resonant two-photon excitation scheme to excite ns/nd Rydberg states of H.

5.2.4 Laser source

121.6 nm VUV laser beam

To achieve VUV radiation at 82259.2850 cm^{-1}, the second harmonic output (532 nm) of a Nd:YAG laser (Continuum Surelite III) providing $\sim$ 430 mJ per pulse at a repetition rate of 10 Hz and pulse width of $\sim$ 9 ns, is used to pump a dye laser (Sirah, Cobra-Stretch) operated with LDS 722 (Pyridine 2) to provide a 729.36 nm IR laser beam [146]. The concentration of the dye solution utilized in the oscillator and pre-amplifier cells is 180 mg/l, and the concentration for the amplifier cell is 32 mg/l. The output of the dye laser (729.36 nm) is frequency doubled by passing through a non-linear KD*P crystal and the remaining fundamental laser beam is separated by using four Pelin-Broca prisms. The optimal crystal angle for frequency doubling is maintained with the aid of the Sirah computer controller. In typical operating conditions, the output power of the UV radiation (λ = 364.68 nm) is maintained at $12 - 15$ mJ per pulse.

In order to perform the frequency tripling, the UV radiation was focused into a 200 mm long stainless steel cell (or tripling cell) using a fused silica spherical lens ($f = 200$ mm). The tripling cell is filled with a mixture of negatively dispersive Kr and positively dispersive Ar rare gases (pKr : pAr = 200 mbar : 580 mbar) [83, 147]. The resultant VUV radiation at the Lyman-α wavelength (121.56 nm) is subsequently refocused into the excitation region using a LiF spherical lens ($f = 150$ mm). This refocused radiation intersects the hydrogen atomic beam at an angle of 45°, and its polarization is set to be perpendicular to the field (*i.e.* perpendicular to the surface normal and parallel to the surface plane). The VUV and UV beams each have distinct focal lengths so that the VUV radiation is focused at the specific excitation point.

$365 - 370$ nm UV laser beam

The second stage of the excitation scheme involves a transition from the $^2P_{3/2}$ state to the high-n level ($n = 29 - 34$) Rydberg states. It is achieved using the frequency doubled output of another dye laser (Sirah, Cobra-Stretch), which is pumped with second harmonic of the Nd:YAG laser (Continuum Surelite III), which produced $\sim$ 430 mJ/pulse at 532 nm. This dye laser (laser 2) is operated using 150 mg/l of LDS 751 (Styryl 8) in the oscillator and preamplifier cells, and 19 mg/l of Styryl 8 in amplifier cell. This provides tuneable UV radiation in the range $\lambda = 365 - 370$ nm, and the typical output power is ~ 5 mJ/pulse. When scanning the laser wavelength, the optimum angle for the doubling crystal is maintained by a Sirah auto controller. The laser 2 beam is not focused as the spectral lines are easily power-broadened. Laser 2 intersects the H atom beam at an angle of 135°, and is counter propagating with respect to laser 1 (VUV beam). The polarization of the UV beam could be set either parallel or perpendicular to the field axis (or quantization axis) by the addition or removal of an extra prism from the beam line. In this study, the polarization of both VUV and UV beams is set to be parallel to each other and both are perpendicular to

the field (or quantization) axis.

5.2.5 Ion detection

After excitation, the H Rydberg atoms travel for 6.5 μs before collision with the Si surface. The H atoms are ionized near the surface (at $Z_{\min} \sim 2.1\ n^2$ a.u.) via Rydberg electron transfer into the conduction band of the Si surface. The resulting ions will continue towards the surface and are accelerated by the attractive interaction between the H^+ ion and its image-charge in the surface. In all the experimental studies, a variable negative potential ($30 - 1250$ V) is applied to the mesh grid, which is typically pulsed on $\sim$ 500 ns after the laser excitation.

For a sufficiently high applied electric field (enough to overcome the image-charge field and the initial momentum of the ion towards the surface), the H^+ ions are extracted away from the surface and towards the mesh grid. The H^+ ions then pass through a 12 cm long field-free-flight tube and arrive at a set of 40 mm diameter Micro Channel Plates (Galileo, Chevron-configuration), which are coupled to a phosphor screen. The field-free-flight tube, front MCP, back MCP and the phosphor screen are typically held at potentials of -1250 V, -1250 V, 0 V and 3000 V respectively. The incident positive ions at the MCP result in a cascade of electrons, which strike the phosphor screen and cause fluorescence. The fluorescence emitted by the phosphor screen is detected by a photo multiplier tube (PMT), and the signal passed to a fast, low-noise pre-amplifier before transfer through a BNC cable to the digital oscilloscope (Lecroy Wave Surfer 452). The TOF data is then transmitted from the oscilloscope to a personal computer using standard LabVIEW^{TM} implemented programs.

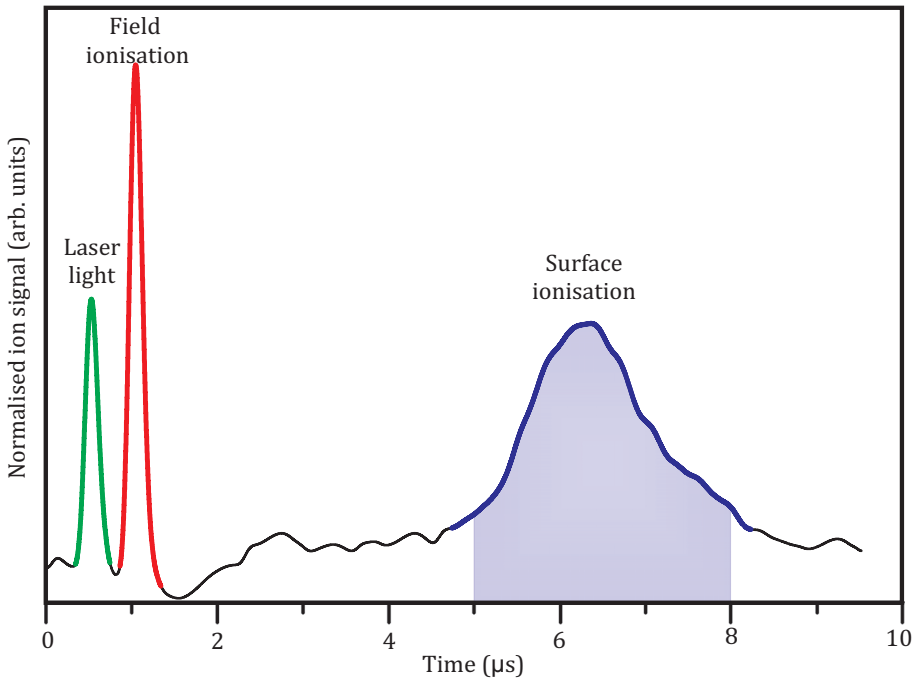

Figure 5.3: Experimental time-of-flight (TOF) displaying the detected ion-signals.

5.2.6 Characterization of ionization spectra

Time distribution of the ionization profiles

A typical experimental time-of-flight (TOF) for the H Rydberg atoms is shown in Fig. 5.3. The extraction field was chosen at the cross-over limit so that both surface-induced ionization and field ionization signals are visible.

As was described in section 2.2 for H_2, the signal produced by the field ionization is sharp and arrives before the surface ionization signal because the direct-field ionization takes place in the gas-phase region, and the surface ionization takes place in the surface region, which is much further down along the gas axis. The field ionization appears as soon as the extraction field is turned on, but the surface ionization signal is independent of the pulse time of the electric field (as long as it is before the surface incidence). The signal from the surface ionization process appears broader in TOF due to the range of collision times at the surface arising from the spatial, rather than velocity spread.

As described in section 2.2.2, the surface ionization time gate is chosen to cover 90% of the surface ionization signal and is well separated in time from the field ionization signal. The surface ionization time gates are fixed at 5.0 μs to 8.0 μs, and the surface ionization profiles are calculated by integrating the ion-signal within the time gates and plotted against the extraction field. The mean velocity of the Rydberg atom and the height of excitation above the surface dictates the time period in which the surface ionization signal appears. The surface and the excitation lasers can be moved relative to the mesh grid using the surface manipulator to ensure the correct arrival time of the surface ionization signal, while minimising the noise which may appear from part of the laser beam '*clipping*' part of the surface mounts and producing background ions. However, this adjustment is avoided where possible, and for most of the experiments the surface position and excitation height is fixed.

Zero-field spectra

The direct-field ionization spectrum of the zero-field populated $n = 28 - 44$ H atom Rydberg states is shown in Fig. 5.4. This spectrum is recorded with the VUV frequency fixed at the $^2P_{3/2} \longleftarrow ^2S_{1/2}$ transition, while scanning the UV radiation from $365.5 - 367.5$ nm. The strength of the pulsed extraction field is 1250 Vcm^{-1}. The excited Rydberg states seem to appear as a single series as the separate $^2S_{1/2}$, $^2D_{3/2}$ and $^2D_{5/2}$ H Rydberg series cannot be resolved due to l-degeneracy, and the very small spin-orbit splitting for higher-n Rydberg states. The varying line intensities observed in Fig. 5.4 are attributed to the power fluctuation of the lasers.

Stark field spectra

The energy of the Stark states can be split out in the presence of an electric field. Figure 5.5 shows the experimental Stark spectrum of the $n = 23$ manifold obtained via direct pulsed field ionization in the presence of a 200 Vcm^{-1} Stark field. The

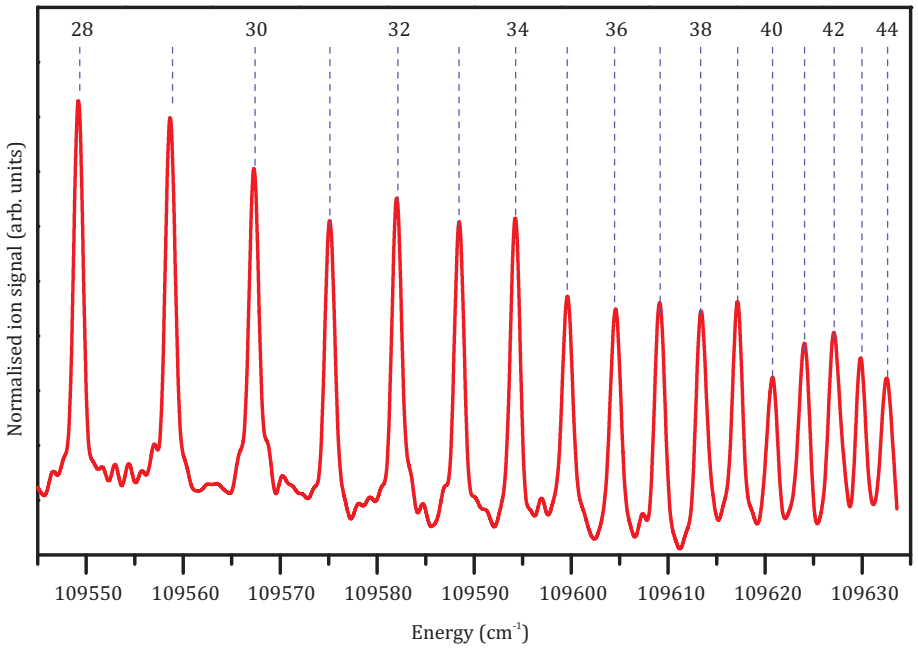

Figure 5.4: Field-free spectrum for the $28 < n < 44$ atomic H Rydberg states as a function of the total energy.

VUV wavelength is tuned to the $^2P_{3/2}$ intermediate level, which is an admixture of $m_l = 0, \pm 1$ states due to spin-orbit coupling although it is mainly the $m_l = \pm 1$ that is populated in the first step as the laser polarization is perpendicular to the field axis. With the 2nd laser also polarized perpendicular to the field axis, the final Stark states populated are mainly $m_l = 0, \pm 2$ (as shown by Fig. 5.5). Therefore, the first step excitation proceeds via the $^2P_{3/2} \longleftarrow {}^2S_{1/2}$ transition predominantly rather than the other transition ($^2P_{1/2} \longleftarrow {}^2S_{1/2}$).

Surface ionization spectra

As in the case of H_2 (explained in section 2.3.2), the surface ionization profiles (surface ionization signal as a function of ion-extraction field) are smoothed using a 5 point FFT filter method and are normalized to the respective field ionization signal. To ease the comparison of many different Si surfaces, the surface ionization profiles were then integrated between the starting point of the surface ionization profile and the

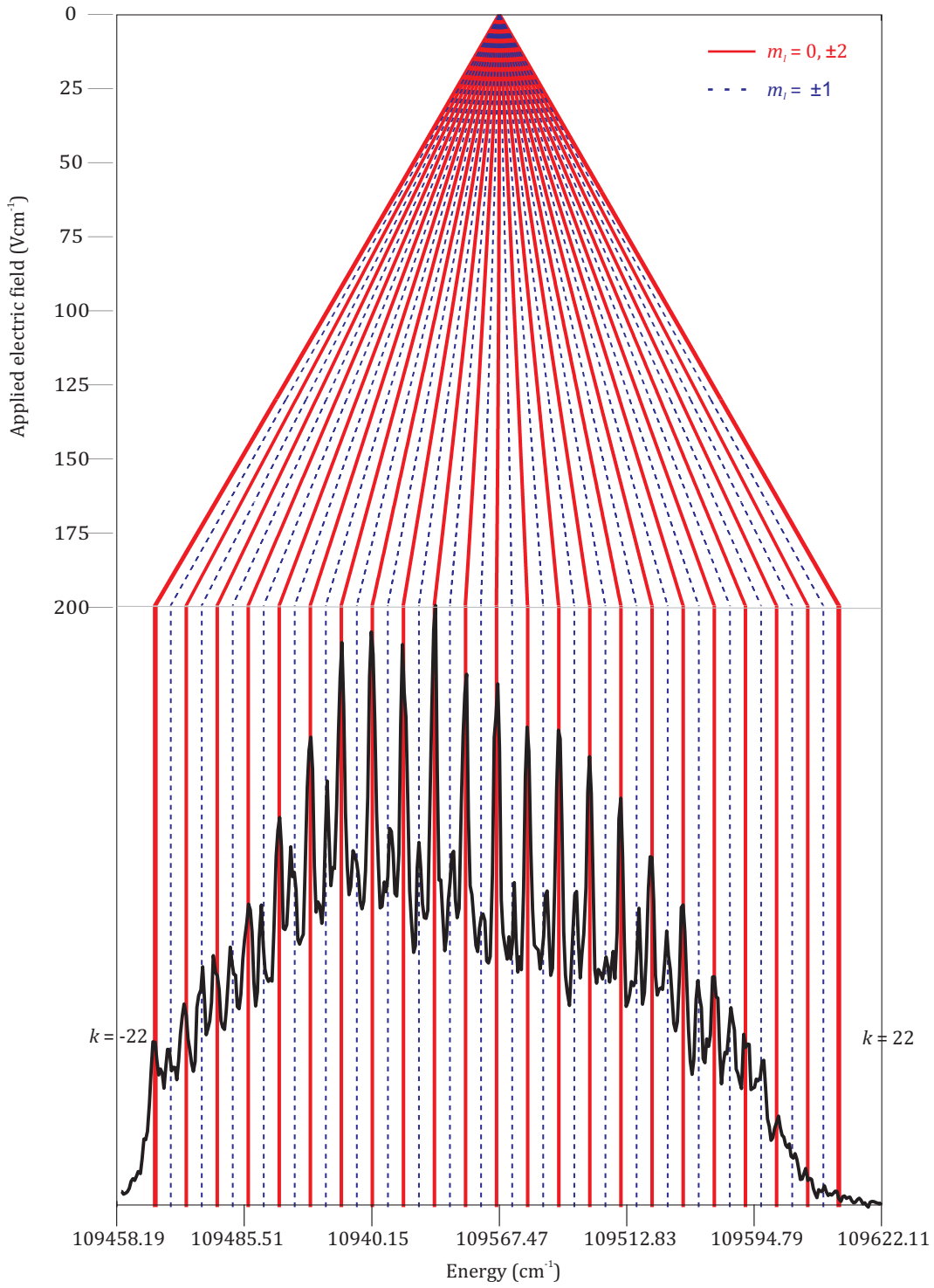

Figure 5.5: Top: Stark map showing the $n = 23$ atomic H Rydberg states, which are excited from the $^2P_{3/2}$ intermediate state. Bottom: Stark spectrum of the $n = 23$ Rydberg states excited in a static electric field of 200 Vcm^{-1}. The full (red) and dashed (blue) lines corresponds to $m_l = 0, \pm 2$ and $m_l = \pm 1$ states respectively.

high-field cut-off limit, and it will be referred to as '*ion detectability*'. Afterwards, it is further normalized to that of the '*standard*' Si surface (heavily doped Si semiconductor surface) (see section 3.3).

5.2.7 Surfaces

The surface ionization of H atom Rydberg states with principal quantum number $n = 29 - 34$, incident at six different doped 3" Si surfaces (PI-CHEM Industry, United Kingdom) was studied. These six surfaces were chosen to be representative of p- and n- type doped Si surfaces over a full range of dopant densities. The p-type doped Si surfaces studied have dopant densities of $N_{\rm D} = 9.00\times10^{14}$ cm^{-3}, 6.21×10^{17} cm^{-3} and 2.10×10^{19} cm^{-3}, and the n-type doped Si surfaces have dopant densities of $N_{\rm D}$ = 3.00×10^{14} cm^{-3}, 2.04×10^{17} cm^{-3} and 1.30×10^{19} cm^{-3}. The characteristic features of these six different surfaces were tabulated in table 2.1. As in section 2.4.1, the Si surfaces are promptly mounted on a xyz vacuum manipulator from a vacuum-sealed pack without further cleaning processes. Experiments were also carried out for an Au surface for comparison with the Si semiconductor surfaces.

5.3 Analysis of the surface ionization profiles

This section presents the experimental results for the surface ionization of H Rydberg atom with p- and n- type doped Si surfaces of various dopant densities. The effect of dopant density and the dopant type on the detected ion-signal is discussed.

5.3.1 Ionization profiles

The surface ionization and direct-field ionization profiles for the zero-field populated, $n = 29 - 34$ H atomic Rydberg states incident on the n-type (arsenic) doped Si surface are shown in Fig. 5.6.

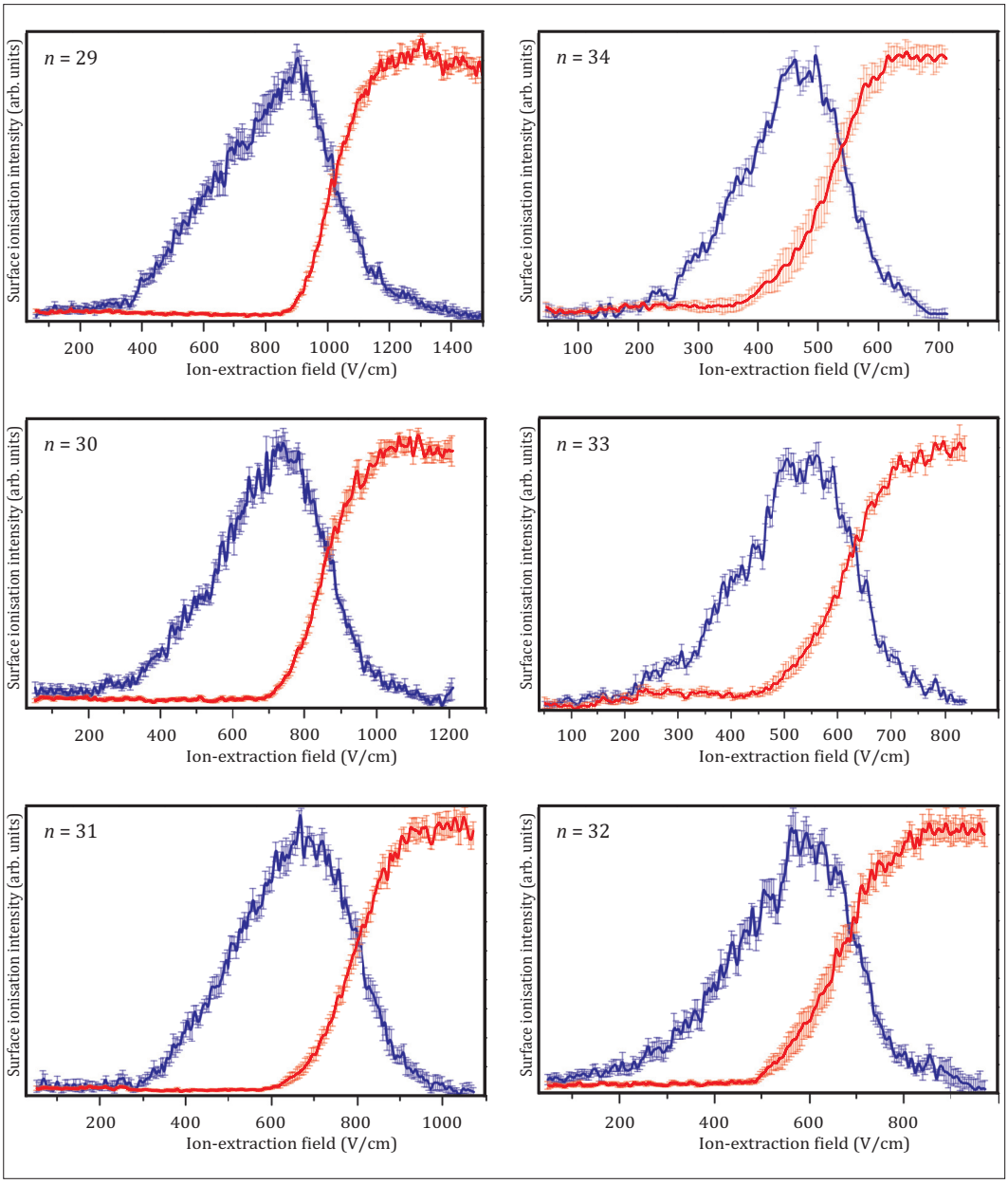

Figure 5.6: Surface ionization (blue line) and direct-field ionization (red line) signal as a function of applied extraction field for population of the $n = 29 - 34$ H atomic Rydberg states incident on the n-type (arsenic ($N_{\mathrm{D}} = 1.30{\times}10^{19}$ cm^{-3})) doped Si surface.

Figure 5.6 shows that the transition between surface ionization and field ionization occurs gradually over a range of fields. This is because the Rydberg states are initially populated in zero-field, and the subsequent ramp of the extraction field effectively spreads the population among the whole Stark manifold.

The profiles show similar general behaviour to the H_2 case; at low fields no signal is detected because the extraction field is not great enough to extract the ions that are formed at the surface from the attraction of their image-charge fields. The surface ionization signals rise with increasing applied electric field, and the sharp drop off observed at the high-field end, is due to the onset of direct-field ionization when the Rydberg states ionize in the gas phase before interaction with the surface.

The blue-shifted Stark states are higher in energy than red-shifted states, and so are classically expected to field ionize at lower fields. However, the observed field ionization limit for the H atom is much higher for the blue-shifted Stark states, because their wave function is polarized away from the saddle point [46], so they are kinetically stable. Thus, the broad range of fields at which field ionization occurs can be attributed to a range of red- and blue- shifted Stark states.

Effect of principal quantum number

Ionization of the H Rydberg atom relies on the loss of the weakly-bound Rydberg electron. The size of the Rydberg electron orbit increases with principal quantum number scaling as n^2, consequently, the atom-surface separation at which the Rydberg ionization occurs also increases with principal quantum number. The effect of principal quantum number on the surface ionization process is shown in Fig. 5.7 for the range $n = 29-34$ incident at the n-type (arsenic) doped Si surface. The results are presented as a function of ion-extraction field with error bars indicating the standard error from repeat experiments.

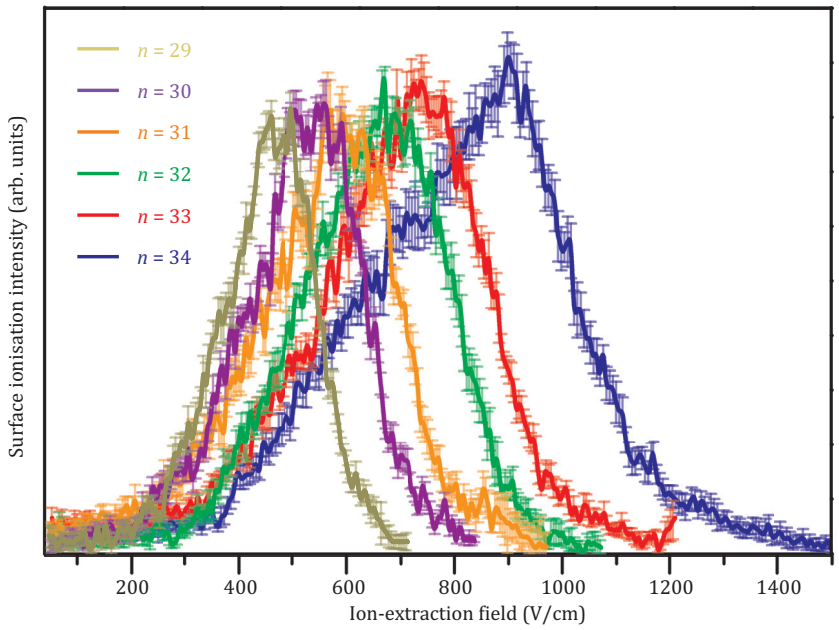

Figure 5.7: Surface ionization signal as a function of applied extraction field for population of the $n = 29 - 34$ H atomic Rydberg states incident on the n-type (arsenic ($N_{\mathrm{D}} = 1.30{\times}10^{19}$ cm^{-3})) doped Si surface.

The lowest principal quantum number for which the surface ionization at Si surfaces are studied in this work for the H atom is $n = 29$. This lower limit is imposed by the maximum ion-extraction field that can be applied, imposed by the detection ion optics outlined in section 2.1.6 (for which the surface is held at ground, and the mesh grid is at some negative potential to avoid the charging of the Si surface). Since the potential applied to the flight tube and front MCP are held at -1250 V, a potential greater than -1250 V applied to the mesh grid would result in some defocusing of the ions before they enter the flight tube and strike the MCP detector. To avoid defocusing, the largest ionization field that can be employed is 1250 Vcm^{-1}, which has been confirmed by SIMION simulations [148]. The lowest principal quantum number that is studied is $n = 29$, since this is the lowest principal quantum number that is fully field ionized at fields $\leq$ 1250 Vcm^{-1}.

Comparison of the surface ionization profiles

This section discusses the variation of surface ionization profiles for each atomic H Rydberg state incident on the metal and semiconductor surfaces, as in section 3.2. A previous investigation with atomic H Rydberg states incident at the rough aluminium surface clearly showed that the surface ionization profile is influenced by surface roughness [46]. The experimental studies carried out here use three different surfaces with nearly equal roughness: atomically flat Au (< 1 nm) and various doped Si (< 1.2 nm) surfaces. For the Si semiconductor surfaces, the bottom of the conduction band lies below the vacuum level so that the Rydberg electron is transferred directly to the conduction band as for a metal surface, *i.e.* the narrow electronic band gap does not affect the electron transfer process into Si semiconductor surfaces. The surface ionization profiles of $n = 30$ Rydberg states incident at the atomically flat Au, n-type (arsenic) doped and p-type (boron) doped Si surfaces recorded as a function of the applied electric field are shown in Fig. 5.8.

The results in Fig. 5.8 clearly show that the surface-induced ionization profiles of an $n = 30$ Rydberg state incident on various target surfaces are noticeably different at low ion-extraction field. The high-field cut-off limit is similar for all three surface ionization profiles because direct-field ionization takes place in the gas-phase region, so is independent of the nature of the target surfaces.

As discussed in section 3.2, the distinguishable variation between these three surface ionization profiles arises from the nature of the target surfaces, *i.e.* distribution of the surface dopant charges and the effect of the β-factor. The β-factor of these three surfaces only varies from ~ 0.889 (for both p- and n- type Si surfaces) to 1 (for metal surfaces); therefore, the effect of β-factor is considerably smaller, as explained in section 3.2.1. In addition, the polarity and the magnitude of surface dopant charge distributions vary with dopant type and dopant density, and will alter the minimum

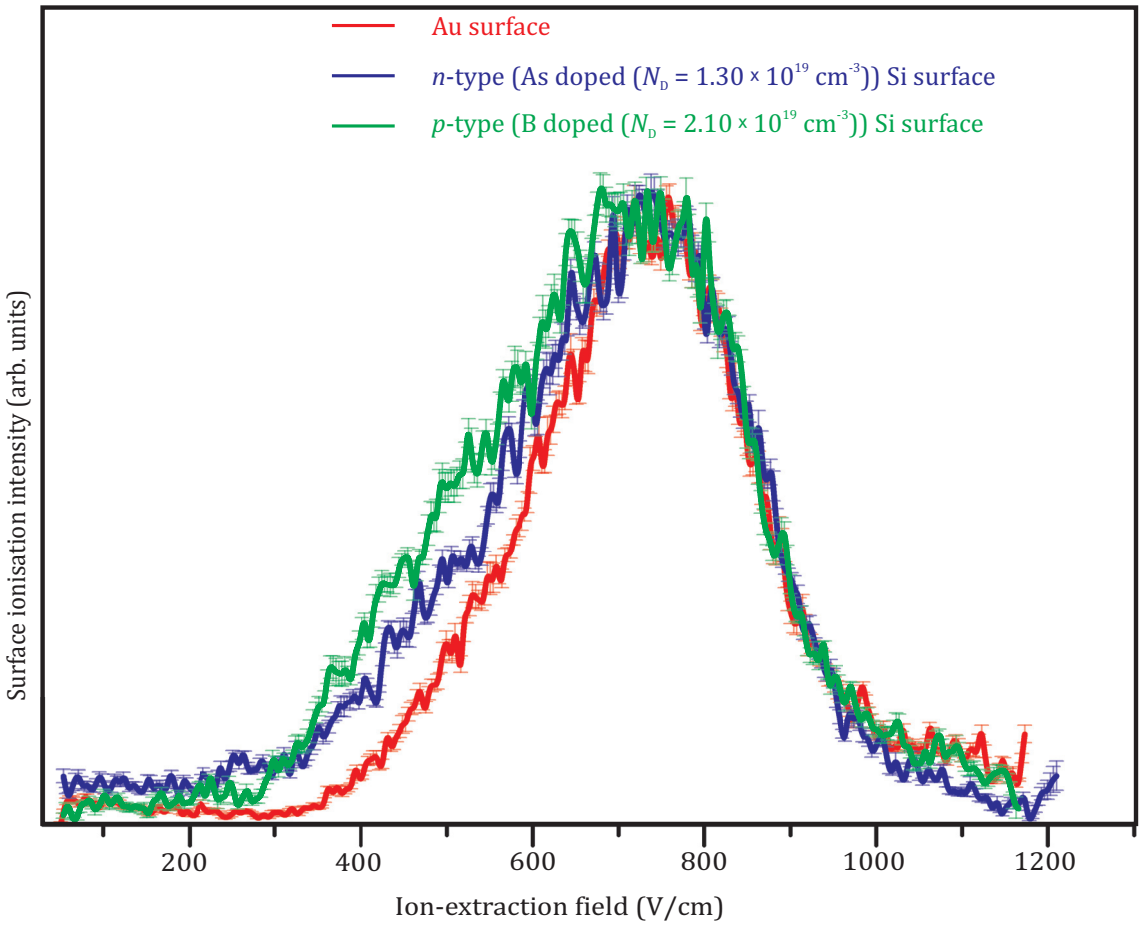

Figure 5.8: Comparing the surface ionization profiles as a function of ion-extraction field for the $n = 30$ Rydberg states incident at the gold surface (red line), n-type (arsenic ($N_{\rm D} = 1.30{\times}10^{19}$ cm^{-3})) doped Si surface (blue line) and at the p-type (boron ($N_{\rm D} = 2.10{\times}10^{19}$ cm^{-3})) doped Si surface (green line).

ionization distances and ion detection probabilities, as discussed in 3.2.2.

This experimental study also clearly shows the variation in surface ionization profiles with dopant density and dopant type of Si surfaces. Previous studies on Xe Rydberg atoms have also shown a similar variation in the surface ionization profiles at heavily doped p- or n- type doped Si surfaces and at the Au surface due to the differences in their positive and negative stray field distributions, which arisen from surface imperfections and adsorbate [55, 56]. However, the positive and negative dopant charges are equally distributed in heavily doped p- and n- type Si surfaces so that the previous study is not sufficient to explain the effect of dopant type in the surface ionization profiles [55]. The next section describes the effect of the nature of the target surfaces in the detected ion-signal, and it will give observable variation in their detected ion-signal between the various dopant types and dopant densities of Si surfaces.

5.3.2 The nature of target surfaces

The previous two chapters (chapters 3 and 4) deal with H_2 molecular Rydberg states and show some characteristic features in their surface ionization profiles, which strongly depended on the nature of the target surfaces. The molecular hydrogen Rydberg states, however, show strong resonance effects in the surface ionization profiles due to energy level crossing in the Stark map between levels of different N^+ and therefore, this system is slightly complicated to study the ionization effect on different surfaces. However, the atomic hydrogen system is a simple system to observe the effect of energy level crossing between the adjacent n manifolds on the surface ionization profiles. For that reason, the similar investigation is repeated again here with atomic H Rydberg states, and it will make clear the conclusion regarding the effect of nature of the target surfaces on the surface ionization profiles.

Effect of dopant type

In order to investigate the effect of dopant type on the detected ion-signal, the surface ionization profile for different *p*- and *n*- type of Si surfaces are investigated for the range of the principal quantum number, $n = 29 - 34$ using the same experimental methodology, outlined in section 5.2. In order to avoid any dopant density effect, this investigation was carried out with similar dopant density of *p*- and *n*- type doped Si surfaces. As discussed in section 3.3, the ion detectability method is the best option to compare many surface ionization profiles. The variation in ion detectability for both *p*- and *n*- type doped Si surfaces for equivalent sets of dopant densities are compared in Fig. 5.9 together with their computed error bars. The primary source of error arises from the calculation of the integrated lower and upper error bar limit of the surface ionization profiles. The ion detectability as a function of principal quantum number is connected through the mean values.

The experimental results clearly shows that *p*-type doped Si surfaces show a comparably higher detected ion-signal than *n*-type doped Si surfaces as seen in Fig. 5.9, which is mostly observed at low ion-extraction fields as seen in Fig. 5.8. As discussed earlier in section 3.3.1, this distinguishable variation arises from the extensively spread delocalized positive surface dopant charges present in the *p*-type doped Si surfaces, which increase the ion detection probability more than the presence of the widely distributed negative dopant charges at *n*-type doped Si surfaces.

Figure 5.9 shows two important characteristic features in the ion detectability variations, such as *p*-type Si surfaces show higher ion detectability than *n*-type Si surfaces, and the overall ion detectability decreases with increasing the dopant density. The similar specific features were also clearly observed throughout the study of H_2 molecular Rydberg states at various doped Si surfaces, as observed in Fig. 3.10. However, the ion detectability variation between the principal quantum numbers for the atomic

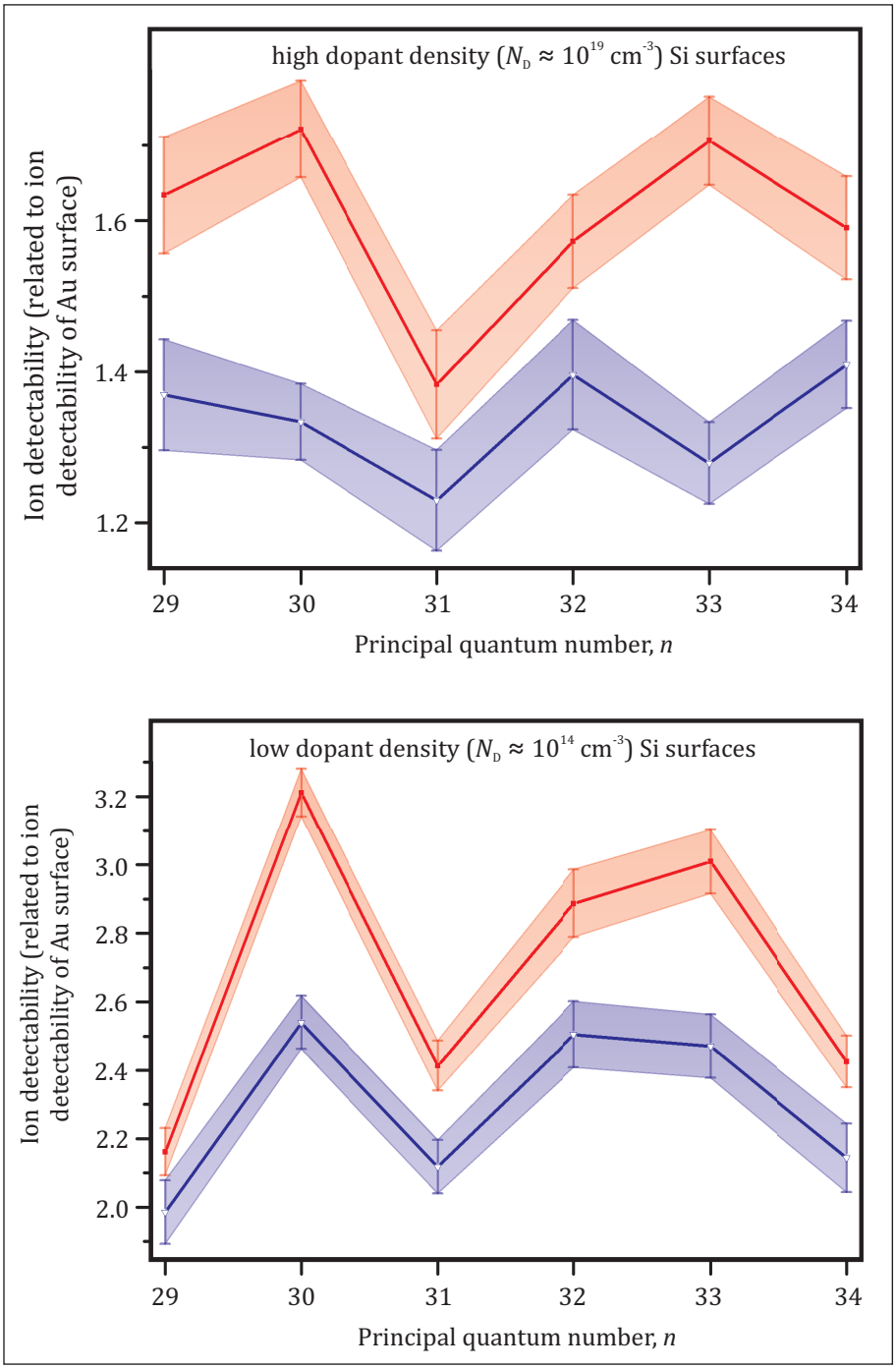

Figure 5.9: Comparison of the ion detectability for the initial population of $n = 29-34$ atomic H Rydberg states incident at the nearly similar dopant density of p- (red line) and n- (blue line) type doped Si surfaces. The shaded area joins the upper and lower error bar points for each principal quantum number, and the solid line are connects to the mean values.

hydrogen Rydberg states is almost similar (compare to the molecular hydrogen Rydberg states) and the ion detectability variation between the principal quantum number doesn't show any clear variation with increasing dopant density, and these variations (from the molecular hydrogen Rydberg states) are clearly explained here.

The ion detectability variation with principal quantum numbers for the specific target surfaces can be attributed due to the variation of minimum ionization distances. Figure 5.10 shows a plot of the minimum ionization distances as a function of ion-extraction field, which is calculated based on Eq. 1.37. It can be seen that the slope at lower extraction field is notably larger than that of the high field. However, the field required to ionize the higher-n ($n = 34$) atomic Rydberg states is at 450 Vcm^{-1} compared to the lower-n ($n = 29$) Rydberg states at 800 Vcm^{-1}. Therefore, the gradient variations between those particular fields are considerably smaller than those for the range of n used in the H_2 Rydberg states. For that reason, the detected ion-fraction between the higher-n and lower-n atomic Rydberg state incident at the Si surfaces shows less significant variation (Fig. 5.9) than for the range of molecular H_2 Rydberg states ($N^+ = 2$, $n = 17 - 21$, see section 3.3.1).

Effect of dopant density

Following the successful demonstration of the ion detectability varying with dopant type of Si surface presented in the previous section, the next intention is to extend these investigations to different dopant densities. The experimental studies are carried out with various dopant densities of *p*- and *n*- type doped Si surfaces, and compared with an atomically flat Au surface. The experimental data were collected for atomic H Rydberg states with principal quantum number in the range of $n = 29 - 34$, and the ion detectability determined is plotted in Fig. 5.11. The error bars are also indicated in Fig. 5.11, and the shaded areas join the upper and lower limits of the error bars.

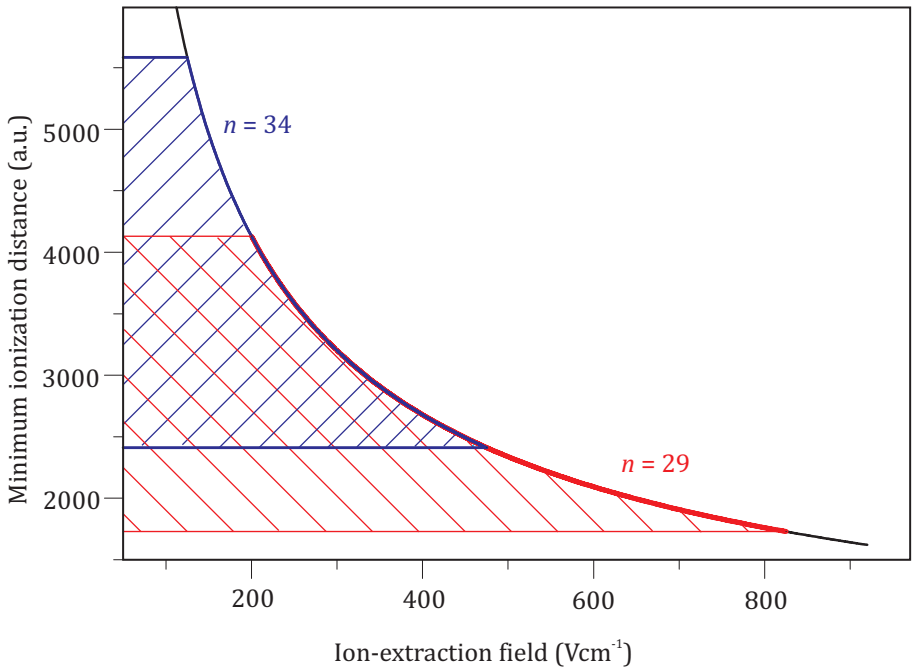

Figure 5.10: The figure represents the variation of minimum ionization distance with extraction field, calculated using the Eq. 1.37.

The mean values were fitted to straight lines to help with the analysis, and clearly show significant differences in the overall ion detectability between each surface with different dopant densities.

The heavily doped Si surface has a much lower ion detectability compared with the lightly doped Si surface. The difference between these ion detectabilities can be rationalized in terms of dielectric constant (ϵ_{Si}) variation and surface dopant charge distribution as before discussed in section 3.3.2. The β factor increases with increasing the dopant density, which enhances the image-charge attraction [55, 99]. Once again, this experimental work is carried out with dopant density of Si surfaces from $N_{\mathrm{D}} \sim 10^{14}$ cm^{-3} to 10^{19} cm^{-3}, resulting in a β-factor from ~ 0.84 to ~ 0.89 (see table. 2.1). This variation in β-factor only changes the minimum ionization distance from ~ 1665 a.u. to ~ 1715 a.u. for $n = 29$ atomic hydrogen Rydberg states, as shown in Fig. 5.12. So the β-factor has only a small effect on the detected ion-signal (the same

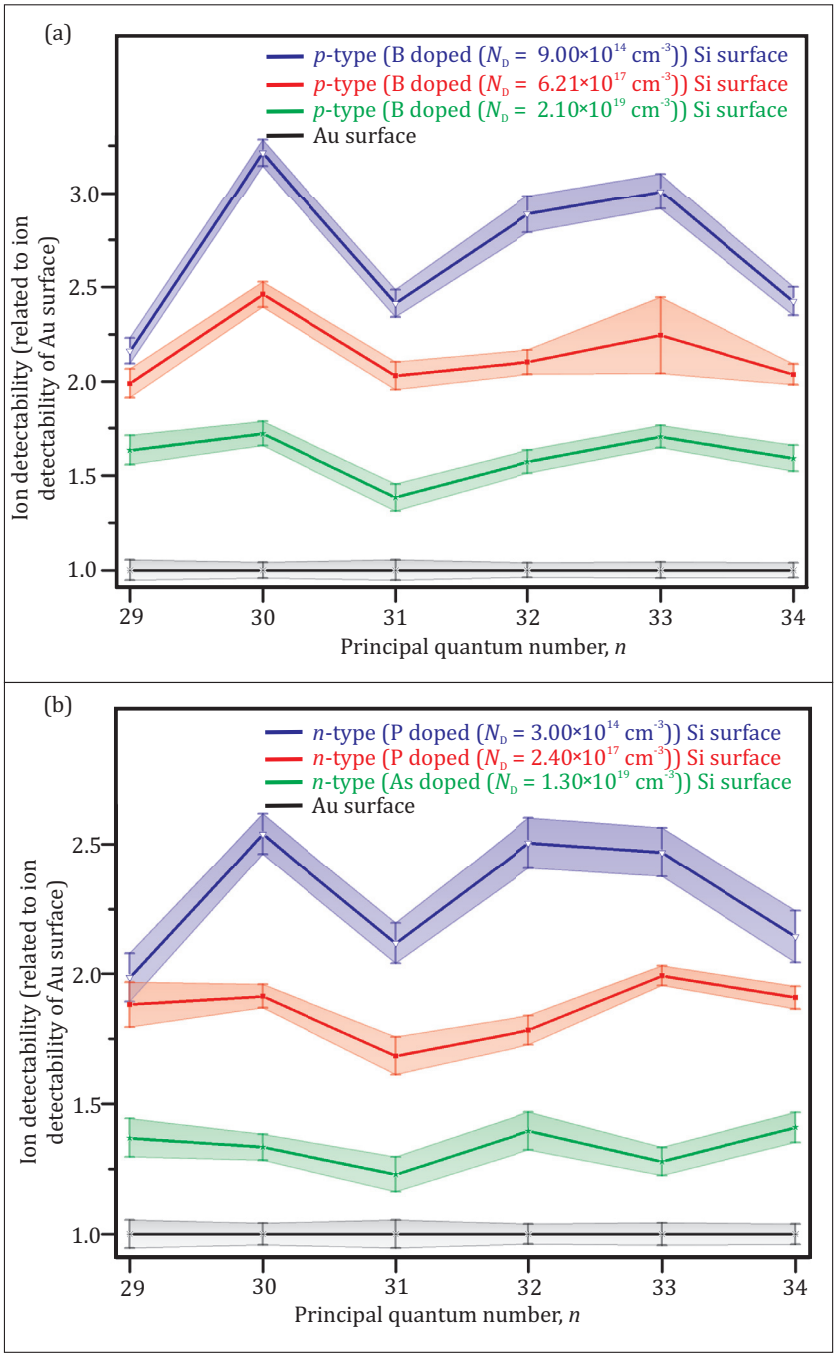

Figure 5.11: The ion detectability for the initial population of the $n = 29 - 34$ atomic H Rydberg states incident at (a) p- type boron $N_{\mathrm{D}} = 2.10{\times}10^{19}$ cm^{-3} (green line), $N_{\mathrm{D}} = 6.21{\times}10^{17}$ cm^{-3} (red line), $N_{\mathrm{D}} = 9.00{\times}10^{14}$ cm^{-3} (blue line) (b) n-type arsenic $N_{\mathrm{D}} = 1.30{\times}10^{19}$ cm^{-3} (green line), phosphorus $N_{\mathrm{D}} = 2.40{\times}10^{17}$ cm^{-3} (red line), phosphorus $N_{\mathrm{D}} = 3.00{\times}10^{14}$ cm^{-3} (blue line) doped Si and Au surfaces. The solid line are connects to the mean values.

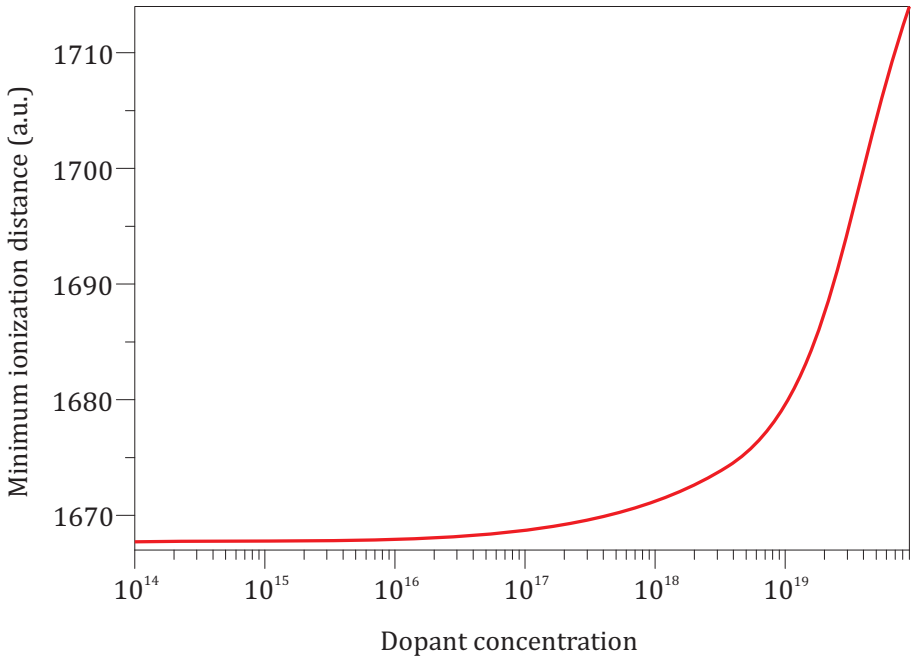

Figure 5.12: The variation of the minimum ionization distance for $n = 29$ atomic hydrogen Rydberg states with respect to the dopant density.

as in the H_2 Rydberg study in the previous section 3.2.1). Therefore, the major part of the ion detectability variation arises from the surface dopant charge distribution.

As discussed earlier in section 3.2.2, the minimum ionization distance increases with the presence of positive surface dopant charges at the same time it decreases with the presence of negative surface dopant charges. However, the incoming atomic H Rydberg states are ionized at the hill of that corrugated '*surface ionization distance*' because H atoms fly at a 15° angle, as shown in Fig. 3.8. Therefore, the distribution area of the positive dopant charges in the surface region influences the Rydberg ionization processes more than the presence of the negative dopant charges, as same as the study of molecular H_2 Rydberg states. Furthermore, after the ionization, the H^+ ions are pushed away from the surface by the presence of the positive dopant charges.

As the dopant density increases, the distribution area of both positive and negative dopant charge field islands become smaller, and the potential variation decays more

rapidly with distance from the surface, so that the effect of the dopant charge near the surface is effectively neutralized, *i.e.* the area sampled by the H^+ ions become effectively '*more neutral*'. Therefore, the detected ion-signal decreases and tends to that of a gold surface. For the above reasons, the ion detection efficiency becomes smaller with increasing dopant density of *p*- and *n*- type doped Si surfaces, and the incident H Rydberg atom at the Au surface shows lower detectable ion-signal than the Si surfaces, as shown in Fig. 5.11.

Furthermore, the slope of ion detectability with principal quantum number increases with decreasing the dopant density, similar to the H_2 Rydberg case. Once again, the gradient of ion detectability with principal quantum number between heavily and lightly doped Si surfaces is smaller for the H atomic Rydberg states than the H_2 molecular Rydberg states due to the smaller variation of the ionization distances for the $n = 29$ to 34 Rydberg states. For that reason, the gradients of ion detectability with principal quantum number at the low and high dopant density of Si surfaces show smaller variation. This effect is clearly shown in Fig. 5.9 and 5.11.

Therefore, this collection of experimental studies clearly shows that the surface ionization profile strongly depends on the dopant density for both *p*- or *n*- type doped Si surface, confirming the previous observation reported for H_2 in chapter 3.

5.4 Conclusion

The results presented in this chapter have demonstrated the interaction of atomic H Rydberg states with Si semiconductor and Au surfaces through study of the surface ionization profiles.

The ion detectability method is used to compare the surface ionization profiles for incident atomic H Rydberg states at several target surfaces. Ion detectability is slightly

higher for p-type Si surfaces compared with n-type doped Si surfaces at similar dopant densities due to the comparably large distribution area of the positive surface dopant charges present at the p-type Si surface. As the dopant concentration increases, the distribution area of surface dopant charges becomes smaller and the potential decay length becomes shorter, so that the area sampled by the H^+ ions become more neutral. Furthermore, the β-factor also increases with increasing the dopant concentration. Therefore, the overall ion detectability decreases with increasing the dopant concentration for both p- and n- type Si surfaces.

The H Rydberg state collisions with the doped Si surface shows similar ion detectability variation with dopant type and dopant density as for the case of the incident molecular H_2 Rydberg states. The surface ionization profiles for both Rydberg species (atomic and molecular hydrogen Rydberg states) show similar effects when altering the dopant type or dopant density. These experimental studies point to a clear conclusion about the detectable ion-signal variations between the different doped Si surfaces, which are purely attributed to the nature of target surfaces (surface dopant charges), rather than the nature of the incident atom or molecule.

Chapter 6

Theoretical trajectory simulations

6.1 Introduction

In this chapter, a theoretical model is developed to describe the surface ionization of Rydberg atoms and molecules and the subsequent detection of the positive ions at various doped Si surfaces.

Previous work by Dunning and co-workers showed that the interaction and ionization of Xe Rydberg states at metal or semiconductor surfaces is highly sensitive to the presence of the stray field at the surface [50, 54–56, 106]. In their work, the effect of patch charges on the surface ionization and ion detection process was included by modeling the surface as a regular array of alternating islands of positive and negative charges [54–56, 106] and solving the Laplace equation for the surface potential at any given point above the surface [50]. Their calculations involved running Monte-Carlo trajectory simulations for both the Rydberg atom or molecule and the subsequent positive ion core. The surface ionization process was described classically by the over-the-barrier (OTB) model [50, 54, 106], assuming a straight line Rydberg trajectory towards the surface, but taking into account the effect of the patch charges on the height of the potential barrier between the ion core and the surface. After ionization

(when the energy of the Rydberg electron is above the height of the potential barrier) the ion trajectory followed simple equations of motion under the influence of the externally applied electric field and the surface fields. Using this approach, Dunning and co-workers were able to successfully model their experimental ionization profiles, but the dimensions of their regularly alternating charge islands were somewhat unrealistic [50].

A scheme similar to the work of Dunning and co-workers will be followed in this chapter, but instead of describing the dopant charges as equally (but arbitrary) sized islands distributed in the surface region (approximately valid for heavily doped Si surfaces), the description of the charge distribution at the surface used in this work is based on the type of the dopant atom (donor or acceptor) and the dopant density of the dopant, and is applicable to any target surfaces with various degrees of roughness.

6.2 Classical over-the-barrier model

Before considering the details of the trajectory simulations and the description of the semiconductor surface charge distribution, it is useful to briefly review the classical OTB model which is employed to describe the surface ionization process [46]. Quantum mechanically, Rydberg ionization can take place through resonant tunneling of the excited electron into a vacant level in the surface. The probability of an electron tunneling through the potential barrier drops off exponentially with the width of the potential barrier (see Eq. 1.1). In the *classical* OTB model, it is assumed that ionization occurs as soon as the height of the electronic potential barrier between the Rydberg ion core and the target surface dips below the energy of the electron (the top of the barrier is a saddle point in the one-electron potential). The ionization probability is therefore assumed to rise from zero to one, or the ionization rate rises from zero to infinity, at the critical ionization distance. The corresponding ionization

profile (detected ion-signal as a function of extraction field) is also expected to be a step function, assuming there is no significant spread of kinetic energies of the incoming molecules.

6.2.1 Saddle point energy

The overall one-electron potential (given by Eq. 1.40 and 1.41) exhibits a saddle point and a finite-width barrier on the surface side of the ion core. The width and height of the potential barrier decrease when the atom approaches the surface, easing the charge transfer processes. The analytic expression for the position of the saddle point in the ion core frame is given for a H atom by [149]:

$$z_{\text{saddle}} = -\left(1+\sqrt{\frac{-5+4\sqrt{2}}{7}}\right) D \approx -0.693673D \tag{6.1}$$

where z_{saddle} is the distance of the saddle point along the atom-surface axis, and D is the Rydberg atom-surface separation. The energy or height of that saddle point is given by

$$E_{\text{saddle}} = \frac{-7\sqrt{5+4\sqrt{2}}}{4D\left(1+2\sqrt{2}\right)} - \frac{1}{4D} \approx \frac{-1.742}{D}. \tag{6.2}$$

The saddle point of the one-electron potential can be expressed differently in the presence of a uniform electric field (F) along the atom-surface axis, and is given by the equation [149]:

$$z_{\text{saddle}} = -0.693673D + 0.044466FD + 0.006259DF^2 + 0.00022DF^3 + OD\left(F^4\right). \tag{6.3}$$

The energy of the saddle point is also altered as [46]:

$$E_{\text{saddle}} \approx -0.693673FD - 1.7422/D. \tag{6.4}$$

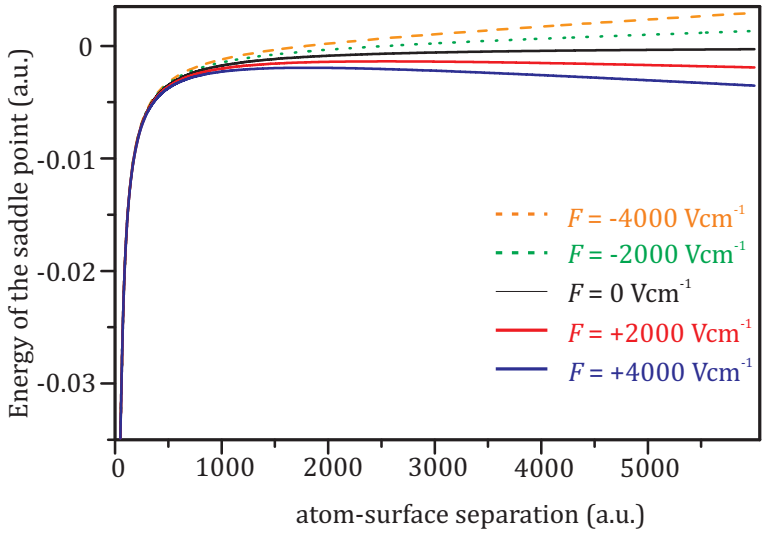

Figure 6.1: The saddle point energy variation with respect to the atom-surface separation at the presence of uniform electric field of -4000, -2000, 0, +2000, and +4000 Vcm^{-1}, which is calculated based on the Eq. 6.4.

The variation of saddle point energy of the one-electron potential with respect to the atom-surface separation in the presence of various uniform electric fields (-4000, -2000, 0, +2000, and +4000 Vcm^{-1}) is illustrated in Fig. 6.1. It clearly shows that the energy of the saddle point increases as the uniform electric field decreases. However, the variation of saddle point positions for the above electric fields is small because the saddle point position is mainly influenced by the atom-surface separation (see Eq. 6.3).

The above equations (Eq. 6.3 and 6.4) clearly show that the saddle point shifts toward the ion core and the saddle height of the overall potential barrier becomes lower (higher) in the presence of positive (negative) surface dopant charges, the effect of which is equivalent to an increased field. Thus at a positive (negative) area of surface dopant charge, the charge transfer process will take place at larger (smaller) distance from the surface, leading to an onset of the ionization profiles at lower (higher) ion-extraction fields.

6.2.2 Ion detection efficiency

After surface ionization, the resulting positive ions are pulled away from collision with the surface and are accelerated towards the detector by the externally applied electric field. For a given ionization distance and velocity of the ion towards the surface, there is a minimum ion-extraction field that is required to pull the ion away from the surface (see Eq. 1.38). As explained above, the OTB approach assumes that ionization occurs at a single surface separation (for a given state σ), such that for a single ion velocity and without the presence of inhomogeneous surface fields, the ionization profile is predicted to be step function, $S_\sigma(E, v_\perp) = h(F - F^\sigma_{\rm crit}(v_\perp))$, at the critical ion detection field $F^\sigma_{\rm crit}(v_\perp)$, as given by Eq. 6.5. Including the velocity distribution of ions ($f_{v_\perp}$) the overall ion detection signal becomes

$$S_\sigma(F) = \int_0^\infty h(F - F^\sigma_{\rm crit}(v_\perp)) f_{v\perp} dv_\perp. \tag{6.5}$$

The lower limit of the critical ion-extraction field ($F^{lim}_{\rm crit}$) and the corresponding ionization distance ($D_{\rm crit}$) can be estimated from the low kinetic energy ion detection limit $F_{\rm min} = 1/4D_i^2$ (see Eq. 1.38). Previous studies using Xe Rydberg atoms have shown that the ion detection field scales as n^{-4} [54, 56]. However, So [46] has shown that the critical ion detection field is no longer independent of principal quantum number due to the non-negligible component of the kinetic energy of the ion, and it was found for H atoms that the corresponding ionization distance varied nonlinearly from $3.9n^2 - 4.5n^2$ a.u. In the absence of inhomogeneous surface fields, the critical ion-extraction field is given approximately by [46]:

$$F_{\rm crit}(n, T_\perp) \approx \frac{0.017}{n^4} + \frac{\sqrt{T_\perp}}{(3.834)^{\frac{3}{2}} n^3} + \frac{T_\perp}{3.834 n^2}, \tag{6.6}$$

such that in the limit of zero velocity (and kinetic energy), the critical ion-extraction field is proportional to n^{-4}.

6.3 Surface potential at Si semiconductor surfaces

It was discussed in chapter 3 that a doped Si semiconductor surface can be modeled as a distribution of localized and delocalized charges, whose polarity depends on the dopant type. It was shown that using such a model, the variations in the experimentally observed ionization-profiles for different Si surfaces could be qualitatively explained. This section further develops the surface dopant charge model described in chapter 3, outlining the calculation of the model surface potential, which is subsequently used in the calculation of the ionization distance and ion trajectory in the Monte-Carlo simulations.

As explained in chapter 3, the charge distribution at the surface can be modeled by a regular repeating unit which includes a point charge representing the dopant atom surrounded by a sea of delocalized charge of the opposite polarity (such that the unit cell is overall neutral). Calculating the surface potential (ϕ) at a given point above this two dimensional surface of known charge distribution involves first solving the *2D* Poisson equation for the potential at the vacuum-surface interface ($z = 0$):

$$\frac{\partial^2\phi}{\partial x^2} + \frac{\partial^2\phi}{\partial y^2} = -\frac{\rho}{\epsilon_o} \tag{6.7}$$

where ϵ_o is the permittivity of the vacuum and ρ is the charge density. The point charge is always chosen to lie in the middle of the unit cell and assigned as an area of 1 a.u., therefore, has a charge density of ± 1 a.u.; whereas the delocalized surface charge was the remaining area of the unit cell ($\lambda^2 - 1$ a.u.) giving a charge of $\mp\frac{-1}{\lambda^2-1}$ a.u. (λ is the length of unit cell, which is equal to the dopant spacing, see Eq. 2.12). The sign

of the charge density at the point charge and delocalized surface charge depends on dopant type. However, the overall charge density of the unit cell is maintained as zero. Applying a *2D* Fourier transform to both sides of Eq. 6.7 and solving for ϕ gives:

$$\phi_{x,y} = \frac{1}{2\pi\epsilon_0} \int_{-\infty}^{\infty} \int_{-\infty}^{\infty} \frac{\int_{-\infty}^{\infty} \int_{-\infty}^{\infty} \rho_{x,y} e^{-ik_x x - ik_y y} dx dy}{k^2} e^{ik_x x + ik_y y} dk_x dk_y \tag{6.8}$$

where k is the wavevector index of the Fourier mode of the Fourier transform, which is related to its components k_x and k_y and is expressed by the following equation:

$$\begin{aligned} k &= \sqrt{k_x^2 + k_y^2} \\ &= \frac{2\pi N}{\lambda} \end{aligned} \tag{6.9}$$

where N is the size of the spanning length in the x and y axes. The resolution of the surface potential used here is $N \times N \equiv 100 \times 100$ pixels spanning the area for each doped Si surfaces.

Figure 6.2 shows an example of the surface potential. Once the potential at the surface has been calculated, the potential at any point above the surface can then be calculated by solving the Laplace equation:

$$\frac{\partial^2 \phi}{\partial x^2} + \frac{\partial^2 \phi}{\partial y^2} + \frac{\partial^2 \phi}{\partial z^2} = 0. \tag{6.10}$$

The electric field can be computed by taking the gradient of the potential. To achieve good agreement between the theoretical and experimental ionization profiles, a single scaling parameter for the surface dopant charge potential is introduced to the work presented below. The best fitting scaling parameter for the point charge density is

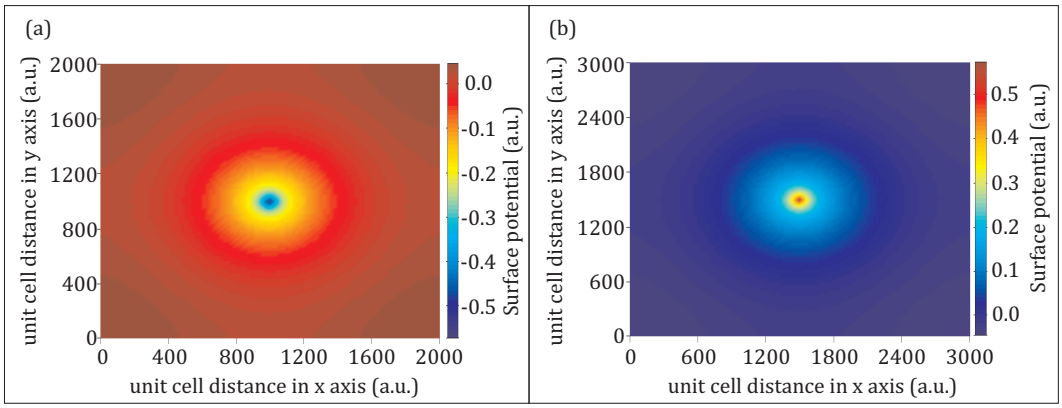

Figure 6.2: The calculated surface dopant potential of (a) *p*-type (boron-doped (N_{D} = 9.00×10^{14} cm^{-3})), and (b) *n*-type (phosphorus-doped (N_{D} = 3.00×10^{14} cm^{-3})) Si surfaces at the surface (z = 0 a.u.), which are calculated by solving Poisson's equation.

chosen as 0.6 a.u. and the delocalized potential of the rest of the area also modified as $\frac{-0.6}{\lambda^2-1}$ a.u. However, this scaling parameter has one drawback; the magnitudes of the surface dopant charges not only vary with dopant type but also with dopant density. Therefore, the scaling parameter also depends on density and the type of the Si surface. These trajectory simulations, however, were carried out with a fixed scaling parameter to reduce the complexity. The following subsections will clearly explain how the distribution area of the surface dopant charge potential near the surface region varies with different doped Si surfaces.

The potential distribution in the surface region becomes inhomogeneous due to the presence of the surface dopant charge field islands. The OTB ionization distance of the Rydberg species and the potential energies are calculated numerically via a searching procedure. For a specific principal quantum number and electric field, a corrugated '*surface ionization distance*' is calculated, which gives the positions above the surface where the saddle height equals the Rydberg energy at particular x, y coordinates. The range of feasible ionization distances leads to a range of critical ion detection fields, so that the ionization profiles are no longer step functions as given by Eq. 6.5. The

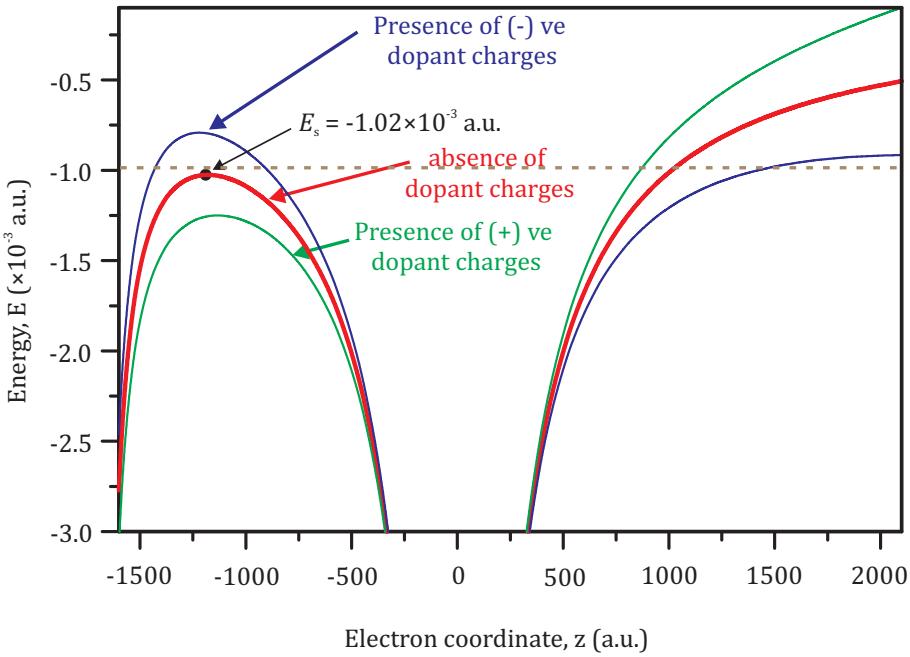

Figure 6.3: The electron potential for $n = 17$, $(nd2)_1$ Rydberg molecule. The horizontal - - - line indicates the binding energy of an $n = 17$, $(nd2)_1$ Rydberg molecule ($\sim 9.57\times10^{-4}$ a.u.).

most positive areas of the surface dopant charges give the ionization at the greatest distance from the surface due to the reduced saddle point height, and an increased repulsive force on the resulting ion. The reverse is true for the larger area of the negative surface dopant charge field and it reduces the ionization distance through an increase the saddle point height [54], shown in Fig. 6.3.

The framework of this potential for an $(nd2)_1$, $n = 17$ Rydberg state of H_2 is shown schematically in Fig. 6.3 in the absence of an applied ion-extraction field and an atom/molecule-surface separation is assumed as $D = 3.1\ \nu_o^2$ a.u., (*i.e.* $D \sim 1700$ a.u. for $(nd2)_1$, $n = 17$ Rydberg states), where ν_o is the effective principal quantum number. The top of the barrier lies at an energy of $\sim -1.02\times10^{-3}$ a.u. in agreement with Eq. 6.2, which is equal to the binding energy of an $n = 17$, $(nd2)_1$ state of H_2 ($\sim$ -9.57×10^{-4} a.u.). This suggests that Rydberg molecules with $n = 17$, $(nd2)_1$ will

be ionized at a perpendicular molecule-surface separation of $D \sim 1700$ a.u. However, the previous theoretical simulation work on H Rydberg atoms has clearly shown that even in the absence of dopant charges the range of minimum ionization distances $D_{\min}$ for a given applied field is broadened by the presence of patch charges due to other surface inhomogeneities, such that some trajectories below $D_{\min}$ are detected while not all trajectories above $D_{\min}$ are detected [46]. The width of the ionization distance spread was found to be given by $\pm$ 1.0 ν_o^2 a.u. [71, 95]. Using these arguments above, the ionization is assumed to occur over the range of perpendicular distances from 2.1 ν_o^2 a.u. to 4.1 ν_o^2 a.u. with a positive skewed probability distribution maximized at 3.1 ν_o^2 a.u. and this effect is superimposed on the potential corrugation due to the dopant atoms.

6.3.1 Potential variation for different dopant type

The *p*-type doped Si surface exhibits positive delocalized surface charges and negative point charges near the surface region, whereas *n*-type doped Si surfaces exhibit negative delocalized surface charges and positive point charges (as explained in the previous section 3.2.2). The calculated potential at the surface for the *p*- and *n*- type doped Si surfaces are illustrated in Fig. 6.2. Note the point charge of the dopant atom is at the centre of the unit.

As explained in the previous sections, the one-electron potential is modified by the surface dopant charges at the surface. Negative (positive) dopant charges present in the surface region induce ionization closer to (further from) the surface. This is illustrated in Fig. 6.4, which shows the calculated ionization distances at both *p*- and *n*- type Si surfaces, and these show similar minimum ionization distance variation. However, the ion detection probability is considerably higher for *p*-type Si surfaces than *n*-type Si surfaces due to the additional repelling force, which is created from their widely

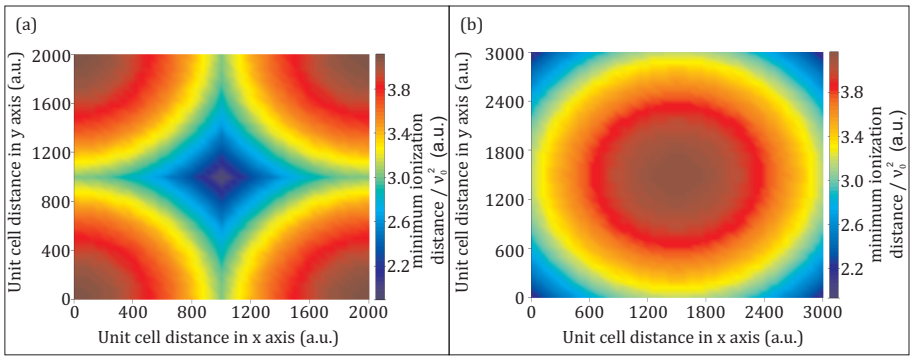

Figure 6.4: The minimum ionization distance at where ionization occurs for the Rydberg states incident at the (a) *p*-type (boron doped ($N_D = 9.00\times10^{14}$ cm^{-3})), and (b) *n*-type (phosphours doped ($N_D = 3.00\times10^{14}$ cm^{-3})) Si surfaces at the presence of a surface potential.

distributed surface dopant charges. Therefore, the ion detection probability is a main factor to determine the detected ion-signal when comparing the *p*- and *n*- type doped Si surface with similar dopant density. This is because the ion trajectory is affected by the potential much closer to the surface than the position of ionization.

6.3.2 Potential variation for different dopant density

In the model used here, the size of the repeating unit cell is equal to the mean dopant spacing, λ. As the dopant concentration increases, the mean dopant spacing, λ, decreases, and introduces higher frequency variations of the surface potential over the xy plane. The higher frequency modes of the surface potential decay away from the surface more rapidly than lower frequency modes, and this is illustrated in Fig. 6.5. Consequently, as the dopant concentration increases, the effective range of the perturbing surface dopant charges decreases, and for Rydberg atoms which ionize at relatively long range from the surface, the perturbation on the ionization distance and ion detection efficiency becomes smaller and tends to that of a surface with heavily doped atoms. This behaviour was illustrated by the experimental results of the Rydberg states of H_2 molecule in section 3.3.2 and the H atom in section 5.3.2.

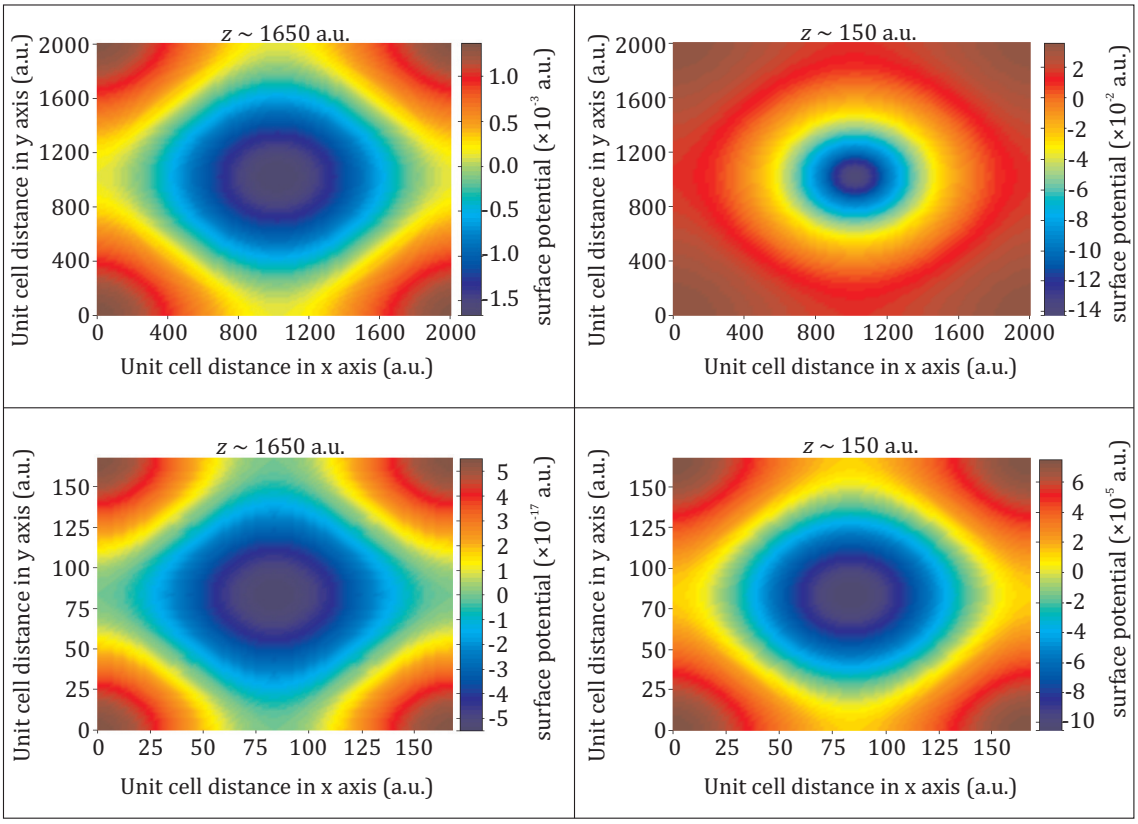

Figure 6.5: The calculated surface dopant potential for lightly (top of the figure) and heavily (bottom of the figure) doped *p*- type Si surfaces at near (left side of the figure) and far (right side of the figure) at distances from the surface. Note the very different scales indicated on each figure.

A further interesting question arises as to how this potential decay influences the ionization process of higher-n and lower-n Rydberg states. The magnitude of the surface potential becomes smaller when increasing the distance between the Rydberg ionic-core and the target surface (shown in Fig. 3.6). Furthermore, the decay rate of this surface potential becomes more rapid with increasing dopant density (it is independent on the dopant type). Figure 6.5 shows the surface potential variation for high and low ionic core surface separation for lightly and heavily dopant densities of Si surfaces. It is clearly shown that the surface potential variation between the large and short Rydberg surface separation is of noticeably higher amplitude for the lightly doped Si surfaces than the heavily doped Si surfaces. For that reason, the experimental surface ionization profiles for the lightly doped Si surfaces show considerable variation in their detected ion-signal between the higher-n and lower-n Rydberg states.

6.4 Trajectory simulation

The numerical simulations of the effect of the dopant charge distribution on the ionization distance and ion detection probabilities are undertaken using two-dimensional Monte-Carlo trajectory simulations. The incoming Rydberg molecule/atom trajectories are constrained to move in the xz plane and were selected from a random set of initial position (x_0), whereas the initial atom-surface separation (z_0) is set at 30 n^2. The Rydberg molecules/atoms are initiated to ionize when the trajectories intersect the pre-computed ionization surface of the given ion-extraction field determined using the OTB model. The trajectory simulations are computed using a Runge-Kutta algorithm, which is implemented using Matlab's ODE 45 differential equation solver [150].

Trajectories are simulated to reproduce the experimental conditions using the following concepts. (i) The pulsed nozzle produces a distribution of velocities in the supersonic

beam. The range of initial velocities is sampled by using a Monte-Carlo technique in which many trajectories are calculated with random initial velocities selected from a velocity distribution corresponding to a temperature of 1 K. Perpendicular and parallel velocity components are added to a mean beam velocity (v) of ~ 2535 ms^{-1} for the molecular H_2 Rydberg states [71, 92] and ~ 1505 ms^{-1} for the atomic H Rydberg states [46]. (ii) The surface is oriented at a 7° or 15° angle to the central beam axis for the molecular H_2 and atomic H Rydberg states respectively, and the velocity components in the x and z directions (with respect to the surface) are calculated according to the following equation:

$$\begin{aligned} v_x &= v\cos\theta \\ v_z &= v\sin\theta. \end{aligned} \tag{6.11}$$

The perpendicular component of kinetic energy ($T_\perp$) is also calculated for each trajectory. (iii) Using the simple classical OTB model, ionization occurs when the electron energy exceeds the height of the saddle point. (iv) The ion trajectories are numerically integrated, including the effects of their image-charge attraction towards the surface, the applied ion-extraction field and the dopant charge field. The trajectory simulation is terminated either when the ion strikes the surface or when the ion escapes the surface and is detected by the MCPs. The signal is calculated from the fraction of trajectories that hit the MCPs. (v) The calculations are repeated for a series of applied electric fields to generate the surface ionization profile, and then the effects of direct field ionization are included by the high field termination of the simulated profile, which is equal to the maximum threshold field that depends on the effective principal quantum number. The effect of field ionization is not included in the simulations, and therefore, simulated profiles do not show the high-field cut-off as in the experiment.

6.5 Comparison with experimental surface ionization profiles

Having found the position of ionization, the minimum field required for ion detection is calculated using the theory outlined above. In this section the ion detection is calculated without considering the effect of the surface dopant charge field and just considering the effect of velocity spread and minimum ionization distance distribution. The minimum ionization distance is chosen to be $3.1 \pm 1\ \nu_o^2$ a.u. [95], and the trajectories were run with the ionization-distance interval of $0.01\ \nu_o^2$ a.u. and a weighting reflecting the positive skewed distribution. Figure 6.6 shows the calculated surface ionization profiles for $n = 21$ molecular H_2 Rydberg states (red line) using the above modified trajectory simulation. This is compared with the corresponding results without considering the velocity distribution and using a fixed ionization-distance (blue line) and including the range of ionization distances (green line).

Figure 6.7 shows the comparison of experimental surface ionization profiles for the heavily doped ($\approx 10^{19}$ cm^{-3}) and the results of the theoretical trajectory simulations. The profile shows the behavior observed when exciting a population of $(nd2)_1$ Rydberg states with a principal quantum number $n = 21 - 17$, as described.

It can be seen that the onsets of the ionization calculated from the trajectory simulations are in good agreement with the experimental results of the n-type arsenic doped Si surface, qualitatively agreeing with the overall envelope of the ionization profile but not showing the resonance structures. Furthermore, these theoretical trajectory simulation results also reproduce our group's earlier theoretical work for the metal surface [71, 95]. Therefore, these results make us confident that our trajectory simulations and their input parameters accurately reflect the experiment. Previous experimental results of rough Al surface ionization profiles show that the long tail

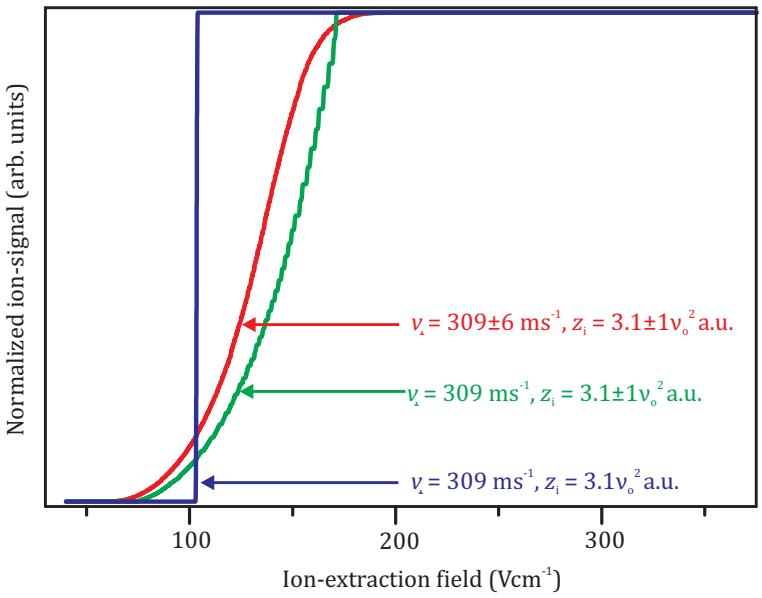

Figure 6.6: Trajectory simulation for $n = 21$ molecular H_2 Rydberg state detected ion-signal as a function of the ion-extraction field (red line): simulation without considering either the velocity distribution or the distribution of minimum ionization distance (blue line) and simulation without considering the velocity distribution, but considering the distribution of minimum ionization distance (green line).

part of the profile deviates slightly from the simulation results because the Rydberg molecule population is redistributed by BBR stimulated transitions [70, 71] and is also affected by the approximation for the surface roughness. Theoretical trajectory simulation for the surface ionization profiles at rough Al surfaces will be explained in section 6.6. However, compared with the 231.9 nm roughness of Al surfaces used in previous experimental studies [71], the Si surface is expected to have a roughness of 1.2 nm due to the formation of SiO_2 [105, 151]. Therefore, the Si surface roughness is less important in the calculation of the minimum field required to pull the ion away from the surface. On the other hand, in the case of semiconductor surfaces, the conducting surface image-charges are reduced by the β-factor [54–56] and the distribution of positive and negative dopant charges appear opposite in sign for the p- and n- type Si surfaces. Therefore, the trajectory simulations are expected to be affected by the effect of the surface dopant charges, and this effect should vary with dopant density

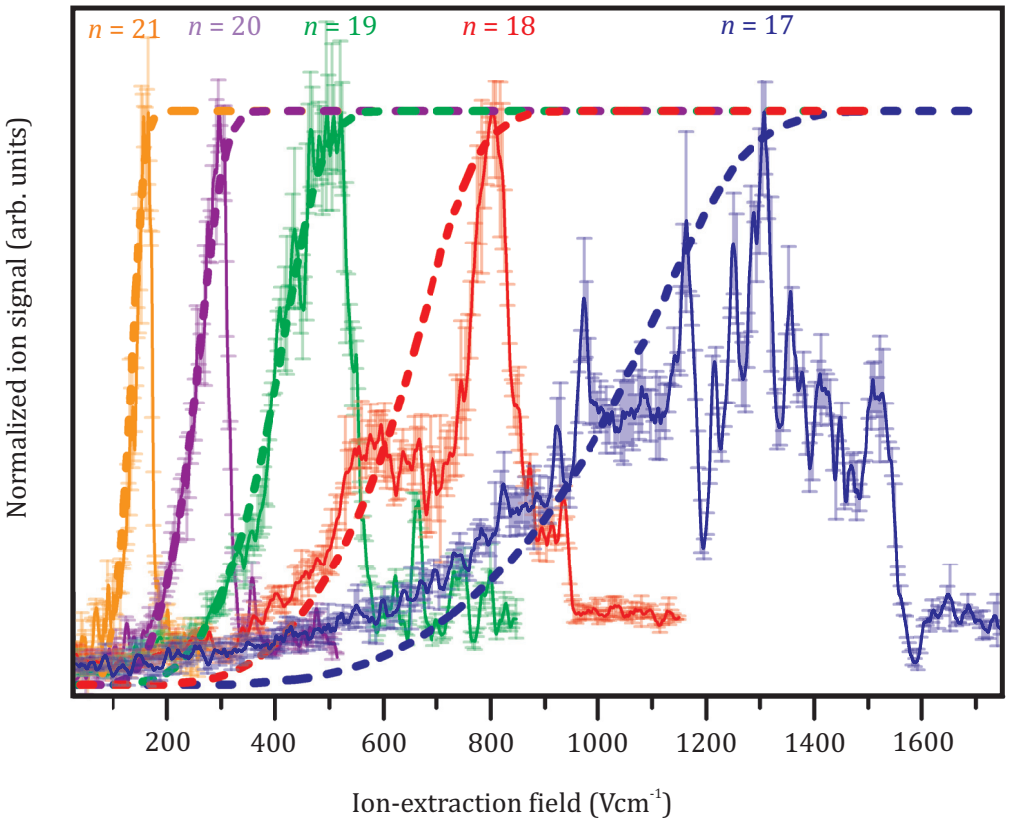

Figure 6.7: Experimental (– line) and simulated (- - - line) surface ionization profiles for the population of $(nd2)_1$, $n = 21-17$ Rydberg states incident on the n-type arsenic doped Si surface, recorded as a function of scaled ion-extraction field.

and type of Si surfaces. The following subsection clearly shows this effect.

6.5.1 Modeling the effect of the β-factor

The minimum extraction field required to pull the ion away from the surface depends on the β-factor, see Eq. 1.38, and the β-factor is correlated to the dopant density of the Si surface. Theoretical trajectory simulations have been carried out with various factors without including the effect of the surface dopant charge field using the same theory outlined previously. The variation of the trajectory simulations for various doped Si semiconductor surfaces due to the effect of the β parameter is clearly illustrated in Fig. 6.8. This simulation study gives a brief idea of how much the β-factor affects the surface ionization profile through the simple classical OTB model. The β-factors of these three surfaces are 0.841, 0.842, and 0.889, and these small changes can have only a small effect on the minimum extraction field, $F_{\min}$, due to altering the image-charge interaction (see section 3.2.1). Therefore, the theoretical trajectory simulations only show minor variations in their surface ionization profiles, as seen in Fig. 6.8.

For heavily doped Si surfaces, the deviation between the experimental surface ionization profiles and the theoretical simulated profiles becomes smaller, as shown in Fig. 6.7 and Figure 6.8. The trajectory simulations for lower dopant density of surface, however, do not fit perfectly with the experimental results at lower extraction field: a higher ion-signal is detected in the low field region compared to the simulation.

These studies clearly show that the trajectory simulations without consideration of the surface potential are not enough to explain the experimental surface ionization profiles for various β-factors of Si surfaces. Therefore, the surface dopant charge field is likely to be the key factor that determines the detected ion-signal in these experimental studies. The β-factor only varies with dopant density of the dopant element, but is independent of the type of the dopant elements. Therefore, these numerical simulations

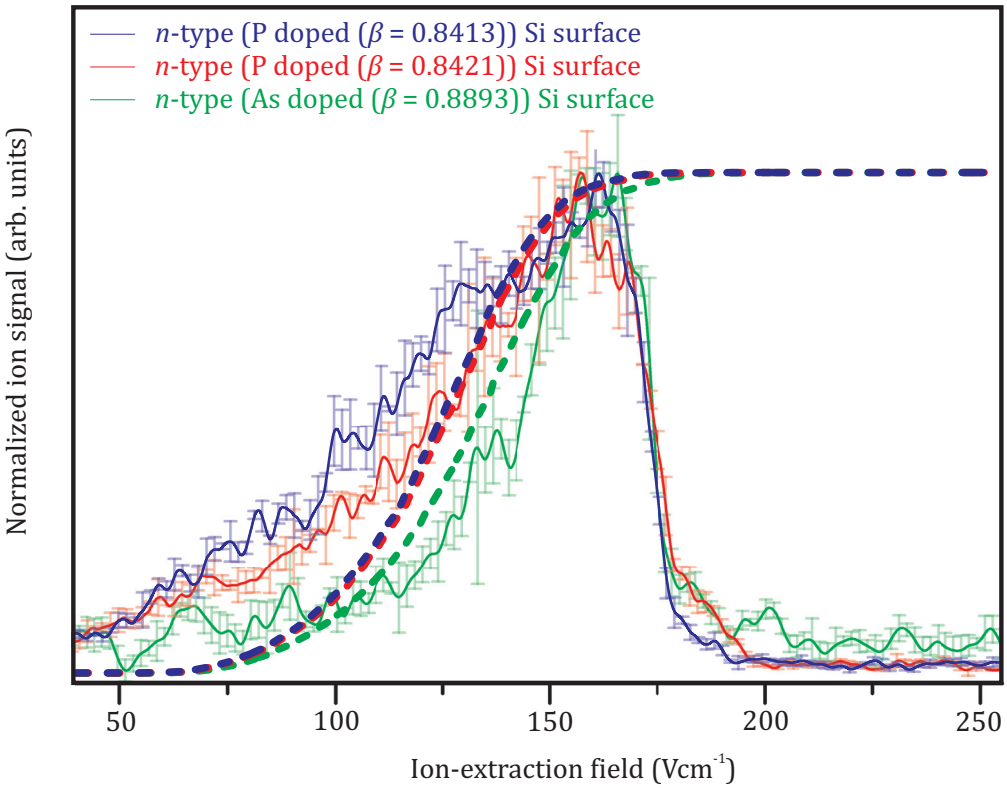

Figure 6.8: Experimental (– line) and trajectory simulated (- - - line) surface ionization profiles for the population of $(nd2)_1$, $n = 21$ Rydberg states incident on the n-type arsenic ($N_D = 1.30\times10^{19}$ cm^{-3}) (green line), phosphours ($N_D = 9.52\times10^{15}$ cm^{-3}) (red line) and phosphours ($N_D = 3.00\times10^{14}$ cm^{-3}) (blue line) doped Si surfaces, recorded as a function of scaled ion-extraction field.

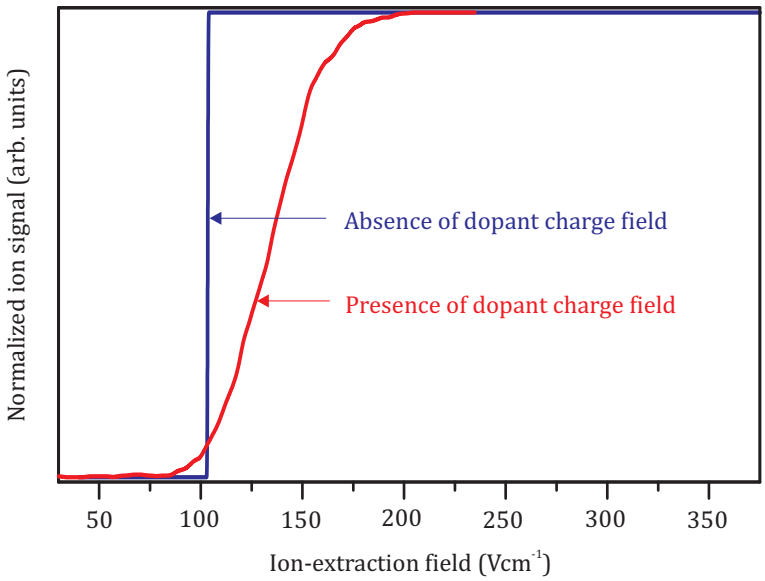

Figure 6.9: The simulated surface ionization profiles for $n = 21$ molecular H_2 Rydberg states with (red line) and without (blue line) the dopant charge field.

for equivalent dopant density of the p- and n- type doped Si surfaces show similar ion detection signals, but experimental studies show some significant differences.

6.5.2 Modeling the effect of dopant type

The numerical trajectory simulations were performed again including the effect of the surface potential. Here, the incident beam angle and magnitude of the perpendicular velocity components are fixed to investigate the effect of the surface dopant charge fields on the surface ionization profiles. Figure 6.9 shows the calculated surface ionization profile for $n = 21$ H_2 Rydberg molecules incident on the Si surface (red line) and compares it with the corresponding simulation without the dopant charge field (blue line).

The trajectory simulation is also extended to both p- and n- type doped Si surfaces. In these simulations, the dopant density and β-factor are kept constant for comparing p- and n- type doped Si surfaces. The distribution area of the positive and negative

charges varies with dopant type, giving different surface potentials. The *p*-type Si surface exhibits a comparably wider distribution of the area of the positive potential than the *n*-type Si surface (see Fig. 6.2). As discused earlier, the positive dopant charge field increases the ionization distance by reducing the saddle point height where as the negative charge field reduces the ionization distance through an increase in the saddle point height, as shown in Fig. 6.3. Therefore, the Rydberg states ionize earlier in the presence of the widely distributed area of positive dopant charges for the *p*-type Si, compared to the *n*-type with its widely distributed area of negative dopant charges (see Fig. 6.4). After ionization, the positive dopant charge fields oppose the approach of the resultant H_2^+ ions to the surface, reducing the extraction field needed to generate a signal. Therefore, *p*-type Si surfaces show a larger fraction of detected ion-signal at low ion-extraction field. The results of the trajectory simulations are compared with the experimental surface ionization profiles for H_2 $n = 20$ Rydberg states incident on the *p*- and *n*- type Si surfaces in Fig. 6.10.

This simple OTB model has provided qualitatively good theoretical predictions for Si semiconductor surfaces of differnt dopant type. The predictions closely match with the experimental results. In the experiment, however, the range of ionization distances and detection probabilities introduced by surface dopant charge fields leads to much broader ionization profiles.

6.5.3 Modeling the effect of dopant density

The trajectory simulations were performed again considering the effect of dopant spacing. The experimental and theoretical trajectory simulations of the surface ionization profiles for the various dopant spacings of Si semiconductor surfaces are shown in Fig. 6.11.

Figure 6.11 clearly show that trajectory simulations for various dopant densities of *p*-

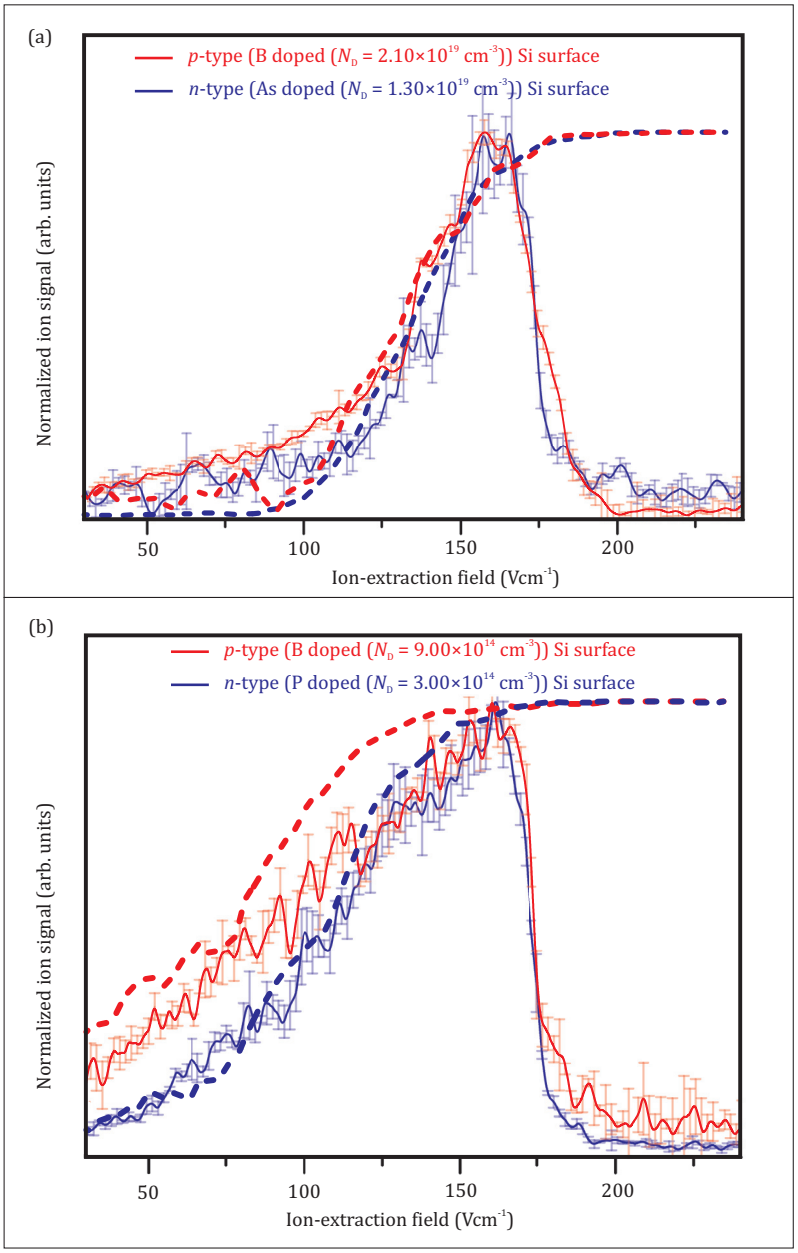

Figure 6.10: Experimental (– line) and simulated (- - - line) surface ionization profiles for the population of $(nd2)_1$, $n = 21$ Rydberg states incident on the (a) heavily doped ($N_{\rm D} \approx 10^{19}$ cm^{-3}) n-type arsenic doped (blue line), and p-type boron doped (red line) (b) lightly doped ($N_{\rm D} \approx 10^{14}$ cm^{-3}) n-type phosphorus doped (blue line), and p-type boron doped (red line) Si surfaces, recorded as a function of ion-extraction field.

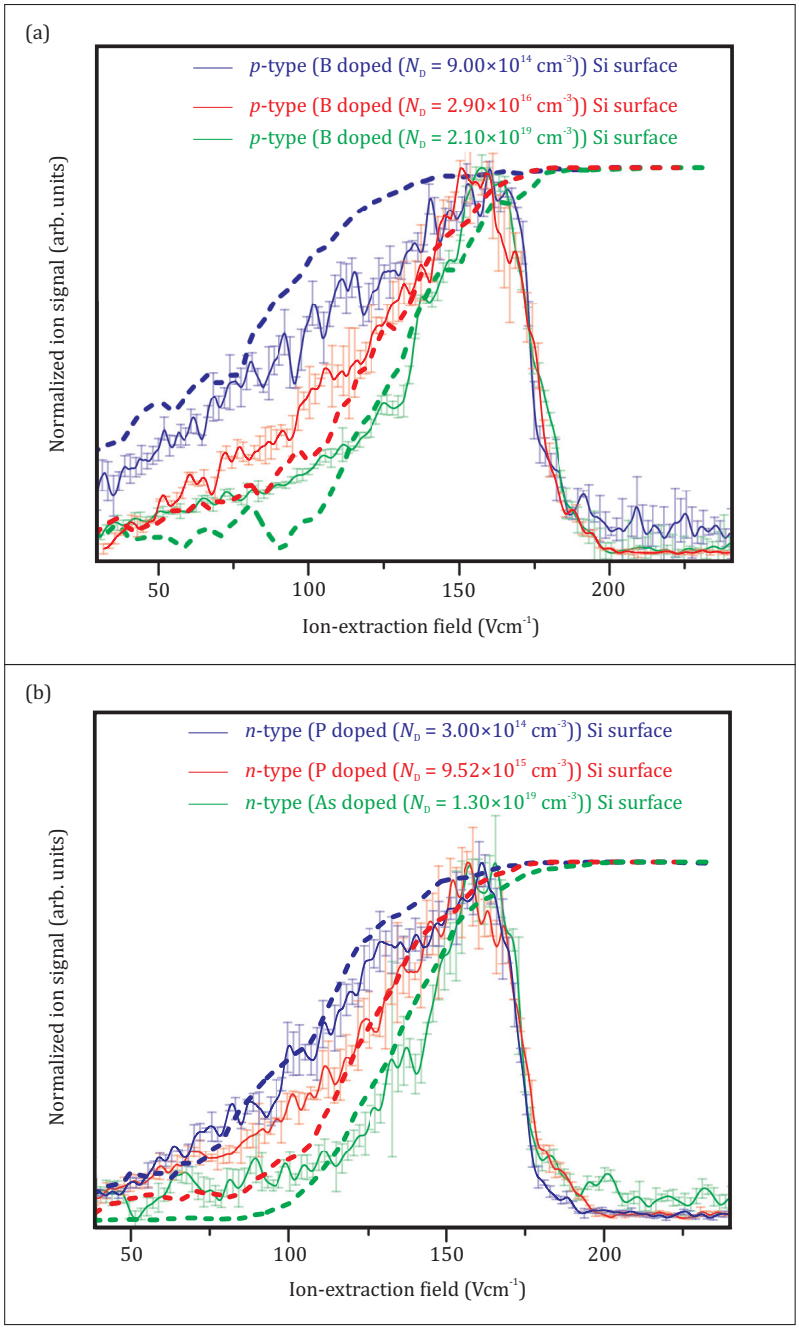

Figure 6.11: Experimental (– line) and simulated (- - - line) surface ionization profiles for the population of $(nd2)_1$, $n = 21$ Rydberg states incident on the (a) p-type boron doped ($N_D = 2.10 \times 10^{19}$ cm^{-3}, green line), boron doped ($N_D = 2.90 \times 10^{16}$ cm^{-3}, red line)and boron doped ($N_D = 9.00 \times 10^{14}$ cm^{-3}, blue line) (b) n-type arsenic doped ($N_D = 1.30 \times 10^{19}$ cm^{-3}, green line), phosphorus doped ($N_D = 9.52 \times 10^{15}$ cm^{-3}, red line)and phosphorus doped ($N_D = 3.00 \times 10^{14}$ cm^{-3}, blue line) Si surfaces, recorded as a function of applied electric field.

and n- type doped Si surfaces qualitatively fit very well with their experimental surface ionization profiles for both dopant types. However, the ion-signal at lowest extraction field in the surface ionization profiles does not quantitatively fit with the experimental surface ionization profiles. The quantitative difference between the experiment and numerical simulation may arise from the surface dopant charge fields producing an inhomogeneous electric field, which causes mixing between Rydberg states of differing m_l states [51] leading to a range of ionization distances. The magnitudes of the surface dopant charge fields are not measured experimentally.

In the future, the surface potential of various doped Si surfaces will be measured using Kelvin probe microscopy [152] (as same as in previous studies [46, 50]). This analysis will give precise information on the magnitude and distribution area of the positive and negative dopant charge fields, improving theoretical simulations.

6.6 Trajectory simulations for a rough Al surface

Previous experimental studies on rough metal surfaces have shown that the surface ionization profiles are broader and shifted to lower extraction field [52, 71]. To date, there has been no theoretical trajectory simulation performed to explain this variation for the rough surfaces. In order to show this variation, trajectory simulations were carried out for a rough metal surface without the contribution of the spatial variation of surface potential, using $\beta = 1$ but considering their surface roughness. The initial velocity distribution is fixed for this simulation as 309 ± 6 ms^{-1}.

In this trajectory simulation, the ionization positions (x_i, z_i) of the Rydberg molecule are calculated as a function of the surface roughness. It is assumed that the surface roughness can be represented by a sine wave of a given wavelength and amplitude,

and is given by the following equation:

$$z_{\rm r} = A \times \sin\left(\frac{2\pi x_{\rm r}}{W}\right), \tag{6.12}$$

where A is the amplitude of the corrugation about the average surface plane position $z = 0$ and W is the spacing of the '*bumps*' in the surface (for the machined Al surface used in refernce [153], the amplitude and spacing of the '*bumps*' in the surface estimated to be $A = 231.9$ nm and $W = 1752.3$ nm).

In this case the ionization positions ($x_{\rm i}$, $z_{\rm i}$) of the Rydberg states relative to a flat plane are given by:

$$\begin{aligned} z_{\rm i} &= z_{\rm r} + \frac{(3.1 \pm 1)\,\nu_o^2}{\sqrt{1 + \left(\frac{2\pi A}{W}\right)^2 \left[\cos\left(\frac{2\pi x_{\rm r}}{W}\right)\right]^2}} \\ x_{\rm i} &= x_{\rm r} + \frac{\left(\frac{2\pi A \times (3.1\pm1)\nu_o^2}{W}\right) \times \cos\left(\frac{2\pi x_{\rm r}}{W}\right)}{\sqrt{1 + \left(\frac{2\pi A}{W}\right)^2 \left[\cos\left(\frac{2\pi x_{\rm r}}{W}\right)\right]^2}}. \end{aligned} \tag{6.13}$$

These equations are determined from the minimum perpendicular distance to any point on the undulating surface (as seen in Fig. 6.12), and this set of coordinates is used as a starting point for a set of ion trajectories. Each ion trajectory will depend on the initial velocity and the image-charge potential, which is assumed to have the same form as Eq. 1.40 and 1.41, and on the applied electric field. The image-charge potential is determined by the perpendicular distance to the surface which itself depends on the surface roughness. The distances between the surface and ions are computed as a function of x and z using regular intervals from $(x_{\rm R} - W)$ to $(x_{\rm R} + W)$. The perpendicular distances ($D_\perp$) are related to those distances along the x and z axes, and typically the program needs to find the nearest of two distances d_1 and d_2 as

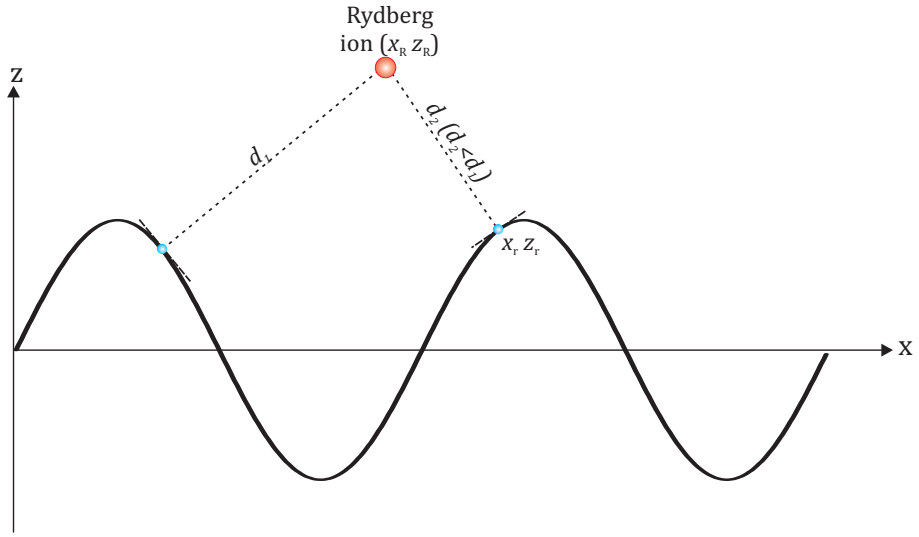

Figure 6.12: Calculated minimum perpendicular distance ($D_\perp = \mathrm{d}_2$) between the ion and the Rough surface.

indicated in Fig. 6.12, and given by:

$$D_\perp = \sqrt{(z_\mathrm{R} - z_\mathrm{r})^2 + (x_\mathrm{R} - x_\mathrm{r})^2}. \tag{6.14}$$

The minimum perpendicular distance is selected, and this smallest distance is used to compute the image-charge potential. This potential is used to find the new velocity and the new position of the ion for each step of the numerical integration of the trajectory. However, the surface roughness may not be constant across wider areas of the surface [70]. Amplitude changes would noticeably contribute to the minimum extraction field, but spacing of the '*bumps*' at the surface (wavelength) would not contribute significantly to the minimum extraction field. Therefore, the amplitude of the surface roughness, A, is calculated randomly, and selected from a Gaussian distribution with a Gaussian width of 0.5 A a.u. and centered at 0.7 A a.u.

The output of the trajectory simulation is compared with the previous experimental study [71], and is shown in Fig. 6.13. It can be seen that the overall envelope of

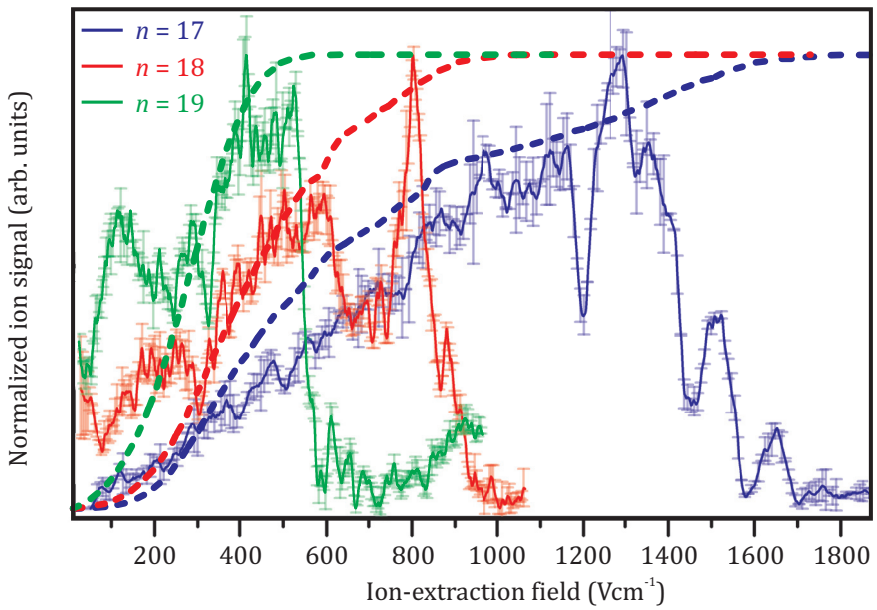

Figure 6.13: Experimental (– line) and simulated (- - - line) surface ionization profiles for $n = 19 - 17$ molecular H_2 Rydberg states incident at the 231.9 nm roughness of the Al surface.

the surface ionization profiles for the calculated trajectory simulation are in good agreement with those seen in the previous experimental study [71]. It is clear that the surface ionization profiles depend strongly on the roughness of the target surfaces.

6.7 Conclusion

In this theoretical work, a simple trajectory simulation model has been presented for the image-charge interaction between a Rydberg molecule with any target surface of varying surface dopant charge field distribution and varying roughness of the surface. Ionization distances as a function of ion-extraction field are calculated using the simple OTB model in the presence of the surface potential. The surface potential variation is calculated by solving Poisson's equation, and it broadens the range of ionization distance. The ion detection probability is also strongly affected by the presence of

surface dopant charges in the surface region through interaction of these charges with the extracted ion. Comparison of the results for the H_2 Rydberg states incident at the various target surfaces with OTB predictions shows a very good qualitative agreement. The simulation study of a semiconductor surface clearly shows that the OTB approximation of ionization processes of the Rydberg molecules is affected by the β-factor, dopant type and dopant spacing of the Si surfaces. Furthermore, the surface ionization profile variation arising from the β-factor is considerably smaller compared with the variation arising from the surface dopant charges.

The trajectory simulations are modified to model the effects of surface roughness. It is found that the surface ionization profiles are very sensitive to the vertical variations than the lateral variations of the model surface. This work has provided a good explanation of the previous unexplained experimental work involving the ionization of the H_2 Rydberg molecule at a rough Al surface [153].

This simulation study offers new opportunities for studying and controlling the reactive process of image-charge interaction.

Chapter 7

Conclusion and future implementation

The interaction of Rydberg molecules or atoms with a metal surface has been studied both experimentally and theoretically by many researchers focusing on different systems using various approaches. The main focus of the work in this thesis is concerned with the surface ionization of molecular and atomic hydrogen Rydberg states incident on *p*- and *n*- type doped Si surfaces with various dopant densities for the first time.

Experimentally determined surface ionization profiles as a function of ion-extraction field have been presented for H_2 Rydberg molecules initially excited into $(nd2)_1$ states or states of the $N^+ = 2$ Stark manifold. Previous work by Softley and co-workers discovered that surface ionization of H_2 Rydberg molecules occurs through what they described as surface-induced rotational autoionization [70–72]. Experimentally determined surface ionization profiles do not vary smoothly as a function of applied ion-extraction field; instead they exhibit strong resonance behaviour due to the coupling between the populated $N^+ = 2$ channels and the energetically overlapping $N^+ = 0$ channel. In the work reported here, the experimental reproduction of these sharp resonances is independent of the nature of the target surface, but the relative inten-

sity of this resonance structure strongly depends on the surface. The low field onset of the observed surface-induced ionization profiles decreases with increasing principal quantum number due to an increase in the ionization distance between the Rydberg molecule and the surface.

The experimental studies presented here involving interaction of atomic hydrogen Rydberg states with Si surfaces also show similar variation of their surface ionization profiles with principal quantum number as a function of the ion-extraction field [123], but does not show the same resonance features.

The ion, or electron, detectability method is the best tool to compare many surface ionization profiles, and it gives a clear measurement of the ion detection probability for various doped Si surfaces. The ion detectability method shows that the p-type doped Si surfaces result in considerably higher ion detectability than the n-type doped Si surfaces and the ion detectability decreases with increasing dopant density for both p- and n- type doped Si surfaces. Furthermore, the atomically flat Au surface shows noticeably lower ion detectability than that of the doped Si surfaces except for the very highest dopant density. This is discussed by considering the distribution area of the positive charge islands due to the dopant atoms, and the magnitude of the dielectric shielding factor.

A trajectory simulation based on the simple OTB model was carried out including the presence of the surface dopant charge islands in the surface region. The surface potential was calculated by solving the linearized form of the Poisson equation with the spectral method. Experimental and trajectory simulated surface ionization profiles at lower ion-extraction field show noticeable variations according to dopant type and density. This variation arises from the distributed area of the surface dopant charge fields and the β-factor. The outputs of the theoretical trajectory simulations are in good qualitative agreement with experimental surface ionization profiles for molecular

hydrogen Rydberg states incident on the various Si surfaces, but quantitatively do not well fit with experimental results at low ion-extraction field. It should be possible to extend the simulations in the future to include the full three dimensional surface potential which can be measured using Kelvin probe microscopy (similar to the previous studies [50, 123]), which will give the actual magnitude of the delocalized surface charge and point charge. The trajectory simulations may then accurately fit both qualitatively and quantitatively when the real magnitudes of the surface potential in the surface region are included.

An interesting aspect of the work described in this thesis is an extension of the experimental studies of H_2 molecular Rydberg states to states populated in the presence of the Stark field. The interaction between $N^+ = 2$ and the $N^+ = 0$ rotational channels is revealed in great detail by the recording of surface ionization profiles of the $n = 17$, $N^+ = 2$ Stark states. In all the surface ionization profiles, an experimentally reproducible resonance signal appears for all k states, and the high-field cut-off limit appears at or just below the $N^+ = 0$ ionization threshold limit. Furthermore, the minimum field required to pull the ion away from the surface shows little or no dependence on the red- and blue- shifted Stark states, attributable to a mixing up of the polarization of the electron wavefunction on passage through the numerous avoided energy level crossings between the adjacent $N^+ = 2$ Rydberg states as the surface is approached, and also between the $N^+ = 2$ and $N^+ = 0$ levels. Once again, the overall ion detectability of the $n = 17$, $N^+ = 2$ Stark states shows similar variation between the various doped Si surface as discussed before, *i.e.* p-type doped Si surfaces have slightly higher ion detectability than the n-type doped Si surfaces, and ion detectability decreases with increasing the dopant density of doped Si surfaces. In general, the variations with dopant type and density show similar behaviour for Stark states, which are red- or blue- shifted, but one or two isolated states (*e.g.* $n = 17$, $k = +2$ Stark

state show more prominent variations in the surface ionization profiles).

Further investigation in this thesis also focused on the detection of electrons following ionization of H_2 molecular Rydberg states ($n = 17$, $N^+ = 2$). The detected electrons are produced from a backscattered loss mechanism as the Rydberg state approaches the surface. Experimental surface ionization profiles arising from the ion and electron detection scheme show similar behaviour in their ionization profiles, but the relative intensity varies, *i.e.* the surface ionization profiles arising from the electron detection scheme have a noticeably higher intensity ratio than the ion detection scheme for *p*- and *n*- type doped Si surfaces. Surprisingly, the *p*-type boron doped (9.00×10^{14} cm^{-3}) Si surface shows the highest intensity ratio in the surface ionization profiles using the ion detection scheme.

The *n*-type doped Si surfaces have shown noticeably higher electron detectability than the *p*-type doped Si surfaces, and the electron detectability increases with decreasing dopant density (similar to the ion detectability). This is discussed by considering the distribution area of the negative charge islands present in the surface region and the increase in the β-factor. However, in the case of *p*-type doped Si surfaces, the electron detectability *increases* with increasing the dopant density because the potential experienced by the electron has lower fluctuations at higher dopant density. At lower dopant density, widely spread out positive charge islands oppose production of backscattered electrons. The opposite behaviour compared to the ion detection scheme clearly indicates that the electron detection scheme follows a different mechanism of ionization. The electron detection scheme is more favourable to the lower dopant density for *n*-type Si surfaces, and the ion detection scheme is more favourable to the lower dopant density for *p*-type doped Si surfaces.

In the future, this research would be extended for example to study the interaction of atomic or molecular hydrogen Rydberg states with hydrocarbon adsorbates.

These studies could be carried out initially with simple systems ($C_6H_6/Cu_{(110)}$ or $C_6H_{12}/Cu_{(111)}$) [154] and then moving to a self-assembled alkane-thiol monolayer (SAM) on an Au surface. The electronic energy of the Rydberg electron is sufficient to cleave a C-H bond and so possibly initiating bond breaking and destruction of the hydrocarbon layers [155, 156]. Alternatively, ionization of the Rydberg molecules may occur in preference to bond fission, and then the molecular ion will undergo a very low energy collision with the adsorbate leading to ion-molecule chemistry; product ions desorbed from the surface could be detected by time-of-flight mass spectrometry. The collision energy for such processes would be determined by the initial kinetic energy of the neutral beam plus any acceleration near the surface after ionization, which is partly determined by the distance of ionization. This highly sensitive technique could also be applied in the C_6H_6/C_6H_{12} adsorbate systems and in the study of degeneration of SAMs [157].

Further experimental investigations could be carried out involving the interaction of different Rydberg molecules (CO, O_2 and N_2) with the surfaces and comparison can be made with H_2 Rydberg molecule. The rotational energy levels are much more widely spaced for H_2 Rydberg states ($B_{H_2^+} \sim 30.8\ cm^{-1}$) than for CO Rydberg states ($B_{CO^+} \sim 1.97\ cm^{-1}$), while the electronic energy spacing is identical. This will affect the nature of the surface-induced couplings between Rydberg series which couple through the molecular degrees of freedom. Many long lived Rydberg species have been observed in mass-analyzed threshold ionization spectroscopy [14], and so there are wide-ranging possibilities for Rydberg surface scattering studies, *e.g.* O_2 Rydberg molecules with $Ag_{(111)}$ and CO/NO Rydberg molecules with $Pt_{(100)}$.

In summary, charge transfer processes of atomic or molecular Rydberg states at Si surfaces are shown to be very sensitive to the distribution area of the surface dopant charge islands, due to dopant atoms in the surface layer. The work presented in this

thesis allowed comparision of the many surface ionization profiles via the relative ion or electron detectability methods. It has provided the opportunity to understand the nature of the various doped Si surfaces and is likely to promote further theoretical and experimental interest in the future. Furthermore, using the various Rydberg energy levels, it is possible to control the surface interaction and ionization dynamics, which can lead to future prospective implementations in surface characterization and surface chemistry.

Bibliography

[1] E. Amaldi and E. Segre. Effect of high pressure on terms of alkaline. *IL Nuovo Cimento (1924-1942)*, 11(3):145–156, 1934.

[2] P. A. Cox. Introduction to quantum theory and atomic structure. *Oxford University Press*, 1996.

[3] J. J. Balmer. Note on the spectral lines of hydrogen. *Annals of Physics*, 261(5):80–87, 1885.

[4] J. R. Rydberg. Royal Swedish vetenskapsakad handlinger. pp. 155., 1890.

[5] G. Alber and P. Zoller. Laser excitation of electronic wave packets in Rydberg atoms. *Physics Reports-Review Section of Physics Letters*, 199(5):232–280, 1991.

[6] G. Herzberg and C. Jungen. Rydberg series and ionization potential of H_2 molecule. *Journal of Molecular Spectroscopy*, 41(3):425–486, 1972.

[7] C. Jungen and O. Atabek. Rovibronic interactions in photoabsorption spectrum of molecular hydrogen and deuterium: An application of multichannel quantum defect methods. *Journal of Chemical Physics*, 66(12):5584–5609, 1977.

[8] P. M. Dehmer and W. A. Chupka. Very high resolution study of photoabsorption, photoionization, and predissociation in H_2. *Journal of Chemical Physics*, 65(6):2243–2273, 1976.

[9] M. Haugh, T. G. Slanger, and K. D. Bayes. Electronic excitation accompanying charge exchange. *Journal of Chemical Physics*, 44(2):837–839, 1966.

[10] J. Olmsted. Excitation of nitrogen triplet states by electron impact. *Radiation Research*, 31(2):191–200, 1967.

[11] T. F. Gallagher. Rydberg atoms. *Cambridge University Press*, 1994.

[12] F. B. Dunning and R. F. Stebbings. Collisions of Rydberg atoms with molecules. *Annual Review of Physical Chemistry*, 33:173–189, 1982.

[13] U. Hollenstein, H. Palm, and F. Merkt. A broadly tunable extreme ultraviolet laser source with a 0.008 cm^{-1} bandwidth. *Review of Scientific Instruments*, 71(11):4023–4028, 2000.

[14] T. P. Softley. Applications of molecular Rydberg states in chemical dynamics and spectroscopy. *International Reviews in Physical Chemistry*, 23(1):1–78, 2004.

[15] N. P. L. Wales, W. J. Buma, C. A. de Lange, H. LefebvreBrion, K. H. Wang, and V. McKoy. Zero-Kinetic-Energy Pulsed-Field Ionization and Resonance Enhanced Multi-Photon Ionization Photoelectron Spectroscopy: Ionization dynamics of Rydberg states in HBr. *Journal of Chemical Physics*, 104(13):4911–4919, 1996.

[16] J. D. D. Martin, J. W. Hepburn, and C. Alcaraz. Efficiency of high-n Rydberg-state stabilization in Pulsed-Field Ionization Zero-Kinetic-Energy Photoelectron Spectroscopy. *Journal of Physical Chemistry A*, 101(36):6728–6735, 1997.

[17] L. C. Zhu and P. Johnson. Mass Analyzed Threshold Ionization spectroscopy. *Journal of Chemical Physics*, 94(8):5769–5771, 1991.

[18] F. Merkt. Molecules in high Rydberg states. *Annual Review of Physical Chemistry*, 48:675–709, 1997.

[19] M. J. Seaton. Quantum defect theory .I. General formulation. *Proceedings of the Physical Society of London*, 88(562P):801–814, 1966.

[20] M. J. Seaton. Quantum defect theory .II. Illustrative one channel and two channel problems. *Proceedings of the Physical Society of London*, 88(562P):815–832, 1966.

[21] U. Fano. Quantum defect theory of l uncoupling in H_2 as an example of channel interaction treatment. *Physical Review A*, 2(2):353–365, 1970.

[22] A. Sommerfeld. For the quantum theory of spectral lines. *Annals of Physics*, 51(17):1–94, 1916.

[23] R. N. Zare. Angular momentum: understanding spatial aspects in chemistry and physics. *Wiley*, 1988.

[24] H. A. Bethe and E. E. Salpeter. Quantum mechanics of one- and two- electron atoms. *Dover*, 2008.

[25] N. Bohr. On the constitution of atoms and molecules. *Philos. Mag.*, 26(1):1–24, 1913.

[26] Y. N. Gnedin, A. A. Mihajlov, L. M. Ignjatovic, N. M. Sakan, V. A. Sreckovic, M. Y. Zakharov, N. N. Bezuglov, and A. N. Klycharev. Rydberg atoms in astrophysics. *New Astronomy Reviews*, 53(7-10):259–265, 2009.

[27] S. A. Gulyaev, S. A. Nefedov, and USSR. Sverdlovsk. Populations of Rydberg states of atoms in nebulae. *Astronomische Nachrichten*, 312(1):27–31, 1991.

[28] J. T. Mendonca. Physics of ultra cold and Rydberg plasmas. *Frontiers of Fundamental and Computational Physics*, 1246:36–44, 2010.

[29] F. Merkt, S. R. Mackenzie, and T. P. Softley. Preparation of ions in selected rotational states by delayed pulsed-field ionization. *Journal of Chemical Physics*, 99(5):4213–4214, 1993.

[30] S. R. Mackenzie and T. P. Softley. New experimental method for studying rotationally state selected ion molecule reactions. *Journal of Chemical Physics*, 101(12):10609–10617, 1994.

[31] M. Matsuzawa. Highly excited Rydberg electron as a spectator to an ion-molecule reaction. *Physical Review A*, 82(5):054701 (1–3), 2010.

[32] S. R. Procter, Y. Yamakita, F. Merkt, and T. P. Softley. Controlling the motion of hydrogen molecules. *Chemical Physics Letters*, 374(5-6):667–675, 2003.

[33] E. Vliegen, H. J. Worner, T. P. Softley, and F. Merkt. Nonhydrogenic effects in the deceleration of Rydberg atoms in inhomogeneous electric fields. *Physical Review Letters*, 92(3):033005 (1–4), 2004.

[34] Q. Y. Shang and E. R. Bernstein. Energetics, dynamics, and reactions of Rydberg state molecules in Van der Waals clusters. *Chemical Reviews*, 94(7):2015–2025, 1994.

[35] K. Siglow and H. J. Neusser. Resolved high Rydberg spectroscopy of polyatomic molecules and Van der Waals clusters. *Faraday Discussions*, 115:245–257, 2000.

[36] M. Schnell and G. Meijer. Cold molecules: Preparation, applications, and challenges. *Angewandte Chemie-International Edition*, 48(33):6010–6031, 2009.

[37] X. Tong, D. Wild, and S. Willitsch. Collisional and radiative effects in the state-selective preparation of translationally cold molecular ions in ion traps. *Physical Review A*, 83(2):023415 (1–10), 2011.

[38] E. S. Chang. Radiative lifetime of hydrogenic and quasihydrogenic atoms. *Physical Review A*, 31(1):495–498, 1985.

[39] T. F. Gallagher and W. E. Cooke. Interactions of blackbody radiation with atoms. *Physical Review Letters*, 42(13):835–839, 1979.

[40] I. I. Beterov, D. B. Tretyakov, I. I. Ryabtsev, A. Ekers, and N. N. Bezuglov. Ionization of sodium and rubidium nS, nP, and nD Rydberg atoms by blackbody radiation. *Physical Review A*, 75(5):052720 (1–13), 2007.

[41] I. L. Glukhov, E. A. Nekipelov, and V. D. Ovsiannikov. Blackbody-induced decay, excitation and ionization rates for Rydberg states in hydrogen and helium atoms. *Journal of Physics B-Atomic Molecular and Optical Physics*, 43(12):125002(1–14), 2010.

[42] X. X. Lu, Y. Sun, and H. Metcalf. Rydberg atom spectroscopy enabled by blackbody radiation ionization. *Physical Review A*, 84(3):033402 (1–7), 2011.

[43] C. E. Burkhardt, R. L. Corey, W. P. Garver, J. J. Leventhal, M. Allegrini, and L. Moi. Ionization of Rydberg atoms. *Physical Review A*, 34(1):80–86, 1986.

[44] T. F. Gallagher. Interaction of Rydberg atoms with blackbody radiation. In R. F. Stebbings and F. B. Dunning, editors, Rydberg states of atoms and molecules, pages 165–186. *Cambridge University Press*, 2011.

[45] P. W. Atkins and R. Friedman. Molecular quantum mechanics. *Oxford University Press*, 4th edition, 2005.

[46] E. So. Interaction of Rydberg hydrogen atoms with metal surfaces, *DPhil thesis*, University of Oxford, 2011.

[47] R. J. Damburg and V. V. Kolosov. Theoretical studies of hydrogen Rydberg atoms in electric fields. In R. F. Stebbings and F. B. Dunning, editors, Rydberg states of atoms and molecules, pages 31–72. *Cambridge University Press*, 2011.

[48] J. R. Rubbmark, M. M. Kash, M. G. Littman, and D. Kleppner. Dynamical effects at avoided level crossings: A study of the Landau-Zener effect using Rydberg atoms. *Physical Review A*, 23(6):3107–3117, 1981.

[49] W. A. Chupka. Factors affecting lifetimes and resolution of Rydberg states observed in zero-electron-kinetic-energy spectroscopy. *Journal of Chemical Physics*, 98(6):4520–4530, 1993.

[50] Y. Pu, D. D. Neufeld, and F. B. Dunning. Ionization of Rydberg atoms at metallic surfaces: Influence of stray fields. *Physical Review A*, 81(4):042904 (1–6), 2010.

[51] F. Merkt and R. N. Zare. On the lifetimes of Rydberg states probed by delayed pulsed field ionization. *Journal of Chemical Physics*, 101(5):3495–3505, 1994.

[52] S. B. Hill, C. B. Haich, Z. Zhou, P. Nordlander, and F. B. Dunning. Ionization of xenon Rydberg atoms at a metal surface. *Physical Review Letters*, 85(25):5444–5447, 2000.

[53] M. A. Cazalilla, N. Lorente, R. D. Muino, J. P. Gauyacq, D. Teillet-Billy, and P. M. Echenique. Theory of Auger neutralization and deexcitation of slow ions at metal surfaces. *Physical Review B*, 58(20):13991–14006, 1998.

[54] D. D. Neufeld, H. R. Dunham, S. Wethekam, J. C. Lancaster, and F. B. Dunning. Ionization of xenon Rydberg atoms at oxidized Si(100) surfaces. *Surface Science*, 602(7):1306–1312, 2008.

[55] H. R. Dunham, S. Wethekam, J. C. Lancaster, and F. B. Dunning. Ionization of xenon Rydberg atoms at Si(100) surfaces. *Nuclear Instruments and Methods in Physics Research Section B-Beam Interactions with Materials and Atoms*, 256(1):46–49, 2007.

[56] F. B. Dunning, S. Wethekam, H. R. Dunham, and J. C. Lancaster. Charge transfer rates for xenon Rydberg atoms at metal and semiconductor surfaces. *Nuclear Instruments and Methods in Physics Research Section B-Beam Interactions with Materials and Atoms*, 258(1):61–67, 2007.

[57] Z. Zhou, C. Oubre, S. B. Hill, P. Nordlander, and F. B. Dunning. Ionization of xenon Rydberg atoms at surface. *Nuclear Instruments and Methods in Physics Research Section B-Beam Interactions with Materials and Atoms*, 193:403–407, 2002.

[58] J. E. Lennard-Jones. Processes of adsorption and diffusion on solid surfaces. *Transactions of the Faraday Society*, 28:333–359, 1932.

[59] H. Winter. Image charge effects in ion surface scattering. *Journal of Physics-Condensed Matter*, 8(49):10149–10183, 1996.

[60] K. Ganesan and K. T. Taylor. Rydberg states of the hydrogen atom near a metal surface. *Journal of Physics B-Atomic Molecular and Optical Physics*, 29(7):1293–1306, 1996.

[61] R. O. Jones, P. J. Jennings, and O. Jepsen. Surface barrier in metals: A new model with application to W(001). *Physical Review B*, 29(12):6474–6480, 1984.

[62] P. J. Jennings, R. O. Jones, and M. Weinert. Surface barrier for electrons in metals. *Physical Review B*, 37(11):6113–6120, 1988.

[63] F. Martin and M. F. Politis. Multicenter-Gaussian representation of resonant charge transfer in atom-surface interaction. *Surface Science*, 356(1-3):247–256, 1996.

[64] P. Nordlander and J. C. Tully. Energy shifts and broadening of atomic levels near metal surfaces. *Physical Review B*, 42(9):5564–5578, 1990.

[65] A. Anderson, S. Haroche, E. A. Hinds, W. Jhe, and D. Meschede. Measuring the Van der Waal's forces between a Rydberg atom and a metallic surface. *Physical Review A*, 37(9):3594–3597, 1988.

[66] C. Fabre, M. Gross, J. M. Raimond, and S. Haroche. Measuring atomic dimensions by transmission of Rydberg atoms through micrometer size slits. *Journal of Physics B-Atomic Molecular and Optical Physics*, 16(21):L671–L677, 1983.

[67] C. A. Kocher and C. R. Taylor. High-Rydberg atoms as probes of surface electric fields and sub-monolayer adsorption. *Physics Letters A*, 124(1-2):68–72, 1987.

[68] F. B. Dunning, H. R. Dunham, C. Oubre, and P. Nordlander. Behaviour of Rydberg energy level shifts atoms at surfaces: and ionization. *Nuclear Instruments and Methods in Physics Research Section B-Beam Interactions with Materials and Atoms*, 203:69–75, 2003.

[69] S. Wethekam, H. R. Dunham, J. C. Lancaster, and F. B. Dunning. Charge transfer rates for xenon Rydberg atoms at a metal surface. *Physical Review A*, 73(3):032903 (1–5), 2006.

[70] G. R. Lloyd, S. R. Procter, and T. P. Softley. Ionization of hydrogen Rydberg molecules at a metal surface. *Physical Review Letters*, 95(13):133202 (1–4), 2005.

[71] G. R. Lloyd, S. R. Procter, E. A. McCormack, and T. P. Softley. Ionization of H_2 Rydberg molecules at a metal surface. *Journal of Chemical Physics*, 126(18):184702 (1–14), 2007.

[72] E. A. McCormack, M. S. Ford, and T. P. Softley. Level crossings in the ionization of H_2 Rydberg molecules at a metal surface. *Journal of Physical Chemistry A*, 114(42):11175–11188, 2010.

[73] D. F. Gray, Z. Zheng, K. A. Smith, and F. B. Dunning. Ionization of K(nd) Rydberg state atoms at a surface. *Physical Review A*, 38(3):1601–1603, 1988.

[74] E. A. McCormack, E. So, M. Dethlefsen, M. S. Ford, and T. P. Softley. Detection of electrons in the surface ionization of H Rydberg atoms and H_2 Rydberg molecules. *Journal of Physics B-Atomic Molecular and Optical Physics*, 45(1):015204 (1–9), 2012.

[75] S. R. Mackenzie, E. J. Halse, F. Merkt, and T. P. Softley. Rotationally state-selected ion-molecule reactions studied using pulsed-field ionization techniques. *Laser Techniques for State-Selected and State-to-State Chemistry III*, 2548:293–304, 1995.

[76] S. R. Mackenzie, E. J. Halse, E. Gordon, D. Rolland, and T. P. Softley. Pulsed-field ionization spectroscopy of CO via the $E^1\Pi$ state and NO via the $B^2\Pi$ state. *Chemical Physics*, 209(2-3):127–141, 1996.

[77] A. A. Radzig and B. M. Smirnov. Reference data on atoms, molecules, and ions. Springer series in chemical physics. *Springer-Verlag*, 1985.

[78] P. Q. Wang, C. S. Cao, and T. H. Sun. Two-photon resonant third harmonic generation in carbon monoxide. *Chinese Physics Letters*, 14(5):360–363, 1997.

[79] C. R. Vidal. Four wave frequency mixing in gases. *Topics in Applied Physics*, 59:57–113, 1987.

[80] A. Yariv. Quantum electronics. *Wiley*, 3rd edition, 1989.

[81] J. Kutzner and H. Zacharias. VUV generation by frequency tripling the third harmonic of a picosecond kHz Nd:YLF laser in xenon and mercury vapour. *Applied Physics B-Lasers and Optics*, 66(5):571–577, 1998.

[82] R. Mahon, T. J. McIlrath, V. P. Myerscough, and D. W. Koopman. Third-harmonic generation in argon, krypton, and xenon: Bandwidth limitations in the vicinity of lyman-α. *Ieee Journal of Quantum Electronics*, 15(6):444–451, 1979.

[83] R. Hilbig and R. Wallenstein. Enhanced production of tunable VUV radiation by phase-matched frequency tripling in krypton and xenon. *Ieee Journal of Quantum Electronics*, 17(8):1566–1573, 1981.

[84] S. D. Kramer, C. H. Chen, and M. G. Payne. Geometry independent, phase-matched measurement of a vacuum ultraviolet oscillator strength in xenon. *Optics Letters*, 9(8):347–349, 1984.

[85] S. D. Kramer, C. H. Chen, and M. G. Payne. Direct measurement of a VUV transition oscillator strength in xenon. *Aip Conference Proceedings*, (119):363–369, 1984.

[86] S. R. Procter. Control of atomic and molecular motion via the Stark effect in Rydberg states, *DPhil thesis*, University of Oxford, 2003.

[87] H. Rottke and K. H. Welge. Singlet gerade Rydberg states of molecular hydrogen. *Journal of Chemical Physics*, 97(2):908–926, 1992.

[88] H. Schmoranzer and J. Imschweiler. Radiative lifetimes and collisional quenching cross-sections of selectively excited vibrational states of the B 2p $^1\Sigma_u^+$ State of H_2. *Physics Letters A*, 100(2):85–87, 1984.

[89] J. M. Brown and A. Carrington. Rotational spectroscopy of diatomic molecules. *Cambridge University Press*, 2003.

[90] G. Herzberg and C. Jungen. High orbital angular momentum states in H_2 and D_2. *Journal of Chemical Physics*, 77(12):5876–5884, 1982.

[91] J. M. Gilligan and E. E. Eyler. Precise determinations of ionization-potentials and EF-state energy-levels of H_2, HD, and D_2. *Physical Review A*, 46(7):3676–3690, 1992.

[92] S. R. Mackenzie. Zero-kinetic-energy photoelectron spectroscopy and the study of state-selected ion molecule reactions, *DPhil thesis*, University of Oxford, 1995.

[93] Y. Yamakita, S. R. Procter, A. L. Goodgame, T. P. Softley, and F. Merkt. Deflection and deceleration of hydrogen Rydberg molecules in inhomogeneous electric fields. *Journal of Chemical Physics*, 121(3):1419–1431, 2004.

[94] T. P. Softley, S. R. Procter, Y. Yamakita, G. Maguire, and F. Merkt. Controlling the motion of hydrogen molecules: design of a two-dipole Rydberg decelerator. *Journal of Electron Spectroscopy and Related Phenomena*, 144:113–117, 2005.

[95] E. A. McCormack. Ionisation of hydrogen Rydberg molecules at surfaces, *DPhil thesis*, University of Oxford, 2010.

[96] W. C. Wiley and I. H. Mclaren. Time-of-flight mass spectrometer with improved resolution. *Review of Scientific Instruments*, 26(12):1150–1157, 1955.

[97] A. Osterwalder. Millimeter wellenspektroskopie hoher Rydbergzustade von atomen und molekulen, *PhD thesis*, ETH Zurich, 2002.

[98] W. L. Glab, K. Qin, and M. Bistransin. Rotational and vibrational interactions of singlet gerade Rydberg states of H_2 near the ionization limit. *Journal of Chemical Physics*, 102(6):2338–2350, 1995.

[99] S. Ristic, A. Prijic, and Z. Prijic. Dependence of static dielectric constant of silicon on resistivity at room temperature. *Serbian Journal of Electrical Engineering*, 1(2):237–247, 2004.

[100] T. Trappmann, C. Surgers, and H. V. Lohneysen. Investigation of the (111) surface of P-doped Si by scanning tunneling microscopy. *Applied Physics A-Materials Science and Processing*, 68(2):167–172, 1999.

[101] M. Schock, C. Surgers, and H. V. Lohneysen. Investigation of single boron accepters at the cleaved Si:B(111) surface. *Physical Review B*, 61(11):7622–7627, 2000.

[102] U. Thumser, P. Beck, and D. Stewark. SiO_2 growth in Stanford Microfab ambient. *Retrieved from: http://snf.stanford.edu/Process/Characterization/SiO_2 Growth0.pdf*, 2001.

[103] E. J. Galvez, C. W. MacGregor, B. Chaudhuri, S. Gupta, E. Massoni, and F. DeZela. Blackbody-radiation-induced resonances between Rydberg-Stark states of Na. *Physical Review A*, 55(4):3002–3006, 1997.

[104] P. Nordlander. Energies and lifetimes of atomic Rydberg states near metal surfaces. *Physical Review B*, 53(7):4125–4132, 1996.

[105] D. Shamiryan, M. Baklanov, and S. Vanhaelemeersch. Silicon surface cleaning after spacer dry etching. *Solid State Phenomena*, 76-77:303–306, 2001.

[106] D. D. Neufeld, H. R. Dunham, S. Wethekam, J. C. Lancaster, and F. B. Dunning. Ionization of xenon Rydberg atoms at Au(111) surfaces: Effect of stray fields. *Physical Review B*, 78(11):115423 (1–7), 2008.

[107] T. Trappmann, C. Surgers, and H. V. Lohneysen. Observation of P donors on the Si(111) surface by scanning tunneling microscopy. *Europhysics Letters*, 38(3):177–182, 1997.

[108] A. Osterwalder, A. Wuest, F. Merkt, and C. Jungen. High-resolution millimeter wave spectroscopy and multichannel quantum defect theory of the hyperfine structure in high Rydberg states of molecular hydrogen H_2. *Journal of Chemical Physics*, 121(23):11810–11838, 2004.

[109] B. B. Clarson, S. R. Procter, A. L. Goodgame, and T. P. Softley. The Stark effect in the predissociating Rydberg states of NO. *Molecular Physics*, 106(9-10):1317–1330, 2008.

[110] A. L. Goodgame, H. Dickinson, S. R. Mackenzie, and T. P. Softley. The Stark effect in the $v^+ = 1$ autoionizing Rydberg states of NO. *Journal of Chemical Physics*, 116(12):4922–4937, 2002.

[111] H. J. Silverstone. Perturbation theory of Stark effect in hydrogen to arbitrarily high order. *Physical Review A*, 18(5):1853–1864, 1978.

[112] M. L. Zimmerman, M. G. Littman, M. M. Kash, and D. Kleppner. Stark structure of the Rydberg states of alkali metal atoms. *Physical Review A*, 20(6):2251–2275, 1979.

[113] I. L. Bolgova, V. D. Ovsyannikov, V. G. Pal'chikov, A. I. Magunov, and G. von Oppen. Higher orders of perturbation theory for the Stark effect on an atomic multiplet. *Journal of Experimental and Theoretical Physics*, 96(6):1006–1018, 2003.

[114] H. H. Fielding and T. P. Softley. Observation of the Stark effect in autoionizing Rydberg states of molecular hydrogen. *Chemical Physics Letters*, 185(3-4):199–205, 1991.

[115] J. B. M. Warntjes, F. Robicheaux, J. M. Bakker, and L. D. Noordam. Autoionizing Rydberg states of NO in strong electric fields. *Journal of Chemical Physics*, 111(6):2556–2564, 1999.

[116] N. J. A. Jones, R. S. Minns, R. Patel, and H. H. Fielding. Observation of the Stark effect in $v^+ = 0$ Rydberg states of NO: a comparison between predissociating and bound states. *Journal of Physics B-Atomic Molecular and Optical Physics*, 41(18):1–8, 2008.

[117] W. L. Glab and J. P. Hessler. Ionization and dissociation of H_2 in a static electric field: Llevels near the ionization threshold. *Physical Review A*, 42(9):5486–5499, 1990.

[118] F. B. Dunning and R. F. Stebbings. Experimental studies of thermal-energy collisions of Rydberg atoms with molecules. In R. F. Stebbings and F. B. Dunning, editors, Rydberg states of atoms and molecules, pages 315–353. *Cambridge University Press*, 2011.

[119] F. G. Kellert, T. H. Jeys, G. B. McMillian, K. A. Smith, F. B. Dunning, and R. F. Stebbings. Study of Rydberg atom l-changing collisions using selective field ionization. *Physical Review A*, 23(3):1127–1133, 1981.

[120] C. T. W. Lahaye, W. Hogervorst, and T. Van der Veldt. Avoided level crossings in bound Rydberg states of barium in an electric field. *Zeitschrift Fur Physik D-Atoms Molecules and Clusters*, 13(2):107–113, 1989.

[121] C. T. W. Lahaye and W. Hogervorst. Stark manifolds and electric-field-induced avoided level crossings in helium Rydberg states. *Physical Review A*, 39(11):5658–5665, 1989.

[122] M. G. Littman, M. L. Zimmerman, T. W. Ducas, R. R. Freeman, and D. Kleppner. Structure of sodium Rydberg states in weak to strong electric fields. *Physical Review Letters*, 36(14):788–791, 1976.

[123] E. So, M. Dethlefsen, M. Ford, and T. P. Softley. Charge transfer of Rydberg H atoms at a metal surface. *Physical Review Letters*, 107(9):093201 (1–5), 2011.

[124] A. L. Goodgame and T. P. Softley. Control of atomic and molecular motion via the Stark effect in Rydberg states. *Journal of Physics B-Atomic Molecular and Optical Physics*, 32(20):4839–4857, 1999.

[125] J. Sjakste, A. G. Borisov, and J. P. Gauyacq. Ionization of Rydberg atoms colliding with a metal surface. *Physical Review A*, 73(4):042903 (1–11), 2006.

[126] E. So, M. T. Bell, and T. P. Softley. Wave-packet propagation study of the charge-transfer dynamics of Rydberg atoms with metal surfaces. *Physical Review A*, 79(1):012901 (1–15), 2009.

[127] N. Lorente, M. A. Cazalilla, J. P. Gauyacq, D. Teillet-Billy, and P. M. Echenique. Auger neutralization and de-excitation of helium at an aluminium surface: a unified treatment. *Surface Science*, 411(3):L888–L893, 1998.

[128] Y. Cho, C. Kim, H. Ahn, E. Cho, T. Kim, and S. Han. First-principles study on secondary electron emission of MgO surface. *Journal of Applied Physics*, 101(8):083710 (1–7), 2007.

[129] I. G. Barber. Secondary electron emission from copper surfaces. *Physical Review*, 17(3):322–338, 1921.

[130] A. G. Borisov, D. Teillet-Billy, and J. P. Gauyacq. Energy shift and broadening of H levels in front of a metal surface. *Nuclear Instruments and Methods in Physics Research Section B-Beam Interactions with Materials and Atoms*, 78(1-4):49–55, 1993.

[131] N. S. Simonovic. Classical chaos in the hydrogen atom near a metal surface. *Journal of Physics B-Atomic Molecular and Optical Physics*, 30(18):L613–L618, 1997.

[132] N. S. Simonovic and J. P. Salas. Hydrogen atom in the instantaneous Van der Waals potential: Pitchfork bifurcation and ro-vibrational structure of the energy spectrum. *Physics Letters A*, 279(5-6):379–384, 2001.

[133] J. A. M. C. Silva, J. Wolfgang, A. G. Borisov, J. P. Gauyacq, P. Nordlander, and D. Teillet-Billy. Effect of a surface Al adatom on the resonant charge transfer between an H^- ion and an Al(111) surface. *Surface Science*, 506(1-2):145–160, 2002.

[134] A. Afaq and M. L. Du. A theoretical imaging method for the photodetachment of H^- near a reflecting surface. *Journal of Physics B-Atomic Molecular and Optical Physics*, 40(6):1309–1321, 2007.

[135] D. Wang, K. Huang, and S. Lin. Semiclassical calculation of ionization rate for Rydberg hydrogen atoms near a metal surface. *European Physical Journal D*, 54(3):699–706, 2009.

[136] B. C. Yang and M. L. Du. Modifying the photodetachment near a metal surface by a weak electric field. *Journal of Physics B-Atomic Molecular and Optical Physics*, 43(3):035002 (1–5), 2010.

[137] A. Kirchberg, J. D. Lange, P. A. G. Pisani, and A. Wipf. Algebraic solution of the supersymmetric hydrogen atom in d dimensions. *Annals of Physics*, 303(2):359–388, 2003.

[138] E. Vliegen and F. Merkt. Stark deceleration of hydrogen atoms. *Journal of Physics B-Atomic Molecular and Optical Physics*, 39(11):241–247, 2006.

[139] E. Vliegen and F. Merkt. Normal incidence electrostatic Rydberg atom mirror. *Physical Review Letters*, 97(3):033002 (1–4), 2006.

[140] E. Vliegen, S. D. Hogan, H. Schmutz, and F. Merkt. Stark deceleration and trapping of hydrogen Rydberg atoms. *Physical Review A*, 76(2):023405 (1–6), 2007.

[141] V. M. Donnelly, A. P. Baronavski, and J. R. Mcdonald. ArF-laser photodissociation of NH_3 at 193 nm: internal energy distributions in NH_2 $\widetilde{X}^2B_1$ and $\widetilde{A}^2A_1$, and 2-photon generation of NH $A^3\Pi$ and $b^1\Sigma^+$. *Chemical Physics*, 43(2):271–281, 1979.

[142] V. M. Donnelly, A. P. Baronavski, and J. R. Mcdonald. Excited-state dynamics and bimolecular quenching processes for NH_2 ($\widetilde{A}^2A_1$). *Chemical Physics*, 43(2):283–293, 1979.

[143] R. D. Kenner, R. K. Browarzik, and F. Stuhl. Two-photon formation of NH/ND ($A^3\Pi$) in the 193 nm photolysis of ammonia 2. Photolysis of NH_2. *Chemical Physics*, 121(3):457–471, 1988.

[144] C. Delsart, L. Cabaret, C. Blondel, and R. J. Champeau. Two-step high-resolution laser spectroscopy of the Stark substates of the $n = 33$ level in atomic hydrogen. *Journal of Physics B-Atomic Molecular and Optical Physics*, 20(18):4699–4713, 1987.

[145] R. S. Freund. High-Rydberg molecules. In R. F. Stebbings and F. B. Dunning, editors, Rydberg states of atoms and molecules, pages 355–392. *Cambridge University Press*, 2011.

[146] B. F. Parsons, D. E. Szpunar, and L. J. Butler. H atom high-n Rydberg time-of-flight spectroscopy of C-H bond fission in acrolein dissociated at 193 nm. *Journal of Chemical Physics*, 117(17):7889–7895, 2002.

[147] J. P. Marangos, N. Shen, H. Ma, M. H. R. Hutchinson, and J. P. Connerade. Broadly tunable vacuum ultraviolet radiation source employing resonant enhanced sum-difference frequency mixing in krypton. *Journal of the Optical Society of America B-Optical Physics*, 7(7):1254–1259, 1990.

[148] M. Dethlefsen. University of Oxford, *Private communication*.

[149] M. Inarrea, V. Lanchares, J. F. Palacian, A. I. Pascual, J. P. Salas, and P. Yanguas. Rydberg hydrogen atom near a metallic surface: Stark regime and ionization dynamics. *Physical Review A*, 76(5):052903 (1–9), 2007.

[150] W. H. Press. Numerical recipes in FORTRAN : the art of scientific computing. *Cambridge University Press*, 2nd edition, 1992.

[151] K. A. Reinhardt and W. Kern. Handbook of silicon wafer cleaning technology. *William Andrew*, 2nd edition, 2008.

[152] N. Gaillard, M. Gros-Jean, D. Mariolle, F. Bertin, and A. Bsiesy. Method to assess the grain crystallographic orientation with a submicronic spatial resolution using Kelvin probe force microscope. *Applied Physics Letters*, 89(15):154101 (1–3), 2006.

[153] G. R. Lloyd. Interaction of molecular Rydberg states with metal surfaces, *DPhil thesis*, University of Oxford, 2005.

[154] D. Yamaguchi, T. Matsumoto, K. Watanabe, N. Takagi, and Y. Matsumoto. Photochemistry of cyclohexane on Cu(111). *Physical Chemistry Chemical Physics*, 8(1):179–185, 2006.

[155] C. Xu and B. E. Koel. Electron-induced dissociation of hydrocarbon multilayers. *Surface Science*, 292(1-2):L803–L809, 1993.

[156] W. Lu, K. G. H. Baldwin, M. D. Hoogerland, S. J. Buckman, T. J. Senden, T. E. Sheridan, and R. W. Boswell. Sharp edged silicon structures generated using atom lithography with metastable helium atoms. *Journal of Vacuum Science and Technology B*, 16(6):3846–3849, 1998.

[157] S. Sohn, M. Schroder, D. Lipinsky, and H. F. Arlinghaus. ToF-SIMS investigations of the degeneration processes of self-assembled monolayers of alkanethiols on gold. *Surface and Interface Analysis*, 36(8):1222–1226, 2004.